UNIVERSITÀ DEGLI STUDI DI TRIESTE

XXVI Ciclo del Dottorato di Ricerca in

Fisica

Broad band acoustic spectroscopy in disordered systems

Settore scientifico – disciplinare: FIS/03 - Fisica della Materia

DOTTORANDO

Andrea Battistoni

DIRETTORE DELLA SCUOLA DI DOTTORATO

Prof. Paolo Camerini

SUPERVISORE DI TESI

PhD. Filippo Bencivenga

ANNO ACCADEMICO 2013/2014

Abstract

The present work of thesis is situated within the framework of the study of disordered systems as liquids and glasses. A liquid is a system characterized by long range translational invariance and by a short range ordered structure. In the liquid state, contrarily to the crystalline one, there is not structural periodicity and all we learnt from solid state physics (Block's theorem, phonons, Brillouin's zones, eigen-states of plane waves, etc.) must be fully revised.

The macroscopic collective properties of condensed matter are the result of inter and intra-molecular interactions that are typified by characteristic time and space scales. A longstanding and powerful tool to investigate the collective nature of the microscopic processes inside the system is the acoustic spectroscopy. While in the case of crystalline phase we could take advantage of the periodical structure of the system, limiting our investigation to the so called first Brillouin zone, in order to characterize a disordered system we need to explore a widest as possible spectral range to access the all time and space scales in which the dynamical phenomena occur. This approach can be called *Broad Band Acoustic Spectroscopy*.

My PhD activity was devoted to the development of new experimental methods and techniques allowing the exploration with continuity of dynamics evolving with timescales from tenth's of ns's to ps's. I could test such Broad Band Acoustic Spectroscopy on a prototypical sample: acetonitrile, the liquid with highest dipole moment, known for its many different inter- and intra-molecular dynamics. Using several experimental and computational approaches I could characterize the main dynamical processes for such compound in its whole liquid phase. Thanks to the crossing of the all acquired information, it was possible to identify a mutual influence between different relaxations whose behaviour otherwise was not possible to correctly understand.

After a brief introduction to contextualize the Broad Band Acoustic Spectroscopy in disordered systems, in Chapter 1 is presented an overview of the experimental techniques used to perform the measurements within this work. In this chapter, the first my original contribution to the extension of acoustic spectral range finds the place. Thanks to the design and realization of particular spatial filters it is now possible to perform Brillouin Light Scattering experiments with angle tunability without incurring in annoying spurious contributions issues. In the chapter are also recalled the main physical principles at the ground of every presented technique, in particular stressing the complementarity of the energy and time resolved spectroscopies.

Because all the information from the inner dynamics of the sample are mediated by the acoustic modes interaction, Chapter 2 is dedicated to the formalism of the

density fluctuations, highlighting the differences between the hydrodynamic model, valid at macroscopic length-scales, and the memory functions approach, necessary to describe the mesoscopic region where the characteristic length-scales of the acoustic modes are comparable to the inter-particles distances.

In Chapter 3 are shown the experimental results obtained thanks to the Broad Band Spectroscopy in the whole temperature range of the liquid phase of acetonitrile. We could first measure some thermodynamical quantities by a non linear spectroscopy named Transient Grating, shedding light on the literature debate on them. Among the obtained results, we appreciated a temperature dependency of the heat capacity ratio which is usually considered a constant. Starting from these results and using the filtering approach introduced in Chapter 1, we could profitably study the vibrational relaxation of acetonitrile discovering some relevant discrepancies with previous studies. In this way we demonstrated the importance to avoid eventual spurious contributions and to have complementary information from different spectral domains. Then there will be shown the results for the so called structural relaxation, obtained in the high energy domain by Inelastic X-ray Scattering. A really interesting correlation has been found with the result obtained by the ultrafast response of the Transient Grating method. Once again, to obtain such comparison was necessary to combine the information arising from many different spectral ranges, fact that highlights the utility and endorses the multi-techniques broad band acoustic spectroscopy method.

The temperature dependence of the aforementioned relaxation processes suggested to evaluate if any coupling there exist between the two. This is exactly what we were able to appreciate in the deep-UV domain and we proposed a phenomenological model to give a picture of the occurring interaction.

To further investigate such dynamics coupling effect, could be extremely useful to explore the soft-UV spectral range but so far any technique was able to access such energy domain. In Chapter 4 we thus present our innovative solution to the problem: a novel table top Fabry-Perot interferometer conceived to operate with UV laser source and with only reflecting optics.

The last chapters of the thesis describe my contribution to the forthcoming Free Electron Laser (FEL) based experiment to further increase the accessible spectral range to the acoustic spectroscopy: the TIMER project. In particular I will show the result obtained with the pilot experiment named "mini-TIMER" in which we could demonstrate the feasibility of a Transient Grating experiment in the Extreme Ultra Violet (EUV) domain. When TIMER will be operative it will be the first experimental setup able to probe the EUV mesoscopic region of crucial importance for the study of glasses and nano-structures. This result paves the way to a new class of intriguing experiments only matter of theoretical considerations so far: the so called four wave mixing experiments with elemental selectivity.

Sommario

Il presente lavoro di tesi si colloca nell'ambito dello studio dei sistemi disordinati quali liquidi e vetri. Un liquido é un sistema caratterizzato da invarianza traslazionale a lungo raggio e da una struttura ordinata a corto raggio. Lo stato liquido, a differenza di quello cristallino, non gode di una periodicità strutturale e tutto ciò che avevamo imparato dalla fisica dello stato solido (teorema di Block, fononi, zone di Brillouin, autostati di onde piane, etc.) deve essere completamente rivisto.

Le proprietà collettive della materia sono il risultato di interazioni a livello inter- e intra-molecolare identificate da caratteristiche scale temporali e spaziali. Uno strumento ormai affermato e utile per lo studio della natura collettiva dei processi microscopici attivi all'interno del sistema é la spettroscopia acustica. Mentre nel caso della fase cristallina si poteva sfruttare la natura periodica della struttura del sistema, limitando lo studio alla cosiddetta prima zona di Brillouin, per caratterizzare un sistema disordinato é necessario esplorare un intervallo spettrale il più ampio possibile cosí da poter aver accesso alle scale spazio-temporali in cui le dinamiche avvengo. Questo tipo di approccio può essere chiamato *Spettroscopia Acustica ad Ampia Banda Spettrale*.

Il mio dottorato é stato dedicato allo sviluppo di nuovi metodi e tecniche sperimentali per esplorare con continuità i processi dinamici la cui evoluzione avviene su scale di tempi tra le decine di ns e i ps. Tale Spettroscopia Acustica ad Ampia Banda Spettrale é stata testata su un campione prototipo di acetonitrile, il liquido con il piú alto momento di dipolo esistente, noto per le sue molteplici dinamiche di orgine inter- e intra-molecolare. Usando diversi approcci sperimentali e computazionali é stato possibile caratterizzare i principali processi di rilassamento per tale composto in tutta la sua fase liquida. Combinando poi tutte le informazioni acquisite, é stato possibile indentificare una mutua influenza tra i diversi processi di rilassamento il cui comportamento altrimenti sarebbe rimasto incompreso.

Dopo una breve introduzione per contestualizzare la Spettroscopia Acustica ad Ampia Banda Spettrale nell'ambito dei sistemi disordinati, nel Capitolo 1 viene offerta una panoramica delle tecniche sperimentali usate per effettuare le misure nel corso di questo lavoro. Trova posto in questo capitolo la descrizione del mio primo originale contributo all'estensione dell'intervallo spettrale acustico. Grazie alla progettazione e realizzazione di particolari filtri spaziali é ora possibile effettuare esperimenti di diffusione di luce Brillouin con angolo di scattering variabile senza dover incorrere in fastidiosi problemi di contributi spuri. Nel capitolo vengono anche richiamati i principali elementi di fisica alla base di ogni tecnica, marcando in particolare la caratteristica di complementarietà tra esperimenti risolti in tempo

e in energia.

Siccome tutte le informazioni a proposito delle dinamiche interne del campione sono mediate dall'interazione coi modi acustici, il Capitolo 2 é dedicato al formalismo delle fluttuazioni di densità, evidenziando le differenze tra il modello idrodinamico, valido per scale spaziali macroscopiche, e l'approccio delle funzioni memoria, necessario per descrivere la regione mesoscopica dove le dimensioni caratteristiche dei modi acustici diventano confrontabili con le distanze tra le particelle.

Nel Capitolo 3 sono riportati i risultati sperimentali ottenuti mediante la Spettroscopia Acustica ad Ampio Intervallo Spettrale nell'intero range di temperature in cui l'acetonitrile permane allo stato liquido. Per prima cosa, attraverso un tecnica fotonica di spettroscopia non lineare (Transient Grating) é stato possibile misurare alcune variabili termodinamiche, potendo fare chiarezza tra i vari contributi presenti in letteratura. Tra i risultati ottenuti, la dipendenza in temperatura del rapporto tra i calori specifici laddove usualmente viene considerata costante. Partendo da questi risultati e usando l'approccio di filtraggio introdotto nel Capitolo 1, é stato possibile studiare il rilassamento vibrazionale dell'acetonitrile scoprendo alcune rilevanti discrepanze con i precedenti lavori riportati in letteratura. Abbiamo cosí dimostrato l'importanza di eliminare eventuali contributi spuri e di poter attingere a informazioni complementari da diversi domini spettrali. Verrà inoltre mostrato il risultato dello studio del cosiddetto rilassamento strutturale effettuato nel range di alte energie grazie allo Scattering di raggi X. Una interessante correlazione si é potuta riscontrare tra i risultati di questo esperimento e quelli ottenuti con la tecnica Transient Grating nella sua risposta ultraveloce. Ancora una volta, per ottenere tale risultato é stato necessario combinare informazioni provenienti da molti intervalli spettrali diversi, confermando la validità di un approccio multi-tecnica come quello della spettroscopia acustica a larga banda spettrale. L'andamento in temperatura dei suddetti processi di rilassamento suggerivano di valutare la presenza di un eventuale accoppiamento tra i due fenomeni. É esattamente ciò che abbiamo osservato esplorando il dominio del profondo ultravioletto e per il quale abbiamo proposto un modello fenomenologico in grado di fornire una rappresentazione delle interazioni in gioco.

Per poter approfondire tale fenomeno di accoppiamento sarebbe estremamente utile poter esplorare l'intervallo spettrale degli UV soffici, ma fino ad oggi nessuna tecnica era in grado accedere a tale range. Nel Capitolo 4 mostriamo la nostra innovativa soluzione al problema: un nuovo interferometro Farby-Perot "table-top", concepito per lavorare con una sorgente UV laser e con sole ottiche riflettive.

Gli ultimi capitoli della tesi descrivono il mio contributo al prossimo esperimento avente come sorgente di luce un laser ad elettroni liberi: il progetto TIMER, destinato ad aumentare ulteriormente il range spettrale sperimentalmente accessibile con la spettroscopia acustica. In particolare, mostrerò i risultati ottenuti nell'esperimento pilota chiamato "mini-TIMER" grazie al quale dimostrato la possibilità di effettuare un esperimento Transient Grating anche nel range spettrale dell'estremo UV (EUV). Quando TIMER sarà operativo sarà il primo setup sperimentale in grado di sondare la regione mesoscopica nell'EUV, zona di cruciale importanza per lo studio dei vetri e delle nanostrutture. Questo risultato apre inoltre la strada ad una nuova classe di interessanti esperimenti ad oggi oggetto solo di considerazioni teoriche: i

cosiddetti esperimenti di “four wave mixing” combinati con la selettività elementale che la radiazione EUV può fornire.

Contents

Introduction

"I stand upon my desk to remind myself
that we must constantly look at things in a different way.
You see, the world looks very different from up here.
You don't believe me? Come see for yourself.
Come on. Come on!"

John Keating, in *Dead Poets Society* (1989)

In the famous movie *Dead Poets Society*, a young Robin Williams, in the shoes of professor John Keating, was inciting his students to look at reality from different points of view to discover how things look different than usual. Thinking of our daily life, this is exactly what happens: reality shows itself to us in different ways depending on the method we use to approach it.

Nowadays everyone knows that the Earth is rotating around it's axis, but this is not the evidence we have if we are resting for a while under a starry sky in a summer night. It would be necessary to observe the sky for a much longer time to realize that something is moving around the North Star. Finally, we can experience this movement only if our observation fits the "right" time-scale of the planet's rotation.

Figure 1: Picture of a starry sky obtained with long exposure of the camera.

Another experiment we can try to perform in our kitchen is to investigate the so called "not-newtonian fluids". It is very easy to find in the web a recipe to prepare a suspension of cornstarch in water named "Oobleck". Such fluid is very peculiar: it exhibits properties of a liquid or of a solid depending on the stress you apply to it. As a consequence, if you are fast enough, you could be able to walk on such fluid without sinking. Depending on the way you approach the material, different will be its response.

The behavior of nature changes also as a function of the energy involved in the interaction with the probe. Let's consider the Earth's atmosphere. At school

we studied the various layers of it: Exosphere, Thermosphere, Mesosphere, Stratosphere, Troposphere. Every layer has its characteristics and composition, but let's focus our attention on the lowest part of the Thermosphere, from 80 to 600 km above Earth's surface: the Ionosphere. Because of UV radiation from the sun, molecules in this layer can be easily ionized resulting in a huge presence of free electrons in the Ionosphere. The interaction between electrons and electromagnetic (e.m.) waves changes depending on the energy of the latter. What happens is that, if the energy of the e.m. radiation is low enough, a resonance effect takes place in the free electrons dynamics. This leads to a phenomenon known as "plasma mirror" effect and the e.m. wave is basically reflected back. If the energy is high, the wave can be transmitted through the Ionosphere. So, depending on the energy of the e.m. wave, the atmosphere is transparent or behaves like a mirror. This is the picture at the basis of the radio transmission (low energy e.m. waves): thanks to the reflection on the Ionosphere it is possible to communicate by radio between two distant places on the Earth.

Summarizing, we have seen, with the everyday experiences above, that nature behaves differently if your probe fits the time-energy/space scales of the phenomenon under study. In particular, we have seen that a macroscopic property of matter is a consequence of an interaction at microscopic level among the matter components. In condensed matter physics a lot of thermodynamical and mechanical properties of the materials are strongly affected by such kind of dependency and it is possible to describe the collective dynamics of the system as a function of the energy ($\hbar\omega$) and momentum ($\hbar Q$) exchanged between the probe and the degrees of freedom inside the system.

We discussed about ordinary experiences to introduce the approach we need to fully explore a special branch of condensed matter physics: liquids and topologically disordered systems.

A liquid is a system characterized by long range translational invariance and by a short range ordered structure. In the liquid state, contrarily to the crystalline one, there is not structural periodicity in such systems and all we learnt from solid state physics (Block's theorem, phonons, Brillouin's zones, eigen-states of plane waves, etc.) must be fully revised.

The macroscopic collective properties of condensed matter are the result of inter and intra-molecular interactions that are typified by characteristic time and space scales. If an external perturbation is applied to the system, it reacts with a transition from an equilibrium state to a perturbed one. Through several dissipative processes the system will relax to its ground state in a characteristic time, τ (see Fig. 2, which sketches the response ($\mathbf{R}$) of the system to a step perturbation ($\mathbf{P}$)). The same kind of relaxation processes are also present without any external perturbation due to the always active thermal agitation. Spontaneous microscopic fluctuations can be studied in order to gain information about the properties of the system.

In 1931 Onsager formulated the so called "fluctuation-dissipation" principle, for which spontaneous fluctuations of a certain observable around its equilibrium state are described by the same equations that regulate the macroscopic relaxation processes. In light of this, from the study of the time correlation functions of a certain

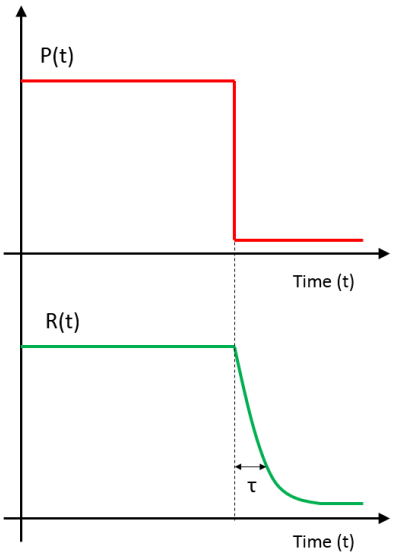

Figure 2: When a system experiences an external perturbation, it is moved by its equilibrium state and it will takes a certain characteristic time, τ, to go back its equilibrium state. In other words, the system is characterized by a response function which is not able to follow instantaneously the external perturbation. This is the case of this sketch: a step perturbation P is activated at certain sudden time, but the response R from the medium suffering the perturbation does not evolve with the same temporal dynamics.

observable it is possible to infer the physics of relaxation phenomena.

We can define a time correlation function as the thermodynamic average of the product of two dynamic variables each of them representing the instantaneous variation of a certain property of the fluid with respect to its equilibrium value. The time correlation function which, first among others, enables us to obtain information about thermodynamics, structural and transport properties of a fluid, is the "density fluctuation ($\delta\rho$) time correlation function".

$$F(Q,t) = \langle \delta\rho(Q,0)\delta\rho(Q,t)\rangle$$

Studying the $F(Q,t)$ or, equivalently, its time-Fourier transform $S(Q,\omega)$ named "Dynamic structure factor", one can follow the time evolution of the density fluctuations. $F(Q,t)$ and $S(Q,\omega)$ are featured by the presence of acoustic modes, which account for correlated density fluctuations and can be regarded as a periodic set of compressed and rarefied regions (i.e. a density wave). These modes have a broad frequency spectrum, extending from 0 Hz up to several THz. Acoustic modes are responsible for energy transport and dissipation inside the system and, since they result from the correlations over lengthscales comparable to Q^{-1}, they can be considered as a "variable lengthscale" probe. In a nutshell, acoustic spectroscopy can provide a large amount of information on macroscopic properties (stiffness, viscosity, thermodynamics, etc.) as well as on microscopic ones, such as the interaction potential and intermolecular interactions (anharmonicity, caging, hopping, etc.) and local structures (symmetry, defects, etc.). All this is very well known and was longstanding used to study crystalline samples. In crystals, the spatial periodicity of

the lattice allows to confine the experimental investigation in a limited Q-region, corresponding to a so-called Brillouin zone, within which acoustic modes span their entire frequency range while, thanks to the crystal symmetry, one may use reciprocal space vectors to "replicate" at higher Q's the information on the characteristic lengthscales of the dynamical processes (see Fig. 3).

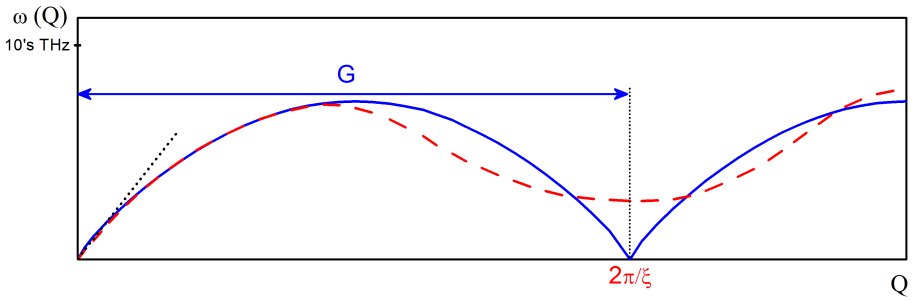

Figure 3: Examples of dispersion curves $\omega(Q)$ of acoustic modes in the case of a crystal (blu/streight line) and of a disordered system (red/dashed line). In the former case there is a periodicity linked to the dimension G of the unitary cell of the inverse crystal lattice which identifies the so called "Brillouin zone". In the second case, we can just define a so called "pseudo Brillouin zone" whose inverse Q-value is related to the characteristic inter-particle distance ξ. In low-Q limit we can observe a linear dependence of the dispersion, in accordance with the hydrodynamic regime. The slope of the linear trend is the adiabatic velocity of the acoustic mode.

In the case of systems without translational periodicity, as fluids or glasses, this is not possible. We should follow the dynamics in a (Q,ω)-range that starts from (0,0) and extends to the largest possible (Q,ω)-range. Only this approach allows to follow the dynamics of density fluctuations in the whole range of interest (i.e. from the microscopic to the macroscopic limits), thus, giving us the chance to unravel the contribution of the different microscopic dynamical processes to the macroscopic sample properties.

At this point it is useful to recall what we said at the beginning of this chapter: matter behaves differently depending on how the time (and length) scales of the probe compares with the intrinsic time and length scales of the dynamical processes. In our case the probes are the acoustic modes. Assuming that the dynamical response of the system can be depicted by the simple relaxation process shown in Fig. 2, when the acoustic frequency is much lower than the characteristic relaxation rate ($\omega\tau \ll 1$, a situation typically met at small phonon wavevectors), then the system can be considered as evolving in subsequent equilibrium states with respect to the dynamical process (relaxed limit), i.e. the acoustic mode "sees" the system as a time independent ensemble average that allows propagation at a certain velocity and that can absorbs (at each acoustic cycle) a given fraction of the energy that it is carrying out. However, the acoustic mode cannot "know" how much time it will take for the energy to be absorbed. In solids and fluids such low frequency (and low wavevector) regime is well described by classical elastic and hydrodynamic theory, respectively. These approaches rely upon the "continuum limit", in which it

is not possible to distinguish different molecules, a situation always met when Q is much lower than the inverse intermolecular distances (usually $\sim$ Å). On the other hand, if the phonon frequency largely exceeds the relaxation rate ($\omega\tau \gg 1$), the system looks like "frozen" with respect to the dynamical variable responsible for the relaxation (unrelaxed limit). In this case the energy stored in the acoustic mode has no longer the time to flow into the associated dissipation channel, it remains stored into the mode hence increasing the propagation velocity. If the dynamical processes responsible for the relaxation in our example are simply molecular collisions and we consider the case of liquids, the relaxed limit reflects a situation in which a large amount of collisions happens during a single acoustic cycle and have the effect to damp the acoustic propagation via viscous interactions (i.e. to absorb the energy that acoustic modes uses to locally compress the system). In the unrelaxed limit collisions have not enough time to occur and such an apparently "frozen" liquid is more similar to a disordered solid. In the high frequency, "solid-like", limit the acoustic energy cannot be dissipated via intermolecular collisions and therefore the sound velocity is larger, as like in a "true" solid (see Fig. 4).

In analogy with what we said at the beginning, a liquid may behave in different manner depending on the probe's timescale: i.e. it can show both elastic (solid-like) and viscous (liquid-like) dynamics. We described the two asymptotic extremities of such "visco-elastic" dynamical transition. In between the two, when $\omega\tau \sim 1$, a new field of research opens up. New theories are necessary to describe such a frequency-dependent visco-elastic behavior of matter. Furthermore, all this may become much more complicated when couplings between density fluctuations and several dynamical processes (also possibly coupled among themselves) are possible, as in the case of molecular liquids or more complex systems. There is no definitive agreement in the description of such regime and, consequently, it is extremely interesting to investigate it experimentally.

This is the reason at the grounds of this thesis, which has the aim to show the effectiveness of a "Broad band acoustic spectroscopy" in disordered systems. The experience accumulated so far by the scientific community in the field of disordered systems points out that most of the phenomena occur in a region of the (Q, ω)-plane included in the $(0.001 - 10)\ nm^{-1}$ and $(1 - 10^4)\ GRad/s$ ranges. We focused on this region and, since part of it is inaccessible by conventional methods, a substantial amount of the work presented in this thesis was dedicated to the development of new methods and experimental approaches to access those dynamic ranges unexplored up to now.

In Fig. 5 the (Q, ω)-plane in log-log scales is presented showing the available techniques up to date to explore the whole range of interest for the disordered systems. Before going into the details of each of them in the next chapter, here we talk briefly about the main differences among them. Basically we can divide all the techniques in two groups: "time-resolved" and "energy-resolved" ones. In both cases there are limitations and advantages. We can say that the two groups of techniques are complementary and it is extremely useful to compare them in the same domain.

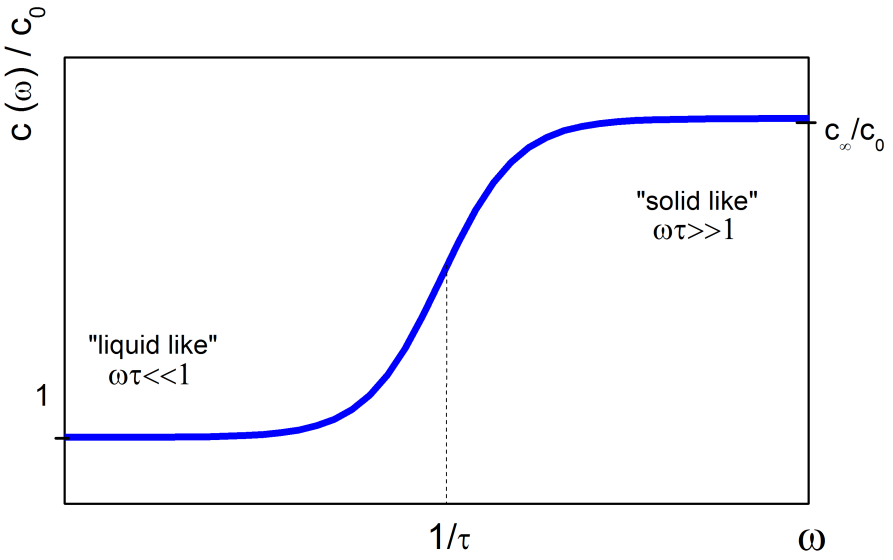

Figure 4: In the plot is sketched a typical dispersive shape occurring in a relaxation process. In particular this could be the shape of the velocity of the longitudinal acoustic modes (c_L), from a low-ω regime (c_0) to an high–ω regime (c_∞). The characteristic relaxation time, τ, define the watershed between the fully relaxed "liquid-like" regime ($\omega\tau \ll 1$) and the not relaxed "solid-like" one ($\omega\tau \gg 1$).

The energy-resolved techniques are based on inelastic scattering experiments: a probe sent to the sample interacts with the available degrees of freedom. The result of the process is a scattered beam from the sample which contains the information on the properties of the sample. The observable measured by this kind of techniques is the Dynamic Structure Factor, $S(Q,\omega)$, from which it is possible to directly extract the information about the ω and the dumping coefficient time of density fluctuations: the acoustic modes.

Coming from the low-energy region of the plane shown in Fig. 5 we first meet the Brillouin Light Scattering (BLS) techniques. These are interferometric based techniques, nowadays mainly using high resolution Sandercock designed Febry-Perot spectrometers. Usually, BLS measurements are performed only in the so called "backscattering geometry", limiting the accessible spectral window just to a single Q value, which depends by the incoming visible wavelength λ_{in}: around $Q \simeq 0.03\ nm^{-1}$ in the case of the most common used $\lambda_{in} = 532\ nm$.

We will see in Ch. 1 the method we developed to enlarge the spectral window to lower Q values. To extend the BLS up to higher Q-values, we are forced to change the incoming wavelength and use a radiation in the UV range. In Ch. 4 we will show the novel Fabry-Perot interferometer we built and characterized with a laser UV source (BLS-UV).

The other approach used in the last ten years is to use monochromators to analyze the light scattered by a sample illuminated with synchrotron radiation in the UV range. This is the case of IUVS which is able to push the Q-spectral window up to $0.1\ nm^{-1}$. Here the constraint in expanding the spectral window is dictated only by the absorption of the samples.

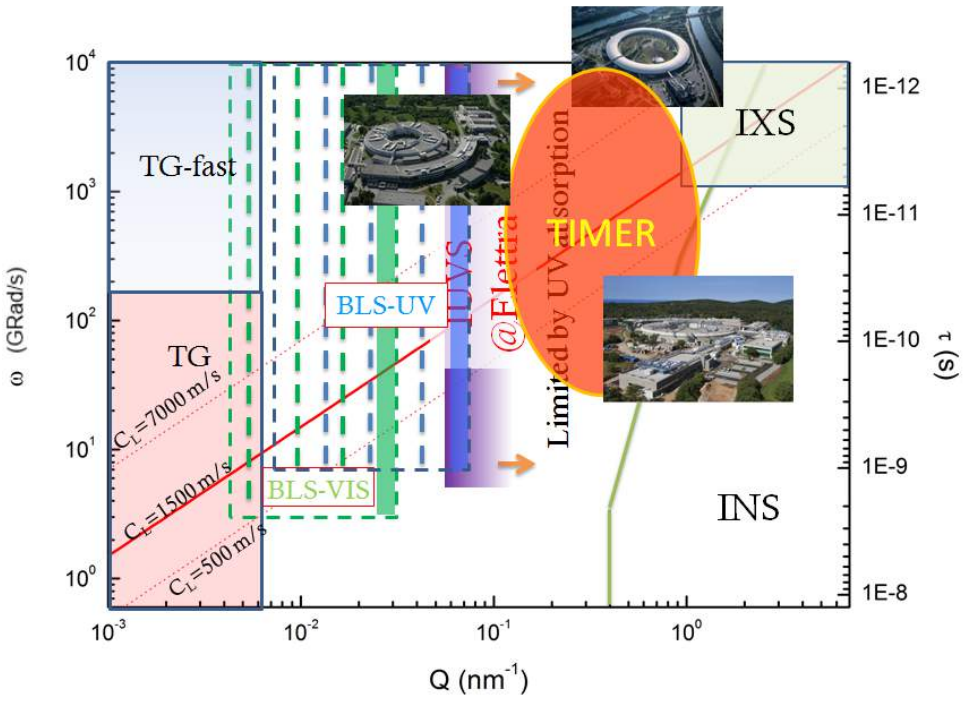

Figure 5: A sketch of all the nowadays available techniques and the next coming ones to cover the (Q, ω)-region of interest to study the main phenomena occurring in disordered systems through the broad band acoustic spectroscopy. The straight and dashed red lines in the graph represent the range in which the longitudinal acoustic velocity (c_L) can vary in these kind of systems. From the low Q-region to the high one we can list at first the table top laser based techniques as follows: Transient Grating (TG), with its different variants, Brillouin Light Scattering (BLS), Brillouin Scattering in the UV range (BLS-UV). Going up to higher values of Q we need to use techniques based on Large Scale Facilities. We just name them as follows: Inelastic Ultraviolet Scattering (IUVS), TIMER, Inelastic Neutron Scattering (INS) and Inelastic X-Ray Scattering (IXS).

To reach the spectral window that matches the single particle limit, it is necessary to change again the source of the incoming radiation. Using large scales facilities it is possible to use X-rays (IXS) or thermal neutrons (INS) to perform inelastic scattering experiments covering such region. These two radiations interact differently with matter: X-rays can probe the electrons dynamics while neutrons the nuclei ones. Thanks to the Born-Oppenheimer approximation, we can consider that electrons follow instantaneously the dynamic of nuclei, therefore the dynamics probed by the two techniques are strongly related.

One of the advantages of INS is that neutrons are neutral particles so they can penetrate bulk materials without damaging the sample (it is a very good point if one wants to study, e.g., paintings or other artifacts). Furthermore it is possible to reach very good energy resolutions (down to few μeV with cold neutrons).

The downside of INS is that, nowadays, the neutrons facilities are low intensity sources and, because of the low interactive characteristic of neutrons, samples need

to be large to achieve enough statistics during the experiment. Because of this latter point, one is also faced with the problem of multiple scattering contamination.

The last property of INS we want to talk about is the so called "kinematic constraints": the exchanged energy and momentum are coupled through the mass of the neutron. This is the reason of the low-Q limit on studying acoustic modes with INS.

Concerning IXS, the photon flux is higher than in the case of INS thanks to the high brilliance of the synchrotron photon sources. Furthermore there are no kinematic constraints. In this case the impossibility to access the low-Q region is due to the achievable resolution with the current setups. Nowadays the available energy resolution in these kind of experiments is in the order of $\sim 1.5\ meV$.

As already stressed in the previous section, a complementary way to investigate the density fluctuation dynamics is through time-resolved spectroscopies. These are pump&probe techniques and they can directly measure the *intermediate scattering function* $F(Q,t)$ with the so called *four wave mixing* experiments.

The simplest and most used setup for these kind of experiments is named *Transient Grating* (TG). Two coherent monochromatic pulsed pump beams are sent, with space and time coincidence, to the sample. Here the fields of the pumps form a "transient grating" as an interference pattern. This grating, with a spatial periodicity defined only by the wavelength of the pumps and their propagating directions, forces the density of the system to oscillate selecting univocally the Q-value involved in the scattering process. Only a certain Q-component of the acoustic modes present into the sample are thus excited and it is a very smart solution to avoid spurious contributions from other components. The life-time of the grating is related to the dumping process of the propagating acoustic mode. To study the dynamics of the grating a probe beam with a different wavelength and geometrical alignment is sent to the sample, in order satisfy the phase matching conditions (basically the Bragg's diffraction condition: the exchanged momentum between the scattered beam and the probe must be the same induced with the grating). If these conditions are satisfied, a non linear effect happens resulting in a fourth beam scattered in a certain direction, along which no radiation is supposed to be. This tricky setup permits to have an high contrast in the measurements which can be further enhanced if a particular detection scheme is adopted (we will give some more details in the next chapter).

As it will be shown in the following pages, with this technique it is possible to study all the dynamics between 100's of fs and units of ns's: molecular rotational dynamics, structural relaxation phenomena, thermal relaxations, etc.

Also in this case, there are some limitations which not allow to use TG in the whole range of interest. In fact, to reach the Q-region with $Q > 0.1\ nm^{-1}$ it would be necessary to have a laser able to produce low wavelength coherent pulses with enough power to be able to induce the transient grating. Such lasers simply don't exist. The absence of this kind of technology has left, so far, a region of the (Q,ω)-plane unaccessible to experimentalists. Only in the very recent years, the advent of synchrotron radiation sources of fourth generation, the Free Electron Lasers (FELs) paved the way to cover such lack. In particular the so called *seeded* FELs can

produce coherent pulsed radiation with wavelength down to tenth's of nm and with pulse duration lower than 100's of fs. Using such kind of coherent radiation sources it is possible to plan novel and challenging experiments, as the four wave mixing (FWM) experiments. This is the aim of the TIMER (TIME-Resolved spectroscopy and mesoscopic dynamics in condensed matter) project. In this thesis we dedicate a section to describe the main characteristic of this innovative experiment and we will show the first results obtained with a pilot experiment (mini-TIMER) to explore the feasibility of future FEL-based FWM experiments, that will be developed in a dedicated beamline (EIS-TIMER, to be realized in 2015-2016 at the FERMI FEL facility in Trieste).

Among the time-resolved pump&probe approaches, we just mention here, to be thorough, the picosecond acoustic (PA) technique, firstly introduced by Maris [1] and further developed in these last years [2, 3, 4, 5]. This technique can be profitably used to study the sound attenuation in amorphous materials, pushing the accessible $(Q-\omega)$-range to the low energy side of the mesoscopic region. In PA an ultrashort pump beam is sent to a metallic thin film deposited on the surface of the sample of interest. The heated metal acts as a transducer and launches an ultrashort acoustic wave-packet into the sample. Thanks to a delayed probe pulse and its coupling with the travelling acoustic wave, it is possible to monitor the propagation and reflection of the acoustic waves inside the sample. In particular it was shown that probing the acoustic wave at the sample/substrate interface, because of the phase matching boundary conditions, the acoustic attenuation can be measured in an angular frequency range of the order of hundreds of GRad/s [6, 7]. Further future developments in the direction of increasing the available spectral range, will candidate PA as a complementary technique of the TIMER experiment.

The present manuscript is structured as follows:

Chapter 1: we will give an overview of all the experimental setups used to perform the measurements for this thesis;

Chapter 2: a basic formalism about time correlation functions is recalled to describe the density fluctuations;

Chapter 3: we will show the results obtained with the broad band acoustic spectroscopy on a prototypical sample: acetonitrile (ACN);

Chapter 4: a further effort to cover the (Q,ω)-plane: the BLS-UV setup;

Chapter 5: the TIMER project;

Chapter 6: first results from the pilot experiment mini-TIMER;

Chapter 7: conclusions.

Chapter 1

Nowadays available techniques

In the previous chapter we have seen a sketch of the nowadays available methods to probe the dynamics in disordered systems through the study of the acoustic modes. We have already classified such experimental techniques in two ensembles: the time-resolved and the energy-resolved ones. This chapter is devoted to a deeper description of all the photonic techniques we have used in the study presented in this thesis.

1.1 Energy-Resolved techniques

All the experiments working in the energy domain are basically drawn with "photon-in photon-out" scheme. A monochromatic beam, with wave-vector $\underline{k}_i$ and angular frequency ω_i, is sent to the sample and interacts with the molecules inside the matter. Accordingly with classical electrodynamics, the charged particles inside the sample, excited by the incoming photons, start to radiate light in all directions [8]. The scattered light, with $\underline{k}_s$ and ω_s, is the result of the energy and momentum conservation rules:

$$\begin{aligned} \hbar\omega &= \hbar\omega_s - \hbar\omega_i \\ \hbar\underline{Q} &= \hbar\underline{k}_s - \hbar\underline{k}_i \end{aligned} \tag{1.1}$$

where $\hbar\omega$ and $\hbar\underline{Q}$ are the energy and momentum exchanged in the process.

In Fig. 1.1 is represented a typical scattering geometry. The scattered light is collected at a certain angle θ with respect to the incoming beam direction ($\underline{k}_i$): it is called "scattering angle". Usually the magnitude of the wave-vectors of incident and scattered light differ very little ($|\underline{k}_i| \simeq |\underline{k}_s| = k$), so we can define the exchanged Q as follows:

$$Q = 2k \sin\left(\frac{\theta}{2}\right) = \frac{4\pi n}{\lambda} \sin\left(\frac{\theta}{2}\right) \tag{1.2}$$

where n and λ are, respectively, the refractive index of the material and the in vacuum wavelength of the incoming radiation.

In this picture of energy and momentum exchange, there can happen two different processes: the creation or the annihilation of a sample excitation with energy $\hbar\omega$ and

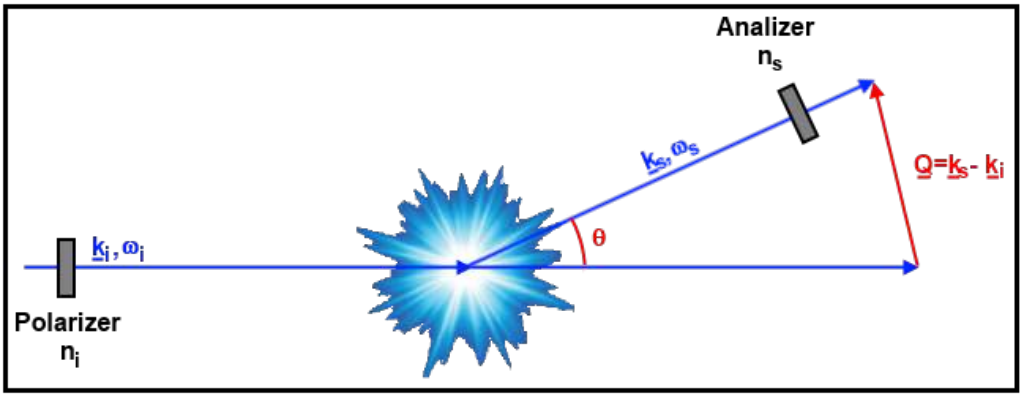

Figure 1.1: "Photon-in photon-out" scheme for a typical scattering process

momentum $\hbar\underline{Q}$. In the case of acoustic spectroscopy, the excitations we are talking about are the acoustic waves. Therefore we can see such creation and annihilation processes as like the interaction between the photon and a propagating or a counter-propagating acoustic mode. The frequency spectrum (see Fig. 1.2) of the scattered light exhibits resonances at frequencies corresponding to the excited transitions. The spectrum is composed by three main bands: Rayleigh, stokes and anti-stokes one. The first one is the result of an elastic scattering process ($\hbar\omega = 0$) while the others are classified as inelastic scattering which is also named as Brillouin scattering.

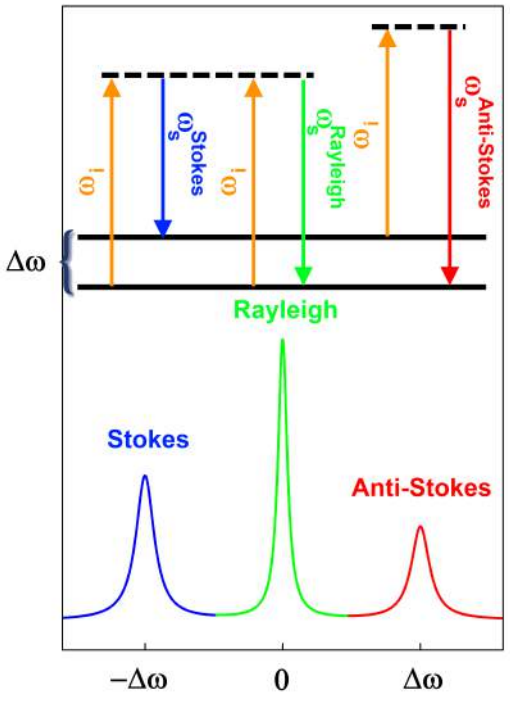

Figure 1.2: Typical $S(Q,\omega)$ spectrum of a liquid. It presents band peaks corresponding to annihilation or creation process activated by the photon-phonon coupling. These peaks are named Brillouin doublet.

Actually such frequency shift are very small compared to the photon characteristic frequency, therefore since the advent of laser and high resolution spectrometers it was not possible to resolve such features. As we said, the frequency shifts in the spectrum are related to the propagating acoustic modes inside the matter. It is not surprisingly that we can extract information about velocity and lifetime of the acoustic modes from the line-shape of the spectrum. We will discuss how to obtain such parameters in the next pages.

1.1.1 Brillouin Light Scattering

We have already discussed in the previous chapter the importance of the density fluctuations time correlation function to gain information on the collective dynamics in disordered systems. Brillouin Light Scattering (BLS) is one of the main and most used techniques which can directly measure such physical observable. In the scale of visible and ultraviolet (UV) wavelengths, we can neglect the single particle interactions and follow a macroscopic approach to describe the theory of light scattering in this energy range. If we consider sample volumes much smaller than the cubic of incident wavelength, λ^3, we can assume that the whole region is illuminated by the same radiation, therefore the scattered light is the result of the interference between the light radiated by the single neighboring domains. If these subregions are characterized by the same optical parameters in principle we should not have scattered light except for the forward direction [9]. On the contrary, when the illuminated regions are optically different, it is possible to have constructive interference in directions different from the forward one, so that we can observe scattered light in a wide range of angles.

This semi-macroscopic picture was conceived by Einstein, he suggested that the scattering process would be the result of local fluctuations of the dielectric constant of the material [10]. In the following we will give a generic formulation for the light scattering based on the fluctuations of the dielectric tensor without specify their origin.

In the approximation of small illuminated sample volumes, we can consider the incident radiation as like a plane wave with polarization $\hat{n}_i$ and wave-vector $\underline{k}_i$:

$$\underline{E}_i(\underline{r},t) = \hat{n}_i E_0 e^{i(\underline{k}_i\cdot\underline{r}-\omega_i t)} \tag{1.3}$$

The material is characterized by a dielectric tensor:

$$\underline{\underline{\varepsilon}}(\underline{r},t) = \varepsilon_0\underline{\underline{I}} + \delta\underline{\underline{\varepsilon}}(\underline{r},t) \tag{1.4}$$

where $\delta\underline{\underline{\varepsilon}}(\underline{r},t)$ is the dielectric fluctuation tensor and ε_0 is the in vacuum dielectric constant (we assumed an isotropic symmetry, as it is generally the case of liquids).

From classical electrodynamics, the electric field component of the scattered light with a certain polarization $\hat{n}_s$ and wave-vector $\underline{k}_s$ at large distance R from the scattering volume V, can be written as follows:

$$\underline{E}_s(\underline{R},t) = \frac{E_0}{4\pi R\varepsilon_0} e^{i\underline{k}_s\cdot\underline{R}} \int_V \mathrm{d}^3 r\, e^{i(\underline{Q}\cdot\underline{r}-\omega_i t)} (\hat{n}_s\cdot(\underline{k}_s\times(\underline{k}_s\times(\delta\underline{\underline{\varepsilon}}(\underline{r},t)\cdot\hat{n}_i)))) \tag{1.5}$$

after some algebra and introducing the spatial Fourier transform for the dielectric fluctuation tensor $\delta\underline{\underline{\varepsilon}}(\underline{Q},t)$, we can write

$$\underline{E}_s(\underline{R},t) = \frac{-k_s^2 E_0}{4\pi R\varepsilon_0} e^{i(\underline{k}_s\cdot\underline{R}-\omega_i t)} \delta\underline{\underline{\varepsilon}}_{is}(\underline{Q},t) \tag{1.6}$$

where

$$\delta\underline{\underline{\varepsilon}}_{is}(\underline{Q},t) = \hat{n}_s \cdot \delta\underline{\underline{\varepsilon}}(\underline{Q},t) \cdot \hat{n}_i \tag{1.7}$$

The time correlation function is:

$$\langle E_s^*(\underline{R},0) E_s(\underline{R},t)\rangle = \frac{k_s^4 |E_0|^2}{16\pi^2 R^2 \varepsilon_0^2} \langle \delta\underline{\underline{\varepsilon}}_{is}^*(\underline{Q},0)\delta\underline{\underline{\varepsilon}}_{is}(\underline{Q},t)\rangle e^{-i\omega_i t} \tag{1.8}$$

thanks to the Wiener-Kintchine theorem, we can write the spectral density of the scattered light:

$$I_{is}(\underline{Q},\omega,R) = \frac{k_s^4 |E_0|^2}{16\pi^2 R^2 \varepsilon_0^2} \frac{1}{2\pi} \int_{-\infty}^{+\infty} \mathrm{d}t\, \langle \delta\underline{\underline{\varepsilon}}_{is}^*(\underline{Q},0)\delta\underline{\underline{\varepsilon}}_{is}(\underline{Q},t)\rangle e^{-i\omega t} \tag{1.9}$$

where $\omega = \omega_i - \omega_s$.

In conclusion, we have shown that an energy resolved spectroscopy using visible or UV light is sensitive to an observable which is the time Fourier transform of a time correlation function. In our case, the final result, following the formalism of classical electrodynamics, is that the spectral density of the scattered light from a sample hit by a laser radiation is proportional to

$$I_{is}^{\varepsilon}(\underline{Q},\omega) = \frac{1}{2\pi} \int_{-\infty}^{+\infty} \mathrm{d}t\, e^{-i\omega t}\, I_{is}^{\varepsilon}(\underline{Q},t) \tag{1.10}$$

where

$$I_{is}^{\varepsilon}(\underline{Q},t) = \langle \delta\underline{\underline{\varepsilon}}_{is}^*(\underline{Q},0)\delta\underline{\underline{\varepsilon}}_{is}(\underline{Q},t)\rangle \tag{1.11}$$

The coefficient which links the latter expression to the actual measurable intensity is proportional to λ^{-4} (see eq. 1.9), in agreement with the Rayleigh's formula usually recalled to explain the blue color of the sky. Furthermore we have to stress that in principle it is not necessary to use a coherent light source to probe the spontaneous fluctuation occurring in the system, what we need, instead, is the monochromaticity of the incident light. Without this property of the light (and an high resolution spectrometer) it would be impossible to discriminate the very low difference in energy ($\hbar\omega$) between the incoming and the scattered beam, typically 5 orders of magnitude smaller than the beams energy.

At the beginning of this paragraph we stated that the Brillouin Scattering is sensitive to the density fluctuations. So far we limited our discussion to a more

general observable, the dielectric fluctuation tensor $\delta\underline{\underline{\varepsilon}}$. Let's see now which is the relation between these two physical quantities.

In the range of visible and UV light, we already said that we are not sensitive to the single particles interactions, simply because the wavelength of the radiation is much bigger than the interparticles distances. We can therefore think at every infinitesimal scattering volume still as a spacial region in which a lot of molecules are contained and interact each other. These involved length-scales finally suggest the idea of a thermodynamic approach for these ensembles, in which is possible to extend the usual thermodynamic concept of *local equilibrium*.

The dielectric constant ε_0 of a pure fluid in total equilibrium is, in general, a function of density ρ_0 and temperature T_0 called *dielectric equation of state*: $\varepsilon_0 = \varepsilon(\rho_0, T_0)$. Locally, in the sample, there will be small fluctuations in density and temperature. These variations reflect on the dielectric tensor fluctuation:

$$\delta\underline{\underline{\varepsilon}}(\underline{r},t) = \left(\frac{\partial\underline{\underline{\varepsilon}}}{\partial\rho}\right)_T \delta\rho(\underline{r},t) + \left(\frac{\partial\underline{\underline{\varepsilon}}}{\partial T}\right)_\rho \delta T(\underline{r},t) \tag{1.12}$$

so we can write the spectral density following the eq. 1.10:

$$I^{\varepsilon}_{is}(\underline{Q},\omega) = (\hat{n}_i\cdot\hat{n}_s)^2 \left\{ \left(\frac{\partial\underline{\underline{\varepsilon}}}{\partial\rho}\right)^2_T S_{\rho\rho}(\underline{Q},\omega) + \right.$$
$$\left. + \left(\frac{\partial\underline{\underline{\varepsilon}}}{\partial\rho}\right)_T \left(\frac{\partial\underline{\underline{\varepsilon}}}{\partial T}\right)_\rho [S_{\rho T}(\underline{Q},\omega) + S_{T\rho}(\underline{Q},\omega)] + \left(\frac{\partial\underline{\underline{\varepsilon}}}{\partial T}\right)^2_\rho S_{TT}(\underline{Q},\omega) \right\} \tag{1.13}$$

$S_{\rho\rho}(\underline{Q},\omega)$, $S_{\rho T}(\underline{Q},\omega)$, $S_{T\rho}(\underline{Q},\omega)$ and $S_{TT}(\underline{Q},\omega)$ are, respectively, the time Fourier transform of the time correlation functions $\langle\delta\rho^*(\underline{Q},0)\delta\rho(\underline{Q},t)\rangle$, $\langle\delta\rho^*(\underline{Q},0)\delta T(\underline{Q},t)\rangle$, $\langle\delta T^*(\underline{Q},0)\delta\rho(\underline{Q},t)\rangle$ and $\langle\delta T^*(\underline{Q},0)\delta T(\underline{Q},t)\rangle$.

The above expression is the complete formula describing the light scattering. Actually, in most of the liquids was found that $\underline{\underline{\varepsilon}}$ is not sensitive to thermal variations and therefore we can simply relate the dielectric fluctuation tensor to the density fluctuation correlation function.

$$I^{\varepsilon}_{is}(\underline{Q},\omega) = (\hat{n}_i\cdot\hat{n}_s)^2 \left(\frac{\partial\underline{\underline{\varepsilon}}}{\partial\rho}\right)^2_T S_{\rho\rho}(\underline{Q},\omega) \tag{1.14}$$

In conclusion of this section, we showed that from a light scattering experiment in the visible and UV range it is possible to directly measure the dynamic structure factor $S_{\rho\rho}(\underline{Q},\omega)$, which embodies the information on the acoustic modes.

In the next chapter we will discuss in more details how to model the $S(\underline{Q},\omega)$. At this stage, we just want to stress that, depending on the region of the (Q,ω)-plane in which we probe the sample, different phenomena have to be taken into account to describe the scattering process. These differences result in a lineshape of the spectrum depending on the Q-energy scales. In Fig. 1.3 is shown the so called *static structure factor* $S(Q)$, which is the integral over ω of the $S(\underline{Q},\omega)$. We will spend

some more words about it in the next, for the moment it is enough to say that from its shape it is possible to extract the particles space distribution inside the sample. In fact, it shows a prominent peak in correspondence of the inverse of the characteristic interparticle distance (ξ) between a scatterer site and its first neighbors. So, using this peak as a reference, we can classify the Q-space in three different regions: well beyond the peak ($Q \gg \xi^{-1}$), the so called *single particle limit*, around the peak region ($Q \approx \xi^{-1}$), the *mesoscopic range*, and the *hydrodynamic limit*, reached for $Q \ll \xi^{-1}$.

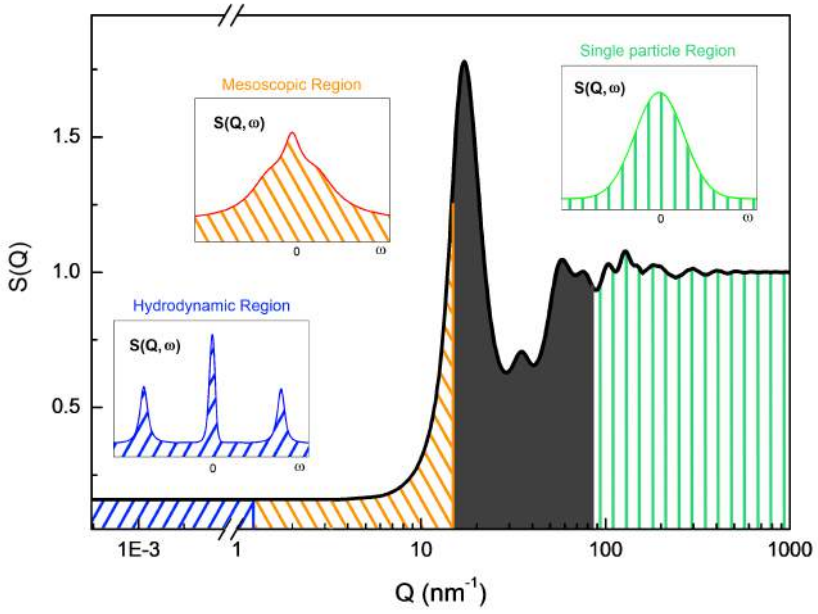

Figure 1.3: Typical $S(Q)$ for liquids. In the insets are represented the different lineshapes of $S(Q, \omega)$ in the different regimes from the hydrodynamic limit to the single particle one.

Visible domain: the Fabry-Perot interferometer

To investigate the dynamics of a system evolving in one order of magnitude around the ns timescale with the acoustic spectroscopy, the typical approach is to use energy resolved techniques. Indeed, is not possible, in such dynamic region, to match both the energy and momentum conservation rules with usual alignments in time resolved setups (more details in the next paragraphs). This means that we must be sensitive, in the frequency ($\nu = \omega/2\pi$) domain, to variations of the order of tenth's of GHz between the incoming and scattered beam frequency. Considering that the visible light has a frequency of the order of $10^5\, GHz$, it implies that we should be able to resolve a variation in frequency which is 5 orders of magnitude lower than the ones of the involved radiations. Before the advent of interferometric techniques, this goal was extremely challenging to be achieved, not to say impossible.

Nowadays the most used setup configuration is based on the so called "scanning multipass Fabry-Perot interferometer". In Fig. 1.4 is sketched the BLS setup we used at laboratories of University of Perugia [11] for some of the measurements in this work. At this stage let's focus our attention only on the detection apparatus: the light scattered by the sample is collected by a system of lenses and mirrors and sent to the pinhole entrance of the spectrometer. At this point the spectrometer allows to measure the spectral profile of the light beam selecting all the photons at each frequency of the spectrum. After this frequency filtering, the photons are sent to a photomultiplier tube which converts the optical signal into an electric current which can be recorder by the DAQ system.

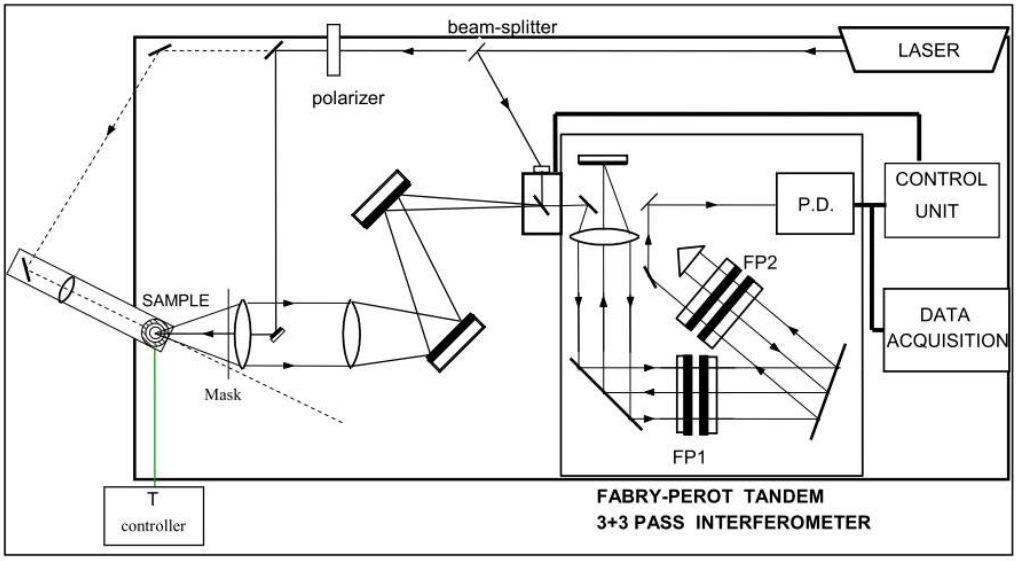

Figure 1.4: BLS setup at Ghost laboratory at University of Perugia.

The Fabry-Perot (FP) interferometer is the main component of such detection apparatus. It is designed, basically, as two highly reflecting faced plane mirrors. These mirrors work as a cavity for the incoming photons which can be transmitted only if their wavelength (λ) satisfies the resonance condition imposed by the mirrors distance (L). So, varying the distance of the mirrors with continuity, we are able to select the desired spectral component of the scattered light beam. In particular, photons can be transmitted by the cavity only if the constructive interference conditions are satisfied by the all beams resulting from the multireflections in the Fabry-Perot. It is not the aim of this paragraph to describe the all details of the FP interferometers, for a deeper description of their characteristics one can profitably refer to the monographs written by Hernandez [12] and Vaughan [13]. Here we just want to give to the reader some basic elements to better understand the work presented in this thesis.

Considering the optical path difference between the transmitted photons (see fig. 1.5) by a generic FP:

$$\delta = \frac{4\pi n'}{\lambda} L \cos\theta' \tag{1.15}$$

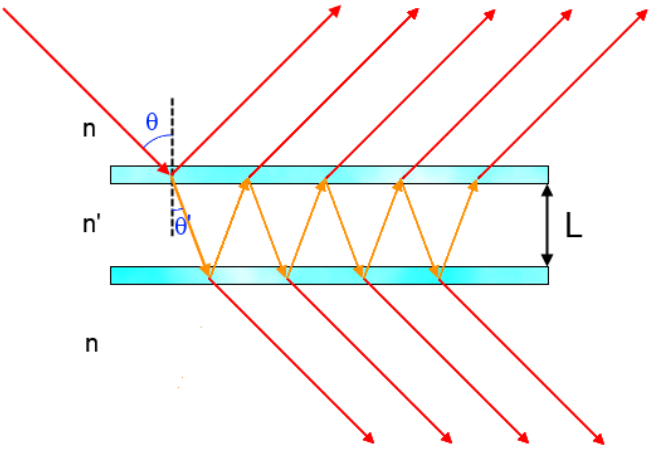

Figure 1.5: Scheme for transmission and reflection of a plane wave on a Fabry-Perot interferometer.

we can write the so called Airy function which is the shape of the spectrum for the transmitted light in the case of monochromatic laser beam and which can be considered as the instrumental response function of the interferometer

$$\frac{I^{(t)}}{I^{(i)}} = \frac{1}{1 + F \sin^2 \frac{\delta}{2}} \tag{1.16}$$

where

$$F = \frac{4R}{(1-R)^2} \tag{1.17}$$

and R is the mirror reflectivity. It's simply to see that the constructive interference condition is obtained for $\delta_m = 2m\pi$ with m an integer number.

The main parameters to characterize a FP interferometer are the *finesse* (f) and the *contrast* (C). The former is the ratio between the mutual spectral distance of two consecutive transmitted peaks ($\Delta\delta = 2\pi$) and their fullwidth half maximum (ε). It can be shown that in real cases f is the result of the combination of different characteristics of the interferometer: the reflectivity of the mirrors (f_R), their flatness (f_M) and the size of the entrance pinhole (f_{ph}) of the spectrometer.

$$f = \frac{2\pi}{\varepsilon} = (f_R^{-2} + f_{ph}^{-2} + f_P^{-2})^{-1/2} \tag{1.18}$$

where

$$\begin{aligned} f_R &= \tfrac{\pi\sqrt{R}}{1-R} \\ f_{ph} &= \tfrac{4\lambda d^2}{D^2 L} \\ f_M &= \tfrac{\lambda}{2M} \end{aligned} \tag{1.19}$$

where d,D and M are, respectively, the focal length of the optics focusing the light into the photomultiplier, the diameter of the pinhole and the flatness parameter of the mirrors.

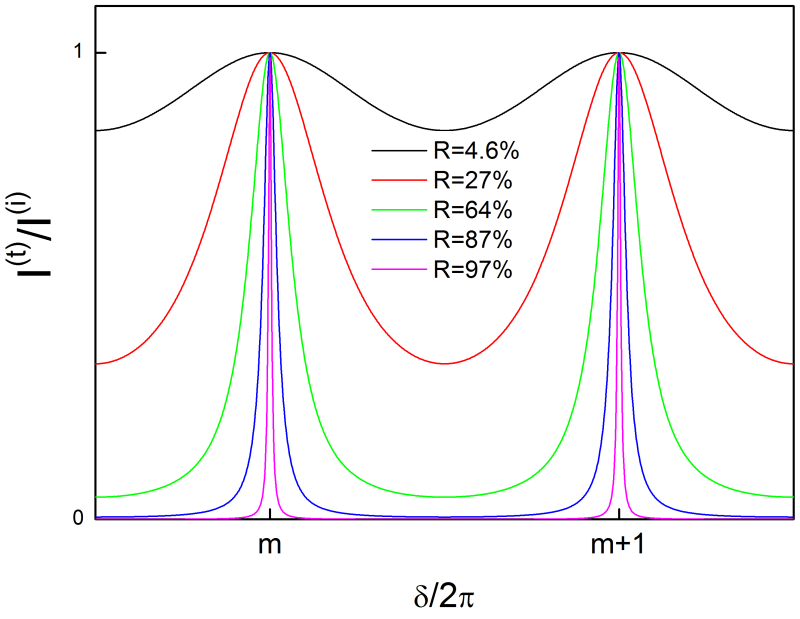

Figure 1.6: Airy function for a Fabry Perot interferometer. As it is evident the resolving power increases enhancing the mirror reflectivity R.

Concerning the *contrast*, it is the ratio between the highest and lowest transmitted intensity and it can be express as a function of the *finesse*:

$$C = \frac{(I^{(t)}/I^{(i)})_{max}}{(I^{(t)}/I^{(i)})_{min}} = 1 + \frac{4f^2}{\pi^2} \tag{1.20}$$

Because of the low scattered signal resulting from the spontaneous density fluctuations, to have an high contrast interferometer is crucial to obtain good quality spectra.

Looking at Fig. 1.6 and at eq. 1.16, we have already observed that for a given wavelength of incoming radiation there are several mirrors distances that will leave the radiation to be transmitted. This means that in an ideal experiment, scanning the L-distance, at certain point we will have a replica of the original signal overlapped to the tails of spectrum we would actually measure. The scanned frequency range of the spectrum "free of replicas" is named also *free spectral range* (FSR) and its width is $FSR = c/2L$, where c is the speed of light and L is the length of the FP cavity.

These replica represent a limitation to obtain a spectroscopy in a wide spectral range. To reduce such problem and extend the spectra measurements to frequencies larger than the FSR without contaminations by the higher orders of transmitted light, one may introduce another FP interferometer, whit a slightly different mirrors distance (L'), just after the previous one. In this way the transmitted orders selected by the first FP are forced to pass through the second one too, but because of the different selection rules (due to the difference in L), the replica orders will be

suppressed resulting in what people is use to call as "ghosts peaks". This process of double filtering, known as *tandem* configuration, is shown in Fig. 1.7.

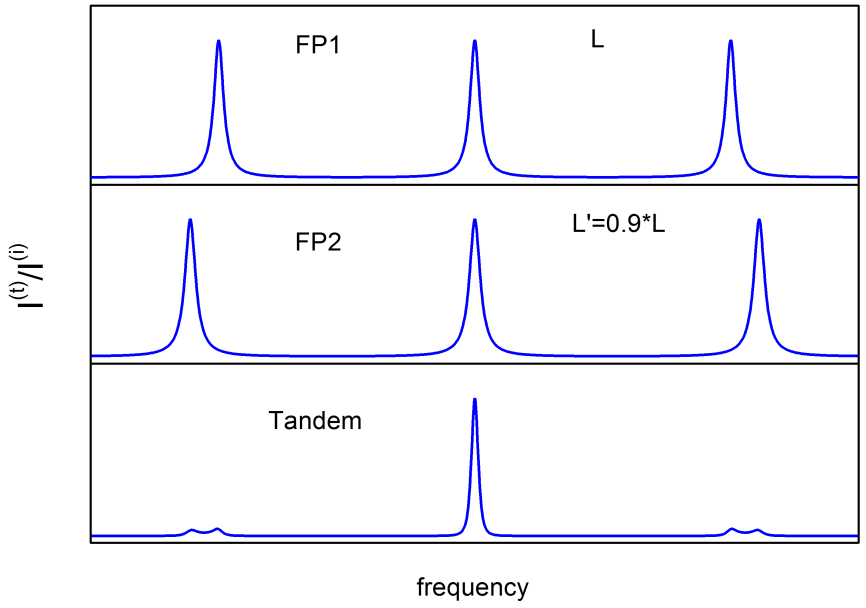

Figure 1.7: In the top panel is drawn a spectrum with its replica obtained with mirror spacing L. In the middle one, the mirror spacing was slightly reduced, L'=0.9L, showing the different frequency selectivity. The spectrum in the bottom panel is the product of the two spectra above, it mimics the effectiveness of the tandem geometry. With this configuration only small "ghosts" are still present in the spectrum and will not seriously represent a problem for the quality of the spectrum desired.

Nowadays the most used tandem configuration is the "Sandercock" one [14]. It is conceived to give synchronous scanning [15] of the two FP's using a translational stage giving a constant ratio between L and L' of $\cos\alpha$ during the whole scan. α is the angle between the lines perpendicular to the FP plates as showed in Fig. 1.8.

Furthermore, in order to enhance the contrast of such kind of spectrometers, it is used to exploit the so called multipass configuration. As it can be seen in Fig. 1.4 the beam passes several times through the couple of FPs, enhancing the filtering efficiency and as a consequence the contrast. In the case of triple-pass interferometer, as like the one we used in the visible domain, the instrumental response function is therefore the sixth power of the Airy function obtained for a single FP. Such multipass configuration gives rise to an excellent contrast, usually of about 10^{10} or better.

The angle resolved Brillouin setup

In BLS experiments, $S(\underline{Q},\omega)$ is usually determined as a function of ω at a given Q-value and it is typically featured by a quasi elastic (Rayleigh) peak centered at

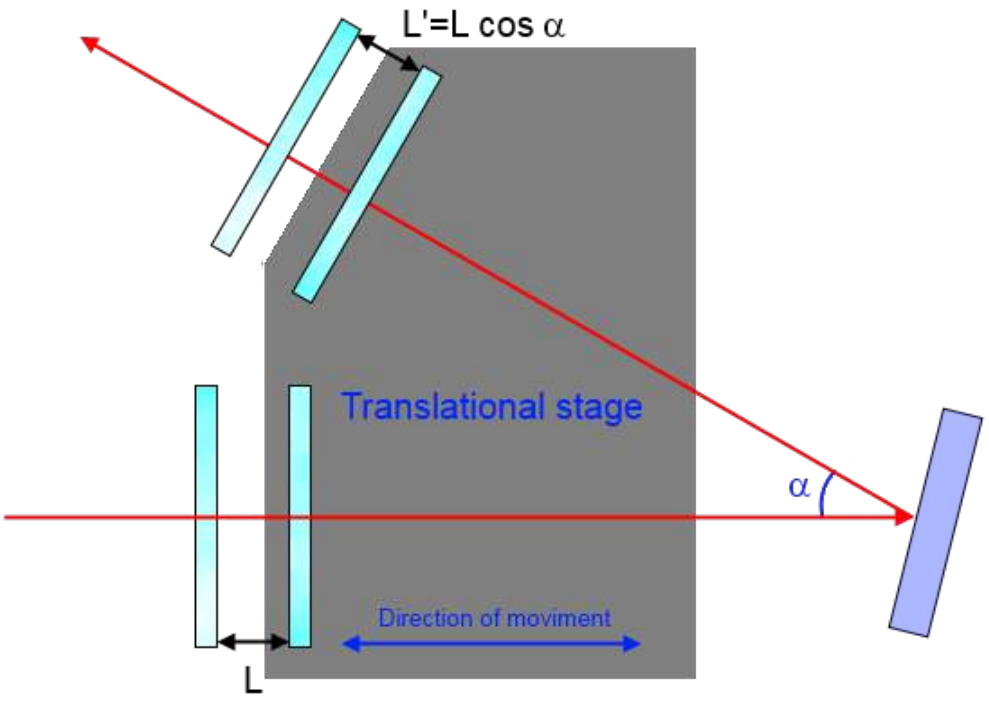

Figure 1.8: Sandercock design for synchronous scanning of the tandem FP.

$\omega = 0$ and two symmetric side peaks, the Brillouin doublet. The frequency shifts (Ω) and line-widths (Γ) of the latter are related to the frequencies and lifetimes of acoustic modes at the selected $\underline{Q}$. To extract the necessary information about the dynamics involved in the system, it would be extremely useful to study the dispersion of the acoustic modes parameters as a function of the probed Q-value. Unfortunately, up to now, it was practically impossible to select many different Q-values with the usual BLS setups. So far, in fact, BLS was mainly used in only two geometrical configurations, corresponding to $\theta = 90°$ and $180°$ (or close to $180°$). This limited range in θ is essentially due to the finite angular acceptance of collection optics, that simultaneously collect a finite distribution of scattering angles around the selected value. Such a distribution turns into a Q distribution (P_Q) with a characteristic extension ($2\Delta_Q$) centered on the selected value (Q_0). As shown in Fig. 1.9, on decreasing θ, the relative Q-spread ($2\Delta_Q/Q_0$) increases. It is mostly due to the decreasing of Q_0 with $\sin(\theta/2)$. This introduces an ineluctable artifact in the determination of $S(\underline{Q},\omega)$, which results to be a weighted sum of spectra corresponding to the different $\underline{Q}$-values convoluted with the instrumental response function.

Sophisticated experimental setups [16] and special data analysis procedures [17, 18, 19] have been proposed to cope with this issue. However, the former are not easily implementable in most of BLS setups (mainly based on Fabry-Perot interferometers of the "Sandercock" type) while the latter require ansatzs on the functional dependency of Ω and Γ on $\underline{Q}$, that are not necessarily *a priori* known. On the contrary, their determination is often the object of the experiment, in particular in studies

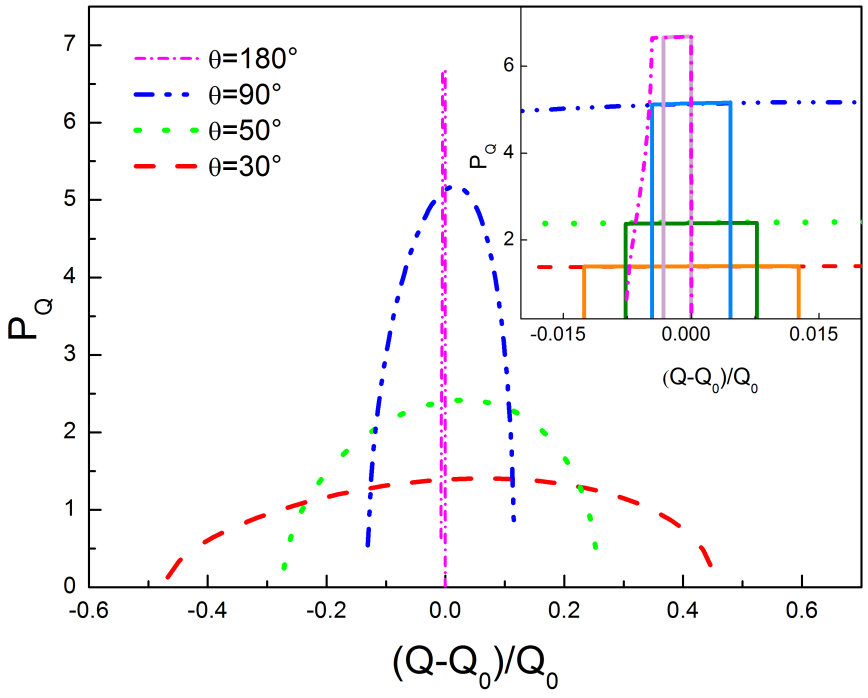

Figure 1.9: P_Q profiles sampled by an optics of 0.25 numerical aperture at various values of θ (see legend). Inset: full/dashed lines are the P_Q profiles with/without a mask with $\Delta_Q = 0.1\,\mu m^{-1}$.

focused on the acoustic dynamics of disordered systems [20, 21, 22, 23, 24, 25].

One of the new tools developed within this thesis is a new, simple and inexpensive approach, which relies on the use of special spatial filters (hereafter referred to as 'masks') able to select the desired P_Q profile in isotropic samples [26].

Fig. 1.10 shows the rationale of the mask's design for an isotropic sample contained in a cylindrical holder with axis orthogonal to the scattering plane and crossing the scattering volume. We assume that the scattering comes from a point-like source (O), chosen as the origin of a Cartesian (x, y, z) reference frame and corresponding to the intersection between the z axis (normal to the plane of collection optics) and $\underline{k}_i$ (located in the (y, z)-plane); we further assume that the divergence of the incoming beam is negligible with respect to that of the scattered one. The locus of the $\underline{k}_s$ vectors corresponding to the same Q-value is thus given by the surface of the cone having as axis $\underline{k}_i$ and angular aperture θ. The scattered photons with a given Q are hence located at the intersection between such a cone and the plane of the collection optics. Given a plane parallel to the one of the collection optics and placed at a distance $d_M \leq f_2$ from O (where f_2 is the distance between O and the plane of the collection optics), the intersection curve can be calculated from the following parametric equation, in which α ranges from $-\alpha_m$ to $+\alpha_m$ (where α_m

depends on the geometry and it is $< 180°$):

$$\begin{aligned} x &= d_s \tan\varphi + d_q \tan[\arcsin(\tfrac{n_s}{n_q}\sin\varphi)] + \\ &+ [\tfrac{d_M}{\cos(\gamma-\beta)} - d_s - d_q]\tan[\arcsin(n_s \sin\varphi)] \\ y &= d_M \tan(\gamma-\beta) \\ \beta &= \arctan(\tan\theta\cos\alpha) \\ \varphi &= \arctan(\tfrac{\sin\theta\sin\alpha}{\sqrt{\sin^2\theta\cos^2\alpha+\cos^2\theta}}) \end{aligned} \tag{1.21}$$

where d_s, d_q and n_q are the inner radius, the wall's thickness and the refraction index of the cylindrical sample container, respectively, while γ is the angle between $\underline{k}_i$ and the z axis (further details about these formulas in Appendix A). We note that Eqs. 1.21 also account for sample/container and container/air refractions. Eqs. 1.21 are derived for a specific geometry, however, following the same rationale, similar equations can be easily derived for any experimental geometry. A mask able to stop the radiation corresponding to Q-values falling outside the selected $Q_0 \pm \Delta_Q$ is simply a slit, which can be easily fabricated by using Eqs. 1.21 to print out the curves corresponding to $Q_0 + \Delta_Q$ and $Q_0 - \Delta_Q$ into a piece of an optically opaque material (we used a black paper sheet) and then cutting the slit.

In order to test the effectiveness of our solution we fabricated masks for several values of θ, i.e.: 30°, 40°, 50°, 60°, 70°, 90° and 180°. For each angle we collected three BLS spectra from a reference sample (water at room temperature): one without masks and the other two with a broadband ($\Delta_Q = 0.7\ \mu m^{-1}$) and a narrow-band ($\Delta_Q = 0.1\ \mu m^{-1}$) mask. The latter corresponds to an almost flat Q-distributions spanning a Q-range < 1.5 % around Q_0, as shown in the inset of Fig. 1.9. The accumulation time substantially increases with decreasing of Δ_Q (i.e., the slit's width) because of the rejection of all photons falling outside the desired (and selectable) $Q_0 \pm \Delta_Q$ range. However this method significantly improves the collected intensity from Brillouin lines with respect to the more traditional approach consisting in the reduction of the numerical aperture of the collecting optics. We can estimate the enhancement of the collected intensity as the ratio between the length and the width of the used slit. For the geometries shown in the present manuscript, this ratio ranges from ≈ 20 to ≈ 50. Furthermore the overall counting for such chosen photons can be improved by using optics with larger numerical aperture.

The experiment was performed at the Ghost laboratory at the University of Perugia (Italy), using a single mode cw laser ($\lambda = 532\,nm$ wavelength), a collection optics with 0.25 numerical aperture and a Sandercock triple pass tandem FP interferometer. The scheme of the setup is shown in Fig. 1.4. The beam laser was, at first, splitted in two paths thanks to a beamsplitter. One part was sent to the side pinhole entrance of the interferometer and it worked as a feedback for the auto stabilization routine of the FP. The brightest, transmitted, part is sent to a mirror mounted on a rotating stage centered on the sample position. Moving such mirror accordingly to the rotational stage, it is possible to vary the direction of the incoming

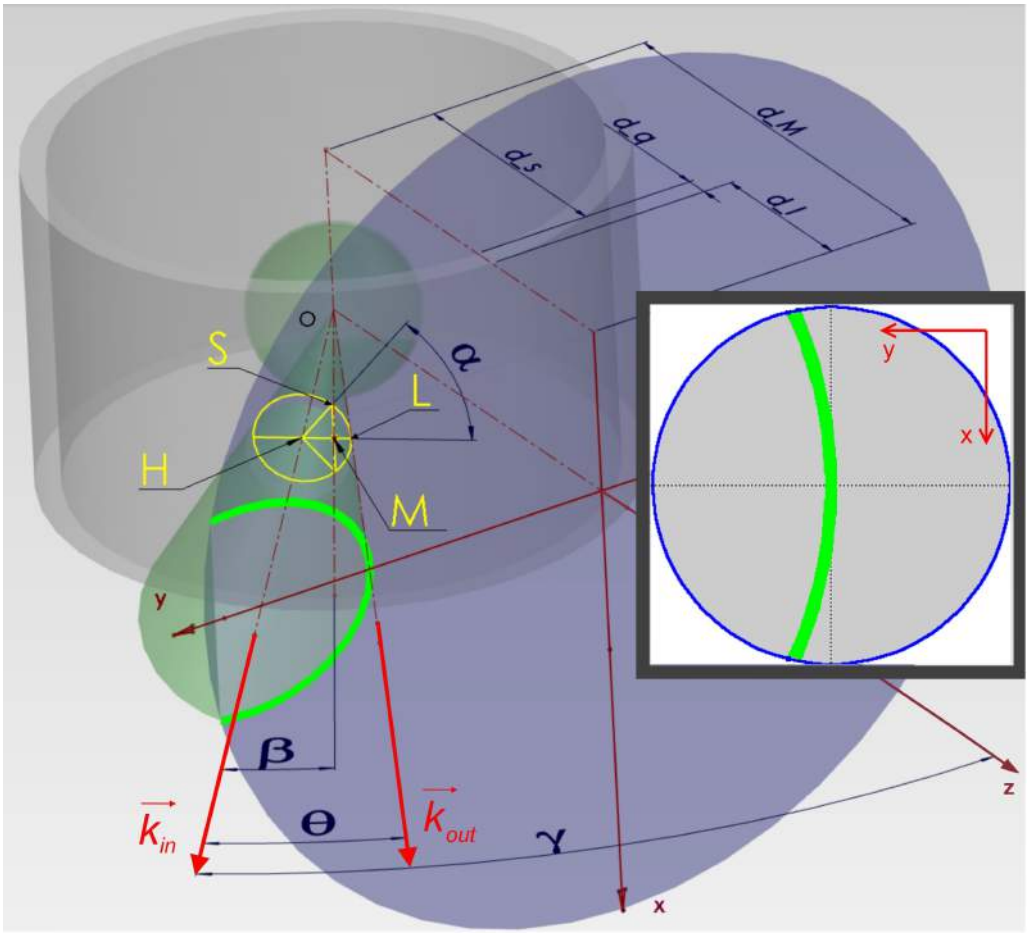

Figure 1.10: The scattering from the sample (embedded in a cylindrical container) originates from O. $\underline{k}_i$ and θ are the wavevector of incoming photons and the scattering angle, respectively, while the green cone is the locus of the $\underline{k}_s$ vectors corresponding to the equal−Q scattering. The shape of the slit (highlighted in glow green) is determined by the intersection between the cone and the plane of the collection optics (in blue). See text for the meaning of the other symbols. Inset: 2 inches diameter mask designed with the following parameters: $\gamma = \theta = 30°$, $d_M = 10\,cm$, $d_s = 3.5\,mm$, $d_q = 1\,mm$, $n_s = 1.33$, $n_q = 1.5$ and $\Delta_Q/Q_0 = 3.7\%$; at $\lambda = 532\ nm$ this mask selects photons scattered by acoustic modes with Q-values in the $(8.1 \pm 0.3)\,\mu m^{-1}$ range.

beam and consequently the scattering angle. In principle, with this setup, we can have a full angle tunability, so enlarging the available spectral window for Brillouin light scattering experiments. The scattered light filtered by our "masks", was then acquired and analyzed by the interferometer.

The sample was controlled in temperature with an homemade sample holder which, thanks to Peltier cells and thermo-resistances, allows to reach temperatures in a range between $-40° \div 80°$ with a stability of about $0.5°$ in the whole temperature range.

At the probed temperature and Q-range the frequency position (Ω_{LA}) and linewidth (Γ_{LA}) of the longitudinal acoustic (LA) modes are related to the adiabatic

sound velocity ($c_s = \Omega_{LA}/Q$) and kinematic longitudinal viscosity ($D_{LA} = \Gamma_{LA}/Q^2$) respectively; reference values for c_s and D_{LA} are available in the literature [24, 25, 27, 28, 29, 30, 31]. In order to extract the experimental values of these parameters we fitted the BLS spectra with a DHO function [32] numerically convoluted [11] with the instrumental response function $R(\omega)$. The latter was obtained measuring the scattered light by a roughened aluminum plate [33].

BLS spectra at two selected values of θ (30° and 90°) are reported in Fig. 1.11 along with $R(\omega)$. The two main effects of the masks on the spectra are readily evident at $\theta = 30°$: (i) on decreasing Δ_Q the line-width of the Brillouin doublet becomes narrower up to become close to that of $R(\omega)$ and (ii) the peak position shifts at lower ω's. Both effects can be understood by recalling that the experimental Brillouin doublet is the sum (weighted by P_Q) of different peaks arising from LA modes with Q in the $Q_0 \pm \Delta_Q$ range, convoluted with $R(\omega)$. Since each peak has its own peak frequency ($\Omega_{LA} = c_s Q$) the finite collected Q-range turns into an spurious broadening $\approx c_s \Delta_Q$. In the present case such a broadening is more pronounced in the high frequency side of the Brillouin doublet because of the $\propto Q^2$ dependence of Γ_{LA} (in addition to the asymmetry of P_Q at low θ; see Fig. 1.9) and turns into a shift in the barycenter of the experimental peak towards higher frequencies. Overall, these effects are expected to be larger when $\Gamma_{LA} < c_s \Delta_Q$, which is the case reported in Fig. 1.11a, while may become negligible on increasing Γ_{LA} well above $c_s \Delta_Q$.

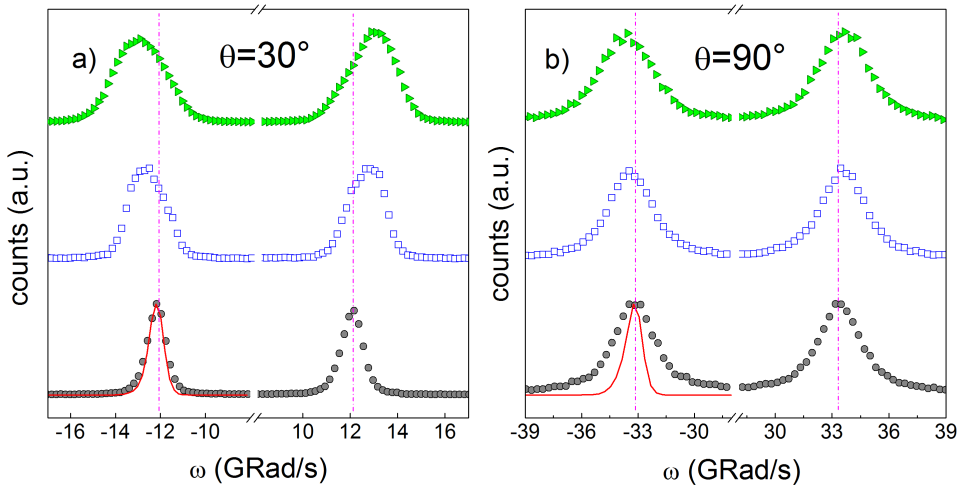

Figure 1.11: BLS spectra of water at room temperature collected without masks (top traces), and with a wide ($\Delta_Q = 0.7\ \mu m^{-1}$; middle traces) and narrow ($\Delta_Q = 0.1\ \mu m^{-1}$; bottom traces) bandpass mask. Data corresponding to $\theta = 30°$ and 90° are reported in panel (a) and (b), respectively. Full lines are $R(\omega)$; vertical dotted lines mark the position of the peaks corresponding to the narrow bandpass mask.

Fig. 1.11b reports data collected at $\theta = 90°$; here Γ_{LA} is ≈ 7.5 times larger than at $\theta = 30°$. At a first glance the use of the masks seems to have marginal effects in this case. However, a closer look to the results of the data analysis and

to literature data (reported in Fig. 1.12) shows that even at $\theta = 90°$ the values of Ω_{LA} and Γ_{LA} (and then those of c_s and D_{LA}) are overestimated when the mask with $\Delta_Q = 0.1\ \mu m^{-1}$ is not used.

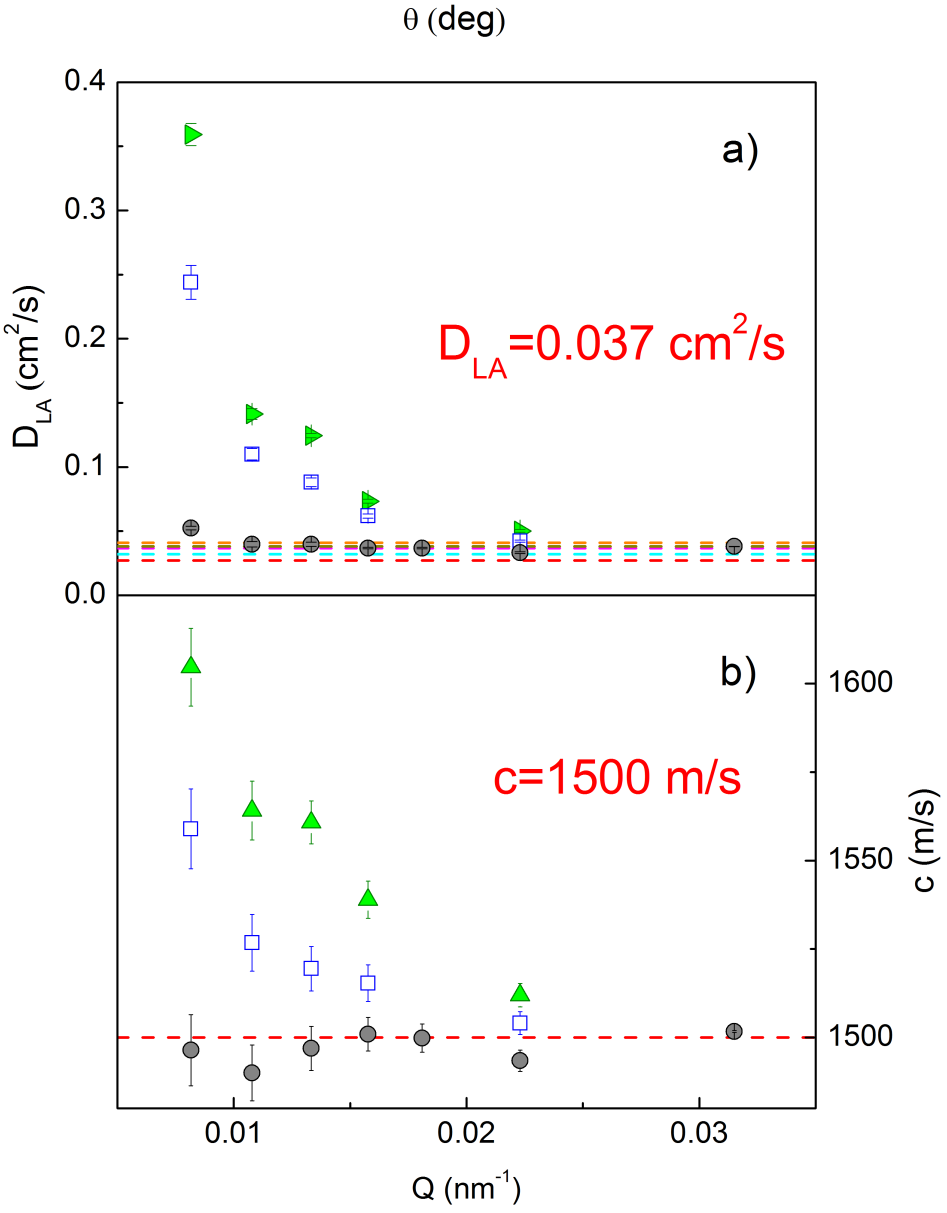

Figure 1.12: Q-dependence of D_{LA} (panel a) and c_s (panel b), as obtained from the fit of BLS spectra. In the upper and lower horizontal scales we report the angles at which experiments were performed and the corresponding Q values, respectively. Green triangles, blue squares and black circles are data obtained without mask and by using the masks with $\Delta_Q = 0.7\ \mu m^{-1}$ and $\Delta_Q = 0.1\ \mu m^{-1}$, respectively. Horizontal lines are the literature values of D_{LA} [24, 25, 28, 29, 30, 31] and c_s [27].

We note that the value of D_{LA} determined at 30° without using the masks exceeds the expectations by one order of magnitude. For $\theta < 90°$ also the values of c_s,

that can be determined by BLS with a typically accuracy < 1 %, are largely overestimated if the narrow-band mask is not used. Conversely, the use of the narrow-band mask provides a good agreement with literature values [23, 24, 25, 27, 28, 29, 30, 31] in the whole exploited θ range; small discrepancies (≈ 1 %) are compatible with the accuracy in the determination of θ ($\pm$ 0.2°). We finally note that in the backscattering configuration ($\theta = 180°$) we did not found advantages from the use of masks, as expected in light of the intrinsic narrowness of P_Q (even narrower than the Q-bandpass of the narrow-band mask; see Fig. 1.9).

In conclusion, we demonstrated the effectiveness of a method to purify BLS spectra from the spurious contributions due to the finite aperture of collection optics. This is an artifact particularly relevant for small values of θ, but it could also affect high-accuracy measurements carried out at $\theta = 90°$, a widely used experimental geometry. The proposed approach can be of potential interest for the whole community of Brillouin spectroscopists, since it is entirely based on general geometrical considerations, and can be easily and inexpensively implemented to any existing BLS setup and sample geometry.

The possibility to collect BLS spectra as a function of θ down to well below 90° with improved count-rate and resolution enables to probe the whole Q-range accessible by BLS spectroscopy without the need to carry out special data analysis based on arbitrary ansatzs on the Q-dependencies of the peak frequency and line-widths. This approach is particularly critical when these Q-dependencies contain information on the dynamical process under investigation, as in the study of relaxation processes in normal [21] and supercooled liquids [34]. Such a broad Q-tunability of BLS can be also exploited, e.g., to study elasticity in nanostructures [35], colloids [36] and phononic crystals [37]. In addition, at a given value of θ the use of the masks becomes more relevant in all the cases when the Q-interval collected by the optics is larger as, e.g., in the cases of UV-BLS [38, 39, 40] (because of the shorter probing wavelength) or micro-BLS setups based on microscope objectives (because of the larger numerical aperture of collection optics) [41]. Finally, we note that the present approach could be of relevance when unavoidable constrains force the use of low-angle scattering geometries as, for instance, in high-pressure BLS experiments carried out in diamond anvil cells. Here the limited optical aperture of the sample environment often restricts the exploitable range in θ [42].

UV domain: Inelastic Ultraviolet Scattering

In the previous paragraph we have shown how to cover a (Q, ω) region larger than usual. Combining BLS and spatial filtering approach it is possible now to investigate, with continuity, the region with $Q = 0.005 \div 0.04\, nm^{-1}$ and $\omega = 2 \div 10^4\, GRad$. The (Q, ω)-region just close to BLS one is extremely interesting because there the hydrodynamic approach starts to fail and, as we pictured in the introduction, matter starts to behave differently, showing interesting transitions between the collective and the single particle limits.

Through eq.1.2 is straightforward that Q depends on the scattering geometry (θ) and on the wavelength of the laser source. It is not possible to probe such dynamic

region just changing the scattering geometry of a BLS experiment: the backscattering configuration already gives the maximum Q and ω limit. Thus, the only way to reach higher Q-energy regions is to change the light source. It means that we have to work in the ultraviolet (UV) range if we want to cover the region characterized by $Q = 0.07 \div 0.15\, nm^{-1}$ and $\omega = 2 \div 10^3\, GRad$. At such wavelengths it is not convenient to use transmissive optics because of the high absorptions. Therefore we cannot use the longstanding interferometric FP-based techniques as they are (in Chapter 4 we will talk about the novel FP-UV setup we realized) and thus we have to operate with reflecting optics such as mirrors and gratings.

Ten years ago people finally could cover such spectral range constructing at Elettra Synchrotron (Trieste) a unique bemaline operating with only reflecting optics and with UV Synchrotron light: BL 10.2L - IUVS dedicated to the Inelastic Ultra Violet Scattering.

In the following we will describe only the main characteristics of the beamline. We refer the reader to ref. [43] for further details. The operating scheme of the end-station is outlined in Fig. 1.13: the synchrotron light is focused with a spherical mirror at the entrance of a monochromator. Then the monochromatic beam is sent to the sample and collected in quasi-backscattering geometry ($\theta \approx 176°$) by another spherical mirror. At this point the beam is sent to another monochromator which have to analyze the light to separate the all spectra components. The diffracted light is collected by CCD camera from which we can obtain the counts for each spectral component at same time.

We hereby discuss a little bit deeper the main characteristic of IUVS beamline. In order to maximize the value of Q achieved by the IUVS beamline and, hence, to probe larger portions of the "mesoscopic range", a fixed backscattering geometry was adopted; the Q-value is changed by varying the incoming beam energy in between 5 and 12 eV. Furthermore, we need incident photon flux on the sample larger than $10^{11} ph/s$ to compensate the low efficiency of the spontaneous scattering process arising from the density fluctuations. A radiation which can satisfy all these requirements is the one resulting from synchrotron light sources. Thanks to the well known properties of synchrotron radiation, a wide range of photon energies are available, allowing also an easy Q-tunability in the scattering experiments. In particular Elettra Synchrotron fits the requirements of photon flux and UV range photon energy.

The requirement of high flux calls for an undulator with maximum possible length compatible with the length of the straight sections of the storage ring ($4.5\, m$). With usual magnet distribution in the undulator it is possible to obtain high emitted power and power density, but in this way the optics in the photon transport can be damaged by such huge intensities. To avoid such problems the beamline was built with an exotic undulator configuration name Figure-8, conceived by Tanaka and co-workers [44]. With this special configuration it is possible to reduce the on-axis power density of the photon beam. Furthermore, to reduce the risk to overheat the optics with the radiation, all the mirrors involved in the beam transportation are water cooled, ensuring a more stable alignment free of heat stress.

The beam resulting from the undulator must be cleaned by the high energies harmonics. To do so a couple of mirrors is used: one made by GLIDCOP with a

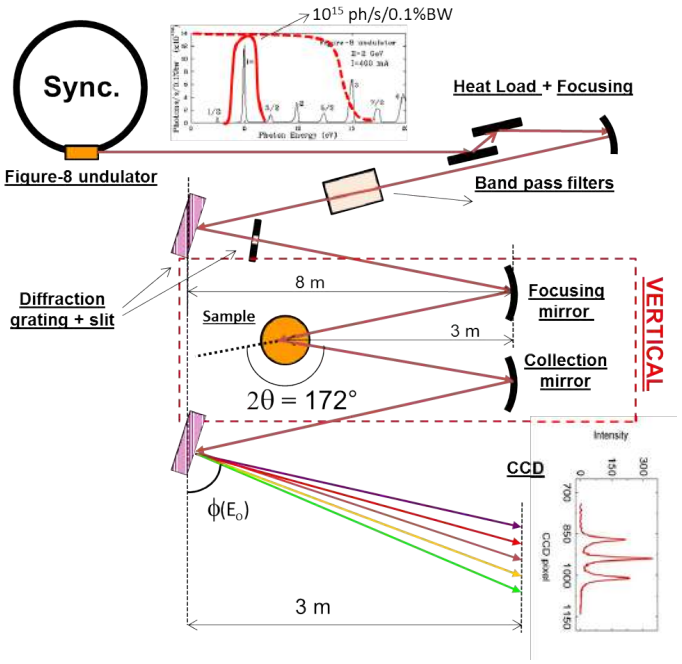

Figure 1.13: The rationale of the IUVS beamline. The broad band Synchrotron light resulting from the undulator is firstly filtered by its higher energy harmonics through the heat load section, then it is focused into the entrance slit of the monochromator. The latter works in the Czerny– Turner normal incidence (NIM) configuration and select a wavelength with a narrow bandwidth. Then the beam interacts with the sample and the scattered light is analyzed by another NIM which separate all the spectra component of the scattered signal that are acquired by a CCD.

gold coating and the other entirely made of silicon. These reflecting systems act as low pass-band filters. The beam is then focused by a spherical silicon mirror onto the entrance slit of the monochromator.

The monochromator used at the IUVS beamline is the Czerny-Turner Normal Incidence Monochromator (NIM). The working outlook of a NIM is sketched in Fig.1.15. The beam coming from the entrance slit is collimated by a spherical mirror and sent to the grating. The latter is an Ag ruled mirror with MgF_2 coating operating in reflection configuration (blazed grating) to be more efficient. The light spectral components, spatially separated, are sent to a collecting spherical mirror which refocuses the beams. At this point, thanks to an exit slit it is possible to select the desired energy.

We now briefly recall the equation to describe the grating diffraction. A monochromatic beam with wavelength λ and impinging the grating with an angle α, results in a diffracted pattern, whose orders have each an inclination β_m:

$$m\lambda = \Lambda(\sin\alpha + \sin\beta_m) \tag{1.22}$$

where α is the angle of incidence of the beam, β_m is the angle of the diffracted order m and Λ is the period of the grating. From eq. 1.22 it is clear that the m-th diffracted order is diffracted with a different angle β_m. All these beams are collected by a spherical mirror which refocuses the beams in its focal plane. From the laws of

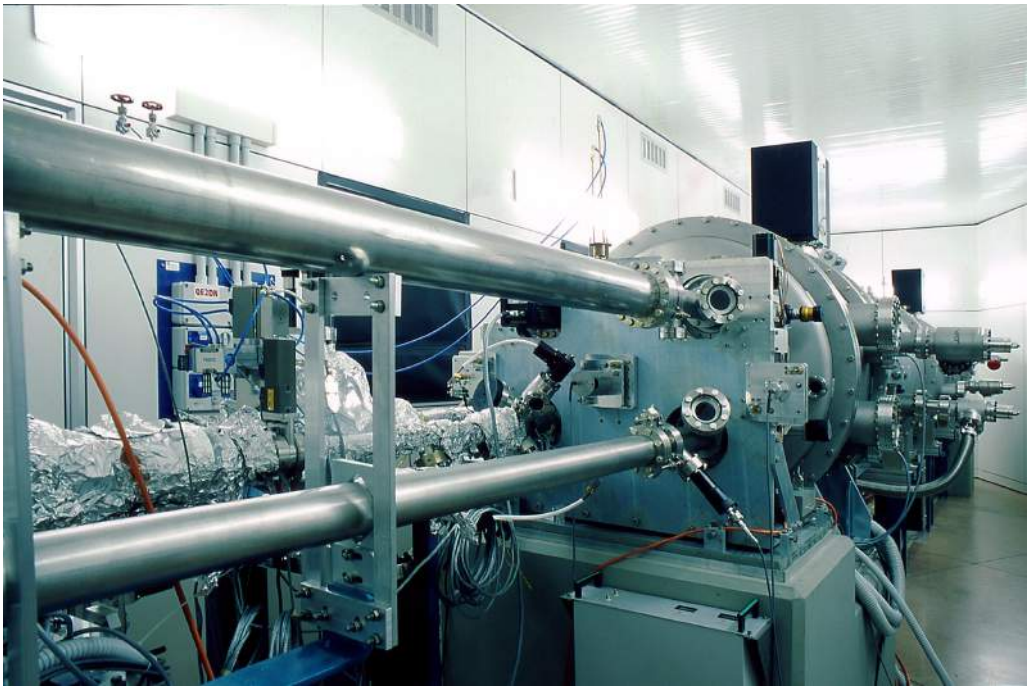

Figure 1.14: The monochromator and analyzer chamber

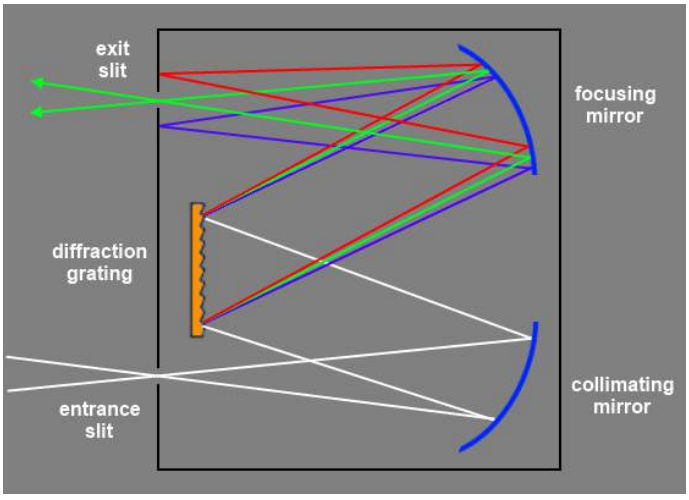

Figure 1.15: The beam coming from the entrance slit is collected, collimated and sent to the grating. The latter separates different spectral components of the beam at different scattering angles. The last spherical mirror collects all these beams and focuses them in a focal plane. According to the laws of the optics: to different incident angles of the collimated beams correspond different points in the focal plane. Thus, to select one of the spectral components it is enough to cut with the exit slit the undesired focused spots.

optics, it is well known the a focusing optics transforms different angles of collected beams in different points in the focal plane. Then it is enough to choose a proper slit to select the diffracted monochromatized wavelength.

At this point, the beam is sent to the sample and interacts with it following the

scattering process already described at the beginning of this chapter. The process results in a scattered beam containing the different spectral components. The beam is collected and refocused by another spherical mirror to the entrance of the analyzer (Fig. 1.16). The latter is a grating twin of the one used as monochromator.

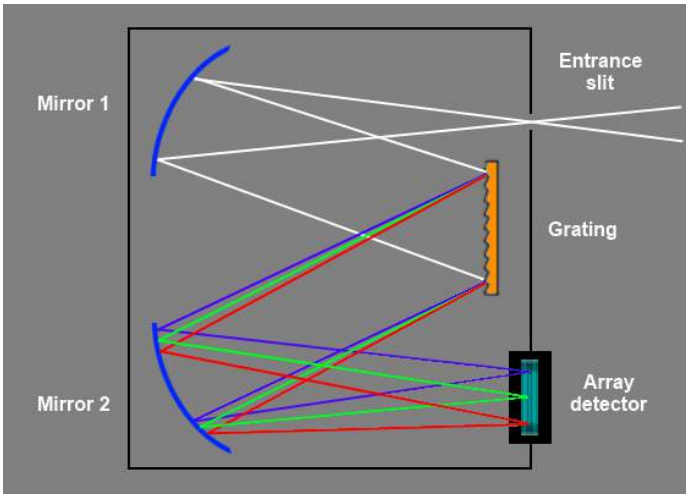

Figure 1.16: The analyzer NIM scheme. The spectral components are directly recorded on a CCD camera allowing the acquisition of the whole spectrum at the same time.

It is now useful to recall other properties of diffraction gratings. Through the fundamental equation (eq.1.22) it is possible to introduce the all quantities which characterize the analyzer. The *free spectral range* (FSR) and the resolving power (P_R).

We have seen that the m-th order of the light with wavelength λ_1 is diffracted at certain angle β_m. It is possible that at the same angle a different order m' of another wavelength λ_2 is diffracted. This means that

$$m\lambda_1 = m'\lambda_2 \tag{1.23}$$

If $\lambda_1 > \lambda_2$, then it follows that $m' > m$. With these constraint the closest λ which can satisfy the eq. 1.23 is that one for which the $(m+1)$-th order is diffracted at β angle.

$$m\lambda_1 = (m+1)\lambda_2 \tag{1.24}$$

So we can define the FSR as the λ-ω range without overlapped diffracted orders:

$$\Delta\lambda = \frac{\lambda_2}{m} \Rightarrow \Delta\omega = \frac{\omega}{m} \tag{1.25}$$

In principle to have a bigger as possible FSR we should work with the first diffraction order. In this way the FSR-ω would be of the order of $\sim eV$ for IUVS. It is much more than enough if we want to study the acoustic modes that are characterized by an exchanged energy of $\sim meV$ or lower. We will see that in order to have an high resolution we need to work at high m-order and therefore to use a

limited FSR, but still large enough to study the acoustic modes. We have already discussed in the case of BLS that, in order to resolve the small energy shifts resulting from the scattering process, we need an high resolution.

It can be shown that

$$\frac{\Delta E}{E} = \sqrt{\left(\frac{\Delta E}{E}\right)^2_{grating} + 2\left(\frac{\Delta E}{E}\right)^2_{slit}} \tag{1.26}$$

with $\left(\frac{\Delta E}{E}\right)_{grating} = \frac{1}{mN}$ and $\left(\frac{\Delta E}{E}\right)_{slit} = \frac{\sigma}{2F}\cot\theta$, where N is the number of illuminated grating lines ($\approx 10^4$ at IUVS), σ is the exit slit width ($\approx 50\mu m$), $F = 8m$ is the focal distance between the mirror and exit of the slits and θ is the blazed angle ($70°$). The resulting $\frac{\Delta E}{E}$ for IUVS is in the order of 10^{-6}.

Once the spectrum is analyzed it is recorded by a CCD camera allowing in one shot to obtain a full spectrum measurement. This enables relative quick measurements, reducing the damage risks for the sample because of a long exposure to UV light.

The whole IUVS beamline is in ultra high vacuum to limit absorption by air of the radiation and to maintain the optics free of eventual impurities. The beamline has an active feedback system that continuously adjusts the optics positions to compensate thermic expansions.

Finally the beamline is equipped with different sample holders to perform temperature and pressure dependent measurements.

1.1.2 Inelastic X-Ray Scattering

This section is dedicated to the last energy-resolved technique used in this work: inelastic X-Ray scattering (IXS).

In order to probe the high-Q, high-energy dynamics we need to work with higher energy probes like X-Rays or neutrons. In the introduction we already stressed the main differences between INS and IXS. For the reason we gave, finally we preferred to use IXS, particularly suitable for the study of disordered systems. In the following we will describe the equations for the matter-radiation interaction and we will show the relation between the total double differential cross section and the dynamic structure factor $S(Q,\omega)$ related, as we already said, to the density fluctuation correlation functions.

Let's start from the Hamiltonian for a free particle in an electric potential U:

$$\mathcal{H} = \frac{\underline{p}^2}{2m} + U_0 \tag{1.27}$$

When an electromagnetic field is turned on, to describe the evolution of the charged particles the $\mathcal{H}$ of the system must be modified. At the energy of x-rays $\approx 20KeV$, magnetic interactions between matter and radiation can be neglected, indeed the Zeeman interaction between the electron spin and the photon magnetic field $(\underline{\mu}\cdot\underline{B})$ and spin-orbit contributions $(\propto \underline{s}\cdot(\underline{p}\wedge\underline{A}))$, are two orders of magnitude lower than the non magnetic contributions.

With these assumption, to take into account the electromagnetic field it is necessary to use the so called *minimal substitution*:

$$\begin{aligned} \underline{p} &\rightarrow \underline{p} + \tfrac{e}{c}\underline{A} \\ \mathcal{H} &\rightarrow \mathcal{H} + e\phi \end{aligned} \tag{1.28}$$

resulting in

$$\mathcal{H} = \frac{1}{2m}\left(\underline{p} + \frac{e}{c}\underline{A}\right)^2 - e\phi + U_0 \tag{1.29}$$

It can be shown that, through eq. 1.29 and the Hamilton equations, it is possible to to obtain the classical motion equation for a charge in an electromagnetic field

$$m\ddot{\underline{r}} = -e(\underline{v} \wedge \underline{B}) - e\underline{E} \tag{1.30}$$

only in the case of the so called Coulombian Gauge, for which $\underline{\nabla} \cdot \underline{A} = 0$. Thanks to this vector potential, the Hamiltonian can be rewritten as follows (with $\phi = 0$):

$$\mathcal{H} = \mathcal{H}_0 + \frac{e^2}{2mc^2}\underline{A}^2 + \frac{e}{mc}\underline{A} \cdot \underline{p} \tag{1.31}$$

the third term was obtain thanks to commutation property $\left[\underline{A}, \underline{p}\right] = 0$ descending from the chosen Coulomb Gauge. This term is the one accounting for absorption phenomena. At the x-rays energies we are working, we can neglect also this term because we are far from the electron transition energies and no resonance effects arise.

Finally, the system can be treated, for low intensities fields, with the perturbation theory conserving the quadratic term in $\underline{\mathrm{A}}$ as the perturbation $\hat{V}$.

To describe formally the scattering process let's introduce the approximation of far sources, therefore we can write the incoming and the scattered photons as two plane waves:

$$\begin{aligned} |\underline{k}_i\rangle &\rightarrow \psi_{\underline{k}_i} = \tfrac{1}{L^{3/2}} e^{i\underline{k}_i \cdot \underline{r}} \\ \left|\underline{k}_f\right\rangle &\rightarrow \psi_{\underline{k}_f} = \tfrac{1}{L^{3/2}} e^{i\underline{k}_f \cdot \underline{r}} \end{aligned} \tag{1.32}$$

where $\underline{k}_i$ and $\underline{k}_f$ are the wavevectors of the incoming and scattered photons. The normalization was set assuming that the scattering process is confined in a sample volume of L^3. From this assumption we will fix also some boundary conditions and we will obtain the formula for the density of finale states.

We can introduce this notation:

$$\left\langle \underline{k}_f \right| \hat{V} \left| \underline{k}_i \right\rangle = \frac{1}{2\pi\hbar} \int \mathrm{d}\underline{r}\; e^{-i\underline{k}_f \cdot \underline{r}}\; \hat{V}\; e^{i\underline{k}_i \cdot \underline{r}} \tag{1.33}$$

In order to evaluate the differential cross section of the scattering process we can use the *Fermi Golden Rule* [45]. The probability for the transition from $|\underline{k}_i\rangle$ to $\left|\underline{k}_f\right\rangle$ is

$$W_{\underline{k}_i \rightarrow \underline{k}_f} = \frac{2\pi}{\hbar} \left| \int \mathrm{d}\underline{r}\; \psi^*_{\underline{k}_f}\; \hat{V}\; \psi_{\underline{k}_i} \right|^2 \rho_{\underline{k}_f}(E_f) \tag{1.34}$$

where $\rho_{\underline{k}_f}(E_f)$ is the density of states $\left|\underline{k}_f\right\rangle$ around energy E_f. The number of scattered photons in the interval E,$E+\delta E$ is

$$\mathrm{d}N(E) = \rho_{\underline{k}_f}(E_f)\mathrm{d}E_f = \rho_{\underline{k}_f}\mathrm{d}k_f \tag{1.35}$$

so we can write

$$\rho_{\underline{k}_f}(E) = \frac{\partial N}{\partial E} = \frac{\partial N}{\partial \underline{k}}\frac{\partial \underline{k}}{\partial E} = \rho_{\underline{k}_f}\frac{\partial \underline{k}_f}{\partial E} \tag{1.36}$$

Fixing the boundary conditions as

$$\psi_{\underline{k}_f}(\underline{r}=0) = \psi_{\underline{k}_f}(\underline{r}=\underline{L})$$

we obtain

$$e^{i\underline{k}_f\cdot L} = e^{ik_x\cdot L_x}e^{ik_y\cdot L_y}e^{ik_z\cdot L_z} = 1$$

so

$$k_j = n_j\frac{2\pi}{L_j} \qquad\qquad j=(x,y,z)$$

where n_j is an integer number. So, in the reciprocal space a photon state occupies a volume $\Delta\underline{k} = \left(\frac{2\pi}{L}\right)^3$. The number of states in a volume $\Omega_{\underline{k}}$ will be $n_{\underline{k}_f} = \frac{\Omega_{\underline{k}}}{\Delta_{\underline{k}}}$ and the density of states will be

$$\rho_{\underline{k}_f} = \frac{n_{\underline{k}_f}}{\Omega_{\underline{k}}} = \frac{1}{\Omega_{\underline{k}_f}}\frac{\Omega_{\underline{k}_f}}{\Delta_{\underline{k}}} = \frac{1}{\Delta_{\underline{k}}} = \left(\frac{L}{2\pi}\right)^3$$

and from eq. 1.36

$$\rho_{\underline{k}_f}(E) = \left(\frac{L}{2\pi}\right)^3\frac{\mathrm{d}\underline{k}_f}{\mathrm{d}E} \tag{1.37}$$

Considering spherical symmetry

$$\mathrm{d}\underline{k}_f = k_f^2\sin\theta\ \mathrm{d}\theta\ \mathrm{d}\phi\ \mathrm{d}k = k_f^2\mathrm{d}\Omega\ \mathrm{d}k \tag{1.38}$$

We said that the photons can be described as plane waves, so $E_f = \hbar\omega_f = \hbar ck_f$ and $\mathrm{d}E_f = \hbar c\ \mathrm{d}k_f$. Combining eq. 1.37- 1.38 finally we obtain:

$$\rho_{\underline{k}_f}(E) = \left(\frac{L}{2\pi}\right)^3\frac{k_f^2\ \mathrm{d}\Omega}{\hbar c}$$

In the more simple case of elastic scattering, the sample is not involved in any creation or annihilation process, therefor $|\underline{k}_f| = |\underline{k}_i|$ and $E_f = E_i$. Considering the scattering from a single electron, we can write the differential cross section:

$$\frac{\mathrm{d}\sigma}{\mathrm{d}\Omega} = \frac{W_{\underline{k}_i\to\underline{k}_f}}{\phi\,\Delta\Omega} \tag{1.39}$$

where ϕ is the photon flux, defined as the number of photons passing, orthogonally, through the surface A in a time interval Δt ($n_{ph} = \phi A\Delta t$). This formulation is equivalent to count the number of photons in a volume $Ac\Delta t$, : $n_{ph} = \rho Ac\Delta t$

(where c is the speed of light and ρ is the density of photons). Combining these equations and with the assumption of single photon interaction ($\rho = 1/L^3$), from eq. 1.34 it follows:

$$\frac{\mathrm{d}\sigma}{\mathrm{d}\Omega} = \frac{k_f^2\hbar^2}{c^2}\left|\left\langle \underline{k}_f\right|\widehat{V}\left|\underline{k}_i\right\rangle\right|^2 \tag{1.40}$$

To extend this result to the inelastic case, we have now to consider that the system can absorb the radiation and exchange energy with it. It means that photons can induce transitions among the atomic states $\langle\lambda|$. When the sample goes from a state $\langle\lambda|$ to a state $\langle\lambda'|$, the energy conservation imposes that the exchanged energy is $\hbar\omega = E_{\lambda'} - E_\lambda$. The cross section can be written:

$$\frac{\mathrm{d}^2\sigma}{\mathrm{d}\Omega\mathrm{d}E_{k_f}} = \frac{k_f^2\hbar^2}{c^2}\left|\left\langle \underline{k}_f\lambda'\right|\widehat{V}\left|\underline{k}_i\lambda\right\rangle\right|^2 \delta(\hbar\omega + E_\lambda - E_{\lambda'}) \tag{1.41}$$

In a more general case we have to think that a set of different initial states for the system is available, each of them with a certain occupancy probability p_λ ($\sum_\lambda p_\lambda = 1$). Concerning the final states of the sample, in absence of particular selection rules, all of them will be detected. Under these considerations we can write the so called Born approximation:

$$\frac{\mathrm{d}^2\sigma}{\mathrm{d}\Omega\mathrm{d}E_{k_f}} = \frac{k_f^2\hbar^2}{c^2}\sum_{\lambda\lambda'} p_\lambda\left|\left\langle \underline{k}_f\lambda'\right|\widehat{V}\left|\underline{k}_i\lambda\right\rangle\right|^2 \delta(\hbar\omega + E_\lambda - E_{\lambda'}) \tag{1.42}$$

Let's go deeper about the nature of the interaction. We can write the interaction potential $\widehat{V}$ between the probe and the sample as the superposition of the single photon-atom interactions:

$$\widehat{V}(\underline{r}) = \sum_j 2\pi\hbar^2\widehat{V}_j(\underline{r} - \underline{R}_j) \tag{1.43}$$

where $\underline{R}_j$ is the position of the j^{th} scattering center inside the sample. With some manipulation it is possible to obtain the double differential cross section

$$\frac{\mathrm{d}^2\sigma}{\mathrm{d}\Omega\mathrm{d}E_{k_f}} = \frac{k_f^2\hbar^2}{c^2}\sum_{\lambda\lambda'} p_\lambda\left|\left\langle \underline{k}_f\lambda'\right|\sum_j e^{i\underline{Q}\cdot\underline{R}_j}\widehat{V}_j(Q)\left|\underline{k}_i\lambda\right\rangle\right|^2 \delta(\hbar\omega + E_\lambda - E_{\lambda'}) \tag{1.44}$$

where $\underline{Q} = \underline{k}_f - \underline{k}_i$ and we used the space Fuorier transform expression for the potential.

Using the integral representation for the δ function and considering that $|\lambda[\lambda']\rangle$ is a full set of eigenstates for the Hamiltonian ($\mathcal{H}\,|\lambda[\lambda']\rangle = E_{\lambda[\lambda']}\,|\lambda[\lambda']\rangle$ and $\sum_\lambda |\lambda\rangle\langle\lambda| = 1$), through the Heisenberg representation for the temporal evolution of the operators, we obtain:

$$\frac{\mathrm{d}^2\sigma}{\mathrm{d}\Omega\mathrm{d}E_{k_f}} = \frac{k_f^2\hbar^2}{c^2}\frac{1}{2\pi\hbar}\int_{-\inf}^{+\inf}\mathrm{d}t\; e^{-i\omega t}\sum_\lambda p_\lambda\langle\lambda|\left(\sum_{jj'} e^{-i\underline{Q}\cdot\underline{R}_j(0)}\widehat{V}_j^+(Q)\widehat{V}_{j'}(Q)e^{i\underline{Q}\cdot\underline{R}'_j(t)}\right)|\lambda\rangle \tag{1.45}$$

To simplify the formal expression, let's substitute $\sum_{\lambda} p_\lambda \langle\lambda| ... |\lambda\rangle$ with $\langle ...\rangle$:

$$\frac{\mathrm{d}^2\sigma}{\mathrm{d}\Omega \mathrm{d}E_{k_f}} = \frac{k_f^2\hbar^2}{c^2}\frac{1}{2\pi\hbar}\overline{|\widehat{V}(Q)|^2}\int_{-\infty}^{+\infty}\mathrm{d}t\; e^{-i\omega t}\sum_{jj'}\left\langle e^{-i\underline{Q}\cdot\underline{R}_j(0)}e^{i\underline{Q}\cdot\underline{R}_j(t)}\right\rangle \tag{1.46}$$

where $\overline{\cdots}$ indicates the thermal averaging.

Defining

$$\widetilde{S}(Q,\omega) = \frac{1}{2\pi}\int_{-\infty}^{+\infty}\mathrm{d}t\; e^{-i\omega t}\sum_{jj'}\left\langle e^{-i\underline{Q}\cdot\underline{R}_j(0)}e^{i\underline{Q}\cdot\underline{R}_j(t)}\right\rangle \tag{1.47}$$

we finally obtain

$$\frac{\mathrm{d}^2\sigma}{\mathrm{d}\Omega \mathrm{d}E_{k_f}} = \frac{k_f^2\hbar^2}{c^2}\overline{|\widehat{V}(Q)|^2}\widetilde{S}(Q,\omega) \tag{1.48}$$

Up to now, we didn't consider the explicit form for the perturbation $\widehat{V}$. Discussing the eq. 1.31 we noticed that the only important perturbative term of the free particle Hamiltonian is the one quadratic in $\underline{A}$:

$$\widehat{V} = \frac{e^2}{2mc^2}\sum_j \widehat{A}(\underline{R}_j,t)\widehat{A}^+(\underline{R}_j,t) \tag{1.49}$$

from which it is possible to obtain

$$\frac{\mathrm{d}^2\sigma}{\mathrm{d}\Omega \mathrm{d}E_{k_f}} = \left(\frac{e^2}{mc^2}\right)^2\frac{k_f}{k_i}\left(\hat{\epsilon}_f\cdot\hat{\epsilon}_i\right)\widetilde{S}(\underline{Q},\omega) \tag{1.50}$$

where $\hat{\epsilon}_f$ and $\hat{\epsilon}_i$ are, respectively, the polarization of the scattered and incident radiation. Actually $\widetilde{S}(\underline{Q},\omega)$ is still not the dynamic structure factor we talked about in the previous sections. It contains the contributions of both the electronic and nuclei correlation functions.

In the adiabatic approximation we can separate the quantum state system $|\lambda\rangle$ into the product of the electronic part $|\lambda_e\rangle$ and the nuclear one $|\lambda_n\rangle$.

From eq. 1.47 and using the substitution $\underline{R}_j = \tilde{\underline{R}}_j + \underline{u}_j$, where $\underline{u}_j$ is the electron position vector in respect to the position of the molecular center of mass $\tilde{\underline{R}}_j$:

$$\begin{aligned}\widetilde{S}(Q,\omega) &= \sum_\lambda p_\lambda\langle\lambda|\sum_{jj'}e^{-i\underline{Q}\underline{R}_i(0)}e^{i\underline{Q}\underline{R}_{j'}(t)}|\lambda\rangle = \\ &= \sum_{jj'}\left[\sum_{|\lambda_e\rangle}p_{|\lambda_e\rangle}\langle\lambda_e|\,e^{-i\underline{Q}\cdot\underline{u}_j(0)}e^{i\underline{Q}\cdot\underline{u}_{j'}(t)}|\lambda_e\rangle + \right. \\ &\qquad \left. + \sum_{|\lambda_n\rangle}\langle\lambda_n|\,e^{-i\underline{Q}\cdot\tilde{\underline{R}}_j(0)}e^{i\underline{Q}\cdot\tilde{\underline{R}}_{j'}(t)}|\lambda_n\rangle\right]\end{aligned} \tag{1.51}$$

Finally we can write

$$\frac{\mathrm{d}^2\sigma}{\mathrm{d}\Omega \mathrm{d}E_{k_f}} = \left(\frac{e^2}{mc^2}\right)^2\frac{k_f}{k_i}\left(\hat{\epsilon}_f\cdot\hat{\epsilon}_i\right)\overline{|f(Q)|^2}S(\underline{Q},\omega) \tag{1.52}$$

where now $S(\underline{Q},\omega)$ is the well known dynamic structure function which takes into account the nuclear distribution. $f(Q)$ is the *atomic form factor* which is related to

the electron distribution in the atom. For $Q \to 0$, $f(Q) = Z$, the atomic number. In the case of molecular systems it is possible to extend this formalism, introducing a molecular form factor usually computed through molecular dynamics simulation.

Because of the form factor Z-dependency, the efficiency of the inelastic scattering process is proportional to Z^2. Unfortunately, the photoelectron absorption, conversely, has a cross-section of the order of Z^4. This implies that for a liquid characterized by high Z number, the Thomson scattering is not a very efficient channel and the dimension of the sample must be decreased to avoid multiple scattering and absorption phenomena.

The flux of the scattered photons in an energy interval ΔE in a solid angle $\Delta\Omega$ is:

$$N = N_0 \frac{\mathrm{d}^2\sigma}{\mathrm{d}\Omega \mathrm{d}E} \Delta\Omega \; \Delta E \; \rho L e^{-\mu L} \tag{1.53}$$

where N_0 is the incoming photon flux, ρ is the density of the scatterers, μ is the total absorption coefficient and L is the sample lenght. Thus, the efficiency can be written as follows:

$$\eta = \frac{N}{N_0} \propto \left(\frac{e^2}{mc^2}\right)^2 Z^2 \, \frac{\rho L}{e^{\mu L}} \approx \left(\frac{e^2}{mc^2}\right)^2 Z^2 \, \frac{\rho L}{1+\mu L} \approx \left(\frac{e^2}{mc^2}\right)^2 Z^2 \, \frac{\rho}{\mu} \tag{1.54}$$

For X-rays with energies around KeV, the absorption is mainly due to photoelectric absorbtion process which scales as Z^4, far from the electron absorption edges. Thus, the efficiency of the process scales as Z^{-2} becoming extremely low for large Z materials.

Fig. 1.17 reports the efficiency for an IXS experiment as a function of Z for a sample with optimum thickness of $L = 1/\mu$ and an incident photon energy of $17.8\,KeV$.

IXS Spectrometer: beamline ID-28 @ESRF and XBL-35 @SPring-8

In Chapter 3 we will show the IXS measurements on a prototypical liquid performed at the beamlines ID28 and BL35XU respectively at ESRF (France) and SPring-8 (Japan). Thanks to the high energy storage rings in Grenoble and in Hyogo, it is possible to generate hard X-rays with energies of the order of tenth ok KeV. As already stated, we would like to observe exchanged energies in the order of $\sim meV$, this means that in order to resolve such small energy shift we need an high resolving power, about $\Delta E/E \sim 10^{-7}$. Both the beamlines cited above are designed with the same rationale: the broadband radiation coming from the undulator is firstly monochromatized thanks to Bragg reflections, then the beam is sent to the sample and, selected the scattering geometry, the energy spectra are collected.

In fig. 1.18 a scheme for ID28 is shown. The X-ray coming from the undulator is pre-monochromatized by a Si(1 1 1) double crystal kept in vacuum and cooled by liquid nitrogen. In this way the beam is not corrupted by thermal deformation of the crystal and the bandwidth can be reduced to $\Delta E/E \approx 10^{-4}$. Actually, this first monochromatization is needed to reduce the heat load impinging on the high

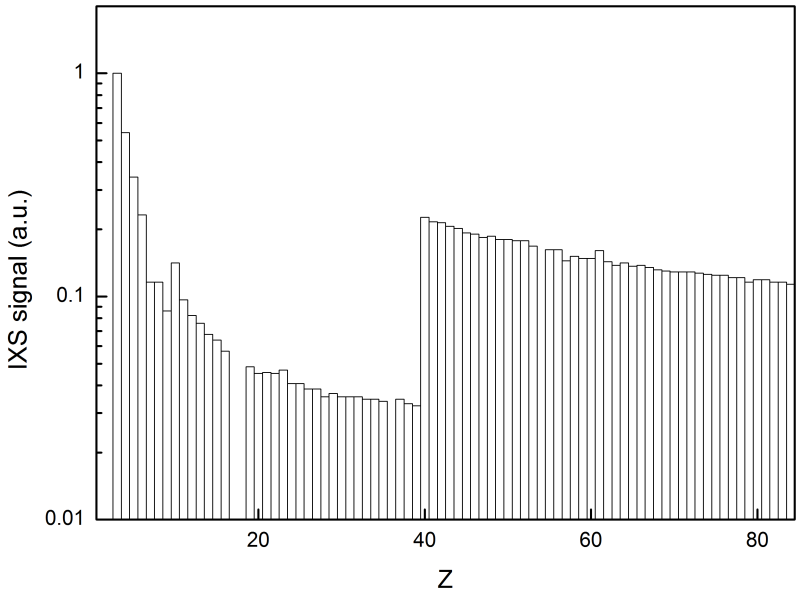

Figure 1.17: Efficiency of IXS scattering method for incoming photon energies of $17.8\,KeV$*, in the small Q-limit* $(f(Q) = Z)$*, in a sample with optimum length* $L = 1/\mu$*. The resulting scattering is led by the Thomson scattering and the photoelectron absorption. It is evident the lowering of the efficiency with the increasing of Z. The large discontinuity around Z=40 has to be addressed to the K absorption edge of Zirconium which occurs at E=18 KeV.*

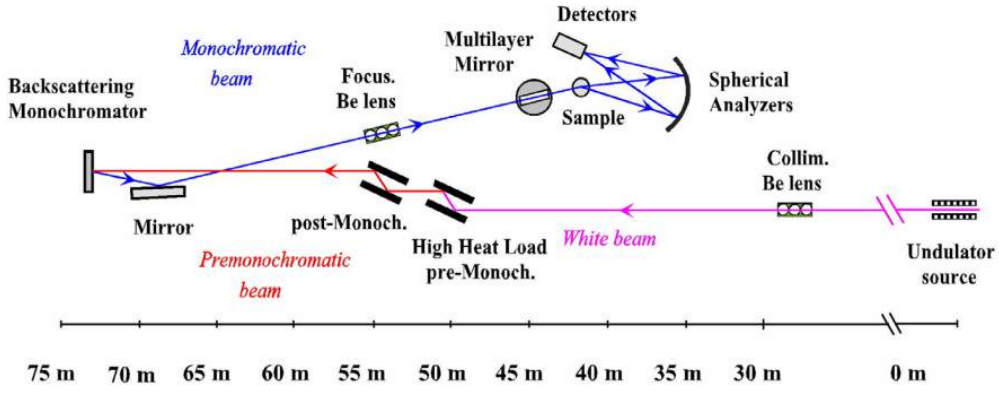

Figure 1.18: Sketch of the ID28 beamline at ESRF (Grenoble).

resolution monochromator. The latter is a Si crystal working at a Bragg angle of 89.98° and at high reflection order. Most of the experiment on disordered systems are usually performed using Si(11 11 11) or Si(12 12 12) reflections. In table 1.1 are listed the performance of the beamline depending on the used monochromatic reflection order. The beam is, at this stage, focused by a platinum coated mirror into the sample $25m$ far.

h	Energy (KeV)	ΔE (meV)	Q_{max} (nm^{-1})	Q_{min} (nm^{-1})	ΔQ (nm^{-1})	Flux (photons/s/200mA)
7	13.840	7.6 ± 0.2	64	1	1.89	1.5 e11
8	15.817	5.5 ± 0.2	74	1	2.16	9.0 e10
9	17.794	3.0 ± 0.2	83	1	2.43	2.7 e10
11	21.747	1.5 ± 0.1	101	1	3.00	6.6 e9
12	23.725	1.3 ± 0.1	111	1	3.24	5.9 e9
13	25.704	1.0 ± 0.1	120	1	3.50	1.5 e9

Table 1.1: Main characteristics of the ID-28 spectrometer, for the different Si(h,h,h) reflections. Energy indicates the incident photon energy, ΔE is the total energy resolution, Q min and Q max indicate the minimum and maximum momentum transfers and ΔQ indicates the Q-spacing between adjacent analyzers. The photon flux values are measured at the sample position.

The scattered light is analyzed by another silicon crystal. The angular acceptance of the analyzer depends on the Q-resolution one wants to have. In principle the analyzer should be a spherical single crystal able to collect the whole scattered light conserving the energy resolution. This, in principle, call for a bendable crystal, but the stress on it could result in an energy resolution broadening. The adopted solution is therefore to arrange about 12000 single crystals cubes ($0.6 \times 0.6 \times 0.3\, mm^3$) onto a spherical substrate with radius R, fulfilling the Rowland circle condition.

The detectors are Peltier cooled silicon diodes with very low dark count (~ 1 count in $30\, min$). On ID-28 there are 9 indipendent inclined detectors with a fixed angular offset of $\sim 0.75°$ between each other. They are mounted on a 7-meters long harm which can vary the θ-scattering angle with continuity between 0° and 55°. Thanks to all these detectors it is possible to obtain a Q-set of 9 spectra at the same time.

The energy scan is done scanning the temperature of the analyzer. Changing the temperature, the lattice constants change and thus the x-ray energy selected by the crystal. To achieve resolution power of the order of $10^{-7} \div 10^{-8}$, it is necessary to have an accuracy in temperature control in the mK range. At ID28, thanks to a special design for the temperature control and an active feedback system, it is possible to set the actual temperature of the crystals with precision of $0.2\, mK$ in the temperature region around $295K$.

1.2 Time-Resolved techniques

We have seen that thanks to inelastic photon scattering it is possible to measure the dynamic structure factor $S(Q, \omega)$, which related the time-space Fourier transform of the time correlation function of spontaneous density fluctuations occurring in the system. Undoubtedly, all these energy-resolved techniques are longstanding and very powerful methods to probe the dynamics in liquids and disorder systems. Nevertheless, sometimes could be convenient to access the time domain instead of the energy one.

We have already discussed, for example, the need of very high resolution instruments to correctly evaluate the low energy components in a Brillouin spectrum. Obviously, there are many technological limitations to push such techniques to higher and higher resolutions, while, instead, would be extremely convenient to study the same spectral range in the time-conjugated Fourier space: i.e. the real time. A method able to do that is the impulsive stimulated scattering approach, which relies upon the exploitation of some selected non-linear third order light-matter interactions, also termed four wave mixing (FWM) processes. We will see in the following chapters, that in some cases, using time resolved techniques is the only possibility to probe certain dynamic regions.

Formally the two approaches are equivalent. With a time-resolved experiment it is possible measure the so called intermediate scattering function $F(Q,t)$ which is the time Fourier back-transform of the $S(Q,\omega)$. In an inelastic light scattering we obtain information about the velocity and attenuation of the acoustic wave inside the medium through, respectively, the position and the linewidth of the Brillouin peaks. Equivalently, we can gain such information by the modulation and the damping of the time resolved signal.

1.2.1 Nonlinear optical spectroscopy: the Four Wave Mixing

So far, we have described techniques all based on the spontaneous scattering process. Because the electric fields of the involved photons are relatively small, all of these energy resolved experiments can be described in the framework of the linear response theory. In particular, we said that the result of the interaction of an electromagnetic (e.m.) wave with matter, thanks to the redistribution of the inner electric charges, is the appearance of a local dipole moment $\underline{P}$:

$$\underline{P} = \varepsilon_0 \chi \underline{E} \tag{1.55}$$

where ε_0 is the in vacuum dielectric constant and χ is the so called susceptibility of the material. In the case of high intensity electric fields, we cannot anymore neglect non-linear contributions and the $\underline{P}$ polarization has to be written in term of higher orders in the sum series:

$$\begin{aligned} \underline{P}(\omega) = \underline{P}^{(1)}(\omega) + \underline{P}^{(2)}(\omega) + \underline{P}^{(3)}(\omega) + ... = \\ = \varepsilon_0 \left[\chi^{(1)}(\omega_1)\underline{E}_1(\omega_1) + \chi^{(2)}(\textstyle\sum_i \pm\omega_i)\underline{E}_1(\omega_1)\underline{E}_2(\omega_2) + \chi^{(3)}\,(\textstyle\sum_i \pm\omega_i)\,\underline{E}_1(\omega_1)\underline{E}_2(\omega_2)\underline{E}_3(\omega_3) + ... \right] \end{aligned} \tag{1.56}$$

where $\chi^{(n)}$ are $n+1$ rank tensors known as nth-order susceptibility. Since the orders of magnitude of $\chi^{(1)}$, $\chi^{(2)}$, $\chi^{(2)}$ are respectively 1, $10^{-12}m/V$ and $10^{-23}m^2/V^2$, it is clear that such high order contributions to the dipole moment are not negligible (in the contrary they can be dominant) only in the case of high intensity electric fields. Actually, such high intensity electric fields are easily obtainable with the modern pulsed laser sources when the beam is focused with a spot-size of about $100\,\mu m^2$. In the case of centro-symmetric samples or randomly oriented (isotropic) molecular liquids the $\chi^{(2)}$ is equal to 0 and therefore the first non linear contribution

arises only at third order. A very simple way to understand such isotropic samples characteristic is to think that every time the electric field acting with the sample is reversed, the polarization has to follow its orientation [46]. Therefore it must be that if

$$P^{(2n)} = \chi^{(2n)} E^{2n} \qquad (n = 1,2,3,...)$$

then, reversing the electric field:

$$-P^{(2n)} = \chi^{(2n)}(-E)^{2n} = \chi^{(2n)} E^{2n}$$

From the comparison of these last equations it must be that

$$P^{(2n)} = -P^{(2n)} = 0$$

Thus, every even order of χ must be null for isotropic systems like liquids and disordered systems.

Therefore, the lowest order non linear processes for all samples are the third order ones, that are at the basis of Four Wave Mixing (FWM) applications. FWM experiments are hence based on the interaction of three photon pulses with the sample, resulting in a (fourth) coherently scattered beam containing the information on the system under study. Since the photon frequency, wavevector, bandwidth, polarization and arrival time of the three incoming pulses can be different from each other, different kinds of FWM experiments can be performed and used to probe various dynamical processes, arising from different components of the χ tensor. Among such classes of experiments, we can cite the optical kerr effect (OKE), spin-photon echo spectroscopy, coherent antistokes Raman scattering (CARS), multidimensional spectroscopy [47], stimulated Rayleigh and Brillouin scattering [48], etc. In general, the only condition that has to be met in all these experiments is the "phase matching", which essentially accounts for energy-momentum conservation in the non linear process. Indeed, the strength of the FWM field can be usually cast in the form [49, 50]:

$$E_4(\underline{k}_4, \omega_4) \propto \chi^{(3)} E_1(\underline{k}_1, \omega_1) E_2(\underline{k}_2, \omega_2) E_3(\underline{k}_3, \omega_3) \operatorname{sinc}\left(\frac{\Delta\underline{k} \cdot \underline{L}}{2}\right) \tag{1.57}$$

where $\omega_4 = \sum_{i=1}^{3} \pm\omega_i$ and $\underline{k}_4 = \sum_{i=1}^{3} \pm\underline{k}_i$ are a given combination of the input photon frequencies and wavevectors, while $\Delta\underline{k} = \underline{k}_4 - \sum_{i=1}^{3} \pm\underline{k}_i$ and $\underline{L}$ is the optical path length. The "sinc" term accounts for the phase matching and has a twofold consequence: on one hand, an appreciable non linear signal can be detected only when $\Delta\underline{k} = 0$ and, on the other hand, such signal is localized in a well-defined direction of space. The latter fact can be exploited to "a priori" select the direction of the FWM signal, which can be often chosen different from the ones of the input beams. The possibility to look for a time dependent "showing up" of the FWM signal over the background usually results in a large enhancement in the signal/noise ratio with respect to other pump-probe methods, in which time dependent variations of some signals (reflectivity, transmission, etc.) have to be detected.

1.2.2 A special FMW experiment: the Transient Grating in the impulsive limit

The simplest configuration for a FWM experiment is that one in which two pulsed beam with the same angular frequency (ω_{ex}) act as excitation pumps and a third beam with a different ω_p is used to probe the induced excitation inside the matter.

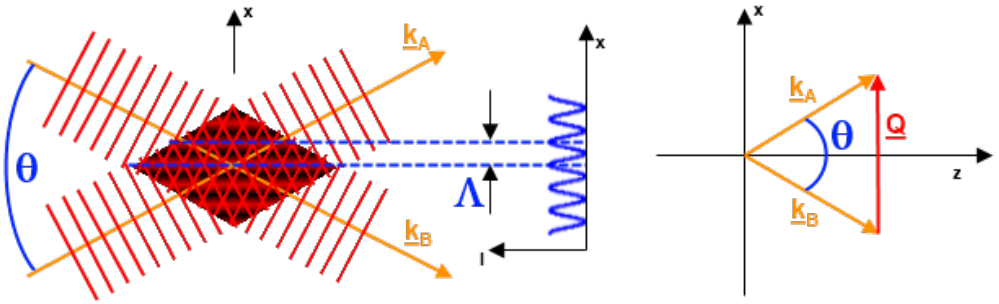

Figure 1.19: Superposition of the pump beams in a TG experiment. The result of interference is a standing e.m. wave.

In Fig. 1.19 is shown a sketch to describe the interference between two equal-intensity (pump) beams sent to the sample with an interbeams angle of θ. As intuitively comprehensible, the interaction between the two beams creates an interference pattern along the $\hat{x}$ direction with a spatial period $\Lambda = 2\pi/Q$ where $\underline{Q} = \pm(\underline{k}_A - \underline{k}_B)$. From geometrical considerations, because $|\underline{k}_A| = |\underline{k}_B| = k_{ex}$:

$$Q = 2k_{ex} \sin\left(\frac{\theta}{2}\right) \tag{1.58}$$

Therefore, changing the angle θ it is possible to change the spatial periodicity of the interference pattern. Let's obtain such Q-relation in a more rigorous way [51]. We can decompose the k-vector of the two pump beams along the cartesian axis $\hat{x}$ and $\hat{z}$:

$$\begin{aligned} \underline{k}_A &= k_z\hat{z} + k_x\hat{x} \\ \underline{k}_B &= k_z\hat{z} - k_x\hat{x} \end{aligned} \tag{1.59}$$

and we can write the expressions for the electric fields:

$$\begin{aligned} \underline{E}_A(\underline{r},t) &= \underline{A}_A e^{i(\underline{k}_A\cdot\underline{r}-\omega t)} = \underline{A}_A e^{i(k_x x + k_z z - \omega t)} \\ \underline{E}_B(\underline{r},t) &= \underline{A}_B e^{i(\underline{k}_B\cdot\underline{r}-\omega t)} = \underline{A}_B e^{i(-k_x x + k_z z - \omega t)} \end{aligned} \tag{1.60}$$

And in the intersection region the resulting electric field is

$$\begin{aligned} \underline{E} &= \underline{E}_A + \underline{E}_B = \underline{A}_A e^{i(k_x x + k_z z - \omega t)} + \underline{A}_B e^{i(-k_x x + k_z z - \omega t)} = \\ &= \left[\underline{A}_A e^{ik_x x} + \underline{A}_B e^{-ik_x x}\right] e^{i(k_z z - \omega t)} \end{aligned} \tag{1.61}$$

Thanks to Poynting theorem, the intensity distribution is

$$\begin{aligned} I &= \tfrac{1}{2}nc\varepsilon_0 \underline{E}\cdot\underline{E}^* = \tfrac{1}{2}nc\varepsilon_0\left[\underline{A}_A e^{ik_x x}+\underline{A}_B e^{-ik_x x}\right]\cdot\left[\underline{A}_A e^{-ik_x x}+\underline{A}_B e^{ik_x x}\right] = \\ &= \tfrac{1}{2}nc\varepsilon_0\left[|\underline{A}_A|^2+2\underline{A}_A\cdot\underline{A}_B\cos(2k_x x)+|\underline{A}_B|^2\right] \\ &= I_A+2\Delta I\cos(2k_x x)+I_B \end{aligned} \tag{1.62}$$

where

$$\Delta I = \frac{1}{2}nc\varepsilon_0\underline{A}_A\cdot\underline{A}_B^* \tag{1.63}$$

is the intensity modulation amplitude. The latter relations shows a space modulation of the intensity distribution in the $\hat{x}$ direction. The space periodicity of such intensity modulation can be easily calculated:

$$\begin{aligned} \cos(2k_x\Lambda) &= 1 \\ 2k_x\Lambda &= 2\pi \\ \Lambda &= \tfrac{1}{2k_x} \end{aligned} \tag{1.64}$$

and

$$Q = \frac{2\pi}{\Lambda} = 2k_x = 2k_{ex}\sin\left(\frac{\theta}{2}\right) \tag{1.65}$$

which is exactly the same expression we wrote in eq. 1.58.

Actually, eq. 1.63 states that the intensity modulation (responsible for the grating formation in the matter) is related to the scalar product between the electric field of the pumps. This would mean that in case of $\underline{A}_A\perp\underline{A}_B$ no grating could be formed. In anisotropic media, or with anisotropic interaction, grating may be also induced in that condition. To take into account such possibility, we introduce a new quantity: the interference tensor $\Delta\underline{\underline{M}}$.

$$\Delta M_{ij} = \frac{1}{2}\varepsilon_0 cnA_{A,i}A_{B,j}^* \tag{1.66}$$

and we redefine

$$\Delta I = |\mathrm{Tr}(\Delta\underline{\underline{M}})| \tag{1.67}$$

Depending on the different polarizations of the electric fields, different kind of gratings can be originated to be sensitive to different dynamics related to different tensor elements. In the case in which both of the pump pulses are vertically polarized (VV - parallel to $\hat{y}$ if we refer to Fig. 1.19) the interference will produce an intensity interference grating (Fig. 1.20.a). A so-called polarization grating is the result of the interaction between to pumps with perpendicular linear polarization (VH). In this case (Fig. 1.20.b), the light intensity is uniform in the beams-crossing region, but the polarization of light is spatially modulated, it varies periodically along the $\underline{Q}$-direction from left circular polarized (lcp) to linear polarised at +45° (p), to right

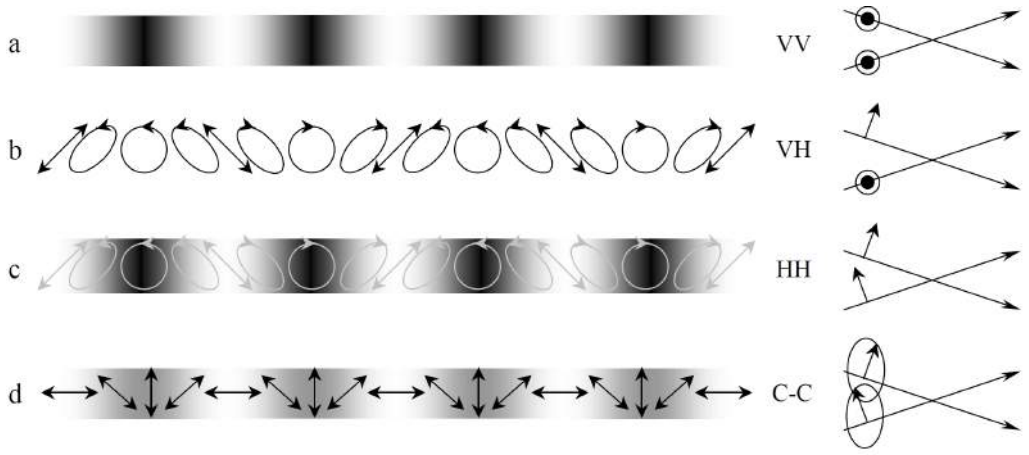

Figure 1.20: The intensity and polarization interference pattern resulting from the interaction of different polarized pumps pulses

circular polarised (rcp) and to linear polarised at $-45°$ (m), and so on. This polarization configuration could be interesting for the investigation of anisotropic media. Both of these two kind of grating are present in the HH and circular-circular (CC) configuration, making the one dominant in respect to the other depending of the θ_{ex}.

Assuming a Gaussian time-shape for the A and B pump beams with an half width half maximum of t_{ex}:

$$I_\alpha(t) = I_\alpha(0)e^{(-t/t_{ex})^2}$$

with $I_\alpha(0) = \frac{1}{2}cn\varepsilon_0 A_\alpha^2$ and $\alpha = A, B$, the time evolution of the interference tensor is:

$$\begin{aligned}
\Delta M_{ij}(t) &= \tfrac{1}{2}\varepsilon_0 cn A_{A,i}(t)A^*_{B,j}(t) = \\
&= \tfrac{1}{2}\varepsilon_0 cn A_{A,i}(0)e^{(t/\sqrt{2}t_{ex})^2} A_{B,j}(0)e^{(t/\sqrt{2}t_{ex})^2} = \\
&= \tfrac{1}{2}\varepsilon_0 cn A_{A,i}(0)A_{B,j}(0)e^{(-t/t_{ex})^2}
\end{aligned}$$

It is interesting to notice that in the case of pulsed beams, the temporal behaviour of the intensity modulation in the crossing region is the same of the original pulses.

So far, we have just showed the modulation of the intensity distribution resulting from the interference of the electric fields of the two pumps. Such intensity distribution can couples with the optical properties of the media, in this way the e.m. modulation will be transformed in, e.g., a density modulation or in a electronic charge distribution in the sample. Depending on the kind of interaction occurring, we can classify two kind of sample grating: *phase grating* and *amplitude grating*. In the former case no resonances between the excitation energy and the internal degrees of freedom is occurring, while in the other one an absorption process is involved,

resulting in a modification of the imaginary part of the optical properties (e.g., the refractive index of the media).

While the modulation of the absorbance, ΔA, is essentially due to the changing in the chemical species populations in the medium, the variation in the real part of the optical properties of the medium can have different origins. Let's consider the variation of the refractive index, Δn. It can be written as the sum of the three main contributions:

$$\Delta n = \Delta n_k + \Delta n_p + \Delta n_d \tag{1.68}$$

where:

- Δn_k is the variation induced by the rotation-translation coupling (R-TC) effects: in an anisotropic molecular liquid the grating tends to align the dipoles inside of the medium, leading to a birefringence grating. When the e.m. field is switched off, the relaxation of the dipole alignment can be measured. This is the mechanism at the base of the OKE.

- Δn_p is related to the population changes and it is the Kramers-Kronig counterpart of the absorption process: ΔA.

- Δn_d is the change in refractive index associated with density changes and it, in turn, can be addressed to three different processes:

  $$\Delta n_d = \Delta n_d^v + \Delta n_d^t + \Delta n_d^e$$

  where Δn_d^v is related to the variation of volume upon population changes: the excitation can induce some chemical reactions and the volume occupied by the reagents could be different from the one occupied by the products. Therefore we will have a periodic density modulation because of the volume changes.

  Δn_d^t is due to the temperature-induced changes. If part of the pumps energy is converted, through non-radiative transition, in heat, the sample will experience a periodic temperature modulation. Because of such local temperature concentrations, the density of the medium will start to oscillate and two counter-propagating acoustic waves will be launched through the sample. The interference between such acoustic waves results in a density grating. Since Δn_d^t oscillates between 0 and positive values, the scattered signal, proportional to square of the density fluctuations, will present the same time periodicity of the latter.

  Δn_d^e takes into account the so-called *electrostriction* process. The periodic concentration of the electric fields forces a rearrangements of the electrical charges inside the medium. The interference field induces an electric dipole in every molecule and the induced dipole moves toward the areas of greatest field intensity. Unlike the thermal grating, now we have compression zones in the maximum light intensity points. This grating produces the same acoustic standing wave but with a phase difference of $\pi/2$ with respect to the previous situation. Consequently, Δn_d^e spans from negative to positive values and since the diffracted signal will be proportional to $|\Delta n_d^e|^2$, it will show a temporal oscillation at twice of the acoustic frequency.

1.2.3 Detection of gratings

So far we have described the interference pattern arising from the pumps interaction and its coupling with the optical properties of the sample. This section is dedicated to the detection of the gratings properties. A third delayed pulse is sent to the sample to probe the characteristics of the pumps induced transient grating. Such probe beam experiences, disregarding the presence of the pumps beam, the presence of a real grating and we can use the usual grating equations to describe the interaction process.

We can divide the gratings in two classes depending of their longitudinal extension: they can be classified as thin or thick grating. In particular if the grating thickness, d, is smaller than or comparable to the pitch of the grating Λ then it is classified as a thin grating, conversely it is a thick grating.

In the first case we can use the well known grating equation (eq. 1.22) to localize the various scattered orders. In the case of thick gratings, on the other hand, the only detectable scattered order is the one for which the Bragg condition (phase matching) is satisfied. This is due to the fact that constructive interference only occurs when all scattered contributions within the thickness of the grating add in phase. In this latter case "transient grating (TG) signal" is scattered at a certain direction and with a certain energy obeying to the energy/conservation rules. Because in TG scheme the pumps have same angular frequencies ω_{ex}, it must be that $\omega_{TG} = \omega_{ex} - \omega_{ex} + \omega_p = \omega_p$ and $\underline{k}_{TG} = \underline{Q} + \underline{k}_p$, where $\underline{Q}$ is the grating vector expressed by eq. 1.58.

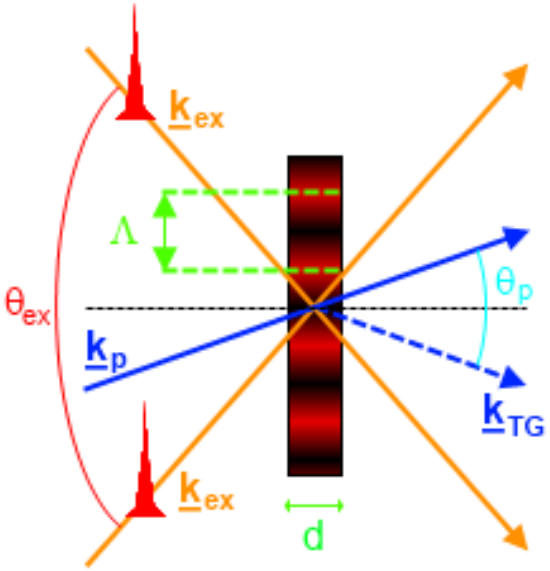

Figure 1.21: Scattering geometry for a thick grating. Obeying to the phase matching conditions, the scattered beam results in a well defined direction ($\underline{k}_{TG}$) and with an angular frequency $\omega_{TG} = \omega_p$.

As it possible to notice by the Fig. 1.21, the resulting TG beam is expected to be scattered in a direction free of other e.m. components. This is one of the advantages of the TG (and more generally of the FWM): you can measure the scattered signal with a very high signal to noise ratio. Finally, scanning the pumps-probe delay time

it is possible to acquire the whole time evolution of the transient grating, and hence the evolution of the relaxation phenomena occurring inside the medium.

Homodyne detection

In eq. 1.57 we have already seen that the scattered signal in a FWM experiment brings the information about the dynamics of the system being proportional to the $\chi^{(3)}$ susceptibility tensor. The direct acquisition of such scattered signal, is known as Homodyne detection (HO). In this case the signal, recorder by a detector, is proportional to the square of the modulus of the scattered electric field.

$$S^{HO}(t) = I_{TG}(t) = \langle |\underline{E}_{TG}(t)|^2 \rangle \tag{1.69}$$

where the squared electric field is mediated over an optical cycle. In Fig. 1.22 is

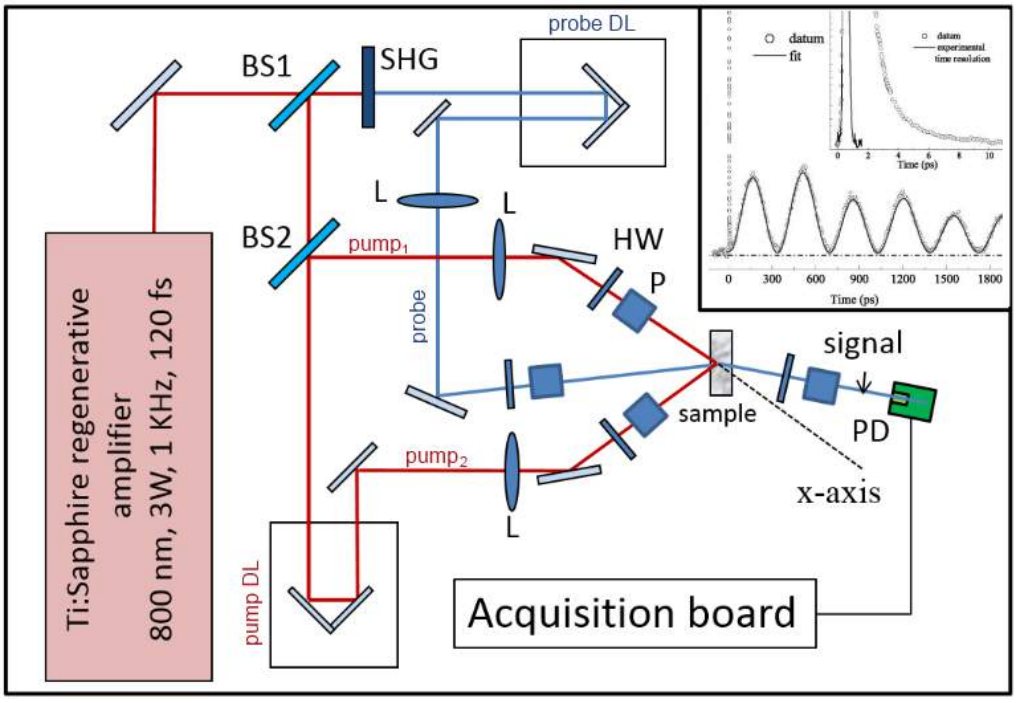

Figure 1.22: TG setup with homodyne detection scheme. Pumps and probe have tunable polarization (by half-wave plates (HW in the figure)) in order to exploit the all possible combinations and allow the measurement of different susceptibility tensor components. In the inset is shown a characteristic HO-TG spectrum: a fast dynamics is recorder at the first ps, while the longer time dynamic is addressed to the density fluctuations resulting from the interference pattern of the pump beams.

shown the TG scheme operating in the HO detection configuration we set up in our laboratory. The source is a Ti:sapphire regenerative amplifier (SPITFIRE PRO-XP, Spectra Physics) able to provide a pulse of 800 nm wavelength, 120 fs time duration, 3 mJ energy at 1 kHz repetition rate. Such laser beam is firstly split in two beams by a beamsplitter (BS1): from one of the two obtained beams it will obtained the probe pulse, the other one is necessary for the pumps path. Concerning the pumps,

the laser will be further split in two by a second BS2 with an efficiency 50%/50%, to obtain two equal-intensity beams. The optical path difference between the two pumps is recovered by a delayline (pump DL) in order to have synchronization of the two pulses at the sample position. Both of the pump beams are focused to the sample and thanks to some mirrors they are overlapped in space at the sample. The probe beam is obtain by the first portion of the laser beam by second harmonic generation. The 800 nm pulse is duplicated in frequency by a BBO (Beta Barium Borate) crystal thanks to a non linear process, hence obtaining a 400 nm pulse. To scan the delay time between pumps and probe, the latter passes through a delay line designed to scan up to 3 ns. Then the beam is focused to the intersection region and it can finally interact with the grating. The scattered signal, at the Bragg angle, will be detected by a photodiode eventually equipped with some electronics devices as like boxcar or lock-in amplifiers. In the showed setup it is possible to select all the possible polarization configuration, just playing with the half-wave plates (HW) and the polarizers.

A characteristic spectrum is shown in the inset of the figure. It presents a fast dynamics, arising from electronic processes, and at longer times an oscillating behaviour addressed to the density fluctuations induced by the pumps interference.

Heterodyne detection

While in the HO-detection configuration, the measured signal is proportional to the square of the density fluctuation, or more generally, to the square of the susceptibility tensor, in the so called Heterodyne (HD) detection scheme the signal is directly proportional to the $\chi^{(3)}$.

In Fig. 1.23 is shown the TG setup we realized in our lab following the rationale introduced by Maznev et al. in 1998 [52]. Differently to the HO setup, here a CW 488 nm laser source is used as a probe. The two laser beams travel collinearly and impinge on a transmitting diffraction grating named "phase mask". The latter is a grating printed, e.g. by lithography, on a transparent substrate and optimized to scatter the main part of the radiation in the ± 1 diffraction orders. Thanks to two optical achromatic twin doublets the diffracted orders of the pulsed and CW lasers are collected and refocused on the sample. For the principle of the inversion of the optical path, we can be sure that the two pumps will form in the sample a transient grating with a pitch equal to the phase mask one. Furthermore, the trick of the phase mask, automatically ensures that the phase mask condition at the sample between pumps and probe is fulfilled.

If one of the CW diffracted order is used as a probe, the other one is used as a "local field" (LF). This is the fundamental innovation at the basis of the HD detection. If the TG signal, resulting from the pumps and probe interaction, is directly detected as in the HO case at the Bragg angle by a photodiode, in the HD case the detector will experience also the presence of the local field, overlapped to the TG signal. Furthermore, while the TG signal will present a time structure, fingerprint of the grating dynamics, the local field is structure-less and results in a flat background under the TG signal. Thus, the acquired intensity will be:

$$S(t) = \langle |\underline{E}_{TG}(t) + \underline{E}_{LF}|^2 \rangle \tag{1.70}$$

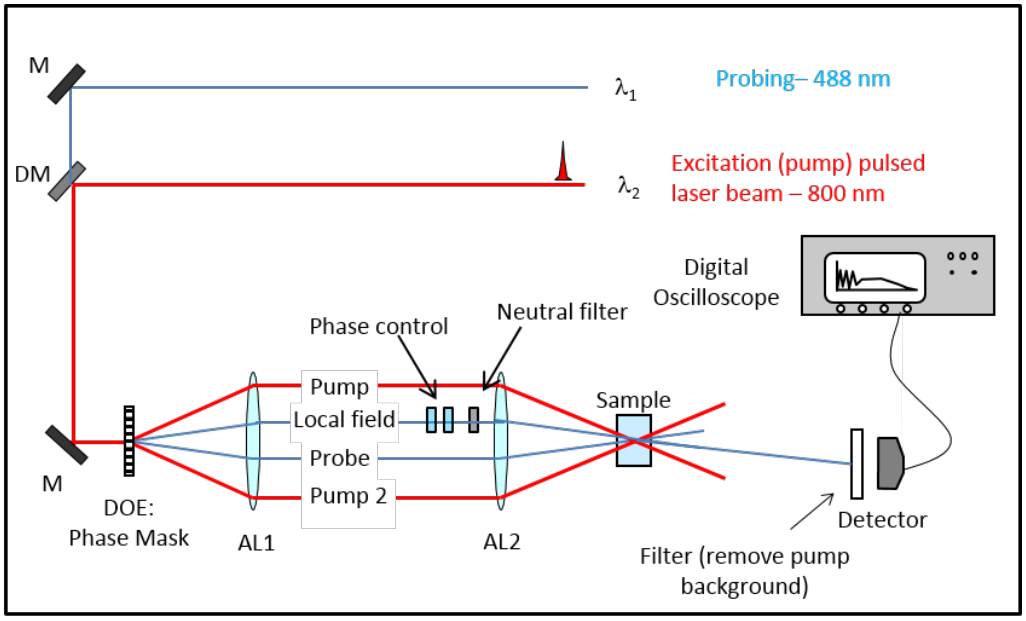

Figure 1.23: HD detected TG. To be noticed is the usage of a CW laser beam for the probe and the diffracted optics element (DOE) to obtain the phase matching condition in a very easy way. The signal is acquired by an oscilloscope fast enough to measure the acoustic oscillation without any scanning pumps-probe delay line. The HD detection is obtained thanks to presence of a fifth beam, the so called local field.

Assuming that the TG signal and LF have the form of a plane waves [53]: $\underline{E}_{TG} = \hat{e}_{TG}\tilde{A}_{TG}(t)e^{i(\underline{k}_s\cdot\underline{r}-\omega_p t)}$ and $\underline{E}_{LF} = \hat{e}_{LF}A_{LF}e^{i(\underline{k}_s\cdot\underline{r}-\omega_p t+\varphi)}$, where $\tilde{A}_{TG}(t)$ is a complex number, A_{LF} a real constant number and φ is the optical phase between the signal and local field, the HD signal will be:

$$S(t) = \langle I_{TG}(t) + I_{LF} + 2\hat{e}_{TG}\cdot\hat{e}_{LF}A_{LF}\{\Re[\tilde{A}_{TG}(t)]\cos\varphi + \Im[\tilde{A}_{TG}(t)]\sin\varphi\}\rangle \quad (1.71)$$

The last term in the above equation is the HD term. It can be isolated by the other contributions, performing two different measurements S_+ and S_- with $\varphi_+ = \varphi_0$ and $\varphi_- = \varphi_0 + \pi$. The mixing the two measurements, it is possible to obtain

$$S^{HD}(t) = S_+(t) - S_-(t) = 4\hat{e}_{TG}\cdot\hat{e}_{LF}A_{LF}\{\Re[\tilde{A}_{TG}(t)]\cos\varphi_0 + \Im[\tilde{A}_{TG}(t)]\sin\varphi_0\} \quad (1.72)$$

the real and imaginary part of the TG signal are related respectively to the birefringence/phase and the dichroic/amplitude gratings. Therefore, by choosing $\varphi = 0, \pi/2$ it is possible to separate such contributions. If the medium is weakly absorbent, then the amplitude grating contributions are negligible and only the real part of the above expression has to be consider. Thus, choosing $\varphi = 2\pi n$ with n integer, the HD signal is simply: $S^{HD}(t) = 4\hat{e}_{TG}\cdot\hat{e}_{LF}A_{LF}A_{TG}(t)$.

It is important to notice that now the signal is directly proportional to the TG signal field. Furthermore, since the local field doesn't have any time structure,

it works as an amplifier of the TG signal. In addition, because the HD signal is effectively a differential method, all the spurious contributions that are not phase sensitive are automatically filtered resulting in a very clean and very high contrast signal (see Fig. 1.24). In our HD-setup the signal is acquired by a fast photodiode

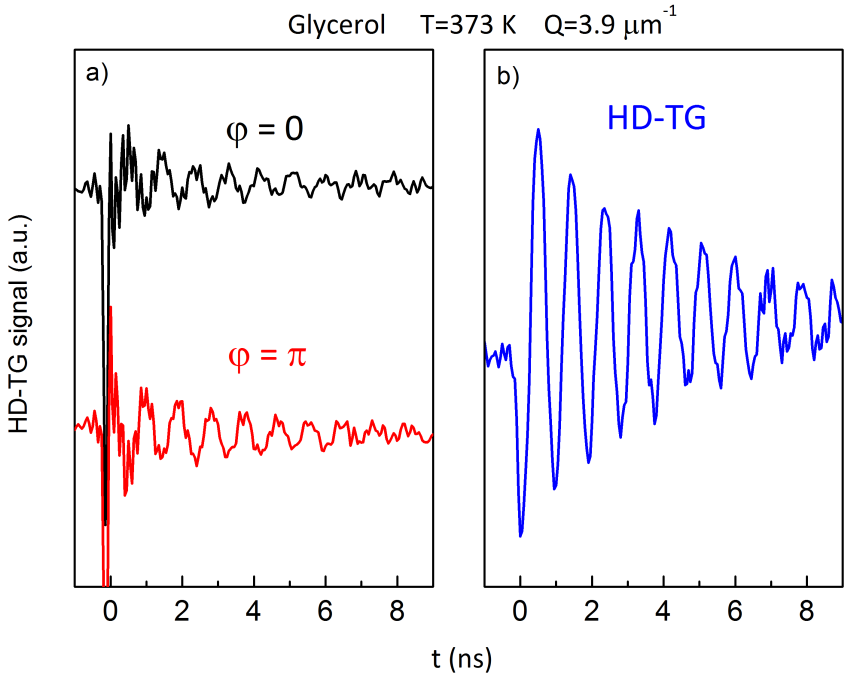

Figure 1.24: Panel b):HD signal for a Glycerol sample at T=373K and Q=3.9 μm^{-1}. The HD signal was obtain by the subtraction of the S_+ and S_- measurements shown in panel a). As evident, the quality of the signal is sensitively increased thanks to cancellation of the noisy contributions

and sent, through optical fiber, directly to a LeCroy oscilloscope. Because of the CW laser used as a probe and thanks to the high performance of the oscilloscope, it is not necessary to do any time scansion. The oscilloscope is fast enough to directly record the time modulation of the acoustic signal. Conversely, the oscilloscope is not so fast to study all the dynamics evolving in the fs timescales. If one wants to study such phenomena is force to use a fully pulsed lased based setup. In that case perform HD measurements is still possible but much more complicated. Furthermore, thanks to the used DOE, the setup results to be extremely simplified in respect to the HO one, and it allows to performed very rapid measurements with very high signal to noise ratio. It is also relatively easy to change the Q induced in the TG experiment, it is sufficient to replace the DOE with another one with a different pitch. Another way to change the Q would be to use a refocusing achromatic doublet with a different focal length. In both cases the phase matching conditions are automatically satisfied. In any case, because of the finite aperture of the optics, we will not be able to explore wide angle (wide Q) geometries contrary to the case of our HO setup.

Chapter 2

Dynamics of fluctuations

In the previous chapter we have seen that the radiation-matter interaction is led by the fluctuations of the optical properties of the medium. In both cases of spontaneous and stimulated scattering processes the spectral density of the scattered light is proportional to time correlation function of the fluctuations of the dielectric tensor $\underline{\underline{\varepsilon}}$ (see eq. 1.10). Since it is possible to write the dielectric tensor as a function of the independent thermodynamic quantities density, ρ, and temperature, T, we can write its fluctuation as in eq. 1.12

$$\delta\underline{\underline{\varepsilon}}(\underline{r},t) = \left(\frac{\partial\underline{\underline{\varepsilon}}}{\partial\rho}\right)_T \delta\rho(\underline{r},t) + \left(\frac{\partial\underline{\underline{\varepsilon}}}{\partial T}\right)_\rho \delta T(\underline{r},t)$$

Finally, we could further simplify the expression for the scattered spectral density (eq. 1.13) considering the weak T-dependency of the dielectric tensor for most of the liquids ($\partial\underline{\underline{\varepsilon}}/\partial T \approx 0$) and we could write the eq. 1.14

$$I_{is}^{\varepsilon}(\underline{Q},\omega) = (\hat{n}_i \cdot \hat{n}_s)^2 \left(\frac{\partial\underline{\underline{\varepsilon}}}{\partial\rho}\right)_T^2 S_{\rho\rho}(\underline{Q},\omega)$$

where, as already said in Chapter 1, $S_{\rho\rho}(\underline{Q},\omega)$ is the Fourier transform of the density fluctuations time correlation function, $\left\langle \delta\rho^*(\underline{Q},0)\delta\rho(\underline{Q},t)\right\rangle$, and it is called *dynamic structure factor*. The latter, or its equivalent $F(\underline{Q},t)$ in time-domain, is the observable in a scattering experiment. In this chapter we will see which information about the dynamics of the density fluctuations can be carried out from the study of the $S(\underline{Q},\omega)$.

We have already discussed the possible different regimes in which the system can be pictured depending on the Q-region accessed by the experimental technique. In the case of the experiments performed in the present work, we are well far from the "single particle" limit. The wavelengths of our probes, in all the experiments we will show, are in fact bigger or in the same order of magnitude of the inter-particle distances. Therefore, we can treat the system as a continuum and use a fully thermodynamic approach to analyze the experimental data in the low-Q region, while a viscoelastic formalism is demanded for the higher Q spectral range.

2.1 Hydrodynamic modes

The aim of this section is to study the dynamics of density fluctuation in the so called hydrodynamic limit where the wavelength of the probe radiation is much bigger than the inter-particles distances ξ and the frequency of the e.m. wave is much lower than the typical relaxation rates τ^{-1} (where τ is the characteristic time necessary for a perturbed state to go back to its equilibrium condition). The Onsager regression hypothesis [54, 55] states that the fluctuation of a certain quantity obeys to the same equations describing the equilibrium situation. In the case of the density fluctuations, the laws we have to take into account are the conservation equations for mass, momentum and energy.

They can be written as follows [9]:

$$\begin{aligned} &\tfrac{\partial \rho(\underline{r},t)}{\partial t} + \underline{\nabla} \cdot \underline{J}(\underline{r},t) = 0 \\ &m\rho(\underline{r},t)\tfrac{\partial v_i(\underline{r},t)}{\partial t} + \nabla_j \tau_{ij}(\underline{r},t) = 0 \qquad (i = 1,2,3) \\ &\tfrac{\partial e(\underline{r},t)}{\partial t} + \underline{\nabla} \cdot \underline{J}_e(\underline{r},t) = 0 \end{aligned} \tag{2.1}$$

where $\rho(\underline{r},t)$ is the number density, $m\underline{v}(\underline{r},t)$ the momentum density, $e(\underline{r},t)$ the energy density and $\underline{J}(\underline{r},t)$, $\underline{\tau}(\underline{r},t)$ and $\underline{J_e}(\underline{r},t)$ are the relative fluxes. In particular:

$$\begin{aligned} \underline{J}(\underline{r},t) &= \rho(\underline{r},t)\underline{v}(\underline{r},t) \\ \tau_{ij}(\underline{r},t) &= m\rho(\underline{r},t)v_i(\underline{r},t)v_j(\underline{r},t) - \sigma_{ij}(\underline{r},t) \\ \underline{J}_e(\underline{r},t) &= e(\underline{r},t)\underline{v}(\underline{r},t) - \lambda\underline{\nabla}T - \underline{v}(\underline{r},t)\cdot\underline{\underline{\sigma}}(\underline{r},t) \end{aligned} \tag{2.2}$$

where $\underline{v}(\underline{r},t)$ is the particle velocity in the fluid and v_i its i-th Cartesian component. $\underline{\underline{\sigma}}$ is the stress tensor, λ the thermal conductivity and T the temperature. It is then possible to separate the stress tensor into the pressure $(-p\delta_{ij})$ and viscous (σ'_{ij}) contributions, where the latter can be written as a function of the shear (η_s) and bulk (η_B) viscosity coefficients:

$$\sigma'_{ij} = \eta_s\left[\nabla_i v_j + \nabla_j v_i - \frac{2}{3}\underline{\nabla}\cdot\underline{v}\delta_{ij}\right] + \eta_B\underline{\nabla}\cdot\underline{v}\delta_{ij} \tag{2.3}$$

If we now write the fluctuation of the quantity x as $x_1 = \delta x(\underline{r},t)$, it is possible to write that $x = x_0 + x_1$, where x_0 is the value at the equilibrium and the fluctuation is expected to be very small (this fact will allow to neglect in the following all the terms higher than the first order in the fluctuations). Considering $v_0 = 0$ it is easy to obtain from the equations above the so called *linearized equations of fluid mechanics*.

$$\begin{aligned} &\tfrac{\partial \rho_1}{\partial t} + \rho_0\underline{\nabla}\cdot\underline{v}_1 = 0 \\ &m\rho_0\tfrac{\partial \underline{v}_1}{\partial t} = -\underline{\nabla}p_1 + \eta_s\nabla^2\underline{v}_1 + \left(\eta_B + \tfrac{1}{3}\eta_s\right)\underline{\nabla}(\underline{\nabla}\cdot\underline{v}_1) \\ &\tfrac{\partial e_1}{\partial t} + (e_0 + p_0)\underline{\nabla}\cdot\underline{v}_1 = \lambda\nabla^2 T_1 \end{aligned} \tag{2.4}$$

At this point we have 5 equations and 7 variables: four scalars ρ_1,T_1,e_1,p_1 and one vector (with the three components) $\underline{v}_1$. The local equilibrium thermodynamic equations of states can be used to reduce the variables to five. Indeed, it is possible to relate the 4 scalar quantities each other. In particular, it is convenient to express the couple (e_1, p_1) as a function of (ρ_1, T_1) because the dielectric constant derivatives $(\partial\underline{\underline{\varepsilon}}/\partial\rho)_T$ and $(\partial\underline{\underline{\varepsilon}}/\partial T)_\rho$ are more readily obtained from experiments. After some algebra and combining the first equation with the third one to eliminate the dependency by $\underline{v}_1$ in the third equation, we can rewrite the linearized equations as follows:

$$\begin{gathered}
\tfrac{\partial\rho_1}{\partial t} + \rho_0\underline{\nabla}\cdot\underline{v}_1 = 0 \\
\tfrac{\partial\underline{v}_1}{\partial t} + \tfrac{c_T^2}{\rho_0}\underline{\nabla}\rho_1 + \alpha c_T^2\underline{\nabla}T_1 - D_L\underline{\nabla}(\underline{\nabla}\cdot\underline{v}_1) + D_S\left[\underline{\nabla}\wedge\underline{\nabla}\wedge\underline{v}_1\right] = 0 \\
\tfrac{\partial T_1}{\partial t} - \tfrac{\gamma-1}{\alpha\rho_0}\tfrac{\partial\rho_1}{\partial t} - \gamma D_T\nabla^2 T_1 = 0
\end{gathered} \tag{2.5}$$

where c_T,α,γ,D_L, D_S and D_T are respectively: the isothermal sound speed, the thermal expansion coefficient, the heat capacity ratio, the longitudinal kinematic viscosity $((\eta_B + \frac{4}{3}\eta_s)/m\rho_0)$, the shear kinematic viscosity $(\eta_s/m\rho_0)$ and the thermal diffusivity. Applying the divergence operator $(\underline{\nabla}\cdot)$ to the second line in eq. 2.5 we will obtain the longitudinal component of the Nevier-Stokes equation, while applying the curl operator $(\underline{\nabla}\wedge)$ we will have the equations for the shear components. The cartesian reference can be chosen, without loss of generality, with one of the axis oriented along $\underline{v}_1$. If we introduce the two new quantities $\psi_1 = \underline{\nabla}\cdot\underline{v}_1$ and $\mu_{1,2} = (\underline{\nabla}\wedge\underline{v}_1)_{1,2}$, we can now write the following set of 5 equations in 5 variables:

$$\begin{gathered}
\tfrac{\partial\rho_1(\underline{r},t)}{\partial t} + \rho_0\psi_1(\underline{r},t) = 0 \\
\tfrac{c_T^2}{\rho_0}\nabla^2\rho_1(\underline{r},t) + \left[\tfrac{\partial}{\partial t} - D_L\nabla^2\right]\psi_1(\underline{r},t) + \alpha c_T^2\nabla^2 T_1(\underline{r},t) = 0 \\
-\tfrac{\gamma-1}{\alpha\rho_0}\tfrac{\partial\rho_1(\underline{r},t)}{\partial t} + \left[\tfrac{\partial}{\partial t} - \gamma D_T\nabla^2\right]T_1(\underline{r},t) = 0 \\
\left[\tfrac{\partial}{\partial t} - D_S\nabla^2\right]\mu_1(\underline{r},t) = 0 \\
\left[\tfrac{\partial}{\partial t} - D_S\nabla^2\right]\mu_2(\underline{r},t) = 0
\end{gathered} \tag{2.6}$$

which can be written using the matrix formalism:

$$\begin{pmatrix}
\frac{\partial}{\partial t} & \rho_0 & 0 & 0 & 0 \\
\frac{c_T^2}{\rho_0}\nabla^2 & \frac{\partial}{\partial t} - D_L\nabla^2 & \alpha c_T^2\nabla^2 & 0 & 0 \\
-\frac{(\gamma-1)}{\alpha\rho_0}\frac{\partial}{\partial t} & 0 & \frac{\partial}{\partial t} - \gamma D_T\nabla^2 & 0 & 0 \\
0 & 0 & 0 & \frac{\partial}{\partial t} - D_S\nabla^2 & 0 \\
0 & 0 & 0 & 0 & \frac{\partial}{\partial t} - D_S\nabla^2
\end{pmatrix}\cdot\begin{pmatrix}
\rho_1(\underline{r},t) \\ \psi_1(\underline{r},t) \\ T_1(\underline{r},t) \\ \mu_1(\underline{r},t) \\ \mu_2(\underline{r},t)
\end{pmatrix} = \begin{pmatrix} 0 \\ 0 \\ 0 \\ 0 \\ 0 \end{pmatrix} \tag{2.7}$$

This differential equations system can be easier solved in the Fourier-Laplace domain. We just remind the reader that a certain quantity $x(\underline{r},t)$ can be transformed in its Fourier-Laplace counterpart through the relation:

$$\widetilde{x}(\underline{Q},s) = \int_0^{+\infty} dt\, e^{-st} \int d^3\underline{r}\; e^{i\underline{Q}\cdot\underline{r}}\; x(\underline{r},t)$$

Applying such transformation at the linearized hydrodynamics matrix we obtain the following matrix equation:

$$\begin{pmatrix} s & \rho_0 & 0 & 0 & 0 \\ -\omega^2(Q)/\gamma\rho_0 & (s+D_LQ^2) & -\alpha\omega^2(Q)/\gamma & 0 & 0 \\ -(\gamma-1)s/\alpha\rho_0 & 0 & s+\gamma D_TQ^2 & 0 & 0 \\ 0 & 0 & 0 & s+D_SQ^2 & 0 \\ 0 & 0 & 0 & 0 & s+D_SQ^2 \end{pmatrix} \cdot \begin{pmatrix} \widetilde{\rho}_1(\underline{Q},s) \\ \widetilde{\psi}_1(\underline{Q},s) \\ \widetilde{T}_1(\underline{Q},s) \\ \widetilde{\mu}_1(\underline{Q},s) \\ \widetilde{\mu}_2(\underline{Q},s) \end{pmatrix} =$$

$$\begin{pmatrix} 1 & 0 & 0 & 0 & 0 \\ 0 & 1 & 0 & 0 & 0 \\ -(\gamma-1)/\alpha\rho_0 & 0 & 1 & 0 & 0 \\ 0 & 0 & 0 & 1 & 0 \\ 0 & 0 & 0 & 0 & 1 \end{pmatrix} \cdot \begin{pmatrix} \widetilde{\rho}_1(\underline{Q},0) \\ \widetilde{\psi}_1(\underline{Q},0) \\ \widetilde{T}_1(\underline{Q},0) \\ \widetilde{\mu}_1(\underline{Q},0) \\ \widetilde{\mu}_2(\underline{Q},0) \end{pmatrix} \tag{2.8}$$

where $\omega(Q) = \sqrt{\gamma}c_TQ = c_sQ$, with c_s the adiabatic speed of sound.

Observing the above expression it is evident that the 2×2 minors in the bottom right of the matrices represent an independent set of equations: they are describing the non propagating shear (transverse) modes. Because of the independency from the density fluctuation it is not possible to gain information about such shear modes from the $S(\underline{Q},\omega)$, at least as far as the hydrodynamic limit is fulfilled. To simplify the expressions, in the following we will concentrate only on the top left 3×3 minor which contains the information about the longitudinal modes evolution. Playing a little bit with the matrices, we can finally write the following expression:

$$\widetilde{M}(s) \begin{pmatrix} \widetilde{\rho}_1(\underline{Q},s) \\ \widetilde{\psi}_1(\underline{Q},s) \\ \widetilde{T}_1(\underline{Q},s) \end{pmatrix} = \begin{pmatrix} \left[\begin{matrix}(s+D_LQ^2)(s+\gamma D_TQ^2) \\ +(\gamma-1)\omega^2(Q)/\gamma\end{matrix}\right] & [-\rho_0(s+\gamma D_TQ^2)] & [-\alpha\rho_0\omega^2(Q)/\gamma] \\ [\omega^2(Q)(s+\gamma D_TQ^2)/\gamma\rho_0] & [s(s+\gamma D_TQ^2)] & [\alpha\omega^2(Q)s/\gamma] \\ [-(\gamma-1)\omega^2(Q)/\alpha\rho_0\gamma] & [-(\gamma-1)s/\alpha] & [s(s+Q^2D_L)+\omega^2(Q)/\gamma)] \end{pmatrix} \cdot \begin{pmatrix} \widetilde{\rho}_1(\underline{Q},0) \\ \widetilde{\psi}_1(\underline{Q},0) \\ \widetilde{T}_1(\underline{Q},0) \end{pmatrix} \tag{2.9}$$

where

$$\widetilde{M}(s) = s^3 + (D_LQ^2+\gamma D_TQ^2)s^2 + [\omega^2(Q)+\gamma D_TD_LQ^4]s + \omega^2(Q)D_TQ^2 \tag{2.10}$$

Because the dominant contribution to the scattered signal arises from the $S_{\rho\rho}(\underline{Q},\omega)$ (eq. 1.14), we are mostly interested on the density-density correlation function. Considering that for $Q\to0$, $\langle\rho_1^*(\underline{Q},0)\psi_1(\underline{Q},0)\rangle = \langle\rho_1^*(\underline{Q},0)T_1(\underline{Q},0)\rangle = 0$, it is possible to obtain it multiplying eq. 2.9 by $\rho_1^*(\underline{Q},0)$ and then ensemble-averaging:

$$\frac{F_{\rho\rho}(\underline{Q},s)}{F_{\rho\rho}(\underline{Q})} = \frac{\langle\rho_1^*(\underline{Q},0)\widetilde{\rho}_1(\underline{Q},s)\rangle}{\langle\rho_1^*(\underline{Q})\widetilde{\rho}_1(\underline{Q})\rangle} = \frac{B(s)}{\widetilde{M}(s)} \tag{2.11}$$

with $B(s) = (s+D_LQ^2)(s+\gamma D_TQ^2) + (\gamma-1)\frac{\omega^2(Q)}{\gamma}$.

The dynamic structure factor can be obtained from the Laplace transform as follows:

$$S_{\rho\rho}(\underline{Q},\omega) = \frac{1}{\pi} S(Q) \Re \left[\frac{B(s=i\omega)}{\widetilde{M}(s=i\omega)} \right] \tag{2.12}$$

where $S(Q) = \langle \rho_1^*(\underline{Q}) \widetilde{\rho}_1(\underline{Q}) \rangle$ is the static structure factor already introduced in Chapter 1, and it's counterpart in the time domain can be found by Laplace inverting:

$$\frac{F_{\rho\rho}(\underline{Q},t)}{F_{\rho\rho}(\underline{Q})} = \frac{\langle \rho_1^*(\underline{Q},0) \widetilde{\rho}_1(\underline{Q},t) \rangle}{\langle \rho_1^*(\underline{Q}) \widetilde{\rho}_1(\underline{Q}) \rangle} = \sum_{i=1}^{3} \left[\lim_{s \to s_i} \frac{B(s_i)(s-s_i)}{\widetilde{M}(s)} \right] e^{s_i |t|} \tag{2.13}$$

where s_i are the roots of the dispersion equation $\widetilde{M}(s) = 0$.

Actually, such equations are very complex as they are, and it is difficult to highlight any spectral feature to be easily interpreted. In order to achieve simpler forms we notice that for most of the liquids $D_L Q^2$ and $\gamma D_T Q^2$ are usually small compared to $\omega(Q)$. Thus, the solution of the dispersion equation can be written as $s = s^{(0)} + s^{(1)} + ... + s^{(n)}$, where $s^{(n)}$ is the therm of order n in any of the small quantities $D_L Q^2$ and $\gamma D_T Q^2$. Arresting such series expansion to the first order, it's easy to find the three roots for $\widetilde{M}(s) = 0$:

$$\begin{cases} s_0 = -D_T Q^2 \\ s_{1,2} = \pm i\omega(Q) - \Gamma Q^2 \end{cases} \tag{2.14}$$

where

$$\Gamma = \frac{1}{2}[(\gamma - 1) D_T + D_L] \tag{2.15}$$

Combining eq. 2.14 and eq. 2.13 we finally obtain

$$\begin{aligned} \frac{\langle \rho_1^*(\underline{Q},0) \widetilde{\rho}_1(\underline{Q},t) \rangle}{\langle \rho_1^*(\underline{Q}) \widetilde{\rho}_1(\underline{Q}) \rangle} &= \left(1 - \tfrac{1}{\gamma}\right) e^{-D_T Q^2 |t|} + \tfrac{1}{\gamma} e^{-\Gamma Q^2 |t|} \cos\left[\omega(Q)|t|\right] + \\ &+ \tfrac{Q}{\gamma} \tfrac{3\Gamma - D_L}{\gamma c_s} \sin[\omega(Q)|t|] \end{aligned} \tag{2.16}$$

while its Fourier transform is:

$$\begin{aligned} \frac{S_{\rho\rho}(\underline{Q},\omega)}{S(Q)} &= \tfrac{1}{\pi} \left\{ \left(1 - \tfrac{1}{\gamma}\right) \tfrac{D_T Q^2}{\omega^2 + (D_T Q^2)^2} + \right. \\ &+ \tfrac{1}{2\gamma} \left(\tfrac{\Gamma Q^2}{[\omega + \omega(Q)]^2 + [\Gamma Q^2]^2} + \tfrac{\Gamma Q^2}{[\omega - \omega(Q)]^2 + [\Gamma Q^2]^2} \right) \\ &+ \left. \tfrac{Q}{\gamma} \tfrac{3\Gamma - D_L}{\gamma c_s} \left(\tfrac{\omega + \omega(Q)}{[\omega + \omega(Q)]^2 + [\Gamma Q^2]^2} - \tfrac{\omega - \omega(Q)}{[\omega - \omega(Q)]^2 + [\Gamma Q^2]^2} \right) \right\} \end{aligned} \tag{2.17}$$

In the expression above now it's easy to recognize among the contributions the sum of three Lorentzian lines shapes (see inset of Fig. 2.1).

The first one is related to the unshifted line of the spectrum, called Rayleigh peak, and arising from the interaction between light and entropy, or heat fluctuations, which are purely diffusive or dissipative modes of the fluid. The second line in

eq. 2.17 is the Brillouin doublet, consisting in two Lorentzians symmetrically shifted by $\omega(Q) = \pm c_s Q$ with a full width half maximum (FWHM) of $2\Gamma Q^2$. The last terms in the expression above is a non-Lorentzian correction to the spectrum line shape which is actually quite weak and difficult to be appreciated in most of the experimental measurements.

Summarising, to obtain the eq. 2.17 we introduced two approximations: that the fluctuations can be described by the simple linearized hydrodynamic equations (we could so neglect the terms of the orders higher than Q^2) and that the width of the Brilluoin peak is small compared to the shift of the peak itself (this condition is implied, through eq. 2.15, with the assumption that $\gamma D_T Q^2 \ll \omega(Q)$ and $D_L Q^2 \ll \omega(Q)$).

Actually, the expression for the $S(\underline{Q},\omega)$ can be further simplified [56] if another approximation is considered: in the case of transparent fluids the thermal conductivity is usually very small and negligible with respect to the kinematic longitudinal viscosity: $D_T \ll D_L$. In this case the eq. 2.15 is simplified in

$$\Gamma = D_L/2 \tag{2.18}$$

and eq. 2.10 can be now factorized as follows:

$$\widetilde{M}(s) = (s + D_T Q^2)(s^2 + 2\Gamma Q^2 s + \omega(Q)^2) \tag{2.19}$$

Neglecting as well as before all the orders higher than Q^2, it can be easily obtained that

$$\begin{aligned} \frac{\langle \rho_1^*(\underline{Q},0)\widetilde{\rho}_1(\underline{Q},s)\rangle}{\langle \rho_1^*(\underline{Q})\widetilde{\rho}_1(\underline{Q})\rangle} &= \frac{B(s)}{\widetilde{M}(s)} = \\ &= \left(1 - \frac{1}{\gamma}\right)\frac{1}{s+D_T Q^2} + \frac{1}{\gamma}\frac{s+2\Gamma Q^2}{[s+\Gamma Q^2]^2+[\omega(Q)^2-(\Gamma Q^2)^2]} \end{aligned} \tag{2.20}$$

and through eq. 2.12

$$\frac{S(\underline{Q},\omega)}{S(\underline{Q})} = \frac{1}{\pi}\left[\left(1 - \frac{1}{\gamma}\right)\frac{D_T Q^2}{[D_T Q^2]^2+\omega^2} + \frac{1}{\gamma}\frac{2\omega(Q)^2 Q^2 \Gamma}{[\omega^2-\omega(Q)^2]^2+[2\omega\Gamma Q^2]^2}\right] \tag{2.21}$$

as in the previous case, the first term is the unshifted Rayleigh peak, the second part is the Brillouin doublet. It is easy to realize that the line-shape of the Brillouin doublet is no more described by a couple of Lorentzians; conversely, the expression we obtained has the same shape of the solution for the case of a damped harmonic oscillator (DHO). This result sheds light on the microscopical origin of the hydrodynamic modes. Indeed, in the contrary of intuition, it means that also in the case of spontaneous emission, despite the term "spontaneous", the system is driven by random thermal forces.

This result might have been anticipated in the limit of small thermal conductivity ($D_T \approx 0$). In such case, the linearize equations (eq. 2.6) can be combined to obtain the following one in the Fourier domain:

$$\frac{\rho_0}{Q^2}\frac{\partial^2}{\partial t^2}\rho_1(Q,t) + \eta_0\frac{\partial}{\partial t}\rho_1(Q,t) + \rho_0 c_T^2 \rho_1(Q,t) = 0 \tag{2.22}$$

which is exactly the DHO equation.

In order to determine the power spectrum of the density fluctuations we can use the so called *fluctuation-dissipation* theorem [57, 58, 59] which relates a certain physical quantity of a system at equilibrium with the dissipative processes involved in the response of the same system to an external perturbation. If $x(t)$ is the quantity of interest and $f(t)$ the perturbation, in the linear response limit we can write

$$x(\omega) = \chi(\omega) \cdot f(\omega)$$

where $\chi(\omega)$ is the generalized susceptibility function which can be decomposed, in the case of activated dissipative processes, in real and imaginary parts $\chi(\omega) = \chi'(\omega) + i\chi''(\omega)$. From the above theorem, the power spectrum of fluctuation of $x(\omega)$ is proportional to $\chi''(\omega)/\omega$.

For eq. 2.22 we can obtain, as a Green function of the differential equation, the generalized susceptibility:

$$\chi(\omega) = \left[-\frac{\rho_0 \omega^2}{Q^2} + M_0 \right]^{-1} \tag{2.23}$$

where $M_0 = \rho_0 c_T^2$ is the low frequency elastic modulus.

If a relaxation phenomenon is occurring with a frequency in the same spectral range of the measured spectrum, we must use a generalized hydrodynamic model replacing M_0 with a complex frequency dependent elastic modulus $M^*(\omega) = M'(\omega) + iM''(\omega)$. The real and imaginary parts of the susceptibility can be written as follows:

$$\chi'(\omega) = \frac{M'(\omega) - \frac{\rho_0 \omega^2}{Q^2}}{\left[M'(\omega) - \frac{\rho_0 \omega^2}{Q^2} \right]^2 + [M''(\omega)]^2} \tag{2.24}$$

$$\chi''(\omega) = \frac{M''(\omega)}{\left[M'(\omega) - \frac{\rho_0 \omega^2}{Q^2} \right]^2 + [M''(\omega)]^2} \tag{2.25}$$

thus, the spectrum of density fluctuations:

$$\frac{S_{\rho\rho}(Q,\omega)}{S_{\rho\rho}(Q)} \propto \frac{1}{\omega} \frac{M''(\omega)}{\left[M'(\omega) - \frac{\rho_0 \omega^2}{Q^2} \right]^2 + [M''(\omega)]^2} \tag{2.26}$$

To be a good approximation of the Brillouin doublet, at least in the proximity of the peak frequency ω_{LA}, the above expression must show a maximum at ω_{LA}. This happens only in the case:

$$M'(\omega_{LA}) = \rho_0 \frac{\omega_{LA}^2}{Q^2} \tag{2.27}$$

To determine the ω-dependency for M'' we now introduce a new parameter Γ_{LA} as the full width half maximum (FWHM) of the Brillouin peak. From the definition of Γ_{LA} it must follows that:

$$2S_{\rho\rho}(Q, \omega_{LA} + \Gamma_{LA}/2) = S_{\rho\rho}(Q, \omega_{LA})$$

In already used approximation of small widths in respect to the frequency shifts, we obtain that:

$$M''(\omega_{LA}) = \frac{\rho_0 \omega_{LA} \Gamma_{LA}}{Q^2} \tag{2.28}$$

and eq. 2.26 can be rewritten as:

$$\frac{S_{\rho\rho}(Q,\omega)}{S_{\rho\rho}(Q)} \propto \frac{\omega_{LA}^2 \Gamma_{LA}}{[\omega^2 - \omega_{LA}^2]^2 + [\omega \Gamma_{LA}]^2} \tag{2.29}$$

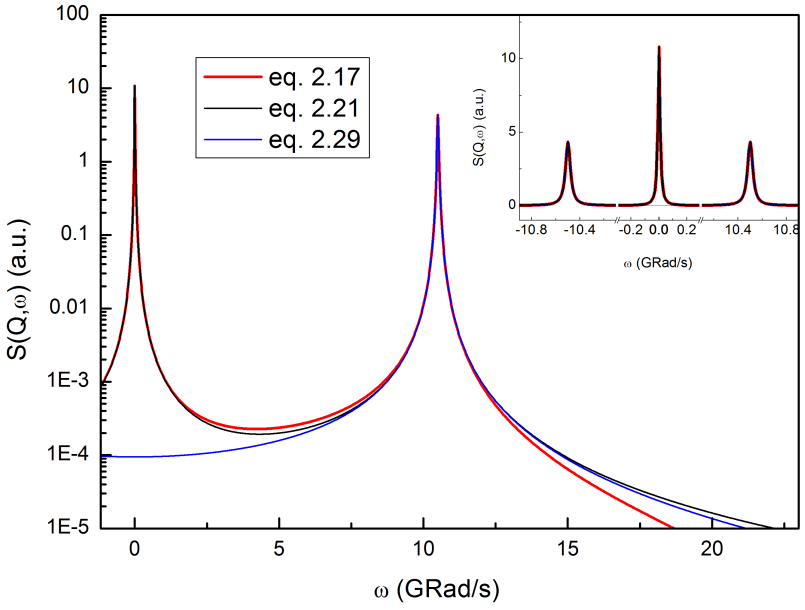

Figure 2.1: In the picture are represented the different lineshapes obtained with eq. 2.17, eq. 2.21 and eq. 2.29 with the following parameter: $D_T = 200\ nm^2/ns$, $D_L = 900\ nm^2/ns$, $\gamma = 1.5$, $c_s = 1500\ m/s$ and $Q = 0.007\ nm^{-1}$. Only small differences can be appreciated on the tails in log scale, while it is evident that the DHO model is not able to describe the low frequency range of the spectrum. In the inset is shown the whole spectrum in linear scale, all the three longitudinal modes are visible: the two shifted Brillouin peaks and the unshifted Rayleigh one.

Comparing now eq. 2.21 with eq. 2.29 it can be easily noticed that, because of the approximation of low thermal conductivity, the latter expression is not able to describe the Rayleigh unshifted peak, but it is a good approximation for the spectrum only at frequencies close to the Brillouin one (see Fig. 2.1). Furthermore, we found the relation

$$\Gamma_{LA} = 2\Gamma Q^2 = D_L Q^2 \tag{2.30}$$

Finally, we showed how it is possible, thanks to the hydrodynamic model, to extract the acoustic information from an inelastic scattering spectrum. In particular, we will see that measuring spectra in a wide set of Q-values, it is possible to reconstruct the elastic moduli dispersion shape and hence obtaining information about the relaxation times of the activated processes.

2.2 Memory function formalism

Heretofore, we focused our investigation to the hydrodynamic limit ($Q \to 0$) in which the continuous medium approximation was appropriate. Such picture of the system was adequate in the framework of a scattering process in which the probe acoustic wave was characterized by long wavelengths compared to the atomic and molecular sizes. Within this condition, we could discard the single particle dynamics and describe the system from a macroscopic point o view, reducing a many-bodies problem to a thermodynamic one, fact that allowed us to use the continuity equations (eq. 2.1). Approaching the so called mesoscopic region (where the wavelength of the probe is comparable to the molecular sizes) the above mentioned approach fails and we need to introduce a new formalism which can explicitly take into account the equations of motion of the single particles involved in the dynamics. The failure of hydrodynamics in the high-Q/high-frequency domain is linked to the presence of dissipative terms in the basic hydrodynamic equations: the latter, unlike the microscopic equations of motions, are not invariant under time reversal [60].

2.2.1 Random forces and Langevin equation

At the end of section 2.1, in the context of the DHO approximation, we interpreted the "spontaneous scattering" as the macroscopic result of microscopic thermal random forces. If the space/time-scales in play between the macroscopic observable and the microscopic forces are very different, it is not necessary a many-particles model to mimic the thermal forces, but they can be described by a generic random fluctuating force acting in the medium. This kind of stochastic phenomenology was used by Langevin to describe the brownian motion of a big and massive particle in a bath of other smaller and lighter particles. In this latter case there are two very different dynamics evolving in the system: the slow relaxation of the velocity of the big particle and the high frequency of collisions between the latter and the particles composing the bath. Langevin hypothesized the following equation of motion for the big particle:

$$m\dot{\underline{v}} = -m\xi\underline{v} + \underline{R}(t) \tag{2.31}$$

where m is the mass of the particle, $\underline{v}$ its velocity, ξ a friction coefficient and $\underline{R}$ the random force arising from the inter-particles collisions. The following hypothesis have to be considered:

- the random forces vanish in mean

$$\langle \underline{R}(t) \rangle = 0 \tag{2.32}$$

- velocity of the big particle and collisions are uncorrelated

$$\langle \underline{R}(t) \cdot \underline{v} \rangle = 0 \tag{2.33}$$

- there is an infinitesimal correlation time between random forces at different times

$$\langle \underline{R}(t+s) \cdot \underline{R}(s) \rangle = 2\pi R_0 \delta(t) \tag{2.34}$$

- which reflects on a constant power spectrum R_0

$$\frac{1}{2\pi}\int_{-\infty}^{+\infty}\langle \underline{R}(t)\cdot\underline{R}\rangle e^{i\omega t}\mathrm{d}t = R_0 \tag{2.35}$$

Under these assumptions and considering the solution for the eq. 2.31:

$$m\underline{v}(t) = m\underline{v}(0)e^{-\xi t} + e^{-\xi t}\int_0^t e^{\xi s}\underline{R}(s)\mathrm{d}s \tag{2.36}$$

it is possible to obtain the relation between ξ and the random force. Squaring and taking the statistical average on eq. 2.36 and using eq. 2.33 and eq. 2.34 it's easy to obtain:

$$m^2\langle|\underline{v}(t)|^2\rangle = m^2\langle|\underline{v}(0)|^2\rangle e^{-2\xi t} + \frac{\pi R_0}{\xi}[1-e^{-2\xi t}] \tag{2.37}$$

now in the limit of $t\to\infty$ we can consider that the big particle will be in equilibrium with the bath independently by the initial conditions. Hence, $\langle|\underline{v}(\infty)|^2\rangle = 3k_BT/m$, so eq. 2.37 can be rewritten as follows:

$$\xi = \frac{\pi R_0}{3k_BTm} = \frac{1}{3k_BTm}\int_0^\infty \langle \underline{R}(t)\cdot\underline{R}\rangle \mathrm{d}t \tag{2.38}$$

It is thus evident the link between the friction coefficient and the random forces. It means basically that the viscosity of the system can be addressed, from a microscopic point of view, to the collisions occurring between the particles.

A step forward in this framework was realized by Langevin considering the more complex case in which the bath is composed by particles with the same dimensions and masses of the reference one. In this case, the markovian approximation whereby the frictional force on the reference particle at a given time is assumed to be proportional only to its velocity at the same time, is not more valid. In that picture, the reference particle could instantaneously follow the modifications of the bath around it, now, more realistically, some time is needed for the coupling between the particle and the properties of the bath. In other words, the frictional force acting on the reference particle is the result of the previous conditions of the system, so it maintains a sort of "memory" of the history of the medium. Eq. 2.31 has to be modified introducing the concept of a "memory function" ξ:

$$m\dot{\underline{v}} = -m\int_0^t \xi(t-s)\underline{v}(s)\mathrm{d}s + \underline{R}(t) \tag{2.39}$$

2.2.2 The project-operator formalism

In this paragraph we are going to present a general theoretical approach for the calculation of the time correlations functions at molecular length scales. As already noticed, we cannot use anymore a thermodynamic approach for the mesoscopic region, but we should take into account the all motion equations and solve a many particles problem.

The time-evolution of a certain quantity $A(t)$ in a system of N interacting particles is described through the Liouville operator $\mathcal{L}$ as:

$$\frac{\mathrm{d}A(t)}{\mathrm{d}t} = \{A(t),\mathcal{H}\} = i\mathcal{L}A(t) \tag{2.40}$$

where $\mathcal{H}$ is the hamiltonian of the N-particles system, i is the imaginary unit and $\{...,...\}$ is the Poisson bracket. So, explicitly, $i\mathcal{L} = \{...,\mathcal{H}\} = \sum_{j=1}^{3N} \frac{\partial \mathcal{H}}{\partial p_j}\frac{\partial}{\partial q_j} - \frac{\partial \mathcal{H}}{\partial q_j}\frac{\partial}{\partial p_j}$, where q_j and p_j are the generalized coordinates in the phase space.

The formal solution for the above equation is:

$$A(t) = e^{i\mathcal{L}t}A(0) \tag{2.41}$$

but it is too complex to be used for the solution of the N-particles problem. We have to find the way to describe such complex problem with lowest as possible number of variables. In this framework we will discuss about the so called projection-operator formalism, developed by Zwanzig and Mori [61, 62, 63]. Let's define the projector operator $\mathcal{P}_A$ to obtain the component of a certain quantity along the $\underline{A}$ direction (in the phase space the quantity $\underline{A}$ is represented by a vector):

$$\mathcal{P}_A = \frac{(\underline{A},...)}{(\underline{A},\underline{A})}\underline{A} \tag{2.42}$$

where $(...,...)$ is the scalar product operation. It can be shown that the complementary operator $\mathcal{Q} = 1 - \mathcal{P}$ is the one devoted to obtain the orthogonal component of a certain vector in respect to $\underline{A}$. Thus, obviously, the following rules are fulfilled: $\mathcal{P}^2 = \mathcal{P}$, $\mathcal{Q}^2 = \mathcal{Q}$, $\mathcal{P}\mathcal{Q} = \mathcal{Q}\mathcal{P} = 0$. Furthermore, because the scalar products are performed in the phase space, they can be interpreted equivalently as a statistical average, so $(...,...) = \langle ...,... \rangle$. We can therefore define the autocorrelation function of the quantity $\underline{A}$ as:

$$C_A(t) = \frac{\langle \underline{A}, \underline{A}(t)\rangle}{\langle \underline{A}, \underline{A}\rangle} \tag{2.43}$$

it's now easy to see that $\mathcal{P}_A(\underline{A}(t)) = C_A(t)\underline{A}$. Our aim is to find the motion equation for the autocorrelation function. From the Laplace transform in s of eq. 2.41 we can obtain:

$$\underline{A} = (s - i\mathcal{L})\widetilde{\underline{A}}(s) = (s - i\mathcal{L})(\mathcal{P} + \mathcal{Q})\widetilde{\underline{A}}(s) \tag{2.44}$$

Now applying the operator $\mathcal{P}$ and $\mathcal{Q}$ to this equation and manipulating the results with some algebra, it is possible to obtain the following equation in Laplace domain:

$$(s - i\Omega_A)\widetilde{C}_A(s) + (\underline{K}, \widetilde{\underline{R}}(s))(\underline{A},\underline{A})^{-1}\widetilde{C}_A(s) = 1 \tag{2.45}$$

where we introduced the quantities

$$i\Omega_A = (\underline{A},\dot{\underline{A}})(\underline{A},\underline{A})^{-1} \tag{2.46}$$

$$\widetilde{\underline{R}}(s) = (s - iQ\mathcal{L}Q)^{-1}\underline{K} \tag{2.47}$$

$$\underline{K} = Q\dot{\underline{A}} \tag{2.48}$$

through the inverse Laplace transformation of eq. 2.47 we obtain the time dependence of $\underline{R}$:

$$\underline{R}(t) = e^{iQ\mathcal{L}Qt}\underline{K} \tag{2.49}$$

expanding it in series it can be seen that $\underline{R}(t) \perp \underline{A}$ at every time. We will discuss about this property in the following. For the moment we are interested on the

time - 0 property: $\underline{R}(0) = \underline{K}$. Using the latter expression in eq. 2.45 and defining the *memory function*

$$\widetilde{M}_A(s) = \frac{\langle \underline{R}, \widetilde{\underline{R}}(s) \rangle}{\langle \underline{A}, \underline{A} \rangle} \tag{2.50}$$

we obtain the following equation for the autocorrelation function of $\underline{A}$:

$$\widetilde{C}_A(s)[s - i\Omega_A + M_A(s)] = 1 \tag{2.51}$$

which leads to the time evolution equations for $C_A(t)$ and $\underline{A}(t)$:

$$\dot{C}_A(t) - i\Omega_A C_A(t) + \int_0^t M_A(t-\tau) \cdot C_A(\tau) \mathrm{d}\tau = 0 \tag{2.52}$$

$$\dot{\underline{A}}(t) - i\Omega_A \underline{A}(t) + \int_0^t M_A(t-\tau) \cdot \underline{A}(\tau) \mathrm{d}\tau = \underline{R}(t) \tag{2.53}$$

if we now compare the latter equation with the Langevin generalized equation (eq. 2.39) we can better understand the meaning of the quantity we introduce in eq. 2.47: it represents the random force acting in the medium. This perspective is supported by the orthogonality property of $\underline{R}$ with respect to the generic observable $\underline{A}$. In fact, such property means that there is not any correlation between the two quantity, which is one of the initial hypothesis of the Langevin problem (see eq. 2.33).

Furthermore we notice that M_A is the counterpart of the "friction" memory function in the generalized Langevin equation. Also in this case it is interesting to observe the parallelism between these two quantity: both of them are related to the autocorrelation function of the random forces.

We can go on with an analogous procedure introducing the random force projector operator $P_R = \langle \underline{R}, ... \rangle \langle \underline{R}, \underline{R} \rangle^{-1} \underline{R}$ which will lead to new evolution equations:

$$\dot{\underline{R}}(t) - i\Omega_R + \int_0^t M_R(t-\tau) R(\tau) \mathrm{d}\tau = f_1(t) \tag{2.54}$$

$$\dot{C}_R(t) - iC_R(t) + \int_0^t M_R(t-\tau) C_R(\tau) \mathrm{d}\tau = 0 \tag{2.55}$$

and counterpart in the Laplace space:

$$C_R(s) = \frac{C_R(0)}{s - i\Omega_R + M_R(s)} \tag{2.56}$$

where $i\Omega_R = \langle \underline{R}, \dot{\underline{R}} \rangle \langle \underline{R}, \underline{R} \rangle^{-1} = \dot{C}_R(0)$, $M_R(t) = \langle \underline{f}_1, \underline{f}_1(t) \rangle \langle \underline{R}, \underline{R} \rangle^{-1}$, $C_R(t) = \langle \underline{R}, \underline{R}(t) \rangle \langle \underline{R}, \underline{R} \rangle^{-1}$.

It is possible to write eq. 2.50 as a function of the new quantities:

$$M_A(s) = \frac{\langle \underline{R}, \widetilde{\underline{R}}(s) \rangle}{\langle \underline{A}, \underline{A} \rangle} = \frac{\langle \underline{R}, \widetilde{\underline{R}}(s) \rangle}{\langle \underline{R}, \underline{R} \rangle} \frac{\langle \underline{R}, \underline{R} \rangle}{\langle \underline{A}, \underline{A} \rangle} = C_R(s) \Delta_{RA} \tag{2.57}$$

and

$$M_A(0) = C_R(0) \Delta_{RA} \tag{2.58}$$

Now combining eqs. 2.51, 2.57, 2.56, 2.58 we obtain the first order approximation in the so called "continued fraction" representation:

$$\frac{C_A(s)}{C_A(0)} = C_A(s) = \left[s - i\Omega_A + \frac{M_A(0)}{s - i\Omega_R + M_R(s)} \right]^{-1} \tag{2.59}$$

to evaluate the quantity in the above equation, we must introduce the relation between them and the frequency sum rules of the correlation function. Thus, writing the correlation functions in the Fourier representation, we have:

$$C_A(t) = \int_{-\infty}^{+\infty} e^{i\omega t} C_A(\omega) \mathrm{d}\omega \tag{2.60}$$

from which we can generalize the property

$$\left. \frac{\partial^n C_A(t)}{\partial t^n} \right|_{t=0} = i^n \int_{-\infty}^{+\infty} \omega^n C_A(\omega) \mathrm{d}\omega = i^n \langle \omega^n \rangle \tag{2.61}$$

We can now combine the latter expression with the $t \to 0$ limit for the eq. 2.52:

$$\left. \frac{\mathrm{d}C_A(t)}{\mathrm{d}t} \right|_{t=0} = i\Omega_A C_A(0) = i\Omega_A$$

where $C_A(0) = 1$ derives directly by the definition in eq. 2.43.

It can be shown with quantum mechanics calculations that dynamic variables evaluated at different times do not commute, and so the order in which they appear in the thermal average is significant. From this fact it is possible to write the so called *detailed balance equation* [64] for which a generic correlation function for a system in thermal equilibrium has to satisfy the following equation:

$$C(Q, \omega) = e^{\frac{\hbar\omega}{k_B T}} C(-Q, -\omega) \tag{2.62}$$

furthermore for spatially invariant systems the correlation function are proportional to Q^2, thus the detailed balance equation can be written regardless of Q:

$$C(\omega) = e^{\frac{\hbar\omega}{k_B T}} C(-\omega) \tag{2.63}$$

which means that the spectrum related to the correlation function is not symmetric in ω but stokes and anti-stokes modes have different intensities. Nevertheless, in the classic limit ($\hbar \to 0$) $C(\omega)$ results to be a symmetric function from the above equation, thus all the odd spectral moments vanish and we can obtain the relation:

$$i\Omega = \left. \frac{\mathrm{d}C_A(t)}{\mathrm{d}t} \right|_{t=0} = i\langle \omega \rangle = 0 \tag{2.64}$$

In a similar way we can obtain $M_A(0)$ deriving in time the evolution equation for the correlation function and obtaining

$$M_A(0) = -\left. \frac{\partial^2 C_A(t)}{\partial t^2} \right|_{t=0} = \langle \omega^2 \rangle \tag{2.65}$$

Finally the eq. 2.59 can be rewritten as follows:

$$C_A(s) = \left[s + \frac{\langle \omega^2 \rangle}{s + M_R(s)} \right]^{-1} \tag{2.66}$$

2.2.3 The case of density fluctuation

Aim of this section is to apply the theoretical projector-operator formalism to the density fluctuation correlation function in order to obtain an adequate memory function to model the dynamic structure factor $S(Q,\omega)$ in the mesoscopic regime. So, if we now consider the variable $\underline{A}(t) = \delta\rho(Q,t) = \rho_1(Q,t)$, accordingly to eq. 2.66, we can write the following:

$$C_{\rho_1}(Q,s) = \frac{\langle \rho_1^*(\underline{Q},0)\widetilde{\rho_1}(\underline{Q},s)\rangle}{\langle \rho_1^*(\underline{Q})\widetilde{\rho_1}(\underline{Q})\rangle} = \frac{F_{\rho\rho}(\underline{Q},s)}{F_{\rho\rho}(\underline{Q})} = \left[s + \frac{\langle\omega^2\rangle}{s + m_L(Q,s)}\right]^{-1} \tag{2.67}$$

where $m_L(Q,s)$ is the second order memory function for the density fluctuations and $\langle\omega^2\rangle$ is the second spectral moment of the dynamic structure factor $S(Q,\omega)$. The latter can be related to the finite-Q generalization of the isothermal sound speed $c_T(Q)$ [65, 66]:

$$\langle\omega^2\rangle = \frac{k_B T Q^2}{mS(Q)} = c_T(Q)^2 Q^2 \tag{2.68}$$

In order to write the expression for the memory function we start to consider its hydrodynamic limit. Thus, it is useful to recall the eq. 2.11. After some manipulation, the latter can be written in continued fractions as follows:

$$\frac{F_{\rho\rho}(\underline{Q},s)}{F_{\rho\rho}(\underline{Q})} = \left[s + \frac{(c_T(Q)Q)^2}{s + D_L Q^2 + \frac{(\gamma-1)(c_T(Q)Q)^2}{s+\gamma D_T Q^2}}\right]^{-1} \tag{2.69}$$

Then, comparing such equation with eq. 2.67, it is possible to write the expression for the memory function in the hydrodynamic limit:

$$m_{L,h}(Q,s) = D_L Q^2 + \frac{(\gamma-1)(c_T(Q)Q)^2}{s + \gamma D_T Q^2} \tag{2.70}$$

which in the time domain reads:

$$m_{L,h}(Q,t) = (\gamma-1)(c_T(Q)Q)^2 e^{-t/\tau_T} + 2D_L Q^2 \delta(t) \tag{2.71}$$

where $\tau_T = (\gamma D_T Q^2)^{-1}$ is the so called thermal relaxation time.

The Rayleigh-Brillouin spectrum can be obtained through the usual Laplace-Fourier relation:

$$\frac{S(Q,\omega)}{S(Q)} = \frac{1}{\pi}\Re\left[\frac{F(Q,s=i\omega)}{F(Q)}\right] = \frac{1}{\pi}\frac{(c_T(Q)Q)^2 m'_{L,h}(Q,\omega)}{[\omega^2-(c_T(Q)Q)^2+\omega m''_{L,h}(Q,\omega)]^2+\omega^2[m'_{L,h}(Q,\omega)]^2} \tag{2.72}$$

where $m'_{L,h}$ and $m''_{L,h}$ are the real and imaginary part of the memory function.

$$m'_{L,h}(Q,\omega) = (\gamma-1)(c_T(Q)Q)^2\frac{\tau_T}{1+(\omega\tau_T)^2} + D_L Q^2 \tag{2.73}$$

$$\omega m''_{L,h}(Q,\omega) = (1-\gamma)(c_T(Q)Q)^2\frac{(\omega\tau_T)^2}{1+(\omega\tau_T)^2} \tag{2.74}$$

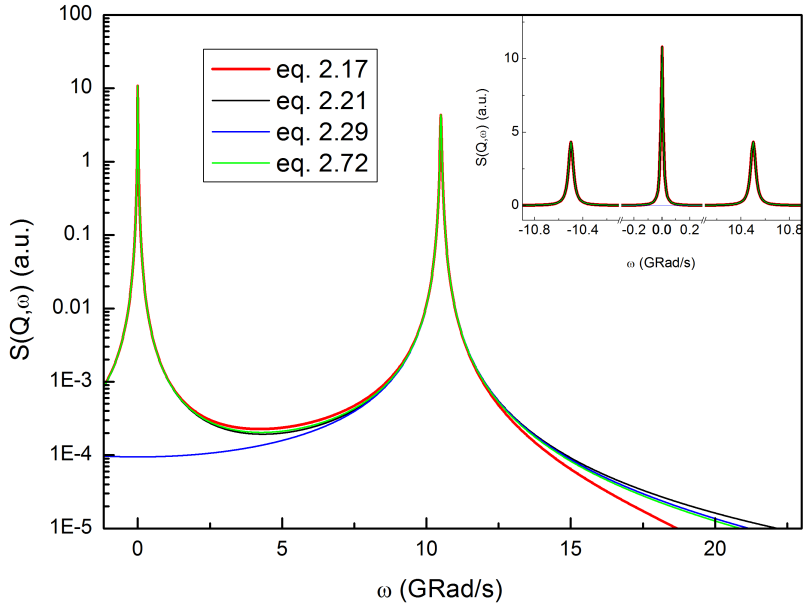

Figure 2.2: In the figure we compare the Rayleigh-Brillouin spectrum obtained with the memory function approach (eq. 2.72) with the previously showed hydrodynamic models. Parameters values are the same of fig. 2.1.

In fig. 2.2 we compare the spectrum obtained with the memory functions formalism (eq. 2.72) with the ones resulting from the hydrodynamics (eq. 2.17, eq. 2.21 and eq. 2.29). As it is possible to notice, the memory function line-shape is well describing the Rayleigh-Brillouin spectrum; moreover, at frequencies much higher than the Brillouin peak position, the spectra tails decay as $\propto \omega^{-4}$, and the 2^{nd} sum rule is always preserved, contrary to the classical hydrodynamic description.

In particular, the hydrodynamic limit of the memory function written above presents two contributions: the first one is a time-decay exponential with a characteristic time τ_T related to a slow thermal relaxation process, the other one is a generic term to consider all those processes so fast to not be directly detectable in hydrodynamic spectral window. The timescales of the latter processes is so small, that they can be safely pictured as a δ-function in time. In the next section we are going to discuss with more details the relaxation processes and their representation in the memory function formalism.

2.2.4 The thermal relaxation

The acoustic waves, propagating into the medium, create "compression-rarefaction" domains with a spatial ($\propto Q^{-1}$) and temporal (ω_L^{-1}) periodicity. The energy stored in the compression zones can be dissipated by the system through heat flow. Such diffusive process is not instantaneous; the system takes a finite time (τ_T) to reach a new thermic equilibrium state. This transition from a perturbed state of the system to a new thermodynamic equilibrium is named "thermal relaxation process".

In the hydrodynamic limit ($Q \to 0$), the thermal relaxation time ($\tau_T \propto Q^{-2}$) can be much higher than the period of the acoustic oscillations ($\tau_L \propto Q^{-1}$), this means that the thermal diffusion process is too slow to be able to dissipate the stored energy in the compression regions. In such case the system remains in a "fully unrelaxed" state. In this limit of $\omega_L \tau_T \gg 1$ the real and imaginary parts of the memory functions (eq. 2.73-2.74) can be rewritten as follows:

$$m'_L = D_L Q^2 \tag{2.75}$$
$$m''_L = (1-\gamma)[c_T(Q)Q]^2 \tag{2.76}$$

and the $S(Q,\omega)$ (eq. 2.72) results in a central Rayleigh peak and two Brillouin side peaks because of the resonance at $\omega_s = c_s Q$.

Moving up to higher Q-values, we will have the opposite limit $\omega_L \tau_T \ll 1$. In this case the thermic diffusion process is fast enough to equilibrate the system in an isothermal state within the period of an acoustic oscillation. Thus, the probe acoustic wave is propagating in an "always" equilibrated system lying in a so-called "fully relaxed" regime. At such conditions:

$$m'_L = (\gamma - 1)(c_T(Q)Q)^2 \tau_T + D_L Q^2 \tag{2.77}$$
$$m''_L = 0 \tag{2.78}$$

Consequently the spectrum will be now resonant at $\omega_T = c_T Q$.

Finally, going from low to high Q regions, the $S(Q,\omega)$ experiences a transition in its resonance angular frequency passing from ω_s to ω_T. We can define a Q-crossing value as the one for which $\omega_L \tau_T = 1$, hence $Q = c_s/(\gamma D_T)$

2.2.5 The structural relaxation

Other kinds of relaxations occur at microscopic length-scales and they can by explicitly express in the memory function shape. Among the others, one of the most important relaxation processes is the so called structural one, widely studied in the framework of glass forming liquids. It can be interpreted as the mechanism leading the transition from the liquid to the glassy state and, in the hydrodynamic limit, it is essentially responsible for the viscous damping. In the memory function formalism one may account for this relaxation by replacing the $\delta(t)$ function in Eq. 2.70 with a function (as an exponential decay) showing a finite relaxation time (τ_α). In such a way the hydrodynamic limit is retrieved for enough low phonon frequency ($\omega\tau_\alpha << 1$), a situation always met below some Q-value in light of the linear dependence of ω on Q. In most of liquids such process evolves in a characteristic timescale $\tau_\alpha \approx ps$, which can be seen as the average time between two subsequent inter-particles collisions or, equivalently, as the life-time of the intermolecular bonds. As already stressed in the introduction, depending on the timescale probed by the acoustic wave, the system can appear as a solid (the intermolecular dynamics is so slow that looks like "frozen" in respect to the short period acoustic wave, $\tau_\alpha \gg \omega_L^{-1}$) or as a liquid ($\tau_\alpha \ll \omega_L^{-1}$). So, rather than of the thermal relaxation, in the low-Q region (low ω_L) we are in the "fully relaxed" regime, while at high Q's (high ω_L) we are in the "fully unrelaxed" one.

To take into account such kind of relaxation in the memory function we can use the so-called Debye ansatz, which consists in replacing the instantaneous term with an exponential term with a characteristic decay-time τ_α and strength Δ^2_α:

$$m_L(Q,t) = (\gamma - 1)(c_T(Q)Q)^2 e^{-t/\tau_T} + \Delta^2_\alpha e^{-t/\tau_\alpha} \tag{2.79}$$

Neglecting for simplicity, the thermal contribute ($\gamma = 1$), $\Delta^2_\alpha = (c^2_\infty - c^2_s)Q^2$ and the real and imaginary parts of m_L:

$$m'_L = \Delta^2_\alpha \frac{\tau_\alpha}{1 + (\omega\tau_\alpha)^2} \tag{2.80}$$

$$\omega m''_L = -\Delta^2_\alpha \frac{(\omega\tau_\alpha)^2}{1 + (\omega\tau_\alpha)^2} \tag{2.81}$$

So, in the liquid-like limit ($Q \to 0, \omega\tau_\alpha \ll 1$), $m'_L = \Delta^2_\alpha\tau_\alpha = D_L$ and $\omega m''_L = 0$ and $S(Q,\omega)$ is resonant in $\omega = c_sQ = c_TQ$ ($\gamma = 1$). Conversely, in the solid like state ($Q \to \infty, \omega\tau_\alpha \gg 1$) $\omega m''_L = -\Delta^2_\alpha$ and the resonance of $S(Q,\omega)$ occurs at $\omega = c_\infty Q$.

Also in the case of the structural relaxation we can define a cross-over Q-value as the one for which $\omega_L\tau_\alpha = 1$, hence $Q = 1/(c_s\tau_\alpha)$.

In conclusion, we have seen that thermal and structural relaxations have competing dispersive effects. If the thermal relaxation at higher Q exhibits a transition from c_s to a lower c_T, in the case of α-relaxation we have a positive dispersion up to c_∞.

2.2.6 The vibrational relaxation

In some molecular liquids other channels for the energy dissipation can be active. When an acoustic wave is propagating through the medium, its energy is firstly absorbed by molecules as kinetic energy in the direction of the propagating wave (compression mechanism) and then it flows into other degrees of freedom through collision mechanism. While translational and orientational channels need relatively small times (few collisions) to equilibrate the pressure changes due to the sound propagation, many collisions are needed to change the energy distribution in the vibrational degrees. The necessary time (typically tenths of ps) to reach the equilibrium between the roto-translational and vibrational degrees is called "Kneser relaxation time" and the systems characterized by such dynamics are classified as "Kneser-like".

In analogy with the previous discussed relaxations, the associated memory function term to describe the Kneser process is $\Delta^2_v e^{-t/\tau_v}$.

2.2.7 The instantaneous relaxation

We can continue, in principle, to add more and more terms to the memory function to take into account every single relaxation process, but obviously it is not a wise strategy. What is used to do is to add a generic instantaneous term to the memory function to take into account all the fast dynamics ($\approx fs$) occurring in the medium

at microscopic length-scales, in general faster that τ_α. Among the processes characterized by such fast dynamics we can list the so called "caging effect" and the relaxations arising from the topological disorder.

In the former case, if we are probing our system in a high-Q spectral window, we will be sensitive to small localized volumes of the sample. In such case, we are no more sensitive to thermal averaged properties, but the interactions between a certain molecule and its first neighbours became dominant. We can, thus, think to a molecule surrounded by a sort of cage made by other neighbouring molecules. Such central molecule can dissipate energy colliding continuously with the molecules forming the cage, up to, eventually, jump out the cage after a certain time.

Concerning the topological disorder, when a liquid is investigated in its elastic regime, it looks like "frozen" and its behaviour is similar to the one of the corresponding disordered solid. Differently to the crystalline phase, at such length-scales the plane waves do not represent a set of eigenstates for the system [67]. As a consequence, an experimentally excited plane wave results to be projected into different eigenstates with different eigenvalues (frequencies). These eigenstates, after a certain characteristic time, τ_d , dephase each other leading to a relaxation process accounting for energy exchanges between the excited wave and the eigenstates of the system.

In this thesis work we simply take into account such fast processes with an instantaneous term in the memory function as $2\Gamma_\mu\delta(t)$.

2.2.8 The proposed memory function

Limiting our attention to the mentioned relaxations phenomena which are the main responsible for the dynamics in liquid systems at mesoscopic length-scales, the complete memory function reads as follows:

$$m_L(Q,t) = (\gamma-1)(c_T(Q)Q)^2 e^{-D_T Q^2 t} + \Delta_\alpha^2 e^{-t/\tau_\alpha} + \Delta_v^2 e^{-t/\tau_v} + 2\Gamma_\mu\delta(t) \qquad (2.82)$$

We just want to remind the reader that all the quantities in the expression above are Q-dependent and they must be correctly evaluated depending of the spectral region under study. We further stress that we have introduced the generalized speed of sound $c_T(Q) = c_T/\sqrt{S(Q)}$. Thus, another quantity we need to determine, as we will see in the next chapter, is the static structure factor S(Q).

Chapter 3

Experimental results

In the previous chapter we discussed some dynamical processes occurring on different time-scales in disordered systems. To fully characterize such systems one should be able to perform experiments in an acoustic spectral window matching the characteristic relaxation time of every process. While in ordered systems as like crystals such approach it is, in principle, feasible thanks to the periodic dispersion of the acoustic modes (i.e. phonons), in liquids and glasses such approach must be revised. Because of the lack of spatial periodicity in fact, the acoustic modes cannot satisfy anymore the Block theorem and therefore, reflecting the disorder of the medium, they results in non-periodic modes so that it is not possible to define anymore the Brillouin zone in which one was used to focus the attention in an experiment with crystalline sample. Because of this absence of periodicity, a way to study all the different relaxation processes is to combine different spectroscopies to explore a Q-range ranging from macroscopic to microscopic lengthscales (ideally from 0 to $\sim$ Å$'s$) in order to probe the entire frequency spectrum of acoustic modes. In this sense we have to consider a "broad band acoustic spectroscopy". So, to study slow processes one should use an experimental technique able to measure low-(Q,ω) acoustic modes; on the contrary, if one is interested in fast relaxations the high-(Q,ω) acoustic region must be exploited. Furthermore, it is worth stressing how such spectral regions are not fully independent one by other, but, as we are going to see in this chapter, to fully characterize a certain spectral domain it is necessary to know complementary information arising from other spectral ranges.

3.1 The sample: acetonitrile

To demonstrate the effectiveness of such broad band acoustic approach, we decided to investigate the dynamics of a widely studied liquid as like acetonitrile (methyl cyanide, CH_3CN). It is the simplest among the organic nitriles compounds and is characterized by a large dipole moment (3.92 D). For this reason it is extensively used as a solvent for ionic and nonpolar compounds. Because of its relatively simplicity and symmetric shape acetonitrile has stimulated a number of theoretical studies on its molecular structure resulting in many proposed potential function to perform molecular dynamic simulations. From the experimental point of view acetonitrile has been investigated by a variety of different methods as like nuclear magnetic

resonance (NMR) [68, 69, 70], vibrational [71, 72, 73] and diffraction [74, 75, 76] techniques. Such liquid, because of its high dipole moment, its sticky shape and

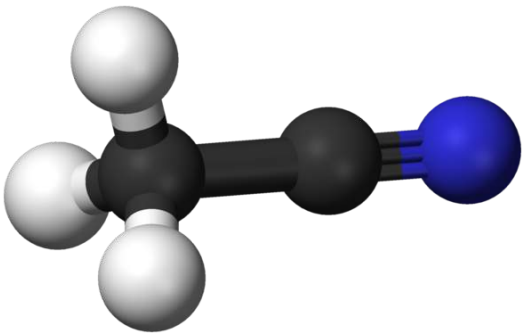

Figure 3.1: Acetonitrile (CH_3CN) is an organic compound characterized by a $C-C-N$ linear sheleton and a CH_3 tetrahedral structure at one side. It is the liquid with the highest electric dipole moment (3.92 D) and it is widely used in chemistry for its solvation properties.

its chemical bounds is characterized by a lot of different dynamical processes as like thermal, vibrational, structural and orientational relaxations. Furthermore the liquid phase of acetonitrile is easily exploitable in a range of temperatures between $227-350\ K$; all this makes acetonitrile a perfect candidate to test the effectiveness of a broad band acoustic spectroscopy in disordered systems.

3.2 The thermal setup

In order to study the dynamical processes occurring in acetonitrile in its whole liquid phase, we performed all the experiments as a function of temperature. In the case of visible spectroscopy techniques (Transient Grating and Brillouin Light Scattering) we used an homemade thermal setup (see fig. 3.2) able to stabilize the sample temperature in a range between 230 and 340 K. The cooling system consists in a commercial Peltier cell coupled with a methanol circulating thermal bath through its hot face. The cold face was in contact with a block of steel equipped with a thermo-resistor tape regulated by a PID controller to stabilize the temperature of the system. The temperature was read by a PT100 thermometer. The same thermal tape was used to heat up the sample up to 350 K, the non damaging threshold for the Peltier cell. On the steel block was allocated the copper sample holder. Indium foils were used to allow a better thermal conductivity in the conjunction points between the all elements. In order to avoid the formation of ice at low temperatures, the system is thought to work in vacuum or with low flux of nitrogen gas. The system is also designed with a cylindrical quartz window to leave the sample accessible from any direction, in this way it is possible to change without limitations the trajectories of the ingoing and scattered laser beams.

In the case of IXS measurements we had to design our own sample holder to perform the measurements as a function of temperature. It is sketched in fig. 3.3.

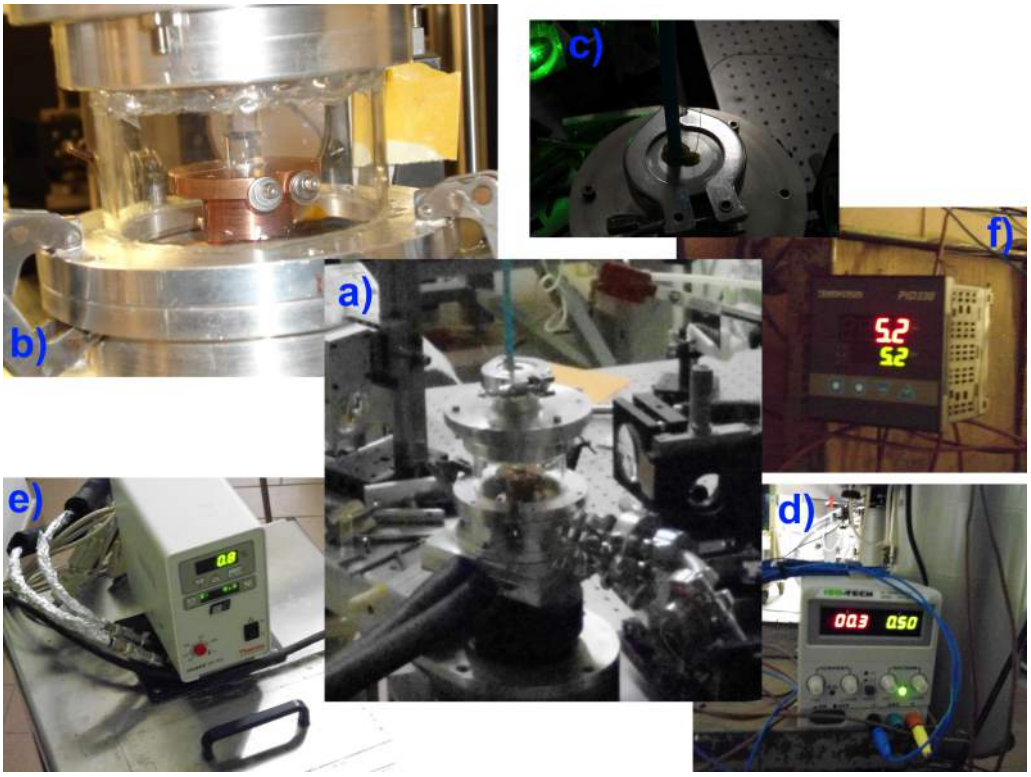

Figure 3.2: In figure is shown the used thermal setup. In inset a) is shown the whole apparatus, while in inset b) is highlighted the copper sample holder part. As it is clear from the picture, the sample holder is embedded in a quartz cylindrical window to allow the laser beams to pass through the sample from any possible direction. This rationale allows to select, without any significant issue, different Q-values in the experiments both in the case of spontaneous or stimulated scattering. Because the setup is designed to reach temperatures under 273.15 K, it is necessary to pump a low vacuum inside the quartz chamber or to realize there an overpressure of nitrogen gas. The latter is the case shown in the inset c), where the blue tube is devoted to the nitrogen flux. During the experiment it was possible to monitor the temperature inside of the liquid thanks to an immersed capillary thermocouple shown in the picture as well. As already stated in the text, the cooling process is led by a Peltier cell powered by a DC supply (inset d)) and coupled with a thermal bath of methanol (inset e)) in contact with the hot face of the cell. Finally, the heating was regulated by a ohmic tape linked to a PID controller shown in inset f).

It is made of aluminum to reduce heat dispersion (we couldn't use copper because is known that acetonitrile reacts with it) and it has to be coupled with the "cold finger" of the cryostat provided by the beamline. As shown in the figure, the sample is confined between to single crystal diamond windows. The latter, transparent to X-rays, are used because of their low-intensity spurious scattering. Furthermore, the velocity of the acoustic modes in diamond is much faster than that of acetonitrile. We hence expect to have well separated spectral features for the diamond and for the acetonitrile. The optical path length of x-ray photons inside the sample was tailored to minimize spurious contributions.

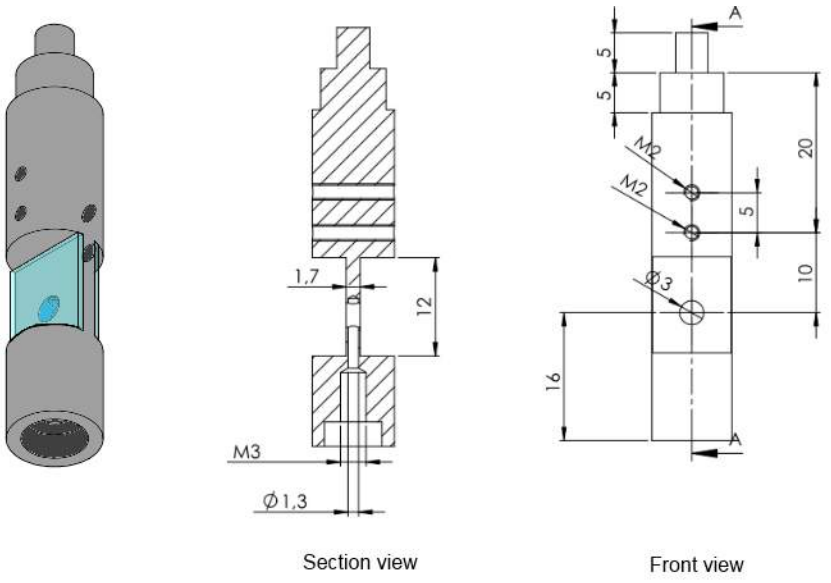

Figure 3.3: The designed sample holder used for the IXS measurements. The sample is confined between two single crystal diamond windows. Such material for the windows was dictated by the transparency and the low-intensity spurious scattered light.

3.3 Estimation of thermodynamic parameters

As we already stressed, it is extremely useful, for the study of dynamical processes in a broad band acoustic spectroscopy, to gain and combine the information arising from the all different spectral ranges. We will see that this strategy is compulsory, for example, in the lineshape analysis we will present in the case of IXS experiments. Among the parameters we can need to know in a broad band acoustic spectroscopy, we have to list the adiabatic speed of sound (c_s), the heat capacity ratio (γ) and the thermal diffusivity (D_T). All of these quantities can be determined with a Transient Grating experiment as described in section 1.2.2. In particular we performed the experiment varying the temperature of the sample, spanning the whole liquid phase of acetronitrile. To obtain a better signal to noise ratio we made use of the Heterodyne Detection (HD) scheme (see section 1.2.3) with $\lambda_{ex} = 800\ nm$, $\lambda_p = 400\ nm$ and a phase mask which allowed the creation of a grating with $Q = 3.9\ \mu m^{-1}$. Once the subtraction between the two HD-measurements has been done, the spectrum looks like as in the fig.3.4.

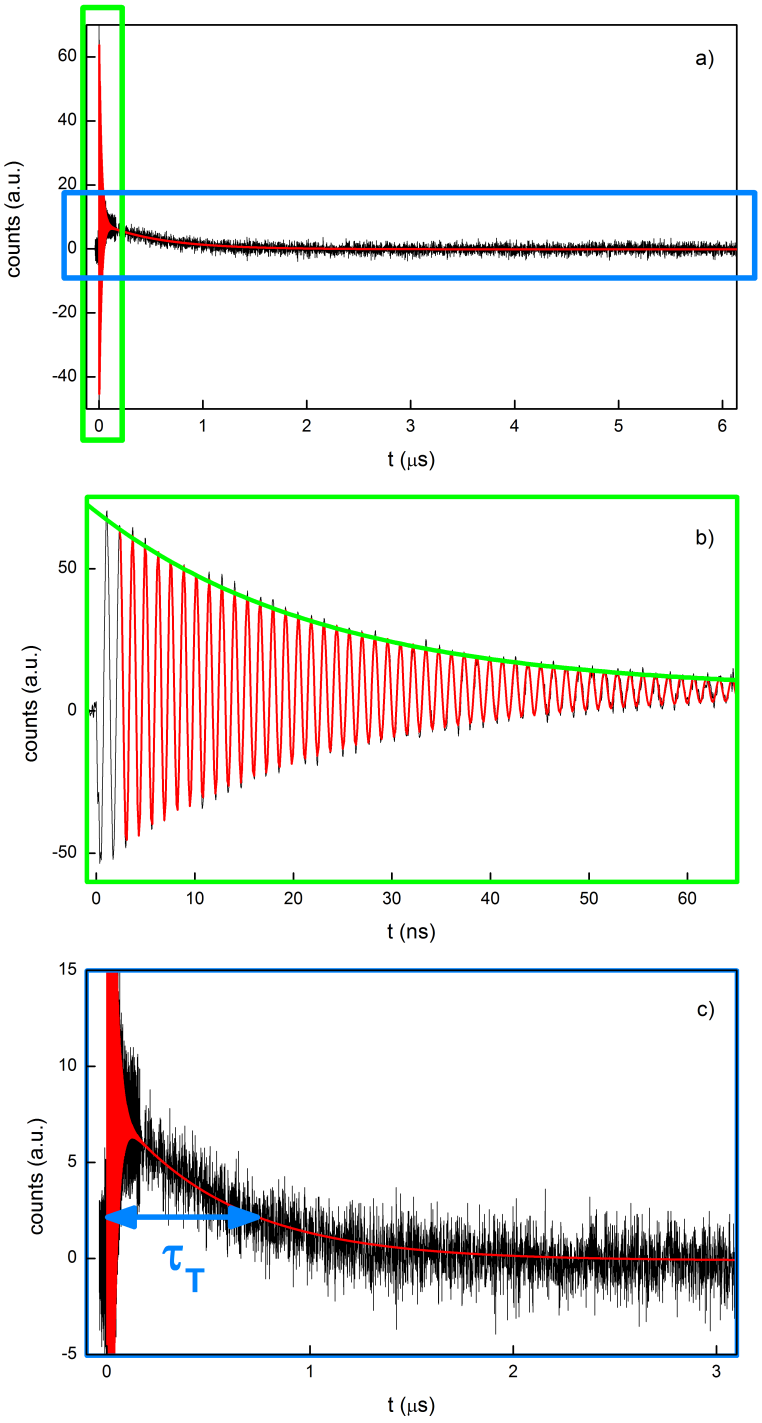

Figure 3.4: a) A typical HD-TG spectrum of acetonitrile in the hydrodynamic limit at T=308 K. The one shown in the figure was obtained with a phase mask with a pitch of $\Lambda = 2\pi/Q = 1.61\mu m$, 100 fs-pulsed pump beams at 800 nm, cw laser probe beam at 400 nm. Two main dynamical features can be distinguished at short and long delay times. The faster dynamic process (panel b)) is related to the acoustic mode evolution and consisting in a damped oscillation, the slower dynamics (panel c)) is an exponential decay due to the thermal relaxation.

As it is possible to see from panel a) the TG signal starts when the time delay between the pumps and the probe is 0 and it shows some dynamics up to the μs timescale. In particular, we can distinguish two main features in such kind of TG spectra: a faster signal modulation in the ns timescale, highlighted with glow green box, and a slower relaxation, highlighted with the blue box. In panel b) we focus the attention on the faster dynamics: the spectrum results in a damped oscillation, as predicted by the hydrodynamic model for the density fluctuations. By the frequency of the oscillation is possible to obtain the information about the adiabatic speed of sound, while the damping represents the lifetime of the acoustic excitation. Panel c) shows the long time dynamic range: the spectrum is well modeled by an exponential decay with a characteristic time $\widetilde{\tau}_T$, describing the thermal relaxation. To quantitatively estimate the physical parameters, we fitted, using the Levenberg-Marquardt algorithm, the whole spectrum with a simplified expression of eq. 2.16:

$$F(Q,t) = Ae^{-t/\tau_G}\sin(c_sQt+\phi) + Be^{-t/\widetilde{\tau}_T} + C \tag{3.1}$$

where $\tau_G = \Gamma Q^2$ and $\widetilde{\tau}_T = D_T Q^2$ [1]. c_s is the adiabatic speed of sound, ϕ is a phase constant to take into account the electrostriction contribution (see sec.1.2.2), A,B and C are amplitude constants. As already discussed in section 2.2.4, the thermal relaxation process is so slow that in the hydrodynamic limit (i.e. low Q-region as the one exploitable with visible TG technique) does not occur any effective heat exchange within the acoustic cycle and, therefore, the system can be considered at constant entropy (i.e. in its adiabatic regime). From the angular frequency of the oscillating feature (ω_s) one hence obtains the adiabatic speed of sound $c_s(T) = \omega_s(T)Q$. Fig.3.5 reports the temperature dependence of c_s compared with the ultrasonic data available in literature [77]. Considering that a small uncertainty is due to the temperature calibration in our experiment, the two set of data are in agreement within the error bars; thus, we can suppose that no relaxation processes are active in the (Q,ω)-range in between the (mm^{-1}, MHz)-range probed by US and the $(\mu m^{-1}, GHz)$-range accessed by TG. Consequently, we can regard the information gained by TG as concerning the the $Q \to 0$ hydrodynamic limit. Thanks to the obtained c_s measurements, we can now find the heat capacity ratio (γ) temperature dependence. As well known $\gamma = c_P/c_V$, where c_P and c_V are respectively the heat capacity at constant pressure and at constant volume. While it is very common to extract c_P values for a medium by calorimetric measurements and a lot of datasheets are available in literature [78, 79, 80, 81], it is not so easy to find the c_V parameters tabulated because of difficulty to directly measure them. For this reason we used the following relation between c_P and c_V [82, 79]:

$$c_V = c_P\frac{k_s}{k_T} \tag{3.2}$$

where k_s and k_T are the isentropic and the isothermal compressibilities and are

[1] We would like to recall the reader that this is not exactly the same quantity we introduced in eq.2.71 and eq.2.82, but because of the strong similarity we decided to call it $\widetilde{\tau}_T$

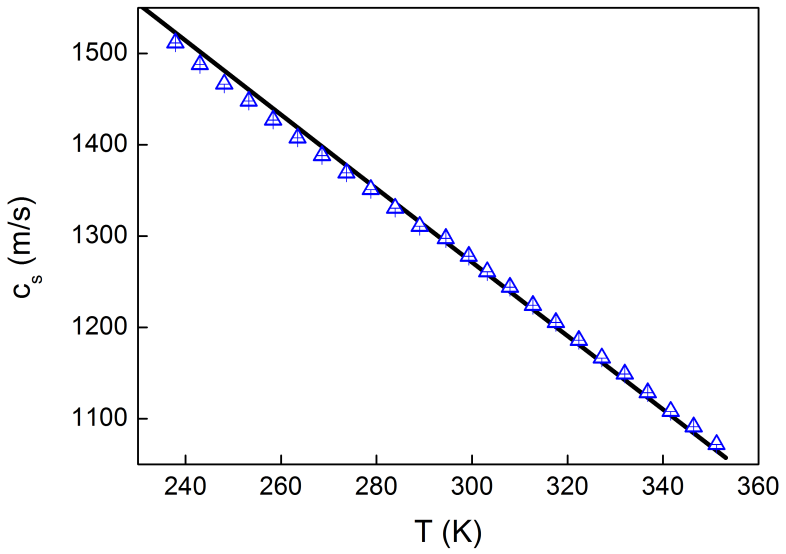

Figure 3.5: Trend of adiabatic speed of sound in temperature. Empty triangles are the data point arising from the TG measurements, while the straight line is obtain from the US studies by Niepmann [77]. The two trends are in agreement within the errorbars, we can therefore consider our TG measurements equivalent to the $Q \to 0$ limit domain.

related each other as follows:

$$k_s = (c_s^2 \rho)^{-1} \tag{3.3}$$

$$k_T = k_s + \alpha^2 \frac{T}{\rho c_P} \tag{3.4}$$

where ρ is the mass density of the medium, α the isobaric thermal expansivity and T the temperature of the system. Despite α and k_T have usually a low T-dependence in proximity of room temperature [81], in the following we will explicitly consider such dependencies. Combining eq.3.2 and eq.3.3 it is easy to obtain the expression for the heat capacity ratio:

$$\gamma(T) = 1 + \alpha(T)^2 \frac{T c_s(T)^2}{c_P(T)} \tag{3.5}$$

At this point the only quantity for which the T-dependency is unknown is $\alpha(T)$. We can obtain it through the definition of α:

$$\alpha(T) = \left(\frac{\partial \log V}{\partial T}\right)_P = V^{-1}\left(\frac{\partial V}{\partial T}\right)_P = -\left(\frac{\partial \log \rho}{\partial T}\right)_P = -\rho^{-1}\left(\frac{\partial \rho}{\partial T}\right)_P \tag{3.6}$$

Using the tabulated values for the density as a function of temperature (we used the data from the Dortmund Data Bank (DDBTS)[2]) we can finally calculate the

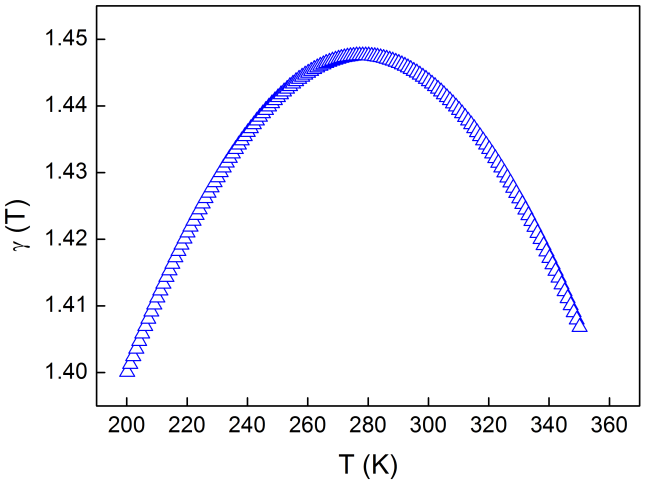

Figure 3.6: T-dependency of the heat capacity ratio γ calculated by TG estimated adiabatic speed of sounf c_s.

T-dependency of the heat capacity ratio. The other dynamic phenomenon we could

gain information on, thanks to the HD-TG measurements, is the thermal relaxation process. In fig. 3.7 we present the values of $\widetilde{\tau}_T$ obtained from the fitting procedure. From this observable can be derived other two quantities: the thermal diffusivity D_T and the thermal conductivity $\lambda = D_T \rho c_P$. For our following aims the quantities of major interest will be the thermal diffusivity and the thermal relaxation time (they are the parameters present in the memory function expression (eq. 2.82)). Unfortunately both of these two quantities are quite rare to be found in literature, while for the thermal conductivity a lot of reference literature exists [83, 84, 85, 86] to make a comparison with our result. In fig. 3.8 and fig. 3.9 the thermal diffusivity and the thermal conductivity are shown. Considering the three different representations, it is evident that in literature there is not a general consensus about the estimation of the thermal conductivity, hence leading to very different T-dependencies both for the thermal conductivity and the thermal relaxation. In this panorama our experiment seems to confirm the measurements reported in the ESDU database. Actually, because our measurements cover a wider range in temperature than the literature's ones, we can obtain a quite different result, especially at high temperature, with respect to one deduced by an extrapolation of the database data. We also notice that our result seems to contradict the one obtain by Lei and coworkers [86] who developed a general model for the thermal conductivities of organic solvents. In their paper they declared a good agreement with the ESDU dataset, but actually they could have a comparison only in the small region around the room temperature. We therefore believe that, as a side result, our data can contribute to definitely characterize the thermal conductivity of acetonitrile.

[2]http://www.ddbst.com/en/EED/PCP/DEN_C3.php

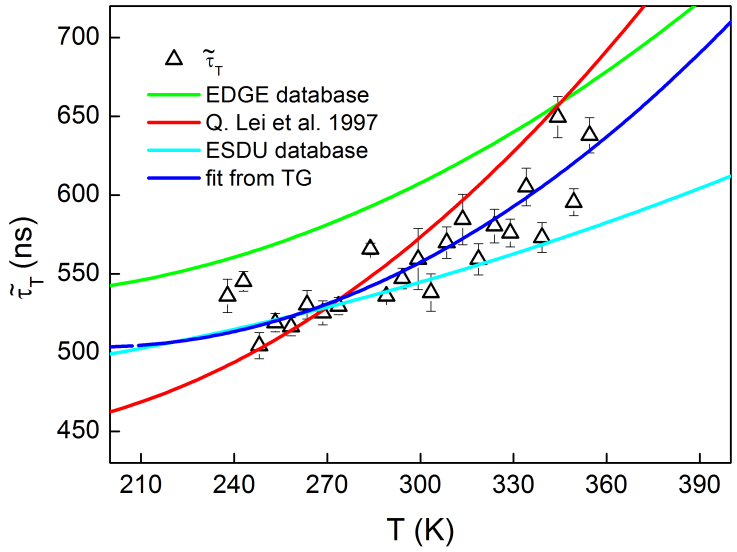

Figure 3.7: In empty triangles are reported the experimental values for $\tilde{\tau}_T$. The blue line is a polynomial fit through such points. The other lines are obtained from the thermal conductivity data available in ESDU database[a] (green line), EDGE database (cyan line) and ref.[86] (red line). See the legend in the graph.

[a] http://www.engineersedge.com/heat_transfer/thermal_conductivity_of_liquids_9921.htm

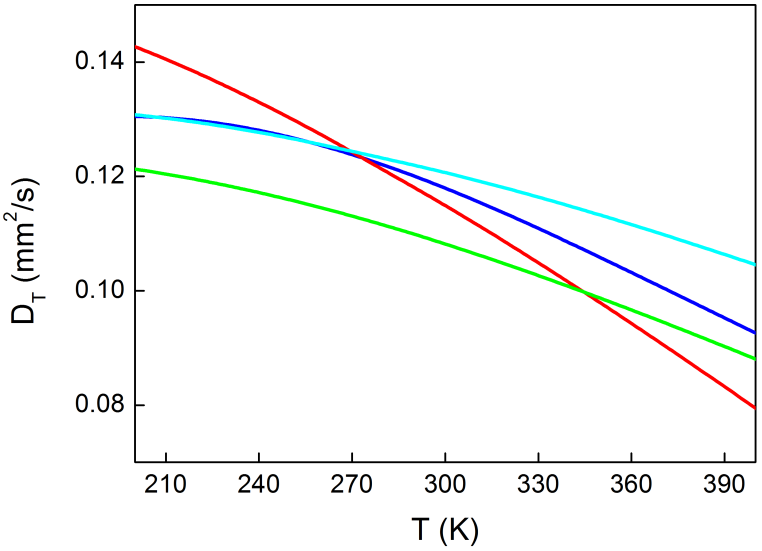

Figure 3.8: Comparison between the thermal diffusivity quantity deduced by the fit of our experimental data (blue line) and the literature ones. Colors are the same of fig.3.7.

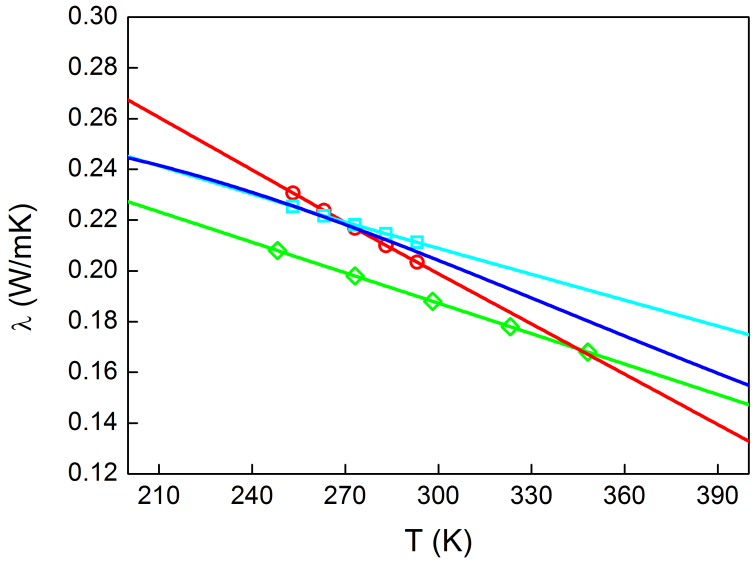

Figure 3.9: Comparison between the thermal conductivity quantity deduced by the fit of our experimental data (blue line) and the literature ones. Colors are the same of fig.3.7.

3.4 The vibrational relaxation

As already anticipated at the beginning of this chapter, acetonitrile is characterized by many different kind of dynamical processes, ranging from the ns timescales (thermal relaxation) to the fs one. In this section we are going to discuss about an intriguing dynamics occurring in the few ps range, already observed by Sassi and coworkers [21] through a BLS experiment in the visible domain. They found out that in the observed spectral region the liquid presents an intramolecular vibrational channel to dissipate the excess of energy induced by the acoustic perturbation. Basically, part of the energy of the acoustic mode is used by the molecules to stimulate vibrations of some chemical bonds within the molecule. Such process is commonly classified as a Kneser type relaxation [87]. Sassi and coworkers identified that the leading vibrational mode involved in such relaxation is the one related to the CCN bending. Though the observed phenomenon is quite evident in their work to be merely addressed to some artifact in the measurements, some critical points have to be carefully considered. Indeed, some of the parameters that they obtained from the fitting of their BLS spectra are not in accordance with the ones obtainable with other experimental techniques (e.g. the low-frequency adiabatic speed of sound is inconsistent with ultrasonic reference data). Furthermore they limit the investigation to temperatures higher than 273 K, while it could be interesting to extend such a study to lower temperatures to verify if the dynamics is really reaching a minimum around 273 K, as one may guess from their data. To our knowledge, this work is one of the few works (not to say the only one) reported in literature in which the angle tunability in a BLS experiment was used. However, any particular care to account for spurious contributions arising from the finite aperture of the collective

optics (see Sec.1.1.1) was adopted. This could be the reason for the aforementioned discrepancy in the estimate of the adiabatic sound velocity; the determination of the other dynamic parameters could be affected as well. This work thus represent a useful reference to evaluate the effectiveness of our masks filtering approach in angle-tunable BLS experiments.

In the following we present the results obtained studying liquid acetonitrile in the whole temperature range (240-335 K) of the liquid phase, done by using the experimental setup described in Sec.1.1.1. Fig.3.10 shows a BLS spectrum of acetonitrile.

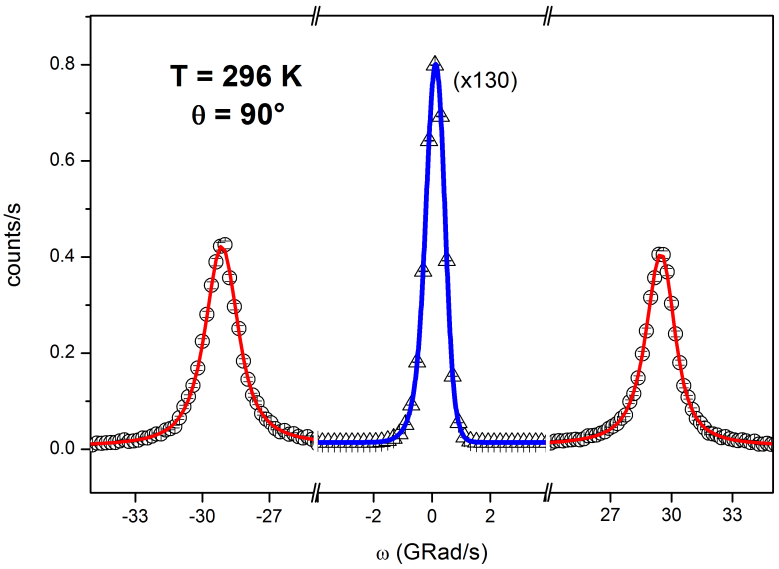

Figure 3.10: In figure is shown a typical spectrum obtained with our angle-tunable BLS setup. The one presented here is obtained with the 90° *geometry configuration and a mask bandwidth of* $\Delta_Q = 0.1\ \mu m^{-1}$ *at T=296 K. The presence of the mask is at the origin of the relatively low count rate. The spectrum presents the well known two side Brillouin peaks from which it is possible to extract the information about the acoustic modes evolution. In the present case, since we are in the hydrodynamic limit, we could profitably fit the data with the simple DHO model (red lines). The central feature of the spectrum is the instrumental response function (blue line is just a guide for eyes) which was obtained by the elastic scattering of a roughened aluminum plate.*

The two symmetric side peaks are clearly recognizable and, through a fitting procedure based on a damped harmonic oscillator (DHO) model, we extracted the values of the angular frequency shift (ω_{LA}) and linewidth (Γ_{LA}). In the following we will use such parameters to make an elastic modulus (M) analysis (see eq. 2.27-2.28). For the moment let's limit our considerations to the observed speed of sound ($c_L = \omega_{LA}/Q$) obtained in backscattering geometry ($\theta = 180°$) in the whole range of temperature. In Fig. 3.11 is reported the comparison of the temperature dispersions of the speeds of sound in the adiabatic regime (open black circles), obtained by HD-TG measurements (we have already shown the equivalence with US measurements in Fig. 3.5),

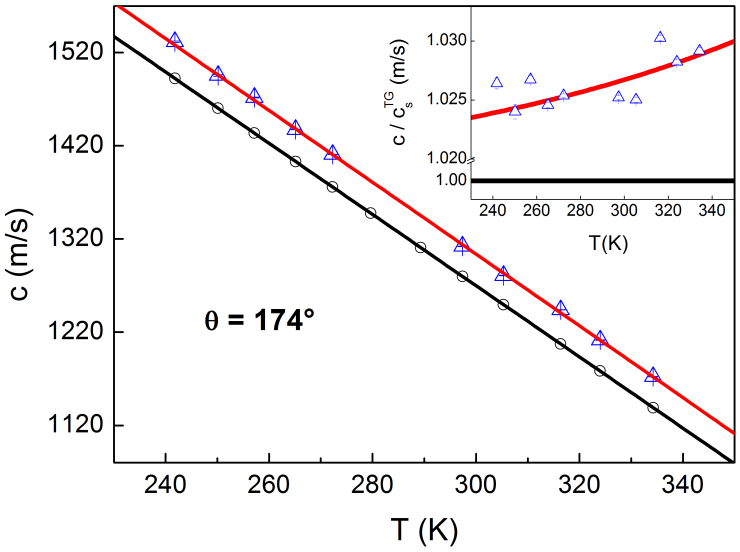

Figure 3.11: In open blue triangles are reported the measured speed of sound with the backscattering geometry configuration. Red line is the linear fit through such points. At a first look the temperature dispersion of the acoustic mode velocity seems to have the same angular coefficient of the one measured by the TG in the adiabatic regime (black open circles). (Inset) Here it is reported the ratio between the two linear dispersions c_L/c_s. This view highlights a weak temperature dependence of the sound speed ratio, fingerprint of the occurring Kneser relaxation process.

and the ones obtain in the present BLS experiment (open blue triangles). Differently to Fig. 3.5, it is now evident that BLS is measuring acoustic velocities different by those measured with TG and US spectroscopies. This is the fingerprint of an occurring relaxation in the spectral window between the one accessible by TG and that probed by BLS. We can infer something more by this plot: at a first look the two dispersions look like to have the same angular coefficient but a closer look reveal a weak temperature dependence of the velocities ratio. In red line in the inset of Fig. 3.11 is the ratio between the two linear fits of the temperature dependence of the sound velocities data (red and black line in the main plot). It possible to notice how the higher is the temperature and the larger is the deviation of the velocity measured by BLS and that measured by TG. Despite the phenomenon is not so pronounced, it is possible to argue something about the temperature behavior of the relaxation. As we have already said in the introduction, when a relaxation phenomenon is occurring in the system at a certain temperature it reveals its presence in a ω-dispersion of the acoustic velocity. The inflection point of such a "S-shaped" velocity dispersion identifies an angular frequency which is comparable to the inverse of the characteristic relaxation time. Changing the temperature of the system it is reasonable to expect that, because of the changes of the thermodynamic conditions, the dynamics of the relaxation will be somehow affected. Depending on the origin of the relaxation, heating up the system we can observe an increase or a decrease of the

relaxation time, reflecting in a shift of the inflection point of "S-shaped" velocity dispersion to lower or higher angular frequencies, respectively. The former is the case of the vibrational Kneser-type relaxation, whose behavior is depicted in fig. 3.12. Following such rationale we will try to qualitative explain the result showed in the

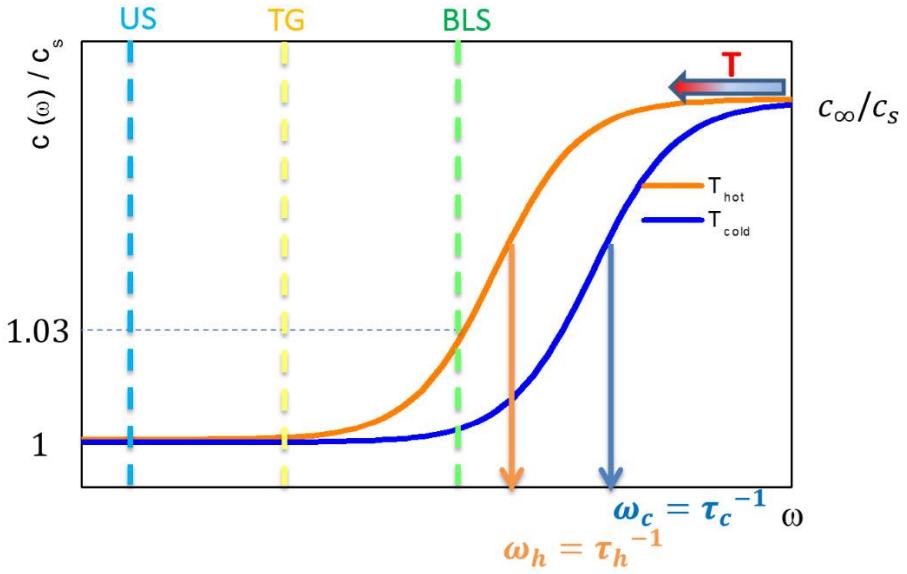

Figure 3.12: Sketch of the typical "S-shaped" dispersion of the acoustic speed of sound when a relaxation is occurring in the system. In particular here it is pictured the behaviour of the acoustic velocity dispersion in presence of a so called Kneser relaxation. Heating up the system, the "S-shape" moves from high angular frequency domain (blue line) to the lower one (orange line), resulting in an increasing of the characteristic time of the relaxation. In the drawing are also represented with vertical dashed lines the spectral region accessible by ultra-sound (US), transient-grating (TG) and BLS spectroscopies. In the case of cold temperatures, all the three spectroscopic techniques will probe the low frequency tail of the relaxation. Heating up the system, the relaxation starts to "enter" in the BLS spectral window. Thus, while US and TG, will continue to measure the same value for the speed of sound (the tail of the relaxation), BLS starts to probe the rising up of the velocity dispersion.

inset of Fig. 3.11. Vertical dashed lines in Fig. 3.12 sketch the spectral regions in which US, TG and BLS spectroscopies can probe the acoustic mode evolution. At low temperature (blu line in the plot) these three techniques could measure almost the same values of the speed of sound. In such a case just the left tail of the relaxation (at most) should be appreciated. When the temperature of the sample is raised, the relaxation time increases and hence the velocity dispersion "moves" towards lower angular frequencies; now BLS starts to be more sensitive to the rising up of the velocity, while US and TG are still probing only the low frequency (fully relaxed) tail of the relaxation. Thus, what we can expect is that in the BLS range the ratio between the probed velocity and the adiabatic one will increase on increasing the temperature of the liquid. This is exactly what we can observe in the inset of Fig. 3.11. To give a quantitative characterization of such Kneser relaxation,

we performed for each temperature a set of measurements at 6 different scattering angles in order to map the velocity dispersion from the adiabatic speed of sound c_s to the upper limit velocity named c_∞^{BLS} as a function of the angular frequency. As anticipated above, we use in this section the formalism of the complex elastic moduli (M^*) introduced in chap. 2. We briefly recall here Eqs. 2.27-2.28 relate the real and imaginary part of the elastic modulus to the Brillouin frequency position and width:

$$M'(\omega_{LA})/\rho = (\omega_{LA}/Q)^2 = c_L^2$$
$$M''(\omega_{LA})/\rho = \omega_{LA} \cdot \Gamma_{LA}/Q^2 = M' \cdot \Gamma_{LA}/\omega_{LA}$$

In Fig. 3.13 are reported real and imaginary parts of the elastic modulus for some representative temperatures. To extract the information about the relaxation from these dispersions curves, we use the simplest expression for M^*. i.e.:

$$M^*(\omega) = M_\infty + \frac{M_0 - M_\infty}{1 + i\omega\tau_\nu} \tag{3.7}$$

from which:

$$M'(\omega) = M_0 + (M_\infty - M_0)\frac{\omega^2\tau_\nu^2}{1 + \omega^2\tau_\nu^2} \tag{3.8}$$

$$M''(\omega) = (M_\infty - M_0)\frac{\omega\tau_\nu}{1 + \omega^2\tau_\nu^2} \tag{3.9}$$

where τ_ν is the characteristic time of the relaxation process and $M_\infty = (c_\infty^{BLS})^2$; M_0 is the low-frequency limit of the elastic modulus and was fixed in the fitting routine to the square of the adiabatic speed of sound (c_s^2) measured in our TG experiment. As can be immediately seen from eqs. 3.8, the quantities M' and M'' are strongly coupled, therefore in our Levenberg-Marquardt routine we fitted at same time both the real and imaginary part. The results of the fit are shown in the plots as red lines. As a general comment to the figure, it is evident that the ω-dispersion of M' starts from the adiabatic regime (M_0) and raises up to higher values. As it can be noticed the relaxation is not fully within the spectral window accessible by BLS, more specifically, by looking at the imaginary parts of the moduli, it seems that the maximum value (corresponding to the inflection point of the velocity dispersion) is reached at the edge of this spectral range. Since in correspondence of such maximum the relaxation time equals to inverse of the angular frequency, we are confident that the probed spectral window is wide enough to correctly estimate the relaxation parameters. In Fig. 3.14 are reported the values for c_∞^{BLS} (open blue triangles) as a function of T, as obtained from our fitting procedure. They show a linear trend in temperature and, as already commented, their values are almost twice bigger than the ones showed in Fig. 3.11 for the backscattering case, which means that the velocity dispersion induced by the Kneser relaxation has almost reached its inflection point towards the upper limit of the BLS window. Finally we show in Fig. 3.15 the obtained temperature dependence of the relaxation time (τ_ν). It ranges from 15 to 30 ps and, as previously observed, it becomes slower on increasing the temperature, a trend typical of Kneser-type relaxations. To conclude this section we compare our results with those obtain in the quoted reference work of Sassi et al. They found

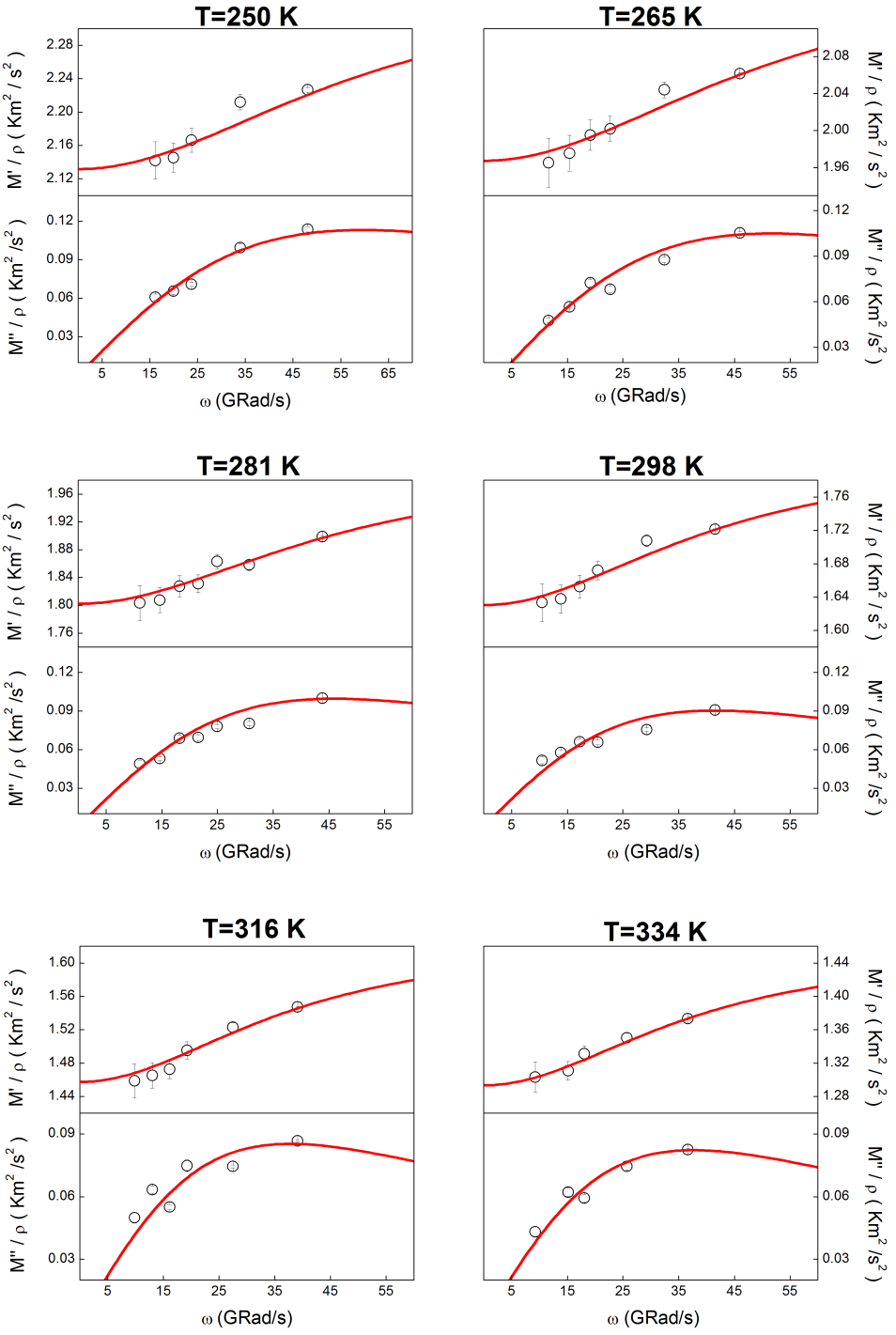

Figure 3.13: Real and imaginary part of the measured elastic modulus for some representative temperatures, plotted as a function of the Brillouin frequency. In red lines the fit functions obtained fixing the low frequency momentum $M_0 = c_s^2$.

values for the relaxation times almost twice bigger than our determinations, which can be due to the fact they left as a free parameter in the fit also the low-frequency speed of sound. Basically they estimated the values of three parameters using seven

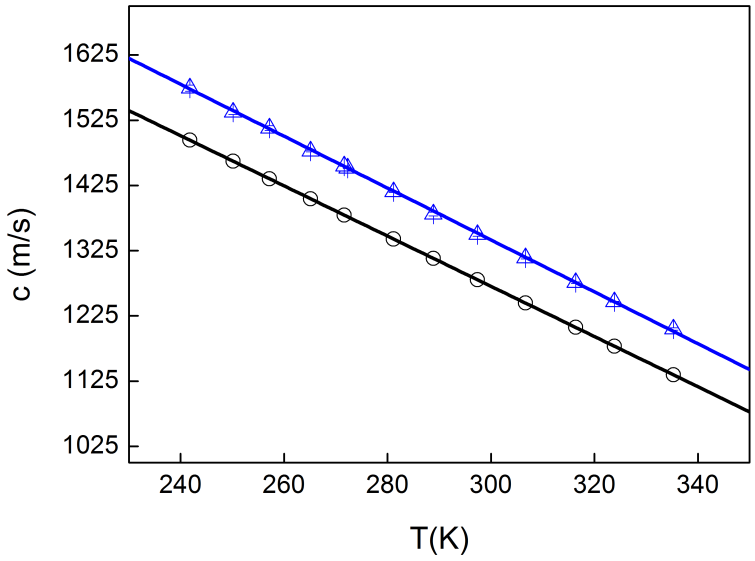

Figure 3.14: The c_∞^{BLS} parameter as a function of T obtain from our fits (open blue triangles) compared to the TG adiabatic speed of sound c_s (open black circles).

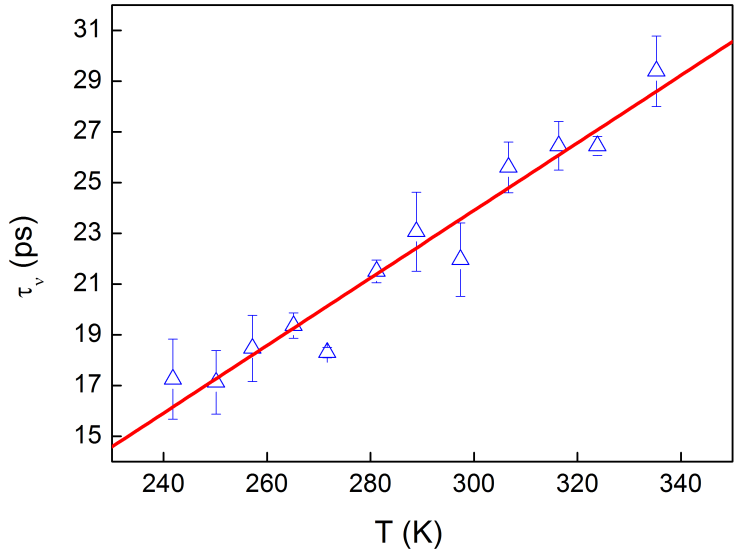

Figure 3.15: The Kneser relaxation time is shown in the figure. Despite its not so strong temperature dependence, it shows a very clear linear ascending trend from lower to higher temperatures. This kind of dependency with T it's proper of such vibrational relaxation processes.

experimental points and, as already stated, the values that they obtained are not in accordance with the speed of sound measured by US methods. This is one of the first evidence of the usefulness of combining different techniques from different

spectral range: we indeed used the TG measurements to verify that any velocity dispersion occur below the BLS range and, furthermore, we could reduce from three to two the number of free parameters in our fitting procedures.

Another possible source of issues is the possible effects of spurious contributions due to the finite aperture of the collection optics. We actually do not know if they took care about that, but it could be a possible explanation for the observed increase of τ_ν's at low temperatures. Additionally, we do not observe any local minimum in proximity of 273 K. We discussed, indeed, that at low temperatures the relaxation starts to move to the high frequency range, *de facto* going outside the BLS spectral window which, at that point, can probe only the low-frequency tail of the relaxation where the velocity dispersion is not so pronounced. As we have seen in Sec. 1.1.1, if one does not take care to limit the spurious contributions when BLS spectra are collected far from the backscattering, then this results is an artificial broadening of the Brillouin peaks and (in practice) to an "effective" deterioration of the instrumental resolution. Therefore, since at low temperature BLS is probing the low-frequency dispersive tail of the relaxation, it could not be able to discriminate anymore such a small velocity dispersion and thus to correctly estimate the relaxation time.

The obtained result of this temperature trend for the relaxation time, suggest that there is not any correlation between such Kneser dynamics and any local modification or destruction of the liquid structure. The latter is known to be related to the viscosity of the system which has usually the opposite trend in temperature of the one observed for τ_ν. In order to further investigate if there is or not any coupling between the vibrational and the structural degrees of freedom, in the next section we will characterize the so called structural relaxation which describe the dynamics of the translational degree of freedom of the system.

3.5 The structural relaxation

In Sec. 2.2.5 we have discussed the nature of such relaxation process, termed also "α-relaxation" because of its huge strength compared to the others. In liquids this relaxation usually evolves at faster timescale ($\approx ps$ and below). This time window is different from both the already explored ones in the cases of thermal and vibrational relaxation. To probe the structural relaxation by using acoustic modes we have to move in the kinematic plane of the available techniques (see Fig. 5) up to the high-Q/high-ω region, that is the realm of the inelastic hard X-rays and thermal neutron scattering (see Sec. 1.1.2).

3.5.1 IXS experiments

In this section we are going to present the results obtained from the experiments performed at ID-28 (@ESRF, Grenoble, France) and XBL-35 (@SPring-8, Riken, Japan) user beamlines dedicated to the IXS. Combining the data collected during these experiments we explored the acoustic modes evolution in the THz frequency

range at several Q-values, ranging from 2 to 12 nm^{-1}, and at 7 different temperatures (spanning the whole liquid phase of acetonitrile). In Fig. 3.16 is shown a characteristic IXS spectrum. As it is immediately evident, already at a first glance this spectrum looks extremely different from the ones measured by BLS. In particular, it is no longer possible to clearly isolate the Brillouin peaks, they can be appreciate in log scale as like two shoulders over an overwhelming quasi elastic peak centered at zero frequency. This is due the fact that IXS spectra are measured in a Q-region much closer to the position of the first maximum ($Q_{max} \approx$ Å^{-1}) of the static structure factor $S(Q)$. In other words, it means that the characteristic length-scale probed by IXS is approaching the molecular dimension and hence the observed dynamics is no more ascribable to a macroscopic collective response, at least not up to the same extend of the BLS case. In this "mesoscopic region" it is no longer appropriate to apply the classical hydrodynamic approach and a lineshape analysis of the spectrum using, e.g., the memory function formalism developed in Sec. 2.2 is needed to extract information on the dynamics. In eq. 2.82 we have proposed an

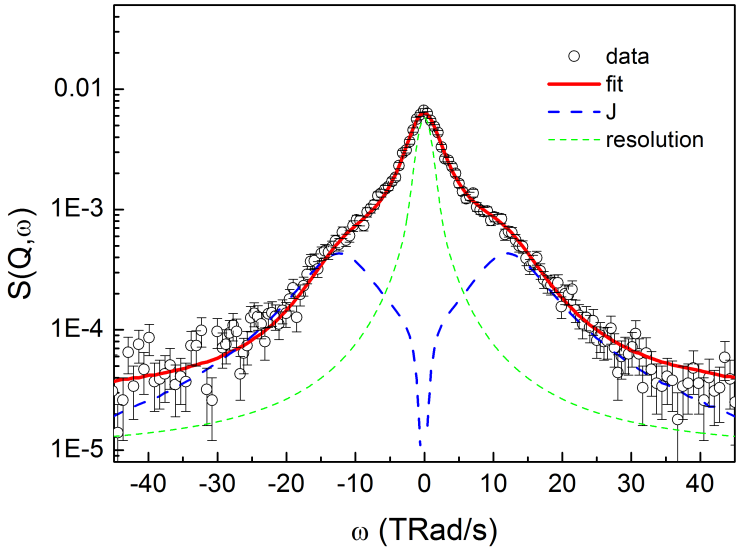

Figure 3.16: A typical IXS spectrum (black open circles) obtained at T=300 K with Q=6.56 nm^{-1} is shown in the figure. As immediately observable, the shape of the $S(Q,\omega)$ is quite different from the one we have already seen in the case of BLS. At this high-Q values it is no more possible to describe the spectrum with the hydrodynamic laws but a lineshape analysis is necessary. The red line is the best fit obtained with the formalism of memory functions. The blue line is the so called current of the spectrum, whose maxima identify roughly the frequency shift of the inelastic peaks. Finally in dashed green line is represented the instrumental response function.

expression for the memory function that takes into account all the relevant relaxation processes occurring in the system. We can further simplify such an expression by neglecting the contribution of the vibrational relaxation, whose amplitude (see the previous section) was found to be much smaller (< 10 %) with respect to the

one of the structural relaxation (see further below). In order to be consistent with previous IXS works, in the data analysis we formally rewritten the α-relaxation contribution to the memory function in terms of the so-called compliance relaxation time ($\tau_\alpha^c = (c_\infty^{IXS}/c_s)^2\tau_\alpha$). The memory function used to fit our IXS data is hence:

$$m_L(Q,t) = Q^2\left(1-\frac{1}{\gamma}\right)\frac{c_s^2}{S(Q)}e^{-D_T Q^2 t} + Q^2\left((c_\infty^{IXS})^2 - \frac{c_s^2}{S(Q)}\right)e^{-\frac{(c_\infty^{IXS})^2}{c_s^2}\frac{t}{\tau_\alpha^c}} + 2\Gamma_\mu\delta(t) \tag{3.10}$$

In spite of the mentioned simplifications, such functional form is still quite complex and presents too many parameters to fit the quite structureless IXS spectra. To reduce the number of free parameters we profitably used the results from our TG-HD experiment, thus fixing the values of c_s, D_T and γ in eq. 3.10 to the ones described in Sec. 3.3. Another quantity we need to know before going on with the fitting procedure is the static structure factor $S(Q)$.

The static structure function S(Q)

In the case of N identical classical particles it is well known that the $S(Q)$ can be regarded as the Fourier transform of the radial distribution function, $g(r)$, of the particles in the system [60], thus reflecting the structural properties of the system. If the $S(Q)$ for such simple systems can be directly measured with an X-ray or neutron diffraction experiment, this is not the case of molecular compounds. In the latter case, the $S(Q)$ can be viewed as the combination of all the intermediated contributions arising from the different species composing the material. Because of the heterogeneity of the atomic species present in molecular systems, each partial contribution needs to be weighted by a particular coefficient depending on the atomic electron distribution (in the case of X-rays diffraction) or on the atomic neutron scattering cross section (in the case of neutron diffraction). Thus, the only one way to obtain the pure $S(Q)$ shape without any correction depending by the used experimental technique, is using molecular dynamic (MD) simulations, able to compute all the different contributions of the different atomic species.

In this section we first recall the equations to correctly compute the $S(Q)$ once the spatial correlation functions are known from MD simulations.

Let's start to write the particle density of the system as $\rho(\underline{r}) = \sum_i \sum_\alpha \delta(\underline{r} - \underline{r}_{i\alpha})$ and it's Fourier counterpart in the reciprocal space $\rho_{\underline{Q}} = \sum_i \sum_\alpha e^{-\imath\underline{Q}\cdot\underline{r}_{i\alpha}}$, where $\underline{r}_{i\alpha}$ is the spatial vector pointing at the α^{th} particle of the i^{th} molecule. For a liquid composed by N molecules of n particles each, we can define the static structure factor as:

$$S(Q) = \langle\frac{1}{n^2N}\rho_Q\rho_{-Q}\rangle = \langle\frac{1}{n^2N}\sum_\alpha\sum_\beta\sum_i\sum_j e^{-\imath\underline{Q}\cdot(\underline{r}_{i\alpha}-\underline{r}_{j\beta})}\rangle \tag{3.11}$$

dividing the intramolecular contributions ($i = j$) by the intermolecular ones ($i \neq j$) we have:

$$S(Q) = \langle\frac{1}{n^2N}\sum_{\alpha\beta i} e^{-\imath\underline{Q}\cdot(\underline{r}_{i\alpha}-\underline{r}_{j\beta})}\rangle + \langle\frac{1}{n^2N}\sum_{\alpha\beta i}\sum_{j\neq i} e^{-\imath\underline{Q}\cdot(\underline{r}_{i\alpha}-\underline{r}_{j\beta})}\rangle \tag{3.12}$$

For a monoatomic liquid we could define

$$\rho g(\underline{r}) = \langle \frac{1}{N} \sum_i \sum_{j \neq i} \delta(\underline{r} - \underline{r}_j + \underline{r}_i) \rangle \tag{3.13}$$

which can be generalized as follows

$$\rho g_{\alpha\beta}(\underline{r}) = \langle \frac{1}{N} \sum_i \sum_{j \neq i} \delta(\underline{r} - \underline{r}_{j\beta} + \underline{r}_{i\alpha}) \rangle \tag{3.14}$$

The Fourier transform of the eq. 3.14 gives:

$$\int \rho g_{\alpha\beta}(\underline{r}) e^{-\imath \underline{Q} \cdot \underline{r}} \mathrm{d}\underline{r} = \langle \frac{1}{N} \sum_i \sum_{j \neq i} e^{-\imath \underline{Q} \cdot (\underline{r}_{i\alpha} - \underline{r}_{j\beta})} \rangle \tag{3.15}$$

thus the intermolecular contribution in eq. 3.12 can be written as

$$\begin{aligned} S(\underline{Q})^{INTER} &= \frac{1}{n^2} \rho \sum_{\alpha\beta} \int g_{\alpha\beta}(\underline{r}) e^{-\imath \underline{Q} \cdot \underline{r}} \mathrm{d}\underline{r} = \frac{1}{n^2} \rho \sum_{\alpha\beta} \int \left[g_{\alpha\beta}(\underline{r}) - 1 \right] e^{-\imath \underline{Q} \cdot \underline{r}} \mathrm{d}\underline{r} = \\ &= \frac{1}{n^2} \sum_{\alpha\beta} \left[S_{\alpha\beta} - 1 \right] \end{aligned} \tag{3.16}$$

because of the isotropy in liquids the integral can be reduce in one dimension:

$$S_{\alpha\beta} - 1 = \rho \int_0^\infty \mathrm{d}r 4\pi r^2 \left[g_{\alpha\beta}(r) - 1 \right] \frac{\sin(\underline{Q} \cdot \underline{r})}{\underline{Q} \cdot \underline{r}} \tag{3.17}$$

The analogous expression for the intermolecular contribution in the case of X-ray diffraction, cab be obtained introducing the X-rays scattering form factors ($f_k(Q)$) as weights for each atomic k-specie:

$$S(Q)^{INTER-Xray} = \left(\sum_{k=i}^{n} f_k(Q) \right)^{-2} \sum_{\alpha\beta} f_\alpha(Q) f_\beta(Q) \left[S_{\alpha\beta}(Q) - 1 \right] \tag{3.18}$$

going back to eq. 3.12 we have now to evaluate the intramolecular contribution to the $S(Q)$. Let's start separating the "self" component ($\alpha = \beta$):

$$S(Q)^{INTRA} = \frac{1}{n} + \langle \frac{1}{n^2 N} \sum_{i\alpha} \sum_{\beta \neq \alpha} e^{-\imath \underline{Q} \cdot (\underline{r}_{i\alpha} - \underline{r}_{i\beta})} \rangle \tag{3.19}$$

defining

$$\rho g_{\alpha\beta}^{INTRA}(r) = \frac{1}{N} \langle \sum_i \delta(\underline{r} - \underline{r}_{i\alpha} + \underline{r}_{i\beta}) \rangle \tag{3.20}$$

and its Fourier counterpart

$$\int \rho g_{\alpha\beta}^{INTRA}(r) e^{-\imath \underline{Q} \cdot \underline{r}} \mathrm{d}\underline{r} = \frac{1}{N} \langle \sum_i e^{-\imath \underline{Q} \cdot (\underline{r}_{i\alpha} - \underline{r}_{i\beta})} \rangle \tag{3.21}$$

we can write

$$\begin{aligned} S(Q)^{INTRA} &= \frac{1}{n} + \frac{1}{n^2}\sum_{\alpha}\sum_{\beta\neq\alpha}\int \mathrm{d}\underline{r}\rho g_{\alpha\beta}^{INTRA}(\underline{r}) = \\ &= \frac{1}{n} + \frac{1}{n^2}\sum_{\alpha}\sum_{\beta\neq\alpha}\left[S_{\alpha\beta}^{INTRA}(Q) - 1\right] \end{aligned} \tag{3.22}$$

while in the case of X-ray diffraction we have to add again the form factors to the expression:

$$S(Q)^{INTRA-Xray} = \left(\sum_\alpha f_\alpha^2\right)\left(\sum_\alpha f_\alpha\right)^{-2} + \left(\sum_\alpha f_\alpha\right)^{-2}\sum_\alpha\sum_{\beta\neq\alpha} f_\alpha f_\beta \rho \int \mathrm{d}\underline{r} g_{\alpha\beta}^{INTRA}(\underline{r}) e^{-\imath\underline{Q}\cdot\underline{r}} \tag{3.23}$$

At this point we have all the instrument to compute the S(Q) from MD simulations and to compare them with experimental X-rays diffraction data.

Because of the wide usage of acetonitrile in chemistry and because of its relatively simple structure, a lot of computational models can be found in literature to mimic the structural characteristic of pure acetonitrile in liquid state. To our knowledge, the best force field proposed so far able to reproduce the main experimental thermodynamic properties of the liquid is the six-site model by Nikitin and Lyubartsev [88]. In collaboration with them, we made MD simulations to obtain the inter- and intramolecular radial distribution functions at the same thermodynamic conditions at which the IXS measurements have been performed. The simulation were carried out in the NPT ensamble at constant pressure of 1 bar and with 1024 particles inside the box.

As an example we report in fig. 3.17 the inter- and intramolecular radial distribution functions obtained using the aforementioned theoretical model. Before computing the S(Q) with the above equations, a last consideration has to be taken into account. We showed in this section that to obtain the S(Q) we have to calculate some Fourier transforms of the g(r)'s. At this point we face with longstanding issue of the finite size effects in MD simulations [89]. It is an intrinsic limit of the simulation technique that prevent the possibility to determine the g(r)'s over the limited range of $r \leq L/2$, where L is the size of cubic simulation cell. If this issue is not really problematic if one in interested in the localization of the maxima in the S(Q), it is really critical if the goal was to obtain the low-Q behavior of it as in our case. A lot of tricky and very complex methods are proposed in literature to overcome such finite size effects. For our aims to rescale the adiabatic speed of sound over the square root of the S(Q) a widely used filtering approach [90] in the Fourier transform computation seems to be quite satisfying. What it is necessary to do is to slightly change the expression in eq. 3.17 which has to be now written as:

$$S_{\alpha\beta} - 1 = \rho\int_0^{L/2} \mathrm{d}r 4\pi r^2 \left[g_{\alpha\beta}(r) - 1\right] \frac{\sin(\underline{Q}\cdot\underline{r})}{\underline{Q}\cdot\underline{r}} \frac{\sin(2\pi r/L)}{2\pi r/L} \tag{3.24}$$

where $\frac{\sin(2\pi r/L)}{2\pi r/L}$ is a Lorch type window function [91] to reduce the effect due to the finite cutoff of r. Following such method, we could finally calculate the $S(Q)$ for each temperature at which we performed the IXS experiments. In order to test

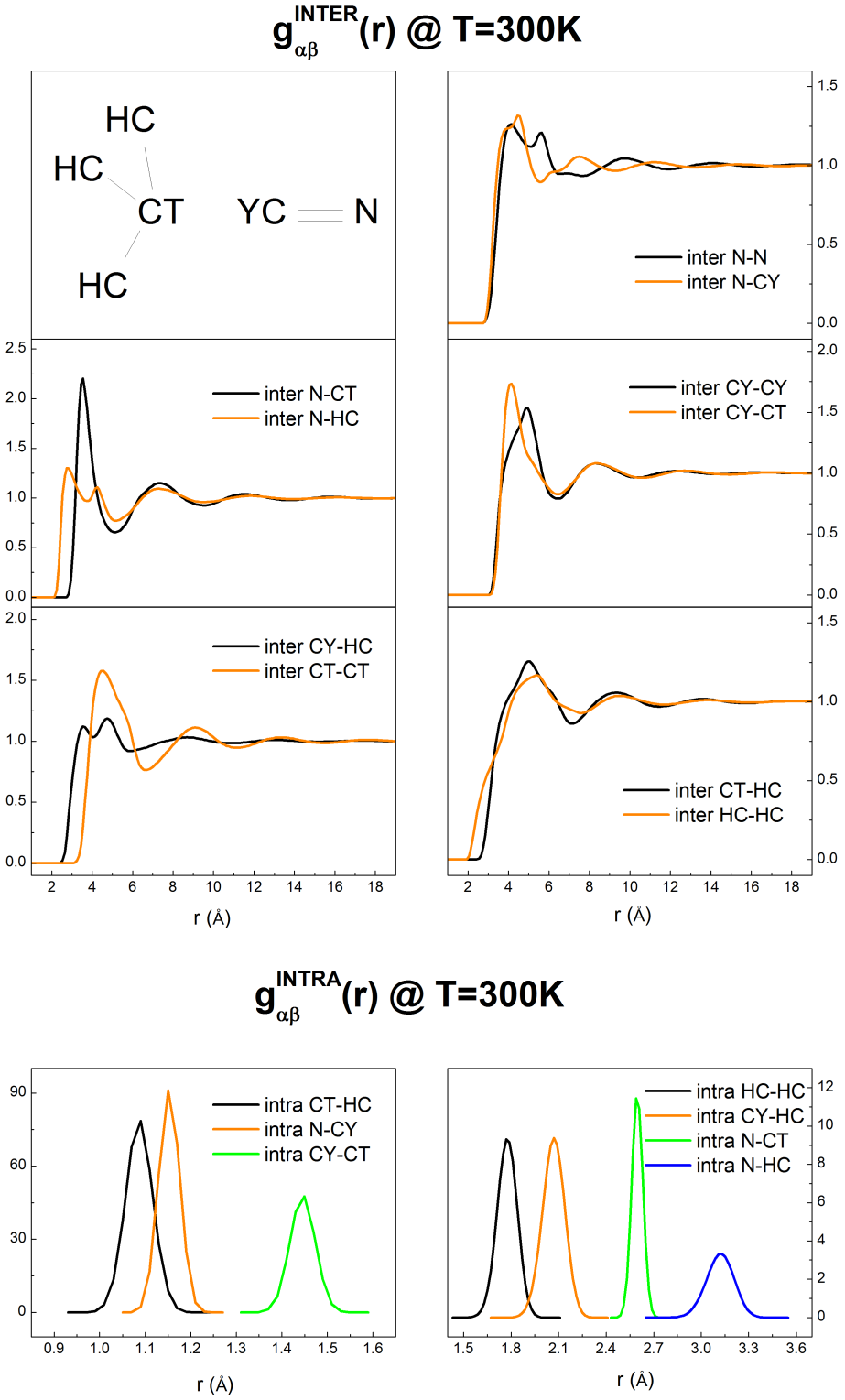

Figure 3.17: Radial distribution functions at T=300 K obtained by MD simulations using the six site model by Nikitin and Lyubartsev

the goodness of our simulated $S(Q)$, we calculated also the corresponding $S^{X-ray}(Q)$ which can be easier compared with the available literature. To calculate such X-rays functions, we made use of the tabulated values of the X-rays form factors available in literature [92][3]. As a further test we could measure at the IXS beamlines also the $S^{X-ray}(Q, \omega = 0)$, which is not, obviously, the static structure factor but at least the position of its maximum should to be similar to that one of the $S(Q)$. In Fig. 3.18 are reported, as an example, the calculated $S(Q)$ at T=300 K (green line), its "X-ray counterpart" (magenta line), a set of X-ray diffraction data points [93] obtained at a temperature similar to the ours, T=293 K, (starred points) and the measured $S^{X-ray}(Q, \omega = 0)$. As it is easy to recognize, all the three X-ray functions seem to share quite well the main peak position. Furthermore it's impressive the agreement between the calculated $S^{X-ray}(Q)$ and the experimental point considering that they are obtained at two different temperatures. We can therefore be confident that the calculated $S(Q)$ is correct and can be used to reduce the number of free parameters in the memory function expression for the lineshape analysis of the IXS spectra.

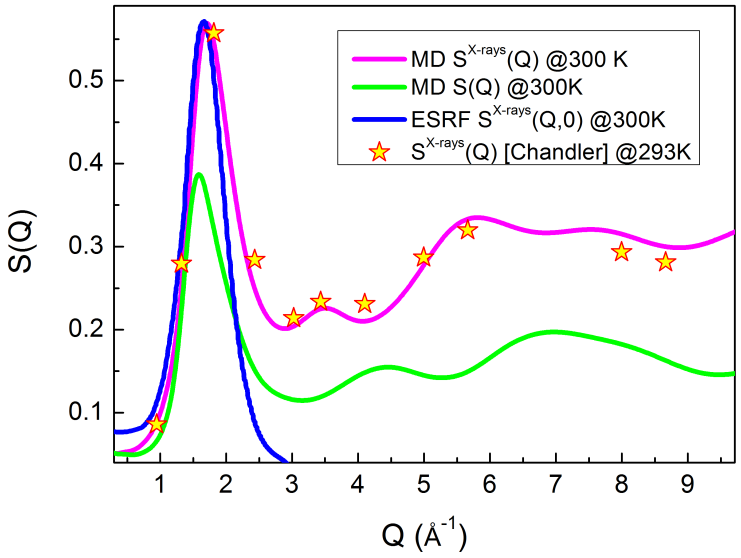

Figure 3.18: Here we report the comparison between our calculated S(Q)'s and some experimental measurements in order to confirm the goodness of our simulations. Because of the impossibility to measure directly the S(Q)in the case of molecular liquids we can only make a comparison between our calculated $S^{X-ray}(Q)$ (pinky line) and the corresponding experimental data obtained by x-ray diffraction (starry points). Despite the temperature difference, the agreement is really good, confirming the goodness of the calculated S(Q) as well. In blue line we also report the measured $S^{IXS}(Q, \omega = 0)$ which confirms the position of the first maximum of the $S^{X-ray}(Q)$.

[3] http://www.ruppweb.org/new_comp/scattering_factors.htm is a web portal from which it is possible to download the form factors values based on the Hartree-Fock calculations made by Cromer [92].

Fits and results

At the end of this huge effort to reduce the number of the free parameters in eq. 3.10, we performed the lineshape analysis from which we obtained the estimates for c_∞^{IXS}, τ_α and Γ_μ. In Fig. 3.19 are reported the fitted spectra for the whole set of measured Q at T=300K. As it is possible to see how on approaching Q-values close to the maximum of the $S(Q)$ it is even more difficult to discriminate the presence of the shoulders due to the acoustic modes contribution into the spectrum. To help the reader to appreciate the Q-evolution of the acoustic features, we show the so-called longitudinal current spectrum $J_L(Q,\omega) = \frac{\omega^2}{Q^2} S(Q,\omega)$ (blue lines), whose maxima correspond to the characteristic frequency of the acoustic modes. In Fig. 3.20 are reported the fitted values for $\omega_\infty = c_\infty^{IXS} \cdot Q$ and ω_J (i.e. the peak frequency of the $J_L(Q,\omega)$ spectra) at T=300K. It can be observed that basically the acoustic frequency (ω_J) modes has already reached its high frequency limit (ω_∞) in the probed spectral region. Since ω_∞ asymptotically reaches a linear trend in Q at low-Q, c_∞^{IXS} can be determined as the initial slope of the Q-dispersion of ω_∞. We hence performed a linear fit of ω_∞ limited to the first low-Q data for each temperature. In Fig. 3.21 it is possible to see the temperature dependence of c_∞^{IXS}, which can be simply modeled by a constant. From this plot it is evident how the amplitude we of the α-relaxation is much larger than the one of the Kneser-type relaxation, thus endorsing the assumption we made in neglecting the latter in the memory function. Concerning the structural relaxation time, we found a typical non linear Q-dependence of τ_α^c from which it is not so obvious to extrapolate the low-Q limit value (see Fig. 3.22). Because of the resolution limits characterizing such kind of measurements we could not explore the Q-range below 2 nm^{-1} and hence it is difficult to argue a low-Q functional behavior without any strong assumption. In order to not heavily model the data forcing them to obey to a particular phenomenology, we decided to fit the Q-dependence of τ_α^c with the simple following function:

$$\tau_\alpha^c(Q) = (\tau_{\alpha,Q=0}^c - \tau_{\alpha,Q=\infty}^c) e^{-Q/Q_1} + \tau_{\alpha,Q=\infty}^c \tag{3.25}$$

Fig. 3.23 and 3.24 are report the T dependence of the parameters involved in the phenomenological function written in eq. 3.25. Concerning the behavior of $\tau_{\alpha,Q=0}^c$ (blue triangles), we can recognize a decreasing trend with increasing of temperature. The blue and black lines in the first plot are guide for eyes and, regardless their actual values, they want to suggest an Arrhenius behavior for such relaxation time. In our opinion it seems to be premature at this stage to give any quantitative conclusion because of the scarce quality of the data, especially in the case of $\tau_{\alpha,Q=0}^c$. Here, we just want to stress the evidence of a T-dependence especially for $\tau_{\alpha,Q=0}^c$ and, at least as a rule of thumb, that this relaxation time in the hydrodynamic ($Q \to 0$) limit should be in the order of few ps. Q_1 is the last parameter appearing in the employed phenomenological function (eq. 3.25). It is reported in fig. 3.24 as a function of T. Again, the large error-bars prevents us to state if there is a weak temperature trend of such parameter or if it is basically constant, we can only note that Q_1 is not randomly scattered in this temperature range. Despite it is difficult to assign any particular physical meaning to such parameter, the latter observation can be considered as a fingerprint of the adequacy of the chosen fitting function.

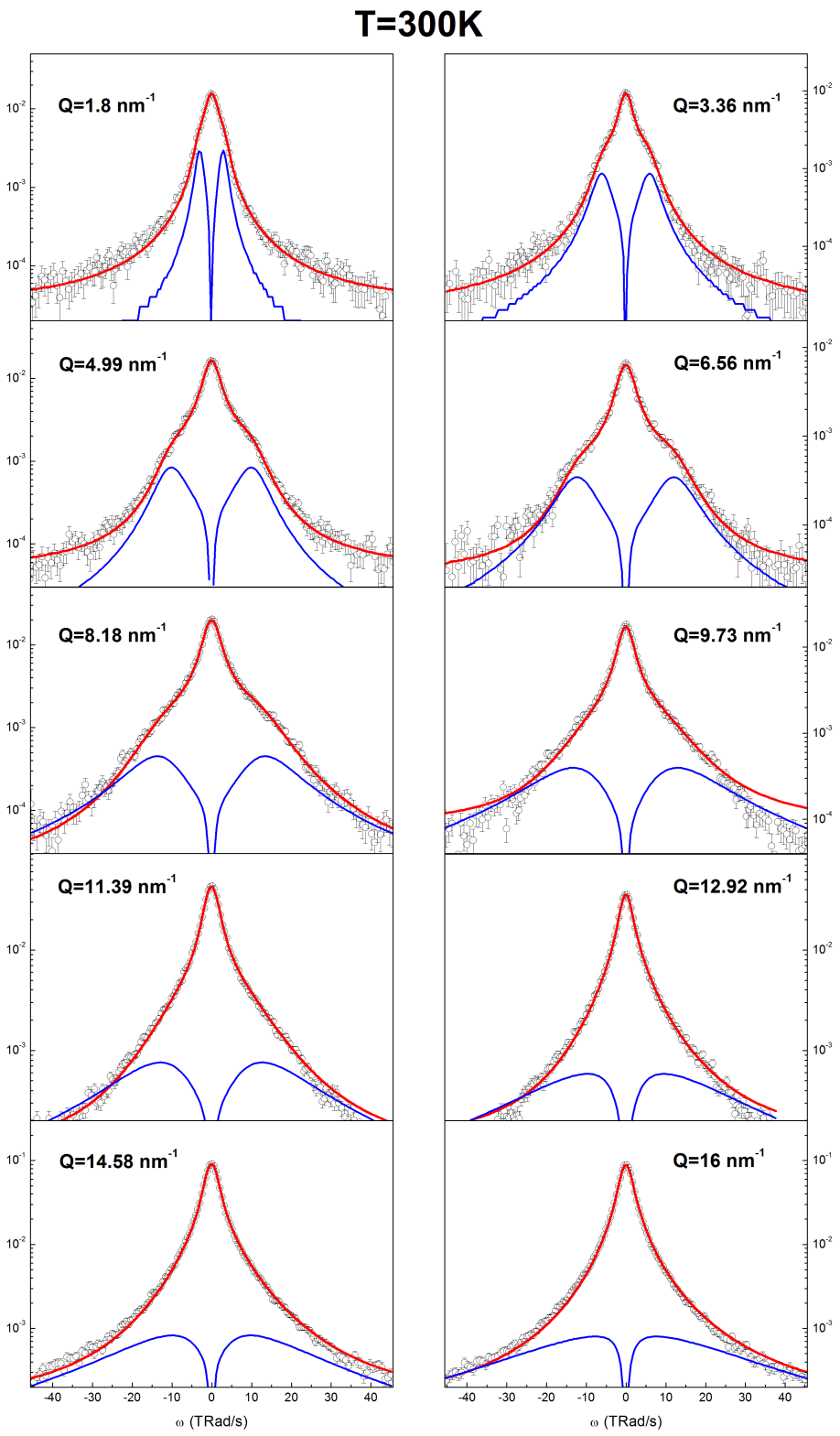

Figure 3.19: The figure it's shown an overview of the fitting results at T=300K. We just notice that approaching the Q-region close to the maximum of the S(Q) it become further difficult to discriminate any acoustic contribution to the signal.

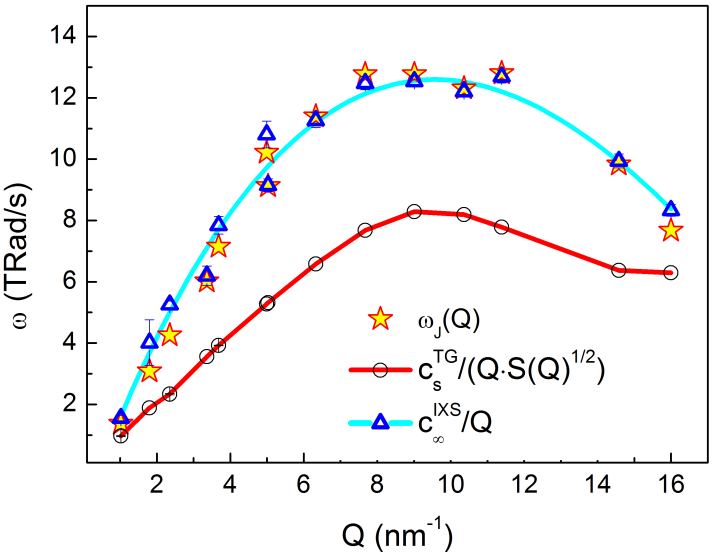

Figure 3.20: Energy dispersion of the acoustic modes at T=300K.

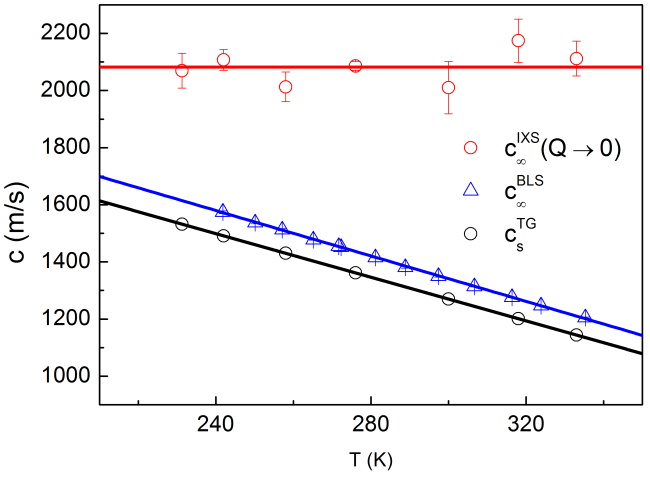

Figure 3.21: Summary of the temperature dependence of the speed of sounds in all the explored regimes. In red open circles are reported the extrapolated values for the $c_\infty^{IXS}(Q \to 0)$, in open blue triangles the unrelaxed speed of sound in the presence of the Kneser relaxation and in open black circles the adiabatic speed of sound.

Let's take in consideration the last parameter left free in the memory function fitting procedure: Γ_μ. This parameter is the amplitude of the $\delta(t)$ term in the memory function and it basically accounts for any dynamics occurring at timescales much faster than the one set by probed phonon frequency range (say faster than 0.1 ps), which, therefore, are seen as "instantaneous" also by high-frequency phonons. In Fig. 3.25 we show the Q-dependence of such parameter for some temperatures. It is quite evident the lack of any clear temperature dependence, while at low-Q it

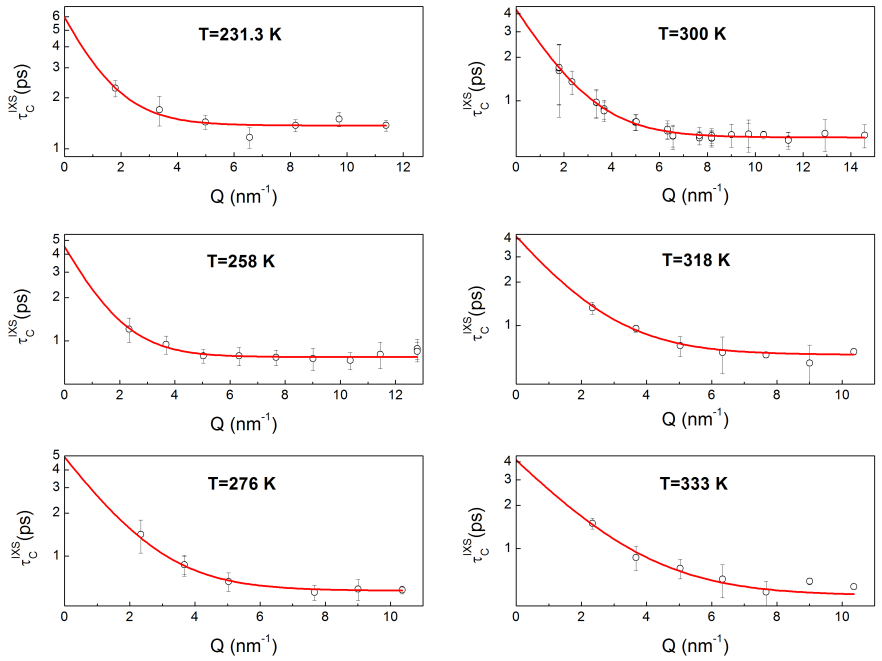

Figure 3.22: Q-dependence of the compliance relaxation time, τ_α^c. Data were fitted (red lines) with a decreasing exponential function as expressed by eq. 3.25

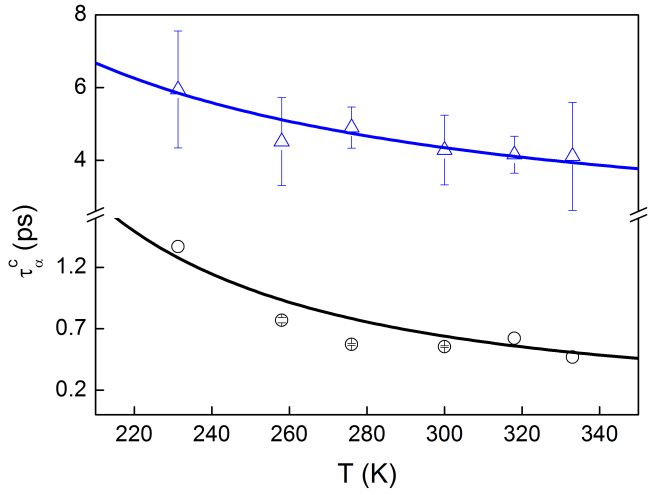

Figure 3.23: In blue open triangles is represented the fitted parameter $\tau^c_{\alpha,Q=0}$, while in black open circles the $\tau^c_{\alpha,Q=\infty}$ parameter as a function of T. Lines are guide for eyes to highlight the Arrhenius like behaviour of both of the observables.

displays a quadratic Q-trend with a coefficient D_0=(0.21 ± 0.02) mm^2/s, which can be assumed as the contribution of such fast processes to the kinematic viscosity of the system.

Another important quantity we can obtain combining the results obtained so far,

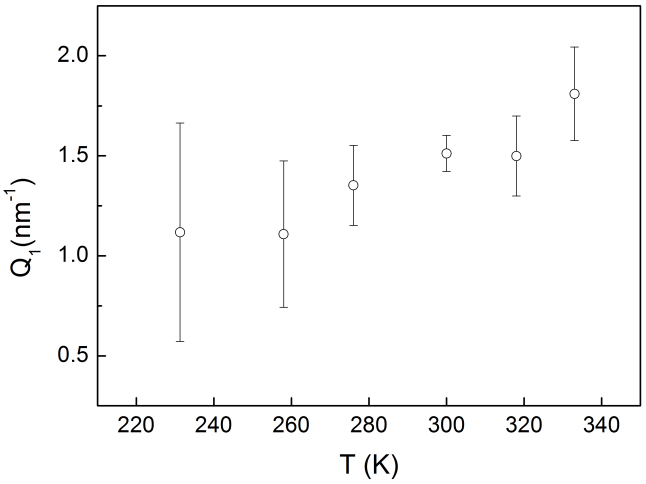

Figure 3.24: We report to be thorough the fitted Q_1 parameter. It is difficult to assign any particular physical meaning to this parameter, but in any case the fact that it has not a scattered behaviour with temperature is a fingerprint of the adequacy of the phenomenological fitting function.

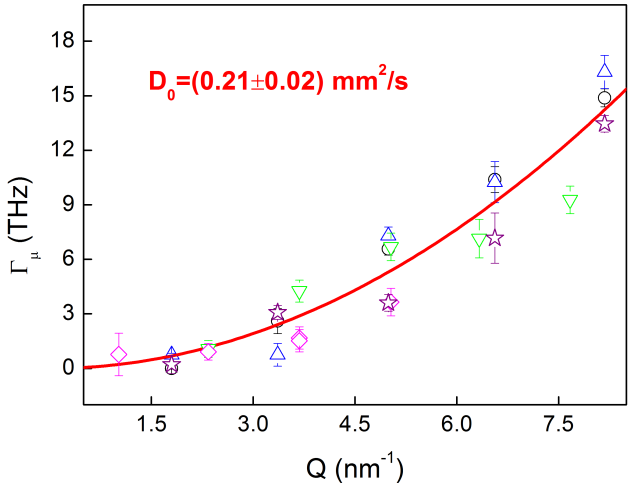

Figure 3.25: In figure are represented the Q-dispersions of the instantaneous memory function term at T=231 K (black open circles), T=242 K (upward blue triangles), T=258 K (downward green triangles), T=276 K (magenta diamonds), T=300 K (purple stars). All the points are compatible within the error bars, and we can describe the trend with a Q-quadratic behaviour independent by the temperature having D_0 as a coefficient and equal to (0.21 ± 0.02) mm^2/s.

is the kinematic longitudinal viscosity, that, in the memory function frame, is given by:

$$D_L = \lim_{Q\to 0} \frac{1}{Q^2}\left[\Gamma_\mu(Q) + \Delta^2 \tau_\alpha^c \frac{c_s^2}{c_\infty^2}\right] \tag{3.26}$$

In Fig. 3.26 are reported the Q-dependence of $D_L(Q)$ at different temperatures

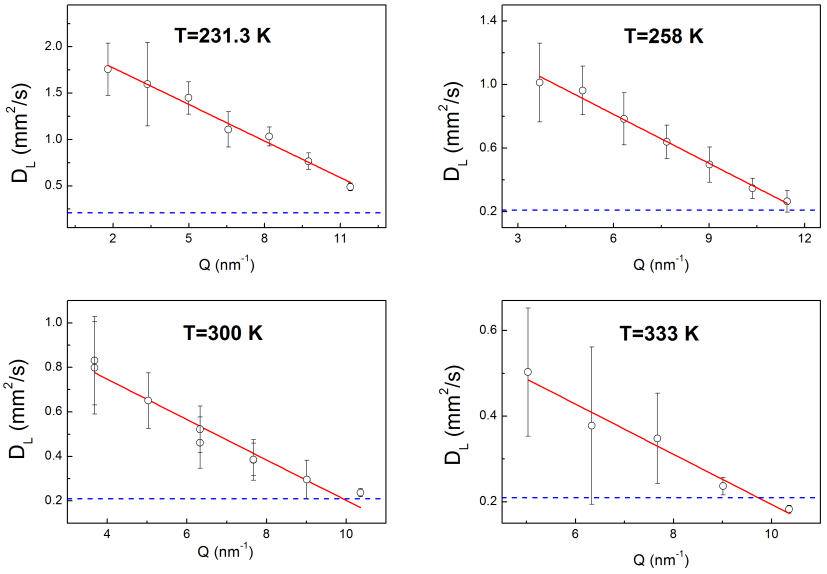

Figure 3.26: Q-dependent kinematic viscosity obtained by the combination of different quantities as expressed in eq. 3.26. Despite the combination of so many parameters, D_L results in a very clean linear dependence with Q. Fitting such data with a linear function (red lines) it was easy to extract the values for the hydrodynamic limit. For a comparison in the plot is reported also the kinematic instantaneous viscosity (dashed blue line). It is interesting to notice that in the high-Q range the dominant contribution to the viscosity is due to D_0, which in fact is related to ultrafast dynamics and to microscopical processes. It looses importance approaching the hydrodynamic region, in which the main contribution to the viscosity would be related to the cooperative dynamics between the molecules inside the liquid.

(black open circles); the contribution of "instantaneous" processes (D_0, dashed blue line) is reported for comparison. While the latter does not present any temperature dependence, $D_L(Q)$ has a strong T-dependence. Furthermore, it is interesting to observe that at high Q's the kinematic viscosity is essentially dominated by the instantaneous contribution, while on approaching the hydrodynamic ($Q \to 0$) limit the latter becomes less important, especially at low temperatures. It is surprising that the combination of so many and quite noisy quantities (let's remind, among the others, the error-bars on the the compliance relaxation time) results in a so straight behavior of $D_L(Q)$ we can observe in the figure. Performing a linear fit to such datasets (red lines in figure) we can obtain the hydrodynamic ($Q \to 0$) limit for the kinematic viscosity. Multiplying the obtained kinematic viscosity values by density, we obtain the longitudinal viscosity η_L. The latter is reported in Fig. 3.27 (in black open circles) with the shear viscosity η_s [94] (blue open triangles) and the instantaneous term (green open diamonds) as a comparison. The temperature dependency of the longitudinal viscosity suggests an Arrhenius behavior.

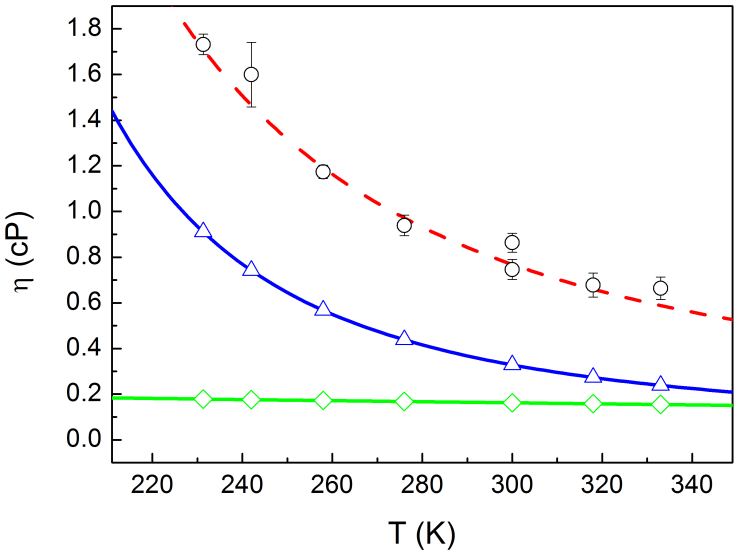

Figure 3.27: Comparison between longitudinal, shear and instantaneous viscosities. The similar temperature behaviour between η_L and η_s suggests an Arrhenius behaviour for the viscosity.

At a first glance longitudinal and shear viscosity seem to have the same temperature dependence and they could be scaled one on the other just applying a factor 2. A closer look to the ratio between η_L and η_s (shown in Fig. 3.28) reveals that actually it has a weak temperature dependence.

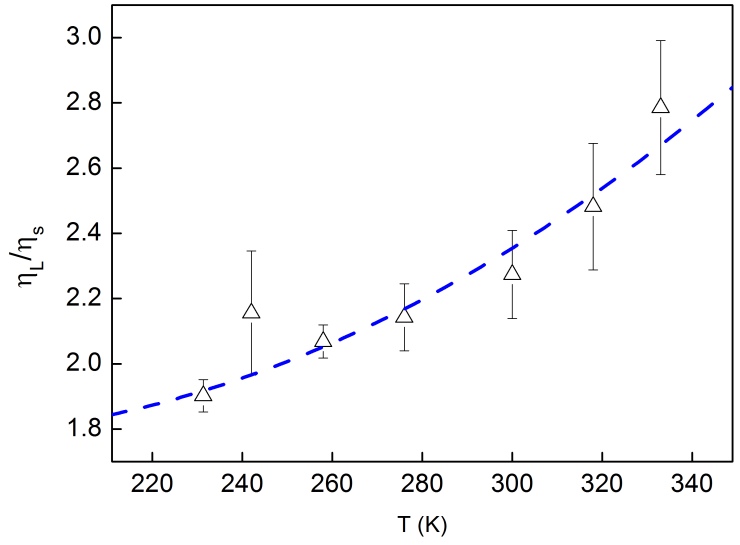

Figure 3.28: A closer look the ratio between η_L and η_s reveals a weak temperature dependence.

3.5.2 Ultrafast TG experiments

In the previous section we have seen the effectiveness of IXS technique to investigate the unrelaxed (high-frequency) limit of dynamical processes. Using IXS we obtained information about the strength of the structural relaxation and a first insight about the characteristic timescale in which such dynamical process evolves. IXS also allowed to characterize the instantaneous relaxation process and, therefore, we gained information about the longitudinal viscosity of the system.

We remind here, that we could obtain the latter result by extrapolating the low-Q (hydrodynamic) limit of our measurements. It is interesting to stress how information about collective properties (as like the longitudinal viscosity and the α-relaxation time) were obtained from in a dynamical range characterized by high Q-values, approaching the inverse of the mean intermolecular separation. This was dictated by the intrinsic nature of the acoustic spectroscopy approach: i.e. the information on fast processes are embodied into the behavior of high-frequency phonons and, in light of the linear Q-dispersion of the acoustic frequency, this turns into the exploitation of such an high-Q regime. The low-Q back-extrapolation of the results is a limit for the IXS method. For instance, we have seen that in the case of the compliance relaxation time we could obtain only a rough estimate, featured by quite large errorbars (see Fig. 3.23).

In this section we are going to discuss some complementary measurements, based on an ultrafast TG approach with polarization selectivity, aimed at directly characterize the structural relaxation time in its low-Q regime. The measurements were carried out in our laboratory with the TG setup described in Sec. 1.2.2 (see Fig. 1.22) and they are compared with the results obtained from IXS experiments.

In order to disentangle the structural relaxation contribution in the TG signal, we needed to vary the relative polarization of pump, probe and signal beams. This allowed use to separate the dynamic contributions due to the orientational and translational dynamics as well as to determine the anisotropic and isotropic response of the system, the latter being related to the structural relaxation. The pump pulse energy (10 μJ) and the focal spot size ($\approx$ 100 μm) were chosen in order to avoid sample damage. The crossing angle between pump pulses was set to 64.3°. Half wave plates and polarizers were used to select the polarization of pump, probe and scattered (signal) pulses. All pulses were contained in the horizontal (x-y) plane. The polarization of pump pulses was fixed along the vertical dimension (z-axis), while that of probe and scattered beams was set for either as vertical and horizontal. The acquisition board is based on a Boxcar integrator, which averages 3000 scattered pulses for each temporal delay, allowing to obtain a signal-to noise ratio of about 10^3.

In the impulsive limit, i.e. when the time duration of the pulses is shorter than the dynamics of interest, the intensity of the TG signal is proportional to $|P^{(3)}(t)|^2$, where $P^{(3)}(t)$ is the time-dependent third order polarization which can be related to the response function, R, of the material. Extending the expression proposed by Tokmakoff [95] to the more general case in which pump and probe pulses have

different wavelengths and angles of incidence onto the sample we obtain:

$$\begin{aligned} P^{(3)}(t) &= R_{ZZZZ}(t)\cos\varphi_4\cos\varphi_3\cos\varphi_2 + \\ &+ R_{ZYYZ}(t)\cos\varphi_4\sin\varphi_3\sin\varphi_2\cos\Phi_3\cos\Phi_2 + \\ &+ R_{YYZZ}(t)\sin\varphi_4\sin\varphi_3\cos\varphi_2\cos\Phi_4\cos\Phi_3 + \\ &+ R_{YZYZ}(t)\sin\varphi_4\cos\varphi_3\sin\varphi_2\cos\Phi_4\cos\Phi_2 \end{aligned} \tag{3.27}$$

where subscripts (1,2,3,4) correspond to the two pumps, probe and scattered beams, respectively, φ_i is the polarization angle with respect to z-axis ($\varphi_1 = \varphi_2 = 0°$) and Φ_i is the angle between a given pulse and the pump pulse labeled as 1 (i.e. $\Phi_1 = 0°$). The propagation direction of the latter pulse was chosen to be the x-axis. A scheme of the angular variables is reported in Fig. 3.29. Choosing different polarizations for the pulses, it is possible to select each element of the response function tensor ($R_{ijkl}(t)$), which is a real function [96]. In the present case we selected

$$\begin{aligned} I_{VVVV}(t) &= R^2_{ZZZZ}(t) \\ I_{HHVV}(t) &= R^2_{YYZZ}(t)C^2, \end{aligned} \tag{3.28}$$

where the first two and last two subscripts of I represent the polarization for the scattered and probe pulses and for the two pump pulses, respectively. $I_{VVVV}(t)$ and $I_{HHVV}(t)$ then corresponds to $\varphi_3 = \varphi_4 = 0°$ and $\varphi_3 = \varphi_4 = 90°$, respectively, while $\varphi_1 = \varphi_2 = 0°$ in both cases. The coefficient $C = cos\,\Phi_4\,cos\,\Phi_3 = 0.648$ is a correction factor taking into account the angles used in the experimental geometry. This coefficient is important when different measured signals are combined to isolate the rotational and translational contributions from the elements of the response function, as shown in the following. A wrong evaluation of C would create an erroneous estimation of such contributions. The TG signal can be divided into a fast contri-

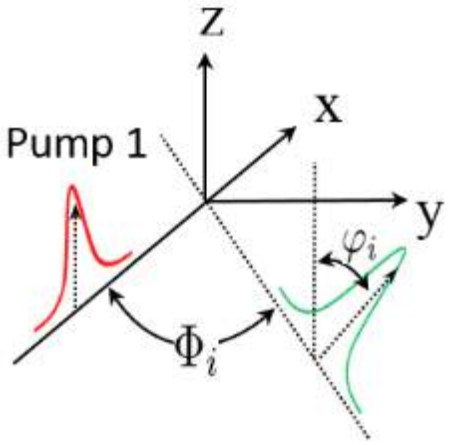

Figure 3.29: Polarization scheme of the HO-TG setup.

bution (electronic response), which essentially follows the time profile of the pulse, and a slower contribution (nuclear response), which contains the information on the relaxation processes of the sample. The electronic response follows the Kleinman

symmetry [97], which fixes the relative amplitude between $R_{ZZZZ}(t)$ and $R_{YYZZ}(t)$, i.e.: $R_{ZZZZ}(t) = 3R_{YYZZ}(t)$ and so $I_{VVVV}(t) = 9I_{HHVV}(t)$. Since in the present case also the factor C must be taken into account, we expect $I_{VVVV}(t) = \tilde{R}I_{HHVV}(t)$, where $\tilde{R} = 9/C^2 \simeq 21.4$. As a matter of fact, the rise of $I_{VVVV}(t)$ and $I_{HHVV}(t)$ profiles of liquid acetonitrile can be perfectly scaled one to each other (see Fig. 3.30) considering the appropriate $\tilde{R}$ factor, which then must be taken into account at large angles to avoid artifacts. The peak at $t \approx 0.1$ ps in $I_{HHVV}(t)$ is due to intermolecular

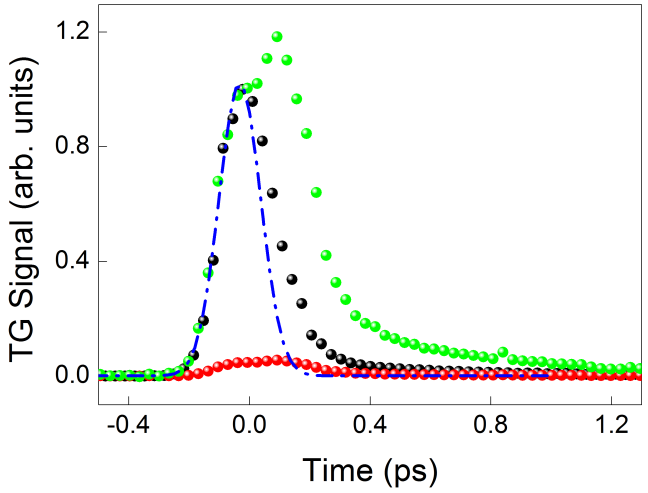

Figure 3.30: $I_{VVVV}(t)$ (black dots) and $I_{HHVV}(t)$ (red dots) from liquid acetonitrile at $T = 293$ K; green dots are $I_{HHVV}(t)$ multiplied by the factor $\tilde{R} \simeq 21.4$; the blue dashed-dotted line is the instrumental response function, measured with the proposed TG setup on SiO_2, which is characterized by only the electronic contribution, reproducing in this way the real shape of the pulse.

vibrational motions [98]: it grows between the electronic response and the following slow relaxation. This feature is more evident in the $I_{HHVV}(t)$ spectrum, as usually found [99]. The contributions from translational and orientational dynamics can be obtained by considering the expressions of $R_{ZZZZ}(t)$ and $R_{YYZZ}(t)$ reported in [95], in which only the nuclear response in the TG signal is taken into account. The eqs. 3.28 can thus be written as:

$$\begin{aligned} I_{VVVV}(t) &= \left\{\left[\alpha^2 + \frac{4}{45}\beta^2 r(t)\right] q(t)\right\}^2 = \\ &= \left[\alpha^4 + \frac{8}{45}\alpha^2\beta^2 r(t) + \left(\frac{4}{45}\right)^2 \beta^4 r^2(t)\right] q^2(t) \\ I_{HHVV}(t) &= \left\{\left[\alpha^2 - \frac{2}{45}\beta^2 r(t)\right] q(t) C\right\}^2 = \\ &= \left[\alpha^4 - \frac{4}{45}\alpha^2\beta^2 r(t) + \left(\frac{2}{45}\right)^2 \beta^4 r^2(t)\right] q^2(t) C^2, \end{aligned} \tag{3.29}$$

where α and β are the magnitudes of the isotropic and anisotropic parts of the polarizability tensor, respectively, while $r(t)$ and $q(t)$ are the time correlation

functions of rotational and translational variables, respectively. Using heterodyne detection the signal is proportional to the response function (and not to its square) and it is straightforward to mix the measured signals for determining $r(t)$ and $q(t)$. This is in principle not possible in homodyne detection. However, the coefficient of the last term in the right hand side of Eqs. 3.29 is lower than the first two ones by at least one order of magnitude (for acetonitrile, 0.17 with respect to 15.69 and 364.70 for the first equation of Eqs. 3.29). This consideration can be easily verified for a very large array of liquids characterized by different molecular structures, considering data and equations given in [100, 101]. Furthermore, $r(t)$ is featured by an exponential-like time decay [95], thus further reducing the relative weight of this term.

On such grounds we neglected this term and, therefore, we were able to extract the following contributions from homodyne detected TG measurements:

$$\begin{aligned} I_{Tr}(t) &= I_{VVVV}(t) + 2\frac{I_{HHVV}(t)}{C^2} \propto q^2(t) \\ I_{Or}(t) &= I_{VVVV}(t) - \frac{I_{HHVV}(t)}{C^2} \propto r(t)q^2(t), \end{aligned} \tag{3.30}$$

where $I_{Tr}(t) \propto R^2_{Iso}(t)$ and $I_{Or} \propto R_{Aniso}R_{Iso}$, $R_{Iso}(t)$ and $R_{Aniso}(t)$ being the isotropic and anisotropic portion of the response function [102], respectively. The characteristic decay time for $R_{Iso}(t)$ and $R_{Aniso}(t)$ can be extracted from $I_{Tr}(t)$ and $I_{Or}(t)$, using the phenomenological model proposed in [98], where an analytical function is squared before convolution with the instrumental response function. Therefore, if we define $f^2(t)$ and $g^2(t)$ as the temporal profile of the model used for fitting $I_{Tr}(t)$ and $I_{Or}(t)$, respectively, $f(t)$ describes directly the time-evolution of $R_{Iso}(t) \propto q(t)$. The same information can be achieved for $R_{Aniso}(t)$, considering that $R_{Aniso}(t) \propto g^2(t)/f(t) \propto r(t)q(t)$.

The obtained profiles of $I_{Tr}(t)$ and $I_{Or}(t)$ are reported in Fig. 3.31 in a semi-logarithmic scale, together with the measured $I_{VVVV}(t)$ and $I_{HHVV}(t)$ ones, and the fitting function. All spectra are normalized to the electronic response, in order to compare the signal from nuclear relaxations. In order to test the proposed approximation, we compared our determinations of dynamical relaxations with literature data. In particular, values for the characteristic time decay (τ_{Aniso}) of the orientational term (in our case represented by $R_{Aniso}(t)$) have been obtained by well-established techniques, like optical Kerr effect (OKE) and Rayleigh scattering. The τ_{Aniso} values as a function of temperature, and the relative uncertainties, were extracted from our $I_{Tr}(t)$ and $I_{Or}(t)$ profiles, using a least-squares fitting procedure (Nelder-Mead simplex algorithm), based on the model described above. Data are reported in Tab. 3.1 and compared with those from [103]. It is readily evident that the agreement is very good over the whole probed temperature range, thus confirming the validity of the proposed approximation. The temporal behavior of $r(t)$ can be also extracted from our spectra, considering that $I_{Or}(t)/I_{Tr}(t) \propto r(t)$, and the measured decay time $\tau_{rot} = 0.4 \pm 0.1$ ps at room temperature is in perfect agreement with the value measured with quasi elastic neutron scattering [104], another well-established method to probe purely rotational dynamics.

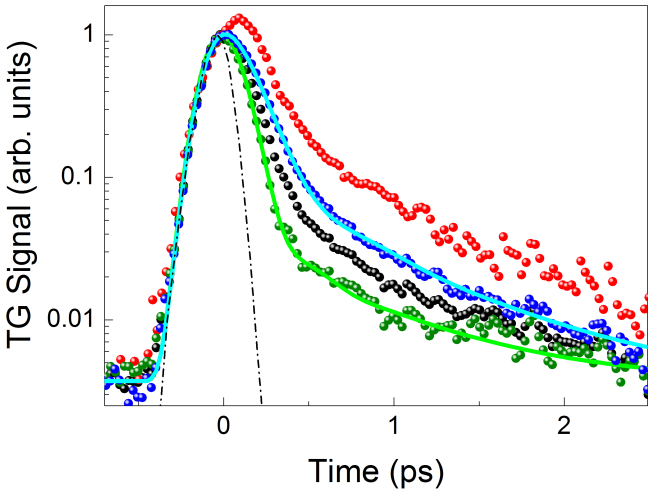

Figure 3.31: Comparison between the measured $I_{VVVV}(t)$ (black dots) and $I_{HHVV}(t)$ (red dots) profiles and the calculated $I_{Tr}(t)$ (blue dots) and $I_{Or}(t)$ (green dots) for Acetonitrile at $T = 303K$, normalized to the electronic response; the dot-dashed line is the instrumental response function, while the full lines through the $I_{Tr}(t)$ and $I_{Or}(t)$ profiles are the best fit result obtained using the model proposed in [98].

	Rayleigh	TG
T(K)	τ_{or}(ps)	τ_{Aniso}(ps)
281	1.8 ± 0.1	1.7 ± 0.1
293	1.5 ± 0.1	1.5 ± 0.1
318	1.2 ± 0.1	1.1 ± 0.1
338	1.0 ± 0.1	0.85 ± 0.15

Table 3.1: Orientational relaxation times at different temperatures, determined by Rayleigh scattering (τ_{or} [103]) and TG (τ_{Aniso}) experiments. In our case, the temperature is controlled by a Peltier cell, with a stability of $\pm 0.1\,K$.

Finally, because of the above reported results, we are confident that the adopted approximation in eqs. 3.29 is adequate and we can use it also to extract the information about the characteristic decay-time of the isotropic signal (τ_{Iso}) as a function of temperature. In Fig. 3.32 we report in an Arrhenius-plot the comparison between such τ_{Iso} (in black open circles) and the α-relaxation time $\tau_\alpha = \tau^c_{\alpha,Q=0}\left(c_s/c^{IXS}_\infty\right)^2$ (blue open triangles) obtained with the IXS experiments. It is quite evident how these two quantities are the same within the errorbars, so that we associated τ_{Iso} with τ_α. From this Arrhenious plot ($\tau_\alpha = \tau^0_\alpha exp\{E^\tau_a/k_BT\}$) we can extract an activation energy $E^\tau_a = (1.50 \pm 0.03) Kcal/mol$. In the same Arrhenius plot is reported the longitudinal viscosity η_L (green open squares) obtained by extrapolating the IXS data. Also this quantity presents an Arrhenius trend with an activation energy of $E^\eta_a = (1.54 \pm 0.08) Kcal/mol$, in perfect agreement with the one obtained

by the isotropic TG signal, thus further confirming its structural nature; we recall that the structural relaxation in the hydrodynamic ($Q \to 0$) limit can be regarded as an overall dynamic response of the system (likely due to several processes) responsible for viscous damping. The obtained value for E_a^τ is in the same order as that found in hydrogen-bonded liquids (H_20, 3.8 Kcal/mol; HF, 1.9 Kcal/mol; NH_3, 2.6 Kcal/mol) and much larger than what found for van der Waals systems (N_2, 0.13 Kcal/mol; Ne, 0.06 Kcal/mol). The latter systems are characterized by a null molecular dipole, while hydrogen-bonded liquids shows a quite large molecular dipole (D=1.5-2.2 Debye). It is interesting to notice how E_a^τ is usually related with a general concept of "average strength" of intermolecular bonds, while an eventual dependence of such quantity on the permanent dipole of the molecular was not considered. Following this line we would conclude that the strength of intermolecular bonds in acetonitrile is somehow in the middle between that of noble gasses and simple hydrogen bonded liquids. Another parameter that contains information on such an "average strength" of intermolecular bonds is the critical temperature (T_c), i.e. the temperature at which the thermal bath is able to break (on average) all the intermolecular bonds, hence preventing the formation of the liquid on macroscopic scales. By looking at this parameter one may collocate acetonitrile ($T_c \sim 550$ K) in between water ($T_c \sim 660$ K) and HF-NH_3 ($T_c \sim$ 400-450 K). The fact that the activation energy of acetonitrile does not fit such a rough "E_a^τ vs T_c" might suggests that the permanent dipole moment would play a role into the definition of the behavior of the structural relaxation, and thus on the value of E_a^τ. However, in order to point out any eventual phenomenological relation, investigations on other polar liquids have to be carried out. In conclusion, this comparison demonstrates that IXS and ultrafast TG with polarization tunability are two very powerful complementary techniques to extract collective dynamical information in disordered systems.

3.6 α- and ν- relaxations coupling

By combining the information obtained with techniques operating in different dynamic ranges we could characterize the thermal, vibrational and the structural relaxations. The obtained results suggest that the letter two relaxation processes evolve, in the range of temperatures explored in our experiments, in two separated timescales: the Kneser process is characterized by a relaxation time one order of magnitude larger than the structural one. Thus, the two processes are active in different timescales and, in principle, no correlations there should be found between the two (see Fig. 3.33 for a pictorial representation). However, we found that the structural relaxation has a very large strength, which can somehow compensate for the difference of timescales and lead to a non negligible effect of such relaxation in the slower time window of the Kneser relaxation. In other words, even though the two relaxations are well separated in time (and angular frequency), the structural relaxation strength is so large to enable some superposition of the structural relaxation tails in the sub-THz spectral range dominated by the Kneser-type relaxation. Furthermore, as shown in Figs. 3.23 and 3.15, we found that the structural and Kneser relaxations have opposite temperature dependencies, the characteristic timescale of the latter

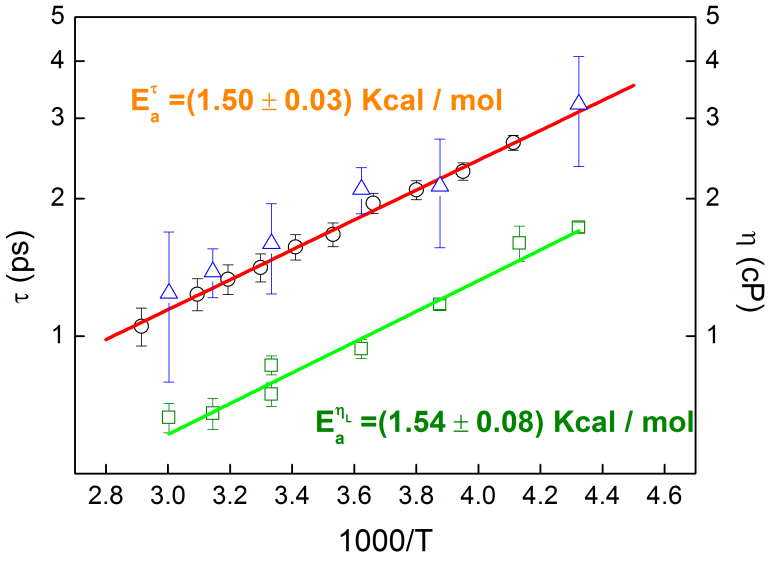

Figure 3.32: Comparison in Arrhenius plot of the α-relaxation times measured with the "fast" HO-TG setup (black open circles) and the IXS (blue open triangles). They show the same Arrhenius temperature dependence with and activation energy $E_a^\tau = (1.50 \pm 0.03) Kcal/mol$. *The same value for the activation energy can be extracted by the hydrodynamic limit of the IXS-longitudinal viscosity (green open squares).*

increases with the increasing temperature, while the one of the former increases on decreasing the temperature, essentially following the temperature dependence of the viscosity. These different temperature trends could be used to investigate if there is any coupling between the two processes at the thermodynamic condition of the liquid phase of acetonitrile, since by changing the temperature of the system we can modulate the overlapping region of the two relaxations in the halfway spectral region between BLS (10's GHz-range) and IXS (> THz). In order to unravel any eventual coupling between these two relaxations we probed such a sub-THz range using the IUVS beamline (@ Elettra, Trieste, Italy; see Sec. 1.1.1), the only instrument able to operate in such an spectral range.

3.6.1 The IUVS experiment

IUVS experiments were performed at 5 different Q-values and at 5 different temperatures from 278 K to 343K. With a simple DHO data analysis we could obtain the peak frequency and the width of the Brillouin doublet and hence we could use the acoustic moduli formalism, shown in the section dedicated to describe BLS experiments.

In Fig. 3.34 is reported the real part of the elastic modulus obtained in the IUVS spectral range (black full points). The black line is the expected trend of the Kneser relaxation, as extrapolated by the BLS measurements. The shaded area represents the BLS spectral range. It can be immediately noticed that the "IUVS data" are not following the expected curve of the Kneser relaxation. This is the fingerprint of some

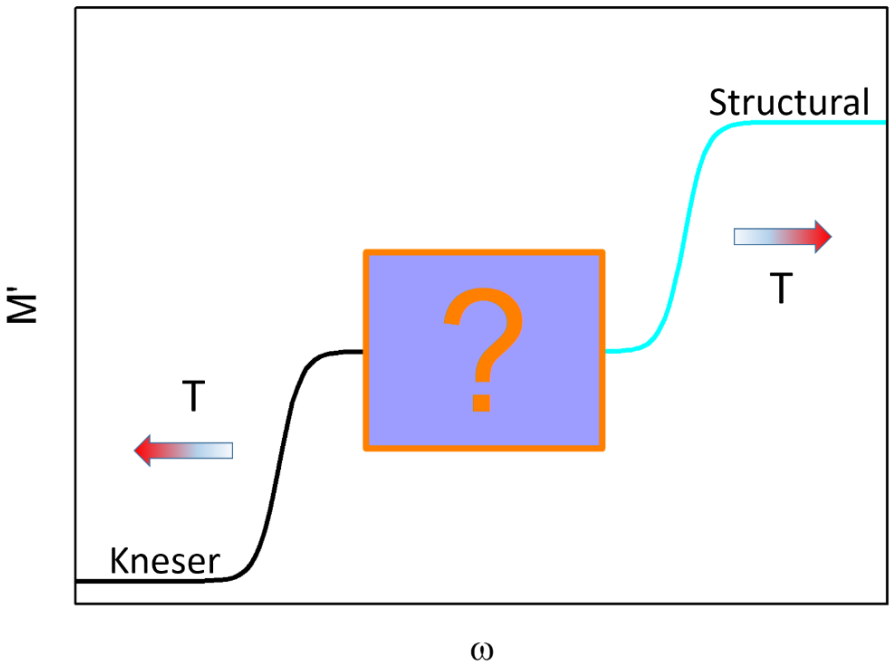

Figure 3.33: In the figure are pictured the vibrational and structural relaxations lying respectively in a low frequency and high frequency spectral range. If any coupling between the two is possible, it should be detected in the intermediate spectral range, where, possibly, the two relaxations coexist and overlap each other at least with their tails.

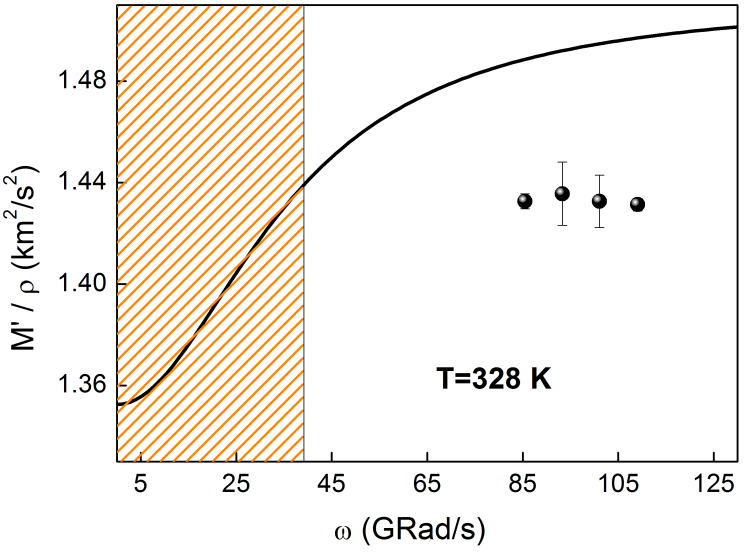

Figure 3.34: Real part of the elastic modulus M^* at T=328 K. Black points are the IUVS measurements, black line is the expected analytical shape on the basis of the BLS fits. The shaded region is the one in which BLS experiments were performed.

occurring phenomenon at these frequency-scales. In fact, if the Kneser relaxation was the only active process in this spectral window, then we should have measured the unrelaxed regime of the vibrational relaxation. So that we basically expect a sound velocity constant and equal to c_∞^{BLS}. We can exclude a simple additive combination between the vibrational and structural relaxation, since in this case we should have observed a small positive dispersion starting from the plateaux value of $(c_\infty^{BLS})^2$. So, something more than a linear combination of these two relaxations is happening in the IUVS spectral range.

For the moment let's introduce just as a phenomenological function, a further relaxation process which, linearly combined with those already existing, is able to fit the experimental points. Because it seems that a local minimum has to be reached in the spectral range between the 60 and 120 GRad/s, it means that such relaxation has to follow an inverse dispersion curve, which brings the elastic modulus from an higher value $M' = (c_\infty^{BLS})^2$, reached at low frequencies, down to a lower value $M' = c_\beta^2$ at high frequencies. Without any knowledge about the nature of such additional relaxation, we can suppose a diffusion-like process. This kind of process foreseen a Q-dependent relaxation time ($\tau_\beta(Q)$), as like in the case of the thermal relaxation (see Sec. 2.2.4), which gets faster on increasing Q in a more than linear trend (usually $\propto Q^{-2}$), i.e.: $\tau_\beta = (D_\beta Q^2)^{-1}$, where D_β is some diffusion coefficient. This turns into an high-frequency limit ($\omega\tau \gg 1$) reached at low-Q, since $\omega \propto Q$ and $\tau \propto Q^{-2}$, rather than at high-Q, as in the usual case in which τ (in such a relatively low-Q range) is not a function of Q. This phenomenological ansatz is able to fit the dispersion profile. Now, by writing $Q = \omega/\overline{c}$, where $\overline{c}$ is the average speed of sound during the β-relaxation process, we can write:

$$\omega^2\tau^2 = \frac{\overline{c}^4}{D_\beta^2\omega^2} = A\omega^{-2} \tag{3.31}$$

where $A = \overline{c}^4/D_\beta^2$ is a constant. The combination of the vibrational, β and α-relaxation reads as follows:

$$\begin{aligned} M'(\omega) &= c_s^2 + \left[\left(c_\infty^{BLS}\right)^2 - c_s^2\right]\frac{\omega^2\tau_\nu^2}{1+\omega^2\tau_\nu^2} + \\ &+ c_\beta^2 - \left(c_\infty^{BLS}\right)^2 + \left[\left(c_\infty^{BLS}\right)^2 - c_\beta^2\right]\frac{A\omega^{-2}}{1+A\omega^{-2}} + \\ &+ \left[\left(c_\infty^{IXS}\right)^2 - c_\beta^2\right]\frac{\omega^2\tau_\alpha^2}{1+\omega^2\tau_\alpha^2} \end{aligned} \tag{3.32}$$

Now, leaving free c_β and A and fixing the other parameters to the values found in the BLS and IXS experiments, we can use eq. 3.32 to fit the IUVS data.

In Fig. 3.35 we report the obtained results (red line) for the data already shown in Fig. 3.34. In black, magenta and cyan lines are reported the Kneser-type relaxation (with the parameters obtained by BLS), the β-relaxation and the α-relaxation (with the parameters obtained by IXS and HD-TG), respectively. The green line is the $\left(c_\infty^{BLS}\right)^2$ asymptote, while the blue line is the fitted value for c_β^2. In order to validate such phenomenological picture, we extend the analysis to the whole set of temperatures. Fig. 3.36 shows the fits corresponding to the other temperatures.

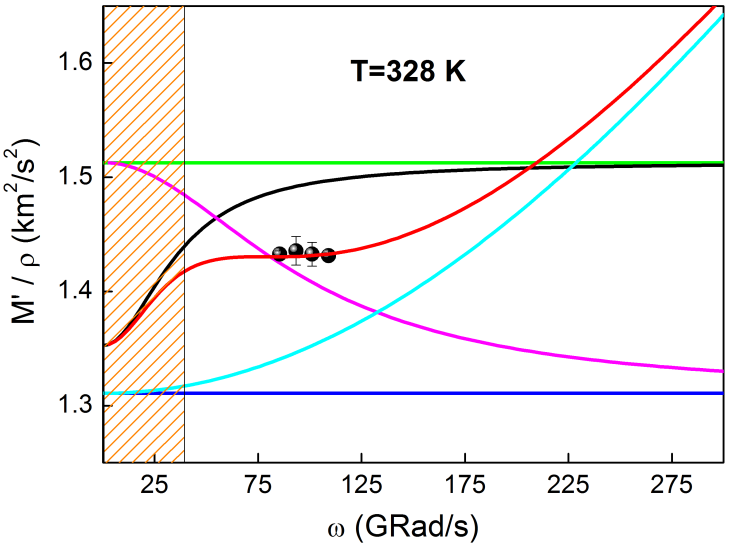

Figure 3.35: Fit (red line) of IUVS dataset with the three relaxations phenomenological function. All the three relaxation components are shown: the Kneser relaxation (black line), the β-relaxation (magenta line) and the α-relaxation (cyan line).

Looking at the whole set of fitting results for the different temperatures we can say that our simple model seems to mimic quite well the experimental data. Basically at all the presented temperature IUVS points lie on a plateaux, while at T=343 K is appreciable a weak rise at higher ω's. This "structured" dispersion can be fitted as well by the phenomenological function endorsing the fairness of our model. In all the figures the red shaded area is the spectral region accessible by BLS. As it is possible to see, in such regions black and red curves are almost overlapped, this fact explains why through our BLS measurements we could not appreciate such additional (β) relaxation, whose dynamical range seems to nicely fit the IUVS domain.

In order to infer some possible physical meanings of our phenomenological function, we can consider the trend of the free fitting parameters. From the obtained values we can define $\Delta_\beta^2/Q^2 = \left(c_\infty^{BLS}\right)^2 - c_\beta^2$, which can be considered the amplitude of our additional relaxation. In Fig. 3.37 we compare this with the amplitudes of the other relaxation processes identified by IXS and BLS. The amplitude of the β process has a clear temperature dependence, experiencing a relative increase from its lower value of ≈ 240 % in the probed temperature range, against the $\approx 12\%$ for the α-relaxation and the $\approx 35\%$ for the Kneser one. So this β-process, whatever it is, becomes much more important in our phenomenological model on decreasing of temperature, while the other two processes are more weakly affected by temperature changes.

We hereby recall the temperature dependence obtained for the Kneser-relaxation time (τ_ν) and for the structural one (τ_α). The former decreases with the decrease of the temperature while the latter had an Arrhenius trend, thus, it increases with the decreasing of the temperature. This opposite behavior reflects (see also Fig. 3.33)

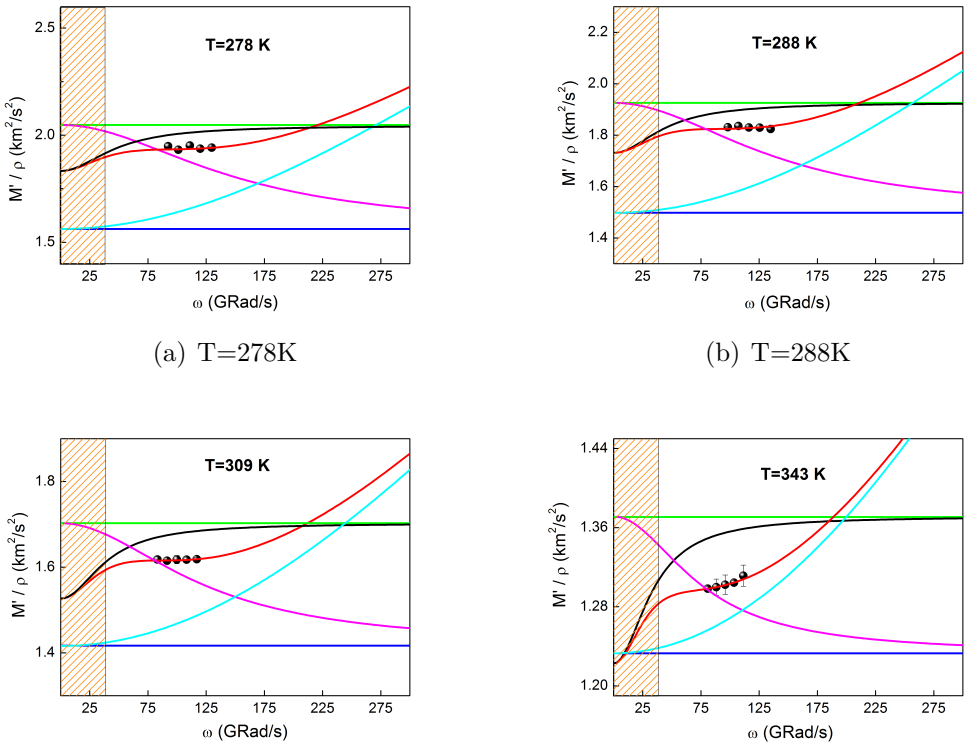

(a) T=278K (b) T=288K

(c) T=309K (d) T=343K

Figure 3.36: The 3-relaxations phenomenological fitting at all the temperatures.

in an opposite "movement" of the relaxations as a function of temperature. In particular, in the IUVS spectral range it happens that at low temperatures these two relaxations get closer in frequency (or, equivalently, in their characteristic timescales) and may start to experience a mutual influence. If we assign to the amplitude of the β-process the meaning of the magnitude of the mutual interaction between the Kneser and structural relaxations, then it is reasonable to suppose that this has to increase at low temperature, when the two relaxations are "closer", as experimentally observed (see Fig. 3.37). In other words, lower is the temperature and higher is the spectral overlapping between the two dynamical processes, and higher is the expected coupling between them. We report in Fig. 3.38 also the coefficient D_β and A, as obtained from the fitting results. From the value of D_β one may appreciate how this is correspond to a relatively slow process, on the order of $\tau_\beta \sim D_\beta^{-1} Q^{-2} \approx$ 10-100 ps in the Q-range ($\approx 0.1\ nm^{-1}$) probed by IUVS, while it would decrease in the IXS Q-range ($\gg nm^{-1}$), hence washing out its effects on the at high-frequency dynamics dominated by the structural relaxation alone. Another possible way to explain the phenomenology reported in Fig. 3.36 and Fig. 3.35 is to assume that the unrelaxed regime ($\omega\tau_\nu \gg 1$) of the Kneser relaxation is still not reached in the IUVS domain. This could happen if $\tau_\nu \propto Q^{-n}$ with $n > 1$ above a certain Q-values (Q^*). In such case, in fact, moving to higher frequencies above Q^* will reflect in a faster Q-decrease in τ_μ with respect to the Q-increase in ω. Similarly to the $\propto Q^{-2}$ dependence assumed above, this prevent the fulfillment of the unrelaxed

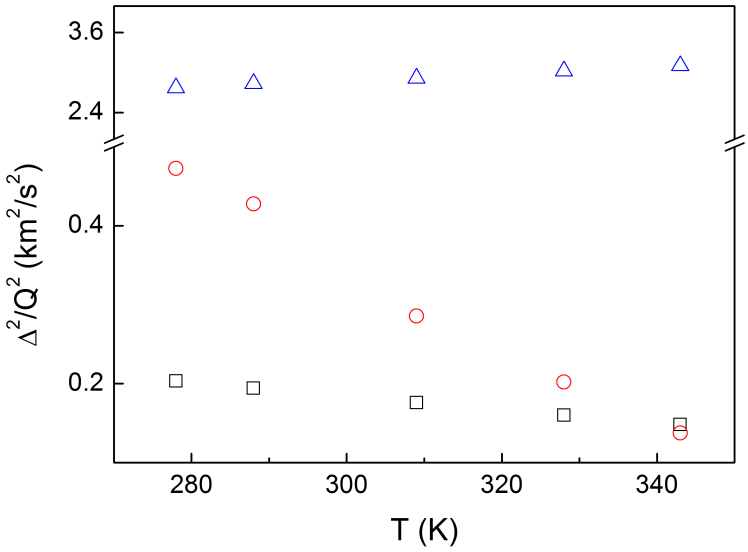

Figure 3.37: In figure are reported the amplitudes for the three relaxations of the proposed phenomenological function. While the structural (blue open triangles) and the vibrational (black open squares) relaxations are weakly temperature dependent, the β process (red open circles) is very sensitive to the temperature changes. The three processes α,ν, and β experience a relative amplitude increment, respectively of 12 %, 37 % and 242 %.

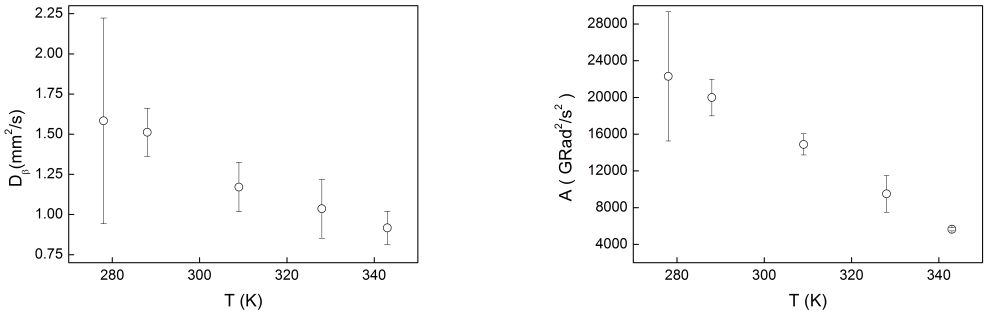

Figure 3.38: The D_β and A parameter obtained fitting the data with the proposed phenomenological function eq. 3.32.

regime ($\omega\tau_\nu \ll 1$) at high-Q. In a few words, this explanation does not require the introduction of an additional relaxation but relies upon a Q-dependence of τ_ν, which turns into a shortening of τ_ν on increasing the Q above a certain threshold (e.g. one may consider a function like $\tau_\nu(Q) = \tau_\nu/(1 + (Q/Q^*)^n)$ with $n > 1$). But which could be the origin of such a shortening? The phenomenon could be explained, again, in term of a coupling between the structural and vibrational relaxation. We have explained the Kneser relaxation as a Q-independent phenomenon for which the molecule is able to dissipate the energy released out by the acoustic wave to establish

compression and rarefaction zones into some intramolecular vibrational degrees of freedom. Now, on cooling down the system the molecules are more closely packed and, most importantly, the characteristic timescale for intermolecular interactions becomes longer (this is reflected by the slowing down of the α-relaxation). The possibility to dissipate energy through intramolecular channels (such as the molecular vibrations associated to the Kneser relaxation) on timescales that increasingly get closer to the one of average intermolecular interactions (structural relaxation time) may facilitate the energy redistribution and dissipation. In this case, the closer and slower are the molecules and the higher is the probability to activate, through intermolecular interactions (e.g. bonding or collisions), intramolecular channels (as intramolecular vibrations) for energy dissipation.

These qualitative ideas proposed to explain the behavior observed in the IUVS range are essentially based on some coupling effect between the vibrational and structural relaxation. This should be formalized in an appropriate model in order to be quantitatively tested, however, at the present stage we can infer that the temperature dependence of the observed discrepancy with respect to the trend expected by combining BLS and IXS data suggests that such deviations are indeed larger when the two relaxations are closer, hence endorsing an origin based on the coupling between vibrational and structural relaxations. In this context it would be extremely interesting to extend the present investigation to even lower temperatures (where in principle such coupling effects should be more evident) on going below the freezing temperature, i.e. in the supercooled liquid phase, as well as to access the whole dynamical range of the Kneser relaxation (see Figs. 3.35 and 3.36). The latter point is nowadays possible thanks to a new instrument (developed within this thesis work) based on an UV interferometric device, which, combined with the aforementioned spatial filters ("masks"), is able to probe with continuity the Q-range between 0.02 nm^{-1} and 0.07 nm^{-1}, which is exactly the spectral domain between BLS and IUVS. Though we did not yet performed measurements on acetonitrile using this instrument, in the next chapter we will focus on the main features of this device.

Chapter 4

The Fabry Perot Ultra-Violet interferometer

Using BLS we characterized the Kneser-type relaxation. The comparison between these results and that obtained using the IUVS beamline at the Elettra Synchrotron, we could speculate on the presence of a further molecular relaxation (and/or on couplings between different relaxation processes) evolving, at the investigated temperatures, in a timescale on the order of tenths of ps. A more comprehensive picture requires to explore the range located in between the Q-ranges of BLS ($< 3 \cdot 10^{-2}\ nm^{-1}$) and IUVS ($> 7 \cdot 10^{-2}\ nm^{-1}$).

In this section we report on a high resolution inelastic UV scattering tabletop set-up conceived for Brillouin measurements. We recently build it up at our lab (hosted by Elettra Synchrotron). The system is based on a tandem 1+1 pass scanning Fabry-Perot interferometer of Sandercock type. Special optics were used in order to adapt such an interferometric device, nowadays only used at optical or IR wavelength (see sec. 1.1.1), to the UV range. The advantages with respect to other UV Brillouin scattering instruments are the larger resolving power and the improved contrast in the low frequency spectral region. To corroborate these features we provide a comparison between data obtained using the described system and those from existing UV Brillouin scattering instruments.

As already shown in the previous chapters, the maximum value of the angular frequency (ω_L) we can probe with a BLS experiment depends on the maximum value of wave-vector (Q) that we can select in the scattering process: $\omega_L = c_L Q = 4\pi n c_L/\lambda$, where c_L is the velocity of the longitudinal acoustic mode propagating into the specimen and n is the refractive index of the sample probed by a laser with a wavelength of λ. Therefore, to extend the spectral range at higher ω/Q values, what we can do is to use a light source characterized by a λ shorter than in the visible case.

Only recently the needs mainly arose by the scientific community involved in the study of liquid and glass dynamics have stimulated the development of the two existing UV-BLS instruments (HIRESUV spectrometer [40] and IUVS beamline [43]), with the aim of probing acoustic properties in a ω-range substantially larger than those typical of VIS-BLS. Indeed, UV-BLS instruments can access larger ω_L-value since they are designed for exploiting λ-ranges shorter than the IR-VIS one. In

particular: i) the HIRESUV spectrometer is based on a fixed wavelength (λ=266 nm) table-top laser and, therefore, the ω_L-value can be increased by a factor $\approx$ 2 with respect to typical UV-BLS values; ii) the IUVS beamline is a synchrotron based instrument designed for working in a broad λ-range (from the visible to $\approx$ 120 nm) without a substantial deGRadation of the resolving power, thus potentially allowing an ω_L-value increase up to a factor $\approx$ 3 (see section 1.1.1). The shorter λ-range probed by UV-BLS could be also relevant for other applications such as, e.g., the study of vibrational modes in nanostructures [105, 106, 107]. Moreover, the possibility given by IUVS to continuously change the wavelength of incoming radiation might also allow applications based on resonant scattering. Both HIRESUV and IUVS instruments employ as ω-analyzers plane gratings working at very high ($> 200^{th}$) diffraction orders. This solution ensures high throughput as well as a sufficient resolving power ($\omega/\delta\omega \geq 10^6$) for determining the small ω-shifts (of about $c_L/c \approx 10^{-5}$, being c the speed of light in the sample) typical of Brillouin experiments. However, the state of the art of BLS instrumentation is represented by multipass scanning Fabry-Perot interferometers, rather than plane gratings. Interferometric devices can indeed provide a much higher resolving power (up to $\approx 10^8$), an exceptionally high contrast ($>> 10^{12}$) and, exploiting a tandem configuration, the useful ω-range can be extended well beyond the free-spectral-range (FSR).

In order to obtain UV-BLS data with spectral resolution and signal-to-noise ratio comparable with those attainable by VIS-BLS we conceived a UV-BLS setup based on an interferometric ω-analyzer [38]. Nowadays any instrument of such kind is documented in literature. We are currently using a setup based on a tandem 1+1 pass scanning Fabry-Perot interferometer of Sandercock type for UV-BLS measurements; we hereby present its performance and we compare them with the existing UV-BLS spectrometers. On a different notice, it is worth stressing that the compact design (it fits in a $\approx 1\ m^2$) and the relatively cheap price of this table-top setup also allow its eventual implementation in any research laboratory.

In the following we are going to describe the experimental apparatus and its performances.

4.1 Experimental setup

The experimental apparatus consists in: i) an Ar^+ ion laser equipped with etalon for single mode operation (mode bandwidth $< 0.1\ GHz$) and intracavity frequency doubling system able to provide 10 mW of UV light at λ=244 nm. ii) An optical system used to bring and focus the UV beam from the laser to the sample, as well as to collect the light scattered by the sample and send it to the analyzer. The polarization of the incident and scattered beams can be independently selected. iii) The interferometric analyzer with a dedicated (active) stabilization and data acquisition system. A scheme of the experimental layout is reported in Fig. 4.1.

4.1.1 Optical layout

The UV radiation coming from the laser is routed towards the sample at the right height by a few high-reflecting dielectric coated mirrors (HRM) and a right angle

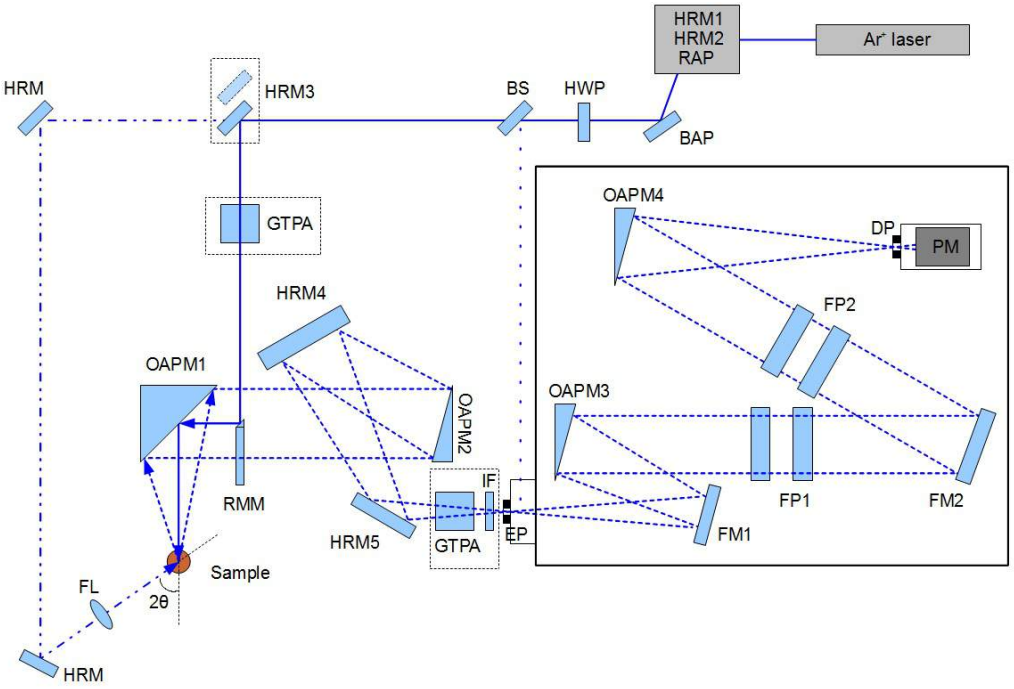

Figure 4.1: Sketch of the experimental apparatus; all the quoted items are described along the text. Arrows coming from/to the the sample indicate the direction of propagation of the beam in back-scattering geometry. Dotted and dash-dotted lines are the reference beam and an exemplificative beam path for a non-backscattering geometry. The reflection angles of the interferometer and collecting optics are enlarged for clarity. The space occupied by the entire system (excluding the laser) is of about $1.3 \times 0.7\, m^2$.

periscope (not shown). The beam then impinges into a Brewster angle polarizer (BAP; extinction ratio $\approx$ 1:500) in order ensure vertical polarization; the polarization can be eventually rotated by 90° using a half waveplate (HWP). A beam splitter (BS; reflect./trans. $\approx$ 10/90 %) is used to derive the reference beam necessary for the automatic alignment of the interferometer. The beam is sent into the sample by a 3 mm diameter 45° rod metallic mirror (RMM) and is focused by a 90° off-axis parabolic mirror (OAPM1) of 50 *mm* diameter and focal length (f=90 *mm*). The light emerging from the sample in back scattering geometry is collected by the same mirror and then impinges into OAPM2 (15° off-axis, 50 *mm* diameter and f=512 *mm*). The choice of using focusing mirrors instead of lenses has been done for minimizing the losses due to UV absorption.

The backscattering geometry allows to use the same optic for focusing and collection. This is undoubtedly the best solution for maximizing the deep of field and, consequently, the overall efficiency of the setup; the loss in the collecting of radiation related with the shadow of RMM is only marginal. Most important, the back scattering configuration is the one matching the main experimental goal, since it allows to probe acoustic modes with the largest possible frequency for a given value of λ.

The scattered radiation is focused into the entrance pinhole (EP) of the interferometer by OAPM2. Six pinholes of different diameter (namely d_P = 0.15, 0.2, 0.3,

0.45, 0.7 and 1 mm) are mounted on a six-fold "revolver" wheel in order to allow the selection of the EP size and, therefore, to set the desired compromise between spectral resolution and throughput. The direction of the light passing through the pinhole can be precisely set using two HRM's (HRM4 and HRM5; 50 mm diameter), which also serve to fine adjust the beam path length between EP and OAPM2 in order to match the focal length of the latter.

As options, a narrow-bandpass interference filter (IF, peak transmission ≈ 8 % at 244 nm) can be placed just before the EP to reduce the amount of light (having $\lambda > 244$ nm) arising from the UV fluorescence of the sample, which, in some cases, is so large to completely hinder the spectrum. Furthermore, a Glan-Thompson polarization analyzer (GTPA; field of view $> 15°$, clear aperture 15 mm, extinction ratio $> 10^5$, optimized for 244 nm radiation) can be inserted between HRM5 and EP (analyzer) and used to selected the polarization of scattered light; an identical element can be used to select the polarization on the UV light impinging onto the sample. The high extinction ratio of these devices allow reliably depolarized Brillouin measurements since the Brillouin peak leakage in the depolarized spectrum can be strongly reduced.

As an alternative to the aforementioned back-scattering setup, by removing HRM3 from the beam path (it is mounted on a translational stage) the incident UV beam can be focused into the sample via additional HRM's and a separate lens (FL). This allows to vary the scattering angle (2θ) and, consequently, to change the actual Q-value down to reach the typical Q-values probed by VIS/IR-BLS. Special cares have to be considered in analyzing BLS spectra acquired far from the back-scattering geometry, since the finite aperture of collection optics does not allow to identify a well defined value of Q and leads to a severe artefact in the spectral shape. In order to avoid this unwanted effect the luminosity of collection optics must be dramatically reduced with the risk of a consequent loss of a reliable signal. An alternative approach which allows to minimize the luminosity reduction of collection optics has been already described in sec. 1.1.1 [26].

4.1.2 The interferometer

The UV-interferometer was designed and realized by JRS-scientific instrument. It is based on the well established and worldwide used concept of scanning tandem Fabry-Perot (FP) interferometer, which relies upon the synchronous scan of two FP cavities (quoted as FP1 and FP2 in Fig. 4.1) of different lengths (d1 and d2). We hereby depict the basic working principle of the system.

The UV light emerging from the EP of the interferometer is collected (via the folding mirror $FM1$) by a 15° off-axis parabolic mirror (OAPM3, f=461 mm) and collimated; the clear aperture of all optics inside the interferometer is ≥ 50 mm. The collimated light passes through FP1 and FP2 cavities, each one is made by a pair of flat mirrors with reflectivity and flatness coefficients: $R = 0.975$ and $M = \lambda/130$, respectively. FP1 and FP2 are tilted against each other by an angle $\alpha \approx 20°$. The light passes through the sequence of the two FP's via FM2. Since FP1 and FP2 have slightly different free-spectral-ranges ($FSR_1/FSR_2 \approx 0.95$, where $FSR_{1,2} = \pi c/d_{1,2}$ rad/s), if light transmission through FP1 and FP2 is allowed for a given pair of

interference orders (say N_{FP1} and M_{FP2}), then transmission of adjacent orders (e.g., $N_{FP1} \pm$ 1,2,3... and $M_{FP2} \pm$ 1,2,3...) is almost suppressed. The ω-scan across the laser frequency ($\omega_i = 2\pi c/\lambda \approx 7.73 \cdot 10^{15}\ Hz$) is achieved with a continuous back-and-forth scan of d_1 and d_2 through piezoelectric actuators (scan frequency $\approx 2\ Hz$). The amplitude of the scan can be selected, typically within the 10-1000 nm range, and, for a given FSR-values, it defines the maximum frequency extension of the spectrum. An identical off-axis parabola (OAPM4) focuses the light transmitted by the tandem FP system into the detector pinhole (DP), used for reducing spurious background scattering. A wheel system similar to the one used for the EP allows to set the size of DP at 0.2, 0.3, 0.45, 0.7, 1 or 1.3 mm diameter. Since OAPM3 and OAPM4 are identical, in practice the EP is one-to-one imaged on the DP plane. As in the case of external optics, any transmission optical element, except for the FP cavity mirrors, are used inside the interferometer in order to reduce the losses due to UV absorption. The signal is recorded by a photon counter consisting in a photomultiplier and a discriminator (MP983, Perkin Elmer); quantum efficiency at 244 nm, dark count and dynamic range are ≈ 10 %, 0.3 Hz and 4 MHz, respectively.

The data are acquired during the FP cavity scans by an electronic board. This device counts the TTL pulses coming from the photon counter and records them into the 256, 512 or 1024 channels (user's selectable) in which the overall scanning time of FP cavities (512 ms) is divided. Data are finally stored into a PC through a dedicated software (GHOST [11]) that also allows a basic data analysis and remote control capability.

The stabilization of the interferometer during the cavity scan is ensured by an active feedback, which continuously adjusts the position of six piezoelectric actuators acting on FP mirrors in order to maximize a reference signal [108]. This light has no appreciable inelastic component and it is confined within a small frequency window ($\Delta\omega_{ref} < FRS$, user selectable) located across the chosen transmission condition for both FP's, i.e. across $\omega = 0$. No reference signal can be detected outside $\Delta\omega_{ref}$, except for some residual leakage, commonly refereed to as "ghost", in correspondence of the adjacent interference orders, located at $\omega \approx \pm(N \cdot FSR \pm \Delta\omega_{ref})$ (being N an integer number). A fast shutter (FS), synchronized with the piezo-actuator responsible for the scan of FP cavities, stops the signal coming from the sample position (through the EP) when the scanning cavities cross a frequency window (with user selectable width, $\Delta\omega_{FS}$) containing the reference signal. The feedback for the active stabilization of FP cavities acts for maximizing only the signal within $\Delta\omega_{FS}$. The scope of the FS is then twofold: i) it provides a faithfully reference signal, unaffected by the scattering of the sample, and ii) it prevents the photomultiplier to be illuminated by too many photons that, in some cases, may arise from the elastic scattering by the sample and/or the sample environment.

4.2 Performance of the setup

The main aim of the instrument is to provide a reliable alternative to available UV-BLS spectrometer. The proposed solution also provides a substantial improvement of the experimental resolution function and a higher contrast in the low frequency

side of the inelastic spectrum. The main quantities characterizing a Fabry-Perot interferometer were already introduced in sec. 1.1.1. Using the relations shown in that section and assuming that the instrumental transfer function for two identical FP cavities in tandem configuration is the square of the one of a single FP cavity, the expected $\delta\omega$ value (the full width at half maximum of the instrumental resolution function) for our system can be estimated to be:

$$\delta\omega \approx 0.64 \cdot FSR \left(6.75 \cdot 10^{-4} + \frac{20.65 \cdot d_P^4}{FSR^2} \right)^{1/2}, \tag{4.1}$$

where d_P and FSR are expressed in mm and $GRad/s$, respectively. Inserting typical values for FSR ($10^2 - 10^3$ $GRad/s$) and d_P ($0.2 - 1$ mm) in the above equation, it can be readily appreciated how an overall resolving power of about $10^6 - 10^7$ can be obtained.

Fig. 4.2a reports some selected examples of instrumental response function (IRF) corresponding to different FSR-values (i.e., 31.4 $GRad/s$, 94 $GRad/s$, 0.31 $TRad/s$ and 0.94 $TRad/s$; $d_P = 0.2$ mm in all the reported cases), as obtained by determining the ω-dependence of the elastically scattered light from a polished metallic slab placed in the focal plane of OAPM1. The metallic slab was tilted in order to avoid back reflections into the interferometer. However, the laser power had to be reduced by a factor $\approx 10^7$ (using a set of reflective normal-incidence filters placed between BS and HRM3) in order to not saturate the PM. For these measurements the reference beam is not needed since in this case the measured elastic signal can be used as feedback for the active stabilization system. Best fits of IRF using a Gaussian functions allows to determine the corresponding $\delta\omega$-values. The IRF's of HIRESUV (from Fig. 7 of Ref. [40]) and IUVS instruments (collected at 220 nm incident photon wavelength) are also reported in Fig. 4.2a for comparison. It can be readily appreciated how the present UV-BLS instrument can be set in order to have an IRF narrower than that of IUVS or HIRESUV. Furthermore, the IRF is more symmetric with respect to those of HIRESUV and IUVS, that present an intrinsic asymmetry due to the slope errors of diffraction gratings [40]. Fig. 4.2b reports the IRF's shown in Fig. 4.2a as a function of ω/FSR. It can be noticed how the residual transmission of adjacent interference orders (ghost), located at ω/FSR-values of about 1.05, are a few % of the maximum transmission. We also notice that in this plot all data essentially lye on a single master curve since at $d_P = 0.2$ mm F_P is substantially larger than F_R and F_M, so that the FSR-dependence in Eq. 4.1 reduces to a scaling factor. As expected, an IRF broadening was instead observed at low FSR values for larger d_P sizes. Furthermore, we recall that the employed tandem configuration allows measuring the spectrum in a ω-range largely exceeding the FSR, therefore, inelastic excitations located in the high-ω sides of the spectrum (i.e., well beyond the "ghosts" shown in Fig. 4.2b) can be eventually detected with the benefit of the narrow IRF associated to a low FSR setting of the interferometer. Indeed, the characteristic energy of inelastic modes detectable in the Q-range exploitable by UV-BLS methods is well within some 100's of GRad/s.

This trend can be appreciated by inspecting Fig. 4.3a. Here we report the parameter $\delta\omega$ as a function of d_P for different FSR's and we compare the obtained data with the expectations given by Eq. 4.1. In Fig. 4.3b we finally compare the

$\delta\omega$-values of our instruments with those of HIRESUV (from Fig. 6 of Ref. [40]) and IUVS. HIRESUV data are plotted as a function of the entrance slits width of the analyzer while for IUVS we report the $\delta\omega$-values corresponding to 266, 244, 220 and 180 nm; being 266 and 244 the UV wavelength employed at HIRESUV and in the present setup, respectively, whereas 220 and 180 nm are typical UV wavelength frequently used at IUVS. The second parameter of interest is the contrast, defined

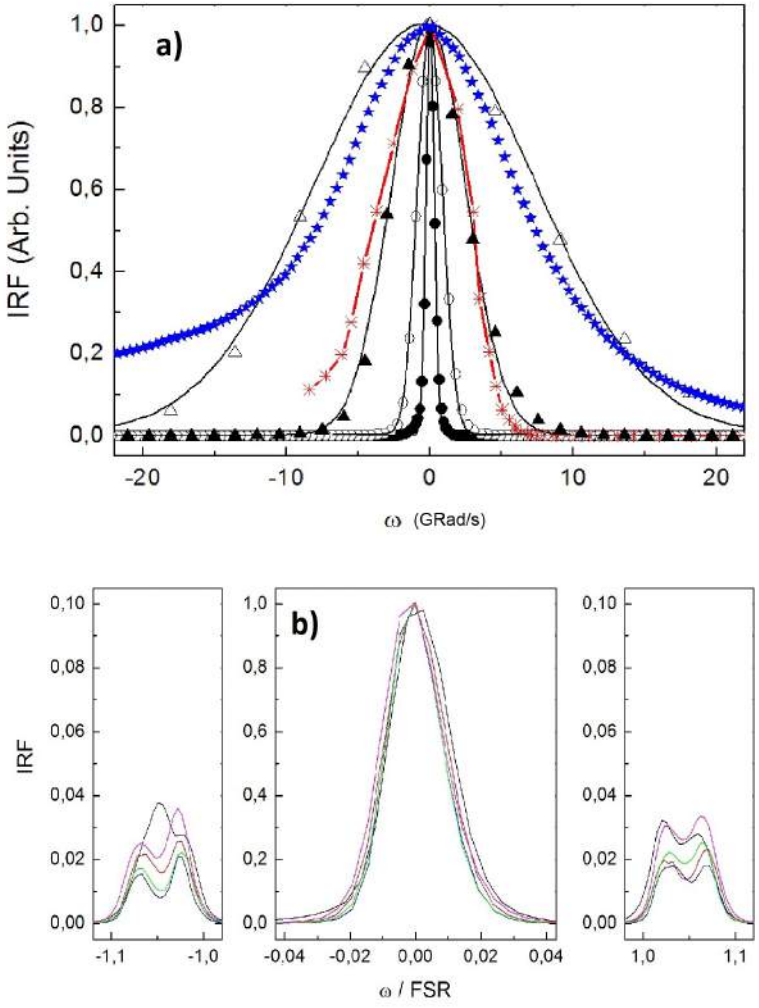

Figure 4.2: Top panel: ω-dependence of IRF corresponding to different FSR values the interferometer: i.e., 31.4 $GRad/s$ (dots), 94 $GRad/s$ (circles), 0.31 $TRad/s$ (full triangles) and 0.94 $TRad/s$ (open triangles); all data have been collected at d_P = 0.2 mm. Full lines through the data are best fits to Gaussian functions. Red asterisks and blue stars are the IRF of HIRESUV (from Fig. 7 of Ref. [40]) and IUVS spectrometers (collected at 220 nm photon wavelength), respectively. In these latter cases lines are guide for the eyes. Bottom panel: aforementioned IRF's of the interferometric analyzer reported as a function of ω/FSR, a few % residual leakage from adjacent interference orders (ghost) can be appreciated at ω/FSR-values of about 1.05.

as: $C = I_{max}/I_{min}$, being $I_{max,min}$ the maximum/minimum intensity transmitted by

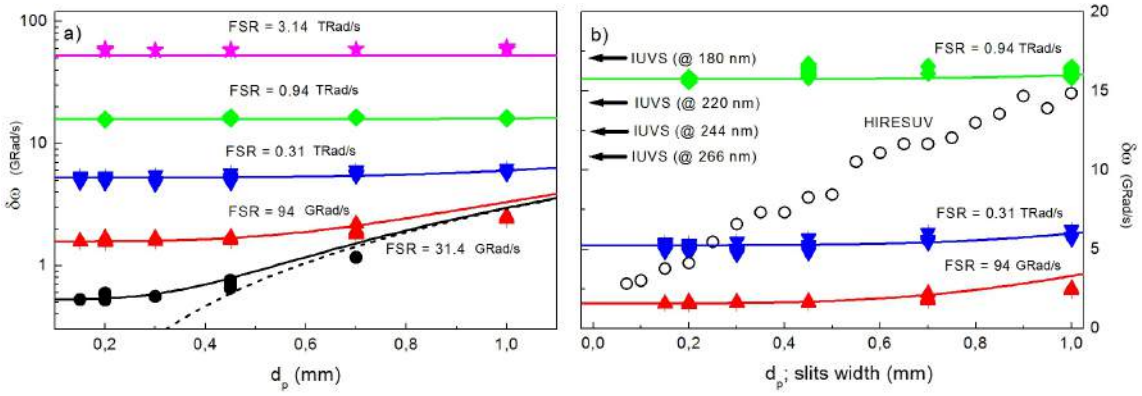

Figure 4.3: Left panel: $\delta\omega$-values (symbols) as a function of d_P at given FSR-values (indicated in the figure), full and dotted lines are Eq. 4.1 and the (FRS-independent) F_P contributions to $\delta\omega$; data are reported in a logarithmic scale. Right panel: subset of data shown in the left panel of this figure compared with the $\delta\omega$-values of HIRESUV spectrometer (opens dots; from Fig. 6 of Ref. [40]), reported as a function of the width of the entrance slits of HIRESUV analyzer. Horizontal arrows indicate the $\delta\omega$-values of IUVS spectrometer at the indicated UV wavelengths.

the interferometer. In interferometer devices C is related to F through the relation:

$$C = \left[1 + \left(\frac{2F}{\pi}\right)^2\right]^N, \tag{4.2}$$

where N in the number of passes through the FP cavities. Therefore $N = 2$ for the system (tandem 1+1 pass interferometer) described in this chapter. It can be shown that C-values of 10^6 are expected, except when F_P decreases down to below ≈ 150: e.g. for $d_P > 0.45$ mm and $FSR < 0.1\ TRad/s$. I_{max} and I_{min} values can be extracted from the IRF measurements shown, e.g., in Fig. 4.2 and C-values of $10^4 - 10^5$ were found. However, the I_{min} values have to be eventually corrected for background contributions, which were measured (several hours of typical acquisition time) at some selected (d_P,FSR)-values. Indeed, a flat (ω-independent) background level of about 1-15 Hz was found. As a rule of thumb, the higher is d_P and the larger is the overall background, which includes the detector dark count ($\approx 0.3\ Hz$, independent from d_P), the leakage of UV fluorescence light from the optics outside the interferometer through IF (0.5-2 Hz for typical laser power of 5-10 mW) and the spurious room light entering the interferometer. For d_P-values ≥ 0.45 mm the latter contribution is definitely the leading one. Such a background signal (I_{bck}^{scaled}), properly scaled for the photon flux (UV fluorescence contribution) and acquisition time (dark count and environmental light contributions), was then used to estimate C through the relation: $C \approx I_{max}/(I_{min} - I_{bck}^{scaled})$. Once corrected for the background, the measured contrast was found to be in the $0.8 \cdot 10^6$-10^5 range. The lower C-value with respect to the expectations could be attributed to spurious (fluorescence and/or diffuse) light from the optics inside the interferometers. An example of IRF plus background measurement is shown in Fig. 4.4, as compared with the IRF of HIRESUV; the IUVS IRF is not reported because of its sensibly lower contrast ($> 10^4$). It is worth noticing how, despite the much lower overall contrast with respect to the

HIRESUV case, in the low frequency spectral range ($\approx \pm 30\ GRad/s$) the IRF of the present instrument has a substantially better contrast. This characteristic is a direct consequence of the use of an interferometric-based analyzer, which is able to provide a sharper IRF lineshape with respect the ones featuring grating-based devices, as HIRESUV and IUVS, that are characterized by less sharp spectral tails. This distinguish feature can be profitably exploited, e.g., both in the cases of low sound speed materials (for instance gases or low-density/high-temperature liquids) or when the lineshape of non-hydrodynamic modes located close to the elastic lines (e.g., the Mountain peak [109]) has to be determined. It is finally worth noticing that C would dramatically increase when a multipass interferometer system, such as a tandem 3+3 passes, is used. Indeed, the conservative choice of realizing a 1+1 system was essentially motivated by the need of minimizing the risk of failure. Moreover, it is fully compliant to demonstrate the possibility to realize a high-resolution/high-contrast interferometer-based UV-BLS setup with a compact (table-top) design easily fitting in small sized laboratories. However, the good agreement between observed and expected performances, the overall stability of the instrument and, as shown further below, its relatively large throughput calls for eventual developments of more sophisticated multipass devices. Fig. 4.5 reports a comparison between UV-BLS spectra

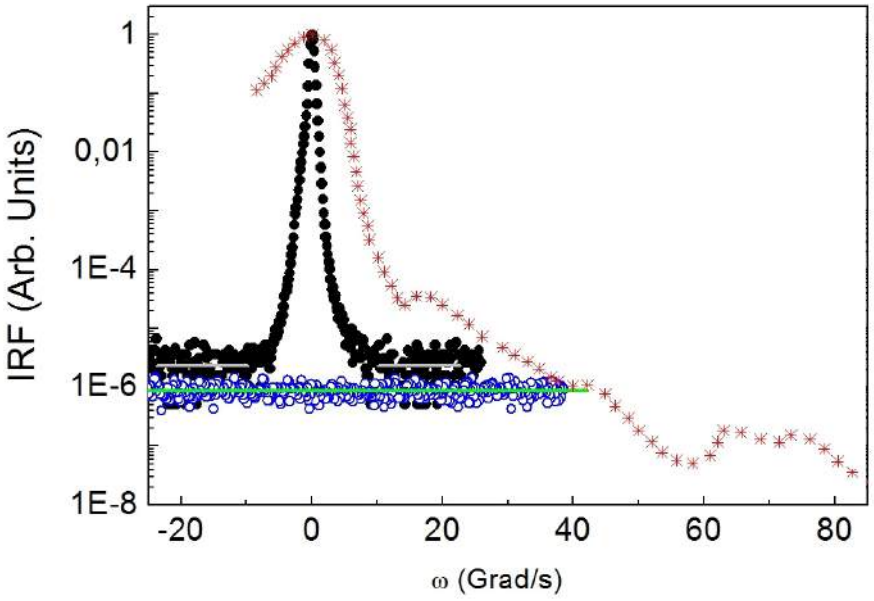

Figure 4.4: IRF corresponding to d_P=0.2 mm and FSR 31.4 GRad/s (dots) as compared with the corresponding background measurement (blue circles), the straight horizontal green/grey lines are the I_{bck}^{scaled}/I_{min} values used to estimate the contrast ($C = 0.7 \cdot 10^6$); red asterisks is the IRF of HIRESUV (from Fig. 7 of Ref. [40]).

from a representative samples (water) obtained with the present set-up and those acquired using HIRESUV (from Fig. 11 of Ref. [40]) and IUVS. The latter measurements were made tuning the undulator source in order to emit 244 nm radiation. All the reported spectra are featured by two symmetric side peaks accounting for propagating longitudinal acoustic (LA) modes. The peak frequency (Ω_L) and broadening

($\widetilde{\Gamma}_L$) of these modes are related with the adiabatic sound velocity (c_s) and longitudinal kinetic viscosity (D_L) through the relations shown in chap. 2. The spectrum reported in Fig. 4.5 was collected from a water specimen at 20 ^oC in a backscattering geometry ($2\theta = 180°$); 3 minutes acquisition time and 5 mW laser power. The d_P and FSR values were 0.7 mm and 0.31 $TRad/s$, respectively, thus giving a $\delta\omega$-value of about 5 $GRad/s$; very similar to the typical resolution bandwidth of HIRESUV and substantially lower than the IUVS one. Such spectrum is compared with a water spectrum from IUVS ($2\theta = 172°$, acquisition time 3 minutes, sample temperature 20 $°C$, photon wavelength 244 nm) and one from HIRESUV ($2\theta = 172°$, sample temperature 26 $°C$); since for the latter spectrum the acquisition time was not reported, it has been scaled by a factor 0.4 for clarity. The first observation concerns the satisfactorily high overall throughput of the instrument, at least with respect to IUVS. The evident shift in Ω_L as well as the larger value of $\widetilde{\Gamma}_L$ with respect to HIRESUV data are mainly due to the different UV photon wavelength used in these experiments. On the other hand the quite larger $\widetilde{\Gamma}_L$ value of IUVS spectrum is instead due to the broader IRF of IUVS. Indeed, Ω_L and $\widetilde{\Gamma}_L$ values fully consistent with the expectations can be extracted from all of the three spectra reported in Fig. 4.5. The developed system demonstrates how a compact-design UV Brillouin scattering instrument, which could be implemented in any laboratory, could be competitive or even better than more complex (eventually synchrotron-based) instruments. The positive test of this first prototype also calls for the design of more sophisticated multipass compact table-top interferometer systems, which are expected to provide an instrumental contrast remarkably better than any available UV-BLS instruments. More generally, the possibility to build up such kind of small-sized UV Brillouin scattering spectrometers may potentially fill the general lack of

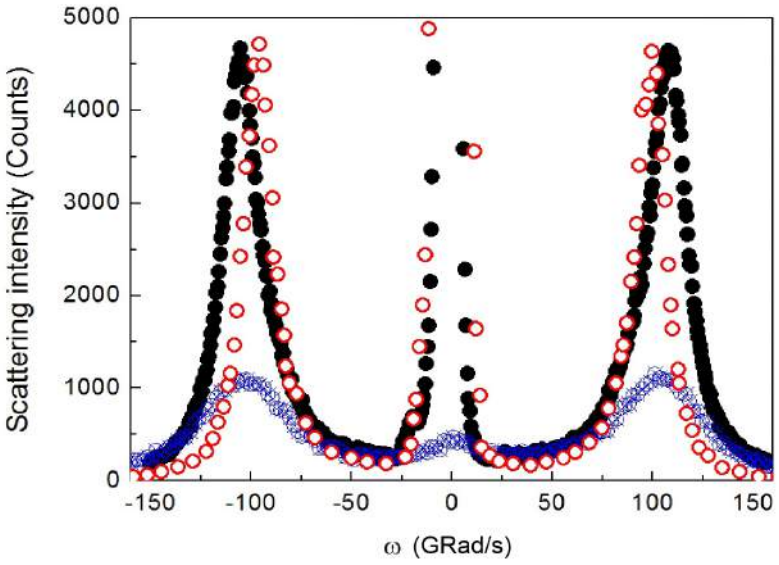

Figure 4.5: UV-BLS spectrum of water collected in backscattering geometry (black dots; $\delta\omega$ set at $\approx$ 6 GRad/s) compared with HIRESUV (red circles; from Fig. 11 of Ref. [40]) and IUVS data (crossed blue circles). See text for further details on the experimental conditions.

UV-BLS instrumentation, which, to date, is basically covered by the (heavily overbooked) IUVS beamline at the Elettra synchrotron radiation facility. Indeed, many experiments would be carried out without necessarily using a tunable synchrotron source. The growing up in the number of available UV-BLS instruments could likely be fruitfully exploited in different scientific applications, ranging from the study of collective dynamics in disordered systems to vibrational modes in nanostructures.

Chapter 5

A look to the future: the EIS-TIMER project

In the previous chapters we demonstrated the need to explore a widest as possible spectral range to study disordered systems. Referring to fig. 5, we gave to the reader an overview of the nowadays available techniques to gain information about the acoustic mode evolution and, hence, about the all dynamical processes occurring in the media.

Optical TG is able to probe the low-Q region of the ω-Q plane, essentially irrespectively to the timescale range, while, also thanks to the tools and instrumentations developed in this thesis work, one can use frequency-resolved Brillouin scattering to cover with continuity the visible-UV spectral range. The high-Q range of the ω-Q plane is the realm of atomic-size probes, such as hard x-rays and thermal neutrons, which can be inelastically scattered by high-Q atomic density fluctuations [110, 111]. Between these low-Q and high-Q extremes, where matter looks like a continuum and an ensemble of distinct atoms, respectively, there is a no man's land, also referred to as "mesoscopic" region, that extends from 0.1 nm^{-1} to 1 nm^{-1}. While the low-Q region can be described within classical elastic theory or hydrodynamics and the high-Q one can be modeled within the single particle (incoherent) approximation, there are not well assessed models to describe the Q-region between 0.1 and 1 nm^{-1} in systems without translational periodicity. Within such range, one would be able to directly observe the system transition between a hydrodynamic behavior (fully relaxed regime) and the single particle limit (not relaxed regime). The chance to have access to this spectral region will give us the unique possibility to better understand the nature of the two physical limits and to shed light on the macroscopic anomalies of glasses, that are supposed to be found there. All techniques listed above use optical/UV laser sources or synchrotron based ones. In both cases there are some technical issues to extend the already existing methods to the mesoscopic region: from the high-energy side, we are limited by the achievable resolution; while the laser based techniques are limited in λ to select high Q-values.

A relevant step forward for optical spectroscopy would be to combine core level spectroscopies and their elemental selectivity with time-resolved methods and nonlinear techniques [112]. To do so, we need novel photon sources capable of delivering ultrafast EUV/x-rays photon pulses with coherence properties comparable to those

of table-top lasers. Toward this direction is moving the development of HHG (High Harmonics Generation) sources [113] that, however, at the present stage, are not brilliant enough for FWM applications.

A new era has begun with the advent of EUV/x-ray FELs [114]. These are much brighter than HHG sources and are able to provide radiation which is (almost) as coherent as optical lasers spatially, and in case of seeded sources like FERMI, also temporally [115]. Thanks to the advances achieved during the last few years, which also include the development of multi-color FEL sources [116, 117, 118, 50, 119], non-linear coherent experiments in EUV/x-ray regime are no longer a mere theoretical speculation. These experiments would allow the study of, for example, ultrafast charge migrations and energy transfer processes with nanometric to atomic spatial resolution and elemental selectivity [120, 50], as well as of collective atomic dynamics in the unexplored (0.1-1 nm^{-1}) wavevector range, which is of the highest relevance for disordered systems and nanostructures [121, 122].

The first simplest step towards the direction of (non-degenerate) EUV/x-ray FWM applications is to consider the particular case in which two pulses having the same polarization and photon frequency are crossed into a sample in time coincidence, and the elastically scattered third pulse is observed. This scheme, also termed Transient Grating (TG), allows to exploit, e.g., impulsive stimulated Rayleigh, Brillouin and Raman scattering processes [48], that are at the base of the rationale of the EIS-TIMER project.

5.1 Scientific Case and Objectives

EIS-TIMER is a beamline under construction at Fermi@Elettra FEL in Trieste (Italy). It will be dedicated to TIME-Resolved spectroscopy of mesoscopic dynamics in condensed matter. At present the experimental end-station has been commissioned, while the complex photon transport system is under construction and it is expected to be partially operational in 2015. One of the main aims of EIS-TIMER is to study the time evolution of density fluctuations in disordered systems (liquids and glasses), in the unexplored ("mesoscopic") wavevector (Q) range between 0.1 nm^{-1} and 1 nm^{-1} [121, 122]. The study of density fluctuations, particularly the Q-evolution of acoustic modes, in disordered systems is a very active field of research. From such kind of study one can gain information about the microscopic processes that are responsible for the macroscopic mechanical and thermodynamical properties of the material. In particular, some of the most debated topics concern: (i) the understanding of the liquid-glass transition, (ii) the excess low-temperature specific heat and the excess density of vibrational states in glasses, (iii) the microscopic origin of sound attenuation in glasses and viscosity in liquids, etc.

EIS-TIMER will exploit the full (i.e. both transverse and longitudinal) coherence of FERMI to extend coherent non-linear methods from the optical into the EUV/soft x-ray spectral domain. In this context, the project is to develop FEL-based four-wave-mixing (FWM) experiments, in particular those based on the transient grating (TG) approach.

As these experiments rely upon the coherent interaction of three FEL pulses, the

key requirement for the EIS-TIMER photon transport system is the capability to split the FEL beam into three parts, that have to be delayed and recombined at the sample at given angles. The idea for the basic configuration is to use both the first and third harmonics of the FEL emission: two first harmonic pulses are sent into the sample with an inter-beams angle 2θ in time coincidence, while a third harmonic beam is time-delayed by a right angle delay line, made out of 4 multilayer (ML) coated mirrors, and then impinges into the sample at an angle $\theta_B = \sin^{-1}(\sin\theta/3)$ to fulfill the so-called phase matching condition. The beam splitting is achieved by a sequence of two wavefront division beam splitters [121, 122, 123], while two additional plane mirrors route the third harmonic beam into the delay line. The focusing of the beams at the desired angles is finally provided by three independent toroidal mirrors.

Such a configuration will allow to perform impulsive stimulated Brillouin, Raman and Rayleight scattering experiments in the unexplored 0.1-1 nm^{-1} wavevector (Q) range, which is expected to be of the highest relevance for the study of dynamics in disordered systems and nanostructures [121]. The possibility offered by FERMI and EIS-TIMER to exploit the aforementioned two-color FEL emission, additional "jitter-free" optical pulses and the independent control of the relative time delays between the three pulses (one of them limited to the -1 +7 ps range), would allow to carry out further FWM-based experiments, such as, e.g., coherent Raman scattering [120, 49, 124], photon echo or multi-dimensional spectroscopy [125]. These methods are currently applied in the optical regime and have demonstrated their capability to probe a large array of dynamical processes, ranging from molecular vibrations to spin waves, with energy-wavevector selectivity and ultrafast time resolution, as well as to investigate dynamical processes inaccessible by linear light-matter interactions. The EUV/soft x-ray analogues of such techniques will potentially extend the range of investigable excitations towards high energy modes, such as valence-band excitons, and will allow for nano to atomic spatial resolution, as well as for atomic selectivity, through the selective exploitation of core resonances.

5.2 Layout of the end-station

The main issue to be taken into account in the design of the EIS-TIMER photon transport system is the high absorbance of all materials at the EUV/soft X-ray wavelengths of interest. This prevents the use of transmitting optics, such as phase masks [52], that are widely employed in traditional TG setups since they lead to a relevant simplification of the layout. The feasibility of an optical scheme based on all-reflecting optics and, in particular, on plane mirrors used as wavefront division beamsplitters was demonstrated in our laboratories by Cucini et al. [123]. Such a strategy to obtain the three input pulses has also the advantage to avoid any relevant pulse chirping.

The absence of phase masks makes difficult to obtain a so-called local field, which can be used for heterodyne detection (HD) of FWM signals [52]. HD is usually employed to largely enhance the overall signal, hence improving the signal/noise ratio, as well as to determine both amplitude and phase of the signal field. The latter

capability can be profitably exploited to study particular kinds of excitations, as polaritons or spin waves. Actually, we recently demonstrated (see sec.3.5.2) the possibility to use optical TG with homodyne detection to disentangle the dynamics related to rotational, orientational and translational degrees of freedom in liquids, a task usually achieved by HD-TG [126]. In order to discriminate all these contributions, it was necessary to perform homodyne detected TG measurements varying the polarizations of the input beams, a solution which is also exploitable at EIS-TIMER thanks to the polarization tunability of the FERMI FEL.

Another issue to be discussed is related to the efficiency of FWM processes in the EUV/soft x-rays range. So far, only calculations and simulations have been performed to estimate EUV/x-ray FWM signals [120, 127, 50, 124] while no experimental data at sub-optical wavelengths are available. In July 2014, we carried out the very first FWM experiment stimulated by EUV transient gratings (see next chapter). We observed a detectable EUV-FWM signal from a vitreous SiO_2 sample, that allowed us to estimate an overall efficiency of the FWM process of about $1.5{\cdot}10^{-7}$, which, in light of our specific experimental conditions, results to be quite similar to that found in the optical regime. Other pioneering coherent non linear X-ray experiments based on second-order processes [128, 129, 130] report a substantial reduction in the experimental signals with respect to the optical analogues (a.g., an amazingly low count-rate of a single photon over hundreds FEL shots at full power is reported in [130] while we observed one million photons per shot with FEL fluxes orders of magnitude lower). This is due to the shorter x-ray wavelengths with respect to EUV photons and to the lower degree of longitudinal coherence of there employed photon sources, as compared to the almost Fourier transform limited pulses delivered by FERMI (this thanks to the unique technology of laser seeding). Fig. 5.1 sketches the conceptual layout of the EIS-TIMER beamline. To fully cover the mesoscopic region (Q=0.1-1 nm^{-1}) it is necessary to exploit the whole wavelength range (100-10 nm) provided by FERMI and exploit large crossing angles (i.e. up to above 90°). We also mention that, following some reconsiderations of the FEL performance and machine upgrades, the minimum exploitable wavelength range of FERMI is now pushed down to the 3-4 nm range. As already stressed, in order to reduce the absorption losses of EUV radiation and to avoid chirping, the beamline was conceived to operate with reflection optics only (plane and focusing mirrors). A first plane mirror is used as a wavefront division beamsplitter in the vertical plane to divide the beam into two halves. One of them is further split by another wavefront division plane mirror working into the horizontal plane into two halves that are used to excite the transient grating. The other half, routed into a right angle delay line by other two plane mirrors (not shown in Fig. 5.1), is used to probe the induced grating. The delay line is equipped by 4 multilayer (ML) mirrors operating at 45° angle of incidence and optimized to reflect the 3^{rd} harmonic of the FEL radiation (wavelength λ_3), whose intensity is of about 1% of that of the 1^{st} harmonic (wavelength λ_1); 4 sets of 4 MLs optimized for the 18, 13.3, 6.72 and 3.17 nm radiation will be available. Such MLs can provide an extinction ratio of the 1^{st} over the 3^{rd} harmonic by more than six orders of magnitude, while the 45° geometry allows probing time delays as large as a few ns. Solid state filters can eventually be used to suppress the residual 1st harmonic component from the probe beam and/or

the 3rd harmonic content from the pump beams. In order to accomplish the phase matching conditions, the angles of incidence of the three beams at the sample have to satisfy the relation: $\sin\theta/\lambda_1 = \sin\theta_B/\lambda_3$, where 2θ is the crossing angle between the two interfering first harmonic beams and θ_B is the angle between the bisector of these beams and the probing third harmonic beam. The three FEL pulses are finally focused into the sample at the correct angles by a set of three toroidal mirrors (TM). In order to change θ (and θ_B accordingly) the three TMs can be removed from the beam path and other three TMs can be inserted downstream; 4 sets of three TMs will be available to exploit the angles θ=9.2°, 13.8°, 39.5° and 52.7°. Since $\lambda_1 = 3\lambda_3$, a given set of ML and TM defines the actual Q-value, according to the relation $Q = 4\pi/\lambda_1 \sin\theta$ (see Table 5.1). In case one would exploit the full wavelength tunability of FERMI, an ultrafast ("jitter-free" [131]) optical pulse tunable in the VIS-UV range can be used as an alternative probe, though the longer wavelength of such pulse will not allow to fulfill the phase matching in the entire λ range. We finally mention that the relative time delay between the two interfering pulses can be adjusted in the -1 +10 ps range.

Concerning the detection scheme, and also in light of our recent experience with the aforementioned EUV stimulated TG experiment, we foresee the use of both a cooled CCD camera in vacuum and fast photodiodes in combination with a boxcar amplifier. The latter can provide faster acquisition times, while the former can be used, in combination with a special setup, to map out the time dependence of the FWM signal into the spatial coordinate; using chirped pulses also the frequency content of the FWM signal can be mapped out on the CCD. Furthermore, the CCD

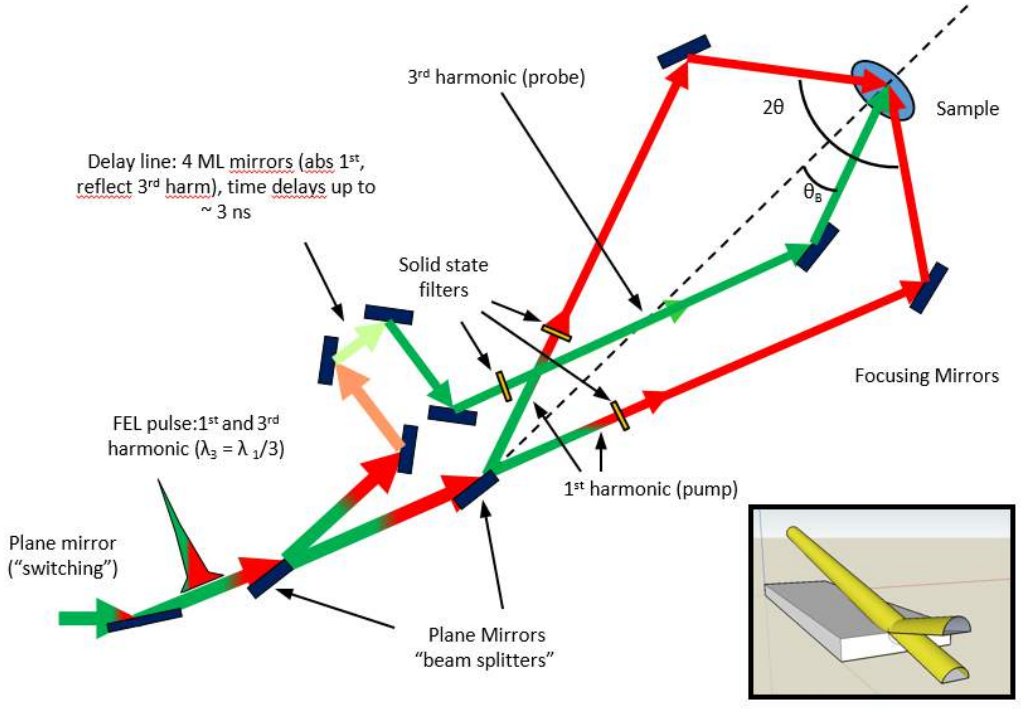

Figure 5.1: Sketch of the EIS-TIMER layout.

$\theta(\downarrow)\lambda_1(\rightarrow)$	54 nm	39.9 nm	20.16 nm	9.51 nm	5 nm	3 nm
9.2 °	0.037	0.05	0.1	0.21	0.4	0.67
13.8 °	0.055	0.075	0.15	0.32	0.6	1
39.5 °	0.15	0.2	0.4	0.84	1.6	2
52.7 °	0.19	0.25	0.5	1.05	2	3.3

Table 5.1: Q-values available at EIS-TIMER as a function of θ (rows) and λ_1 (columns); the last two columns on the right corresponds to λ_1 values achievable by FERMI but not foreseen by the present layout of EIS-TIMER.

detector will permit to determine the full footprint of the FWM signal, which can be of relevance when the phase matching conditions are relaxed due to thin grating effects. The latter are very likely if one uses optical radiation for probing the FEL-induced EUV/soft x-ray gratings, since in those cases the penetration depth of the FEL radiation is usually shorter than the optical wavelength in the material. TG signals (either optical of EUV/soft x-ray) could be in principle detected both in transmission and in reflection geometry.

We finally mention the possibility to use CW optical probing with sub-ns sampling to study dynamics longer than the ns range and to use permanent gratings, created in situ by high-flux irradiation with FEL pulses, to generate local fields for HD-TG measurements.

Chapter 6

The mini-TIMER experiment

In this section we report about the first EUV-FWM experiment we performed ad the seeded Fermi Free Electron Laser as a proof of feasibility per the TIMER project. Here we proposed a revised compact and simplified setup in respect to that one shown in Ch. 5 using two coherent EUV pulses as pumps and an optical probe.

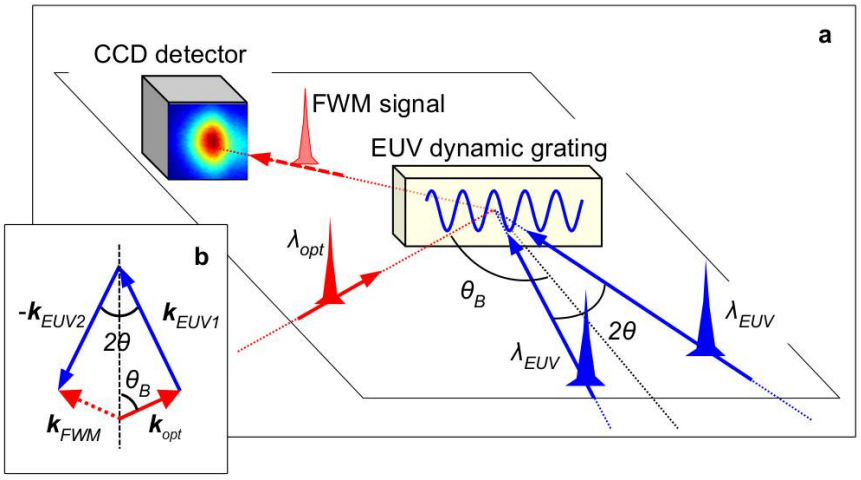

Figure 6.1: FWM experiments with EUV transient gratings. ***a****, sketch of the FEL-based FWM experiment:* 2θ*=6.16°,* θ_B*=49.9°,* λ_{EUV}*=27.6 nm and* λ_{opt}*=392.8 nm are the crossing angle between the two FEL beams that generate the EUV dynamic grating, the angle between their bisector (dashed black line) and the optical beam, the FEL and laser wavelength, respectively. A CCD sensor is placed along the expected propagation direction of the FWM signal beam (*$\underline{k}_{FWM}$*), which is determined by the "phase matching" (shown in (****b****); here* $\underline{k}_{opt}$*,* $\underline{k}_{EUV1}$ *and* $\underline{k}_{EUV2}$ *are the wavevectors of the optical and of the two FEL pulses, respectively).*

Fig. 6.1a shows a sketch of the experiment: two FEL pulses (λ_{EUV} = 27.6 nm, estimated time duration 60-80 fs, pulse energy $I_{EUV1} \approx I_{EUV2} \approx 5\mu J$, spot size 0.04 mm^2) are crossed (angle: 2θ=6.16°) on a vitreous SiO_2 sample with the surface oriented orthogonally to the bisector of the FEL beams. The interference of the two pulses generates EUV transient gratings (TG) with a spatial periodicity $L = \lambda_{EUV}/2\sin(\theta) \approx 256.8nm$. An optical pulse ($\lambda_{opt}$=392.8 nm, time duration ≈ 100

fs, pulse energy $I_{opt} \approx 2\mu J$, spot size $\approx 0.002 mm^2$), coplanar to the FEL beams, was sent into the sample at an angle of incidence θ_B=49.8°. The polarization of the fields was orthogonal to the scattering plane. The chosen (λ_{EUV},λ_{opt},2θ,θ_B)-values fulfill the phase matching condition (see Fig. 6.1b), which in the present TG experiment reduces to: $\lambda_{EUV} \sin(\theta_B) = \lambda_{opt} \sin(\theta)$. This determines the propagation direction of the FWM signal: $\underline{k}_{FWM} = \underline{k}_{EUV1} - \underline{k}_{EUV2} + \underline{k}_{opt}$, where $\underline{k}_{EUV1,2}$ and $\underline{k}_{opt}$ are the wavevectors of the EUV fields and of the optical one, respectively. Along $\underline{k}_{FWM}$ the non-linear signal, radiated by different portions of the sample, adds coherently, yielding to a FWM signal propagating downstream the sample as a well-defined beam.

The experiment was carried out at the DiProI end-station using a purposely designed experimental setup based on reflective optics (see Appendix B). Such a setup lets us to adjust 2θ, θ_B, the time delay between the crossed FEL pulses ($\Delta t_{EUV-EUV}$) and those between the FEL pulses and the optical one (Δt). FEL-pump/optical-probe transient reflectivity measurements were used to determine $\Delta t_{EUV-EUV} = 0$ and to equalize the fluence of the two FEL pulses in the interaction region. The FWM signal was detected by a CCD placed along $\underline{k}_{FWM}$. After illumination by about 100's FEL shots, creation of permanent gratings was observed at FEL fluences larger than $\approx 50 mJ/cm^2$ per pulse (see Appendix B). The illumination of these permanent gratings by the optical laser led to a diffracted signal along $\underline{k}_{FWM}$ even in the absence of the FEL pulses. During the FWM measurements the FEL fluence was kept below 50 mJ/cm^2 in order to avoid the creation of permanent gratings.

Fig. 6.2a shows a CCD image of the FWM signal beam acquired at Δt=0, whereas Figs. 6.2b and 6.2c report the same measurement for Δt=-0.5 ps and 70 ps, respectively. The observation of a signal that propagates along $\underline{k}_{FMW}$ for Δt >0 in the concurrent presence of the three input beams undoubtedly demonstrates the occurrence of FWM processes stimulated by EUV transient gratings. The large angular spread observed along the plane of the input beams can be attributed to relaxed phase matching conditions, likely due to the fact that both L and the EUV absorption length ($L_{EUV} \approx$ 30 nm) are shorter than λ_{opt}. The total intensity of the FWM signal (I_{FWM}) at Δt=0 was $\approx 6 \cdot 10^5$ photons/shot, corresponding to an efficiency $\eta_{FWM} = I_{FWM}/I_{opt} \approx 1.5 \cdot 10^{-7}$. Concerning magnitude justifications, the strength of the FWM field radiated by the sample (E_{FWM}) is related to those of the input fields as $E_{FWM} \sim \chi^{(3)} E_{EUV1} E_{EUV2} E_{opt}$. In the present case we estimated $E_{EUV1} \approx E_{EUV2} \approx 0.8 \cdot 10^9$ V/m, so that an effective value for the 3^{rd} order susceptibility $|\chi^{(3)*}| \approx (\eta_{FWM})^{1/2}/(E_{EUV1} E_{EUV2}) \approx 6 \cdot 10^{-22}\, m^2/V^2$ (at Δt=0) can be estimated. This value is within the expected order of magnitude, since $|\chi^{(n)}|$ scales as E_a^{1-n}, where $E_a \approx e/(4\pi\epsilon_0 a_0^2) \approx 5 \cdot 10^{11}$ V/m is the atomic field strength (here e, ϵ_0 and a_0 are the elementary charge, the dielectric constant and the Bohr radius, respectively) [49, 124, 50, 132].

The time evolution of η_{FWM} is shown in Fig. 6.3a. The data are scaled by the factor $\alpha = I_{EUV1}(\Delta t = 0) I_{EUV2}(\Delta t = 0)/[I_{EUV1}(\Delta t) I_{EUV2}(\Delta t)]$. Approaching Δt=0 from negative delays a fast rise of the FWM signal, compatible with a cross-correlation profile ($R_{cc}(\Delta t)$), was detected. For Δt>0 an appreciable FWM signal is observed over the whole probed Δt-range (i.e. up to 130 ps). The signal observed at

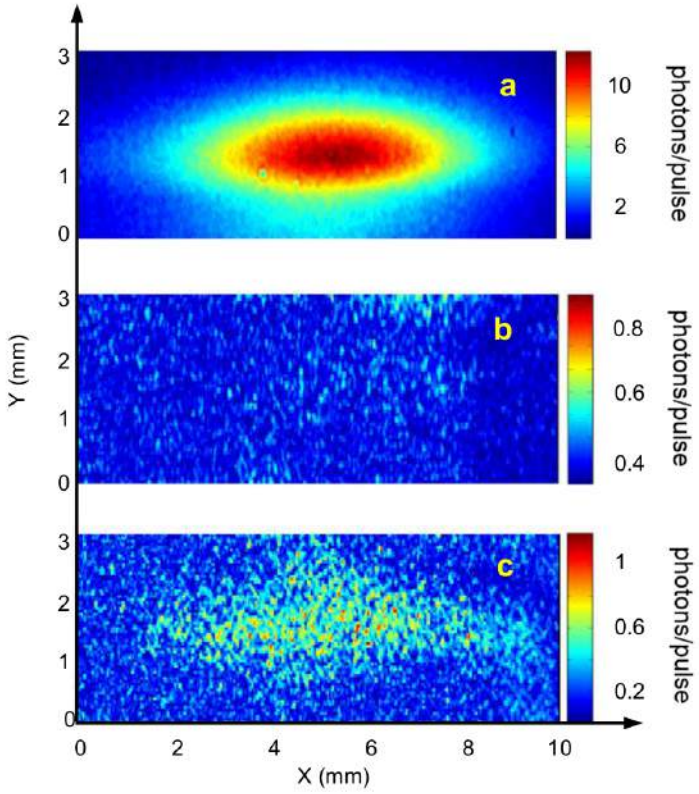

*Figure 6.2: FWM signal stimulated by EUV transient gratings. Images from the CCD placed along $\underline{k}_{FMW}$ (X and Y are the directions parallel and orthogonal to the scattering plane, respectively). The images were acquired at $\Delta t = 0$ ps (**a**), Δt=-0.5 ps (**b**) and Δt=70 ps (**c**), respectively.*

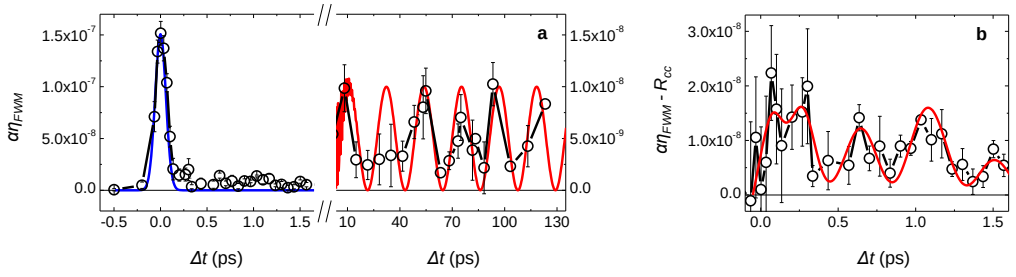

*Figure 6.3: Time evolution of the FWM signal. **a**, black circles connected by lines are the time dependence of the FWM signal, scaled to the intensity of the input beams (error bars are estimated as one standard deviation of the set of CCD images corresponding to the same Δt value); the blue and red lines are R_{cc} and the expected signal modulation due to acoustic modes, respectively. **b**, black circles connected by lines is the FWM signal after R_{cc} is subtracted. The red line is the modulation due to oscillations at frequencies ν_1=1.15 THz and ν_2=4.1 THz.*

large Δt's (>10 ps) can be ascribed to thermal relaxations and longitudinal acoustic modes [48]. The latter is expected to induce a signal modulation at frequency $\nu_{LA} = c_s/L \approx 23.2$ GHz (where c_s=5970 m/s is the sound velocity of vitreous SiO_2), which is compatible with our data. Fig. 6.3b displays the FWM signal in the 0-1.6 ps range after $R_{cc}(\Delta t)$ is subtracted. Here the time structure of the FWM signal is compatible with two oscillations at frequencies ν_1 ≈1.15 THz and ν_2 ≈4.1 THz. The latter frequency roughly matches that of the ν_{2b} Raman modes, due to tetrahedral bendings, while the former, that accounts for the leading modulation of the observed FWM signal, can be ascribed to F_1 hyper-Raman modes, that involve rotations of SiO_4 tetrahedra (see Appendix B). Our results demonstrate the generation of dynamic EUV gratings using fully coherent FEL pulses. The non-linear interactions between the induced grating and an optical pulse allowed us to observe the first FEL-stimulated FWM signal, that encodes the dynamics of impulsively stimulated collective vibrational modes with wavevector $\underline{k}_{ex} = |\underline{k}_{EUV1} - \underline{k}_{EUV2}|$. This suggests how EUV transient gratings can drive coherent excitations into the sample and pave the way for the practical exploitation of non-linear optics in the EUV/SXR range. In this context, the next step that we will illustrate in the near future is to replace the optical pulse with an EUV/SXR one (EUV probing of optically stimulated transient gratings was already reported [133, 134]) to probe vibrational modes in the 0.1-1 nm^{-1} $\underline{k}_{ex}$-range. This range, inaccessible by optical FWM (see Fig. 6.4a), can be probed by using photon wavelengths down to 10 nm (i.e. well within the range of FERMI), and is of special relevance for the investigations of disordered systems. Indeed, the origin of their thermodynamic peculiarities (e.g. the highly debated excess specific heat) seems to be related to "mesoscopic" heterogeneities extended over a few nm length-scales, which can be revealed by the anomalous behavior of vibrational modes in the 0.1-1 nm^{-1} $\underline{k}_{ex}$-range. An opportunity offered by the FEL technology is the use of two-colour FEL pulses [117, 116, 118] to generate coherent populations of excited states via FWM processes, such as coherent Raman scattering (CRS). In CRS the excitation energy and wavevector are set by the photon energy difference ($\omega_{ex} = \omega_1 - \omega_2$) of the stimulating pulses and by the grating vector $\underline{k}_{ex} = \underline{k}_1 - \underline{k}_2$, respectively (see Figs. 6.4b and 6.4c). Compared to the optical regime, EUV/SXR pulses (10-1000 eV) will allow to coherently stimulate excitations at higher energy (e.g. excitons with ω_{ex}=1-10 eV). These can be probed by a third pulse, generated by the FEL or by an external source. Furthermore, when the field frequencies of the stimulating and/or probing pulses are tuned to core resonances of given atoms, the localization of core shells turns into an atomic-scale localization of the site at which the selected excitation is created and/or probed (see Figs. 6.4c-6.4d). In a nutshell, by tuning the field frequencies and time delay it is possible to use FWM to gain real-time information on the excitation transfer between selected atomic sites. This possibility is forbidden in linear inelastic scattering where the light-matter interaction takes place at the same atomic site. Further-on multi-wave interactions allow the application of a time delay (τ, see Fig. 6.4c) between the excitation pulses (e.g. by setting $\Delta t_{EUV-EUV} = \tau \neq 0$ in our setup). This is a substantial step towards multi-dimensional spectroscopy and may consent to distinguish resonant and non-resonant FWM signals. On experimental grounds the core-resonant FWM is still an unexplored field, though solid theoretical approaches and numerical studies

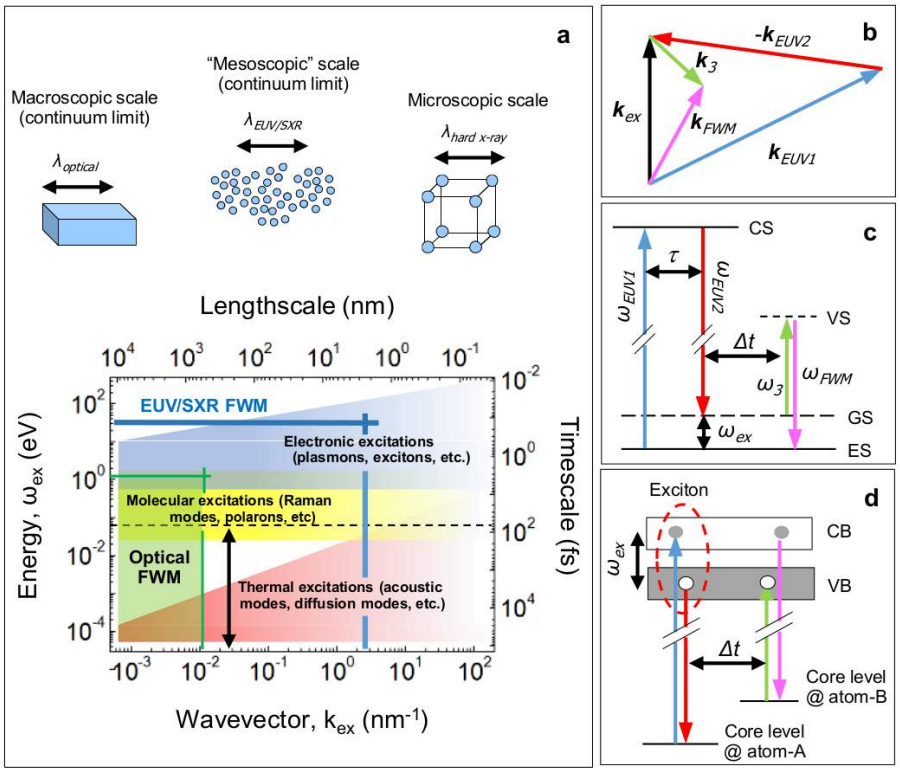

Figure 6.4: Outlooks. ***a****, energy-wavevector ($\omega_{ex} - \underline{k}_{ex}$) range of typical excitations in condensed matter and corresponding time-length scales. The green area sketches the range accessible by optical FWM while the double-ended blue vertical arrow is the range probed in the present work; the horizontal dashed line is the time duration of the excitation pulses. The area delimited by the thick blue lines represents the ($\omega_{ex} - \underline{k}_{ex}$) range accessible by EUV/SXR FWM, with the addition of a EUV/SXR probe and the development of EUV/SXR CRS.* ***b****, wavevector arrangement for a CRS process involving two-colours FEL excitation pulses ($|\underline{k}_{EUV1}| \neq |\underline{k}_{EUV2}|$); $\underline{k}_3$ and $\underline{k}_{FWM}$ are the wavevectors of the probe and signal beams, respectively.* ***c****, level scheme in case ω_{EUV1} is tuned to the energy of a core state (CS) transition and $\omega_{EUV1} - \omega_{EUV2}$ to a lower energy excitation (ω_{ex}). GS and ES are the ground and excited states, respectively, while VS is a virtual state (in standard CRS the CS is replaced by a VS); τ is the eventual time delay between the two excitation pulses while ω_3 and $\omega_{FWM} = \omega_3 + \omega_{ex}$ are the photon energies of the probe and signal beams, respectively.* ***d****, the independent control of three EUV/SXR input beams might allow to separately tune the energy of the excitation and probe beams to CS's of two distinct atoms (atom-A and atom-B), hence allowing for monitoring the excitation dynamics among two different atomic sites (a valence band exciton in this sketch; here VB and CB are the valence and conduction bands, respectively).*

in the SXR are available [120, 135, 136]. Core resonant FWM will soon be tested at FERMI, since many elements (C, Mg, Al, Si, Ti, etc.) have resonances within the photon energy range of FERMI (20-310 eV). The third harmonic of the FERMI FEL emission (photon energy range: 60-930 eV) and the forthcoming construction

of self-seeded SXR FEL sources with a wider photon energy range (e.g. SCLS-II, SwissFEL and PAL-XFEL) could be most likely used to exploit resonances at higher energy.

FWM with elemental selectivity could have relevant applications for instance to study charge transfer dynamics in electrocatalytic processes occurring in photoelectrochemical cells, devices that mimic natural photosynthesis to convert sunlight into chemical energy (solar fuels). These are typically based on molecular complexes adsorbed on TiO_2 substrates and have a conduction/valence band dominated by the Ti/O orbitals. FWM with elemental selectivity may disentangle the timescales of electron and hole migration, by exploration of the Ti and O resonances, as well as to shed light on the water oxidation dynamics taking place at the catalyst by separating the signal originating from reaction centers. Since elements of biological interest (C, N, O) have resonances in the EUV/SXR range, applications in life sciences are also very likely.

The demonstration of FEL-based FWM represents a fundamental milestone towards the development of non-linear optics at sub-optical wavelengths. We demonstrate that EUV FWM is already possible by using fully coherent FEL pulses, as those routinely delivered by FERMI and, in the foreseeable future, by other EUV/SXR FEL facilities. The exploitation of this approach will allow to detect real-time correlations and charge/energy flows between different atoms, a capability unattainable by linear methods, as well as to probe the dynamics of elementary excitations (phonons, polarons, etc.) in an energy/wavevector range inaccessible by optical non-linear methods. These classes of non-linear experiments would become a powerful tool for revolutionary advances in physics, chemistry and biology.

Conclusions

In this thesis we used different experimental methods to study the dynamics of a prototypical disordered system, liquid acetonitrile, featured by a rich relaxation phenomenology. The main feature of the performed work is the multi-technique approach, which includes the use of both time and frequency resolved methods for the determination of the acoustic response of the system in an unprecedented frequency-wavevector (ω, Q) range. Indeed, the common characteristic of the employed experimental techniques is their capability to probe the real-time evolution or the frequency spectrum of density fluctuations correlation function. The latter is featured by the presence of acoustic modes, which can be regarded as a coherent set of compression and rarefaction zones. Acoustic modes are characterized by a broad (ω, Q)-spectrum, continuously ranging from 0 Hz and 0 m^{-1} up to some 10's of THz and nm^{-1}, i.e. from macroscopic length and time scales down to the characteristic time and length scales of intermolecular interactions and interparticle separation. The study of the acoustic response of the system carry out different information on several aspects of the system under study, essentially depending of the (ω, Q)-range at which the experiment is performed. In the low-(ω, Q) domain acoustic spectroscopy is used to study macroscopic properties (stiffness, viscosity, etc.) while at high-(ω, Q) these experiments can be used to gain information on microscopic physical quantities, such as, e.g., the anharmonicity of the interaction potential, caging and hopping effects. Acoustic spectroscopy also carries out information on the local structure (crystal symmetry, defects, etc.) and on thermodynamics, the latter requires in principle the determination of the whole (ω, Q)-range of vibrational modes. In crystalline materials the whole acoustic spectrum can be probed in a limited Q-range, corresponding to a single Brillouin zone. In disordered systems, the lack of a translational periodicity prevents that and the (ω, Q)-evolution of the acoustic mode has to be followed by using different experimental methods.

In light of its wide applicability and richness of information, acoustic spectroscopy is commonly used in a large array of research fields for various purposes. However, in most cases, the investigation is confined in limited frequency-wavevector ranges, matching the time-length scales of the phenomena of interest for a particular application. In this thesis work we show how a multi-technique approach can be profitably exploited to gain a comprehensive picture of the dynamical processes occurring in disordered systems, which include the effects of the relaxation processes associated to different dynamics occurring in different time-length scales. Furthermore, we point out that a more meaningful description of data collected in a given spectral range can be obtained by complementing the information arising from

different ranges. This is the case of the data obtained by inelastic hard X-ray scattering (a frequency-resolved method that represents the highest frequency acoustic technique), whose description requires the knowledge of parameters related to slow thermal dynamics, which can be attained by time-resolved transient grating methods (the lowest frequency technique employed in the present work). This example also underline the benefit of having access to inherently complementary techniques, as the time- and frequency-resolved ones. As showed in Ch. 3 we needed to consider also the structural information of the liquid (embodied in the static structure factor S(Q)) to analyze the IXS experiment. We then combined experimental techniques with molecular dynamic simulations. The latter in fact is the only way to obtain the S(Q) for molecular compounds. Taking special care of issues due to finite size effects in this computational approach, we could finally use them to properly reproduce the dispersion of the acoustic modes in the high-Q region typical of inelastic X-ray scattering. The information obtained from molecular dynamics simulations and transient grating experiments allowed us to soundly analyze, through the memory function approach, the quite structureless inelastic X-ray spectra. From those we were able to characterize the temperature dependence of the parameters accounting for the structural and instantaneous relaxations. The latter can be regarded as the process essentially related to intermolecular interactions (inter-particles collisions, intermolecular bonding, etc.) while the former basically accounts for any process faster than the fastest phonon mode of the system. In classical hydrodynamics both processes are responsible for viscous damping. The structural relaxation also rules the liquid-to-glass transition, which, naively speaking, can be observed either on a macroscopic scale (i.e. the real liquid-to-glass transition) or on a "microscopic one", by probing the response of the normal liquid over times so short (much shorter than the structural relaxation time) that molecules appear "frozen", hence loosing the distinctive feature of liquids with respect to solids, i.e. the unfixed particle positions. This latter case is the one we experienced in our inelastic X-ray scattering experiment. Data allowed us to determine the contribution of both processes to the viscous response of the system. The "instantaneous" process was found to be almost independent on temperature, while the "structural" one was found to have an activation behavior, as expected in light of its relationship with the continuous forming and breaking of the intermolecular bond network. We also determined the characteristic timescale for the structural relaxation and the related activation energy, which was found to be much larger than for weakly bonded liquids (as Van der Walls systems: neon and nitrogen) and similar to that of other strongly bonded liquids (as hydrogen bonded systems: water, ammonia and hydrogen fluoride). Interestingly enough, we found that the activation energy of the structural relaxation is smaller than what one may expect by scaling the ones of hydrogen bonded liquids by the critical temperatures. This might suggest a more complex role played by the large permanent dipole of acetonitrile with respect to other liquids.

Aimed at enlarging the accessible spectral range to study the evolution of the acoustic modes in disorder systems, during this thesis work, we conceived a novel and simple approach to obtain Brillouin light scattering measurements without artifacts arising from the finite aperture of the collection optics. We built so called "masks", spatial filters able to purify the collected scattered light by such spurious

contributions, and we successfully demonstrated their effectiveness on a reference sample. These results show how our masks can be used to collect Brillouin light scattering data also at scattering angles lower than the ones commonly used, i.e. 180° (backscattering geometry) or 90°. Thanks to these results, one could now extend, with continuity, the accessible spectral range from ≈ 0.002 (or even lower depending on the specific apparatus) to ≈ 0.03 nm^{-1}. Furthermore, this solution could be applied to any cases in which experimental constraints require the use of very large numerical apertures (e.g. micro-Brillouin experiments) or unconventional scattering angles (e.g. diamond anvil cells). We used this new tool, together with a data analysis based on frequency-dependent elastic moduli, to revise some precedent works on acetonitrile. As a result, we found a set of temperature-dependent parameters for the Kneser-type relaxation that are compatible with the low-frequency determination of the sound velocity, which was as well carried out within this thesis work and is fully compatible with previous ultrasonic data (see sec. 3.4). The values for the characteristic relaxation time determined in such a way differ by a factor 2 with respect to what previously reported and do not show any minimum in the temperature-dependence, while they still show the peculiarity to increase with temperature (a trend opposite to that of the structural relaxation).

The results obtained in the IUVS spectral range is a main demonstration of the effectiveness of such a broad band acoustic spectroscopy approach. Indeed, by looking at only these data one may infer the presence of some relaxation process responsible for the weak dispersion of the sound velocity; one might further analyze these data in a standard way and find values for the relaxation time and amplitude, etc.. However, these results would likely be incorrect. In fact we demonstrated that the dispersive behavior of acetonitrile in such a region is anomalous, as it cannot be accounted for by simply combining the results from the lower (Brillouin light scattering) and higher (inelastic X-ray scattering) spectral ranges. Without these information from the side spectral regions, we could not be able to interpret the obtained results, which are most likely due to some coupling effects between these two different relaxation processes. Thanks to the characterization of such relaxations in a wide spectral range as a function of temperature we were able to appreciate the soundness of the data and of the proposed interpretation. Indeed, a possible Kneser-structural coupling is endorsed by the fact that on decreasing temperature the two relaxation times gets closer and, concurrently, the deviation of the data with respect to the sum of the trends extrapolated from both higher and lower frequencies increases. We are aware that our interpretation of the observed phenomenon cannot be conclusive, but it paves the way to new interesting experiments to be carried out in the future on acetonitrile. In particular we stressed the importance of obtaining information from the intermediate spectral region between the BLS and IUVS, to have a continuous sampling of the occurring relaxation. In this perspective, we realized during these years of PhD, the first table-top experimental setup able to cover the aforementioned spectral region with an unparalleled contrast and resolution.

In this thesis we presented the first characterization of such an instrument which, combined with the spatial filters shown in sec. 1.1.1, is so far the unique technique able to bridge the BLS and IUVS spectral range. In the course of this thesis work we were able to combine many different experimental techniques and we had the

chance to conceive innovative solutions to cover those spectral range not accessible so far. Another approach that was followed in this thesis work to characterize the fast relaxation dynamics was the transient grating technique with sub-ps time resolution and polarization selectivity. When used to probe acoustic dynamics, the transient grating method is commonly used with ns time resolution, since the acoustic frequency in the wavevector range probed by transient grating is in sub-GHz range. However, by properly combining transient grating signals collected with certain polarizations of the input and output beams, it is possible to extract the time dependence of the isotropic component of the correlation function of density fluctuations. This quantity in principle contains the information on the time dependence of the structural relaxation irrespectively to the value of the acoustic frequency. In other words, if we have enough time resolution and the ability to control the polarization, we could probe directly the time decay of density fluctuations on the ps scale, that it is essentially due to the structural relaxation. In such a way we can get the desired information without using acoustic modes at THz frequency as a probe, without studying their dispersion relation and without being forced to employ some (often quite arbitrary) low-wavevector extrapolation of the data; furthermore, acoustic modes at THz frequency can be probed only through inelastic hard X-ray or thermal neutron scattering, methods only available at large user facilities. The comparison between data collected with ultrafast transient grating and with inelastic hard X-ray scattering shows an excellent agreement, thus suggesting that the proposed approach can be used to access the ultrafast dynamics of density fluctuations without being constrained, de facto, to the linear "frequency vs wavevector" (or, equivalently, "time vs space") relation strictly related to acoustic spectroscopy.

In spite of our efforts, a key region in the frequency-wavevector plane (located in the $\approx$ 0.15-1.5 nm^{-1} wavevector range) is still a "no men's land". In this framework we presented in this thesis the TIMER project, described in Chap. 5, which will give us the chance to access this unexplored "mesoscopic" region. This region is expected to be of special interest, e.g., for the study of dynamics in amorphous solids, since most of the anomalies of the glassy phase should be ascribed to the role played by acoustic-like modes located in such a range, presently inaccessible experimentally. Furthermore, this wavevector range compares with the typical size of so-called "elastic heterogeneities", that were recently proposed to account for glass dynamics. Besides glasses, the acoustic dynamics (and hence the related information mentioned above) of any sample featured by spatial periodicity in the 10's of nm range, such as many nanostructures, could be as well determined. As a proof of feasibility, we reported in Ch. 6 the first experimental evidence of a four-wave mixing experiment based on extreme ultraviolet transient gratings, recently obtained at the FERMI Free Electron Laser. This result is extremely promising for a forthcoming new class of coherent non-linear experiments that would exploit the powerfulness of the four wave mixing approach at sub-optical wavelengths. These experiments would extend beyond the acoustic spectroscopy, as different kind of four-wave-mixing interactions would be used to probe in real time and with energy-wavevector selectivity a large array of dynamical processes (excitons, plasmons, polarons, spin waves, etc.) in a frequency-wavevector range far beyond that accessible by optical spectroscopy. Furthermore, the multi-wave nature of this approach, combined with the extreme

ultraviolet and soft X-ray range accessible by FERMI, would allow to exploit the elemental selectivity to study, e.g., ultrafast charge and energy transfer processes between selected atoms in a sample.

Appendix A

Masks supplementary material

In this supplementary material we provide: (i) additional information on the equation to calculate the 'equal-Q' locus presented in Ch.1; (ii) the relation between the Δ_Q parameter and the width of the mask's slit; (iii) a set of masks designed for common experimental conditions, that may be printed and cut out to be directly used, without needing to write a software to generate them.

A.1 Equal-Q locus equation

In the following we describe step by step how to derive Eqs. 1.21 of the main paper:

$$\begin{aligned} x &= d_s \tan\varphi + d_q \tan[\arcsin(\tfrac{n_s}{n_q}\sin\varphi)] + \\ &+ [\tfrac{d_M}{\cos(\gamma-\beta)} - d_s - d_q]\tan[\arcsin(n_s \sin\varphi)] \\ y &= d_M \tan(\gamma-\beta) \\ \beta &= \arctan(\tan\theta\cos\alpha) \\ \varphi &= \arctan(\tfrac{\sin\theta\sin\alpha}{\sqrt{\sin^2\theta\cos^2\alpha+\cos^2\theta}}) \end{aligned} \tag{A.1}$$

where d_s,d_q,d_M are, respectively, the inner radius of the cylindric sample holder, the thickness of the walls of the sample holder and the distance between the center of scattering (O) and the plane of the collection optic; n_s and n_q are, respectively, the refractive indexes of the sample and of the sample holder material; γ, θ and α are, respectively, the angle between the axis perpendicular to the plane of the collection optic and the wave-vector of the incoming light beam ($\underline{k}_i$), the scattering angle and an auxiliary angle used to generate the mask profile.
As already stressed in the main paper, this equation in valid for a cylindric geometry in which refraction effects are taken into account. If you consider the (x,y) Cartesian reference frame shown in Fig. A.1, the equal-Q locus is the intersection between the plane (hereafter quoted as filter plane; in blue in Fig. A.1) parallel to the one of the collection optic and the curve resulting from the cone (originating from O and having

aperture and axis equal to θ and $\underline{k_i}//\overline{OH}$, respectively) after that the sample/sample holder and sample holder/air refractions are taken into account.

Because of the cylindrical symmetry, any beam coming from O is not affected by refraction in the y-direction. If we consider the generic point S lying on the scattering cone, then one can found that the y-coordinate of its projection on the filter plane is (see also fig. A.2):

$$y = d_M \tan(\gamma - \beta). \tag{A.2}$$

To determine β one has to consider the base of the cone perpendicular to $\overline{OH}$. There you can draw the radius $\overline{HL}$ lying on the plane perpendicular to the (x-y) Cartesian plane. Now the point S is univocally determined by the angle θ and α, the latter being the angle $\widehat{SHL}$. Being M the projection of S on $\overline{HL}$:

$$\beta = \arctan\left(\frac{\overline{HM}}{\overline{OH}}\right) = \arctan\left(\frac{\overline{HS}\cos\alpha}{\overline{OH}}\right) = \arctan\left(\frac{\overline{OH}\tan\theta\cos\alpha}{\overline{OH}}\right) = \arctan(\tan\theta\cos\alpha) \tag{A.3}$$

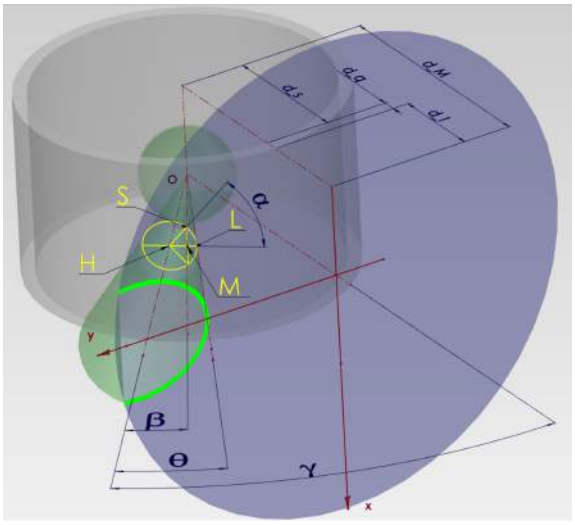

Figure A.1: The glow green line is the equal-Q locus on the plane of the collection optic for the cylindrical symmetry. Details are in the text.

Considering fig. A.1-A.2 it is easy to obtain:

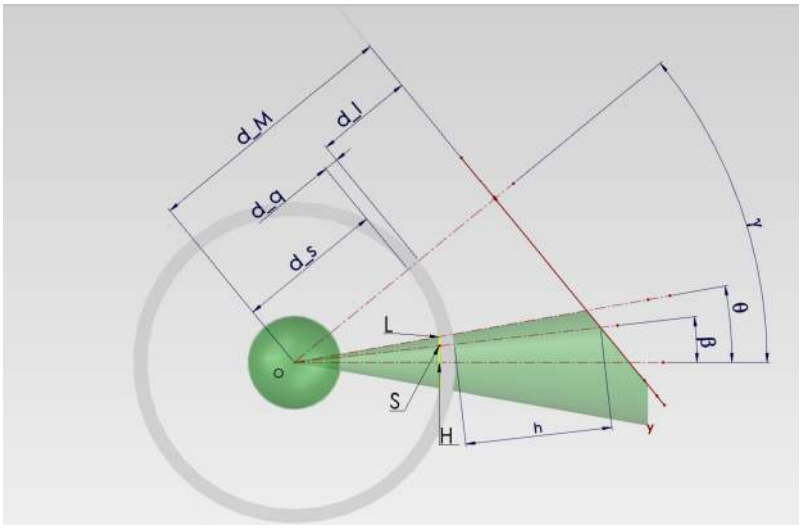

Figure A.2: Top-view of the scattering geometry.

$$
\begin{aligned}
\overline{OL} &= d_s \\
\widehat{OHL} = \widehat{OHS} &= \tfrac{\pi}{2} \\
\overline{HS} = \overline{HL} &= d_s \sin\theta \\
\overline{OH} = \overline{OL}\cos\theta &= d_s \cos\theta \\
\overline{SM} = \overline{HS}\sin\alpha &= d_s \sin\theta \sin\alpha \\
\overline{HM} = \overline{HS}\cos\alpha &= d_s \sin\theta \cos\alpha
\end{aligned}
\tag{A.4}
$$

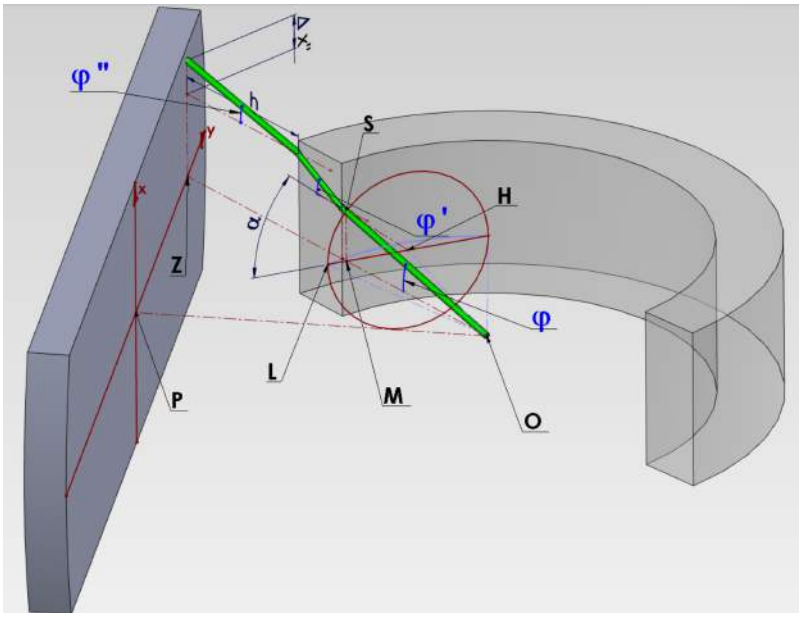

Figure A.3: Side-view of the scattering geometry.

Let's consider fig. A.3:

$$
\begin{aligned}
\overline{OM} = \sqrt{\overline{HM}^2 + \overline{OH}^2} &= \sqrt{{d_s}^2 \sin^2\theta\cos^2\alpha + {d_s}^2\cos^2\theta} = d_s\sqrt{\sin^2\theta\cos^2\alpha + \cos^2\theta} \\
\widehat{SOM} = \varphi = \arctan\left(\frac{\overline{SM}}{\overline{OM}}\right) &= \arctan\left(\frac{\sin\theta\sin\alpha}{\sqrt{\sin^2\theta\cos^2\alpha+\cos^2\theta}}\right)
\end{aligned}
\tag{A.5}
$$

Our aim is to follow the propagation of the $\overline{OS}$ beam taking into account all the refractions in play. In this way we can obtain the x-coordinate for the point resulting from the intersection between the photon beam and the filter plane.

The $\overline{OS}$ beam impinges the inner surface of the cuvette in S' (See fig. A.4). Let's call x' the x-coordinate of its projection on the (x, y)-plane. Therefore:

$$\tan\varphi = \frac{x'}{d_s}$$
$$x' = d_s \tan\varphi = d_s \frac{\sin\theta\sin\alpha}{\sqrt{\sin^2\theta\cos^2\alpha+\cos^2\theta}} \tag{A.6}$$

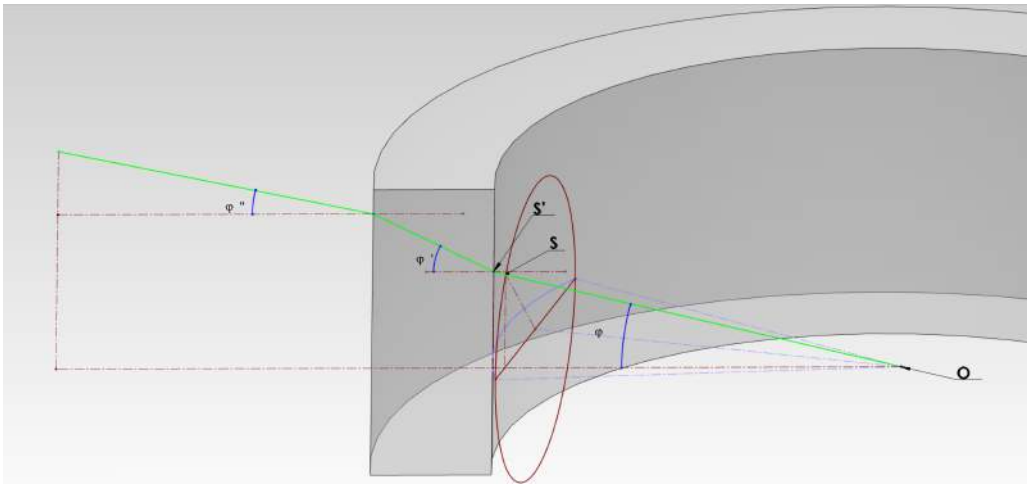

Figure A.4: Side-view of the scattering geometry.

Now we have to consider the refraction due to the thickness of the sample holder. The beam will be deviated at an angle φ' following the Snell-Cartesius law:

$$n_s \sin\varphi = n_q \sin\varphi' \qquad \varphi' = \arcsin\left(\frac{n_s}{n_q}\sin\varphi\right) \tag{A.7}$$

This beam will cross the external surface of the sample holder in a point whose projection on the (x, y)-plane has the x-coordinate at:

$$x'' = x' + \Delta x' \tag{A.8}$$

where

$$\Delta x' = d_q \tan\varphi' \tag{A.9}$$

At this point the last effect one has to consider is the refraction due to the transmission into the air. From the Snell-Cartesius law we have:

$$n_q \sin\varphi' = \sin\varphi'' \qquad \varphi'' = \arcsin\left(n_q \sin\varphi'\right) \tag{A.10}$$

The ray will continue to rise up for a quantity $\Delta x'' = h\tan\varphi''$ (See Fig. A.3 and Fig. A.2). Now we determine the x-coordinate of the intersection point between the beam-path and the filter plane as $x = x'' + \Delta x''$. From Fig. A.2 it can be seen that:

$$\frac{d_M}{\cos(\gamma-\beta)} = d_s + d_q + h$$
$$h = \frac{d_M}{\cos(\gamma-\beta)} - d_s - d_q \tag{A.11}$$

therefore

$$\Delta x'' = \left[\frac{d_M}{\cos(\gamma-\beta)} - d_s - d_q\right]\tan\varphi'' \tag{A.12}$$

Combining the latter equation with Eq. A.6,- A.7 - A.8 - A.9 - A.10 we obtain the final equation for the 'equal-Q' locus, i.e.:

$$x = x'' + \Delta x'' = d_s\tan\varphi + d_q\tan\left[\arcsin\left(\tfrac{n_s}{n_q}\sin\varphi\right)\right] + \left[\tfrac{d_M}{\cos(\gamma-\beta)} - d_s - d_q\right]\tan\left[\arcsin(n_s\sin\varphi)\right] \tag{A.13}$$

Summarizing, the whole parametric equation is:

$$\begin{aligned} x &= d_s\tan\varphi + d_q\tan[\arcsin(\tfrac{n_s}{n_q}\sin\varphi)] + \\ &+ [\tfrac{d_M}{\cos(\gamma-\beta)} - d_s - d_q]\tan[\arcsin(n_s\sin\varphi)] \\ y &= d_M\tan(\gamma-\beta) \\ \beta &= \arctan(\tan\theta\cos\alpha) \\ \varphi &= \arctan(\tfrac{\sin\theta\sin\alpha}{\sqrt{\sin^2\theta\cos^2\alpha+\cos^2\theta}}) \end{aligned} \tag{A.14}$$

We just want to mention the possibility to obtain, from such an expression, the equation for the case of spherical geometry, in which no refractions occur. This can be derived by just setting $n_s = n_q = 1$. After some straightforward algebra one obtains:

$$\begin{aligned} x &= \tfrac{d_M}{\cos(\gamma-\beta)}\sin\beta\tan\alpha \\ y &= d_M\tan(\gamma-\beta) \\ \beta &= \arctan(\tan\theta\cos\alpha) \end{aligned} \tag{A.15}$$

A.2 The Δ_Q-parameter

In the paper we presented the 'equal-Q' locus equation (Eq. A.1) for photons characterized by a certain $Q_0 = \frac{4\pi n_s}{\lambda}\sin\left(\frac{\theta}{2}\right)$. To draw the borders of the mask's slit we introduced the Δ_Q-parameter, which defines the thickness of the slit's gap in order to allow the transmission of those photons whose Q-value is in the range $Q_0 \pm \Delta_Q$. In this section we describe the equations that relate Δ_Q with the the thickness of the slit's gap.

Using the equations derived in the previews section, we may determine the loci for the beams whose scattering angle leads to the following Q-values:

$$\begin{aligned} Q_{max} &= Q_0 + \Delta_Q \\ Q_{min} &= Q_0 - \Delta_Q \end{aligned} \tag{A.16}$$

The corresponding values for θ_{max} and θ_{min} are:

$$\begin{aligned} \theta_{max} &= 2\arcsin\left[\sin\tfrac{\theta}{2} + \tfrac{\lambda\Delta_Q}{4\pi n_s}\right] \\ \theta_{min} &= 2\arcsin\left[\sin\tfrac{\theta}{2} - \tfrac{\lambda\Delta_Q}{4\pi n_s}\right] \end{aligned} \tag{A.17}$$

Using these angles in eq. A.1 one can draw the borders of the slit.

The filters presented in the next section were made using *TheMask_1.1*, a C/C++ homemade software able to draw the parametric equations for θ_{max} and θ_{min} and calculate the corresponding photon distributions (as those shown Fig. 1 of the main paper). *TheMask_1.1* is also able to make some crosschecks to ensure, for example, that the photons selected by the Δ_Q parameter are still within the effective area of the collection optic. In the software is integrated an additional tool to calculate.

A.3 Masks Set

In this section we want to provide some already prepared masks, to eventually allow for a rapid use of this new tool without needing to make an own program to draw them.

The equations presented above are valid in the most general case, though the most used configuration is the one in which $\gamma = \theta$; all the following masks have been designed with this condition. The radius of the mask, colored in blue in the following drawings, is 1".

Furthermore we note that, within reasonable limits, the parameters of the sample holder are not very influent. Indeed, if the wall thickness of the holder is in the 0-20 mm range, the shape of the masks are almost the same. This is also the case of the inner radius of the sample holder, as we do not appreciate significant variation in the mask shape for a range of values between 3 to 15 mm.

For these reasons in the following drawings we fixed the parameters of the sample holder at: $n_q = 1.5$, $d_q = 1\,mm$ and $d_s = 4\,mm$ (typical for a quartz cylindrical cuvette).

We also stress that one may use a focal length of the collection optic equal to d_M and insert the filter just after the collection optic, since all the beams coming from O propagate parallel after it.

As you can see in the drawings further below, the dependence of the mask's profile on the value of the refractive index is significant only for small θ's. For this reason we plot the masks at four different refractive indexes only for small angles, while for large angle geometries only the case $n_s = 1.3$.

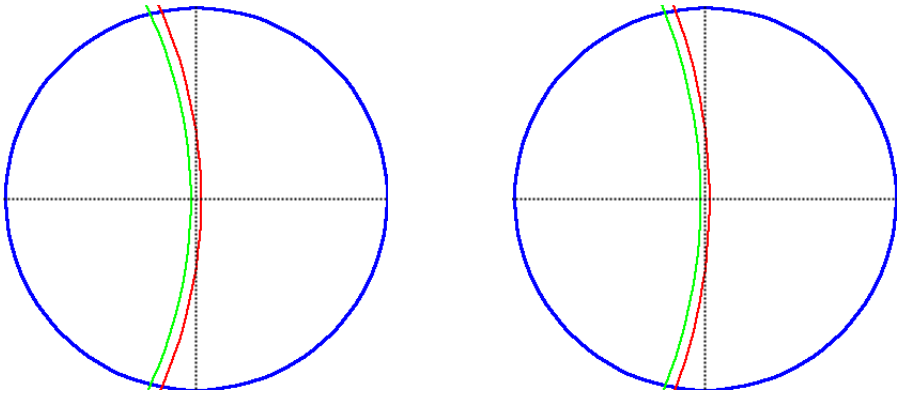

(a) $n_s = 1.3$ (b) $n_s = 1.4$

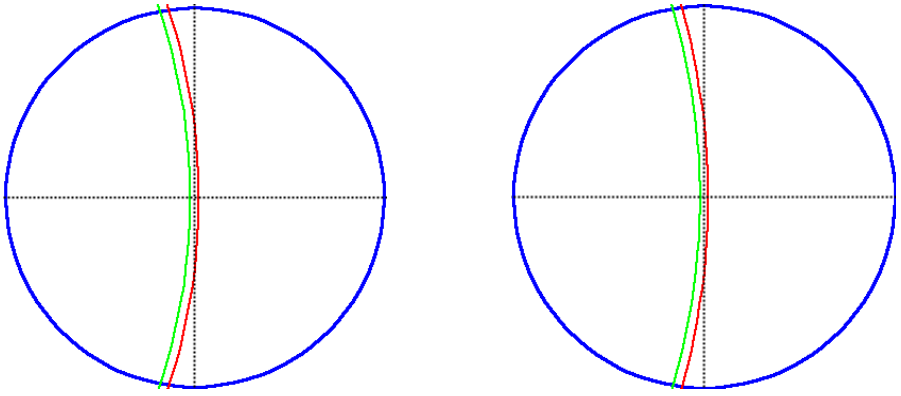

(c) $n_s = 1.5$ (d) $n_s = 1.6$

Figure A.5: Masks set with the following parameters. $\lambda = 532\,nm, d_M = 100\,mm, \Delta_Q = 0.1\,\mu m^{-1}, \theta = \gamma = 20°$. *The* n_s *indexes are indicated in each drawing.*

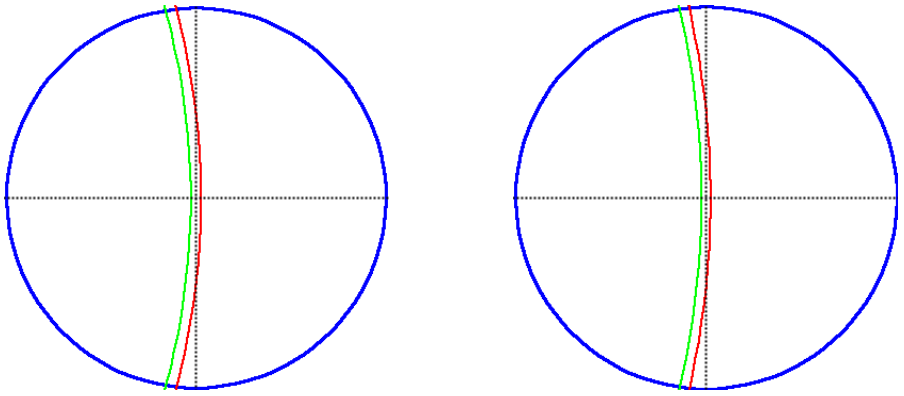

(a) $n_s = 1.3$ (b) $n_s = 1.4$

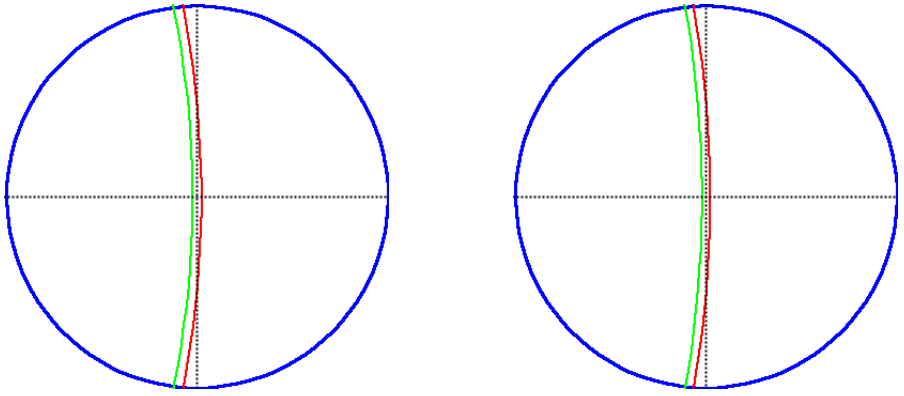

(c) $n_s = 1.5$ (d) $n_s = 1.6$

Figure A.6: Masks set with the following parameters. $\lambda = 532\,nm, d_M = 100\,mm, \Delta_Q = 0.1\,\mu m^{-1}, \theta = \gamma = 30°$. *The* n_s *indexes are indicated in each drawing.*

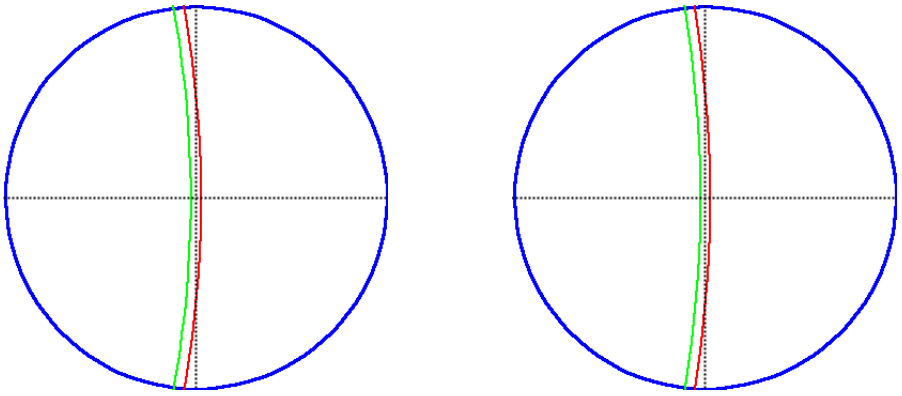

(a) $n_s = 1.3$ (b) $n_s = 1.4$

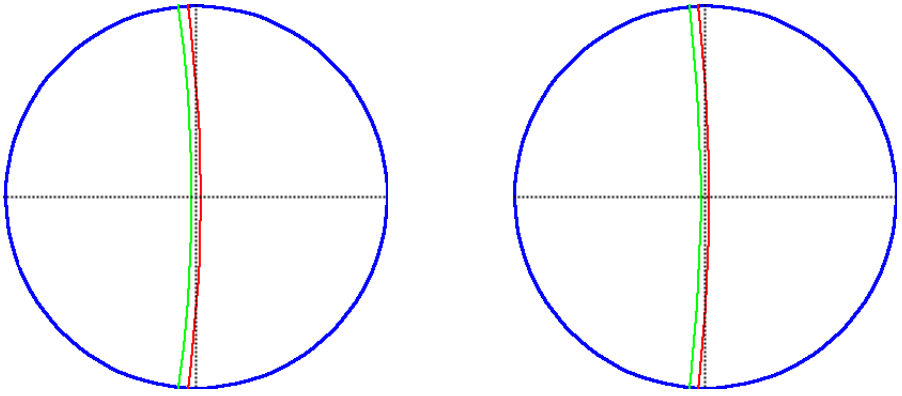

(c) $n_s = 1.5$ (d) $n_s = 1.6$

Figure A.7: Masks set with the following parameters. $\lambda = 532\,nm, d_M = 100\,mm, \Delta_Q = 0.1\,\mu m^{-1}, \theta = \gamma = 40°$. *The* n_s *indexes are indicated in each drawing.*

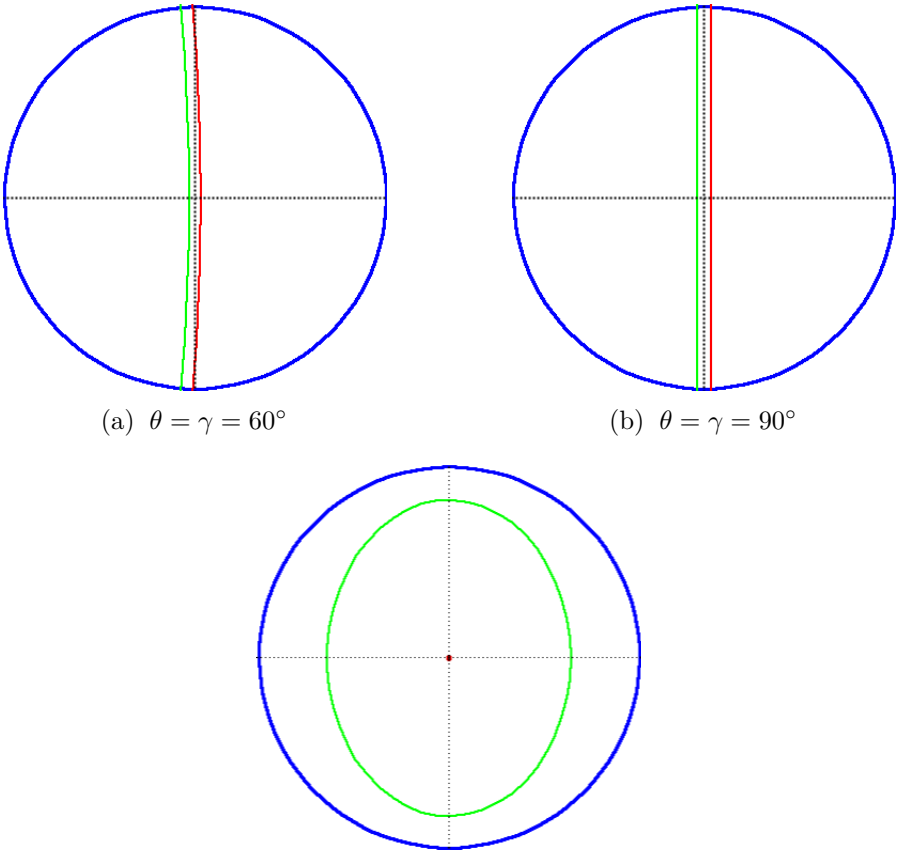

(a) $\theta = \gamma = 60°$ (b) $\theta = \gamma = 90°$

(c) $\theta = \gamma = 180°$

Figure A.8: Masks set with the following parameters. $\lambda = 532\,nm, d_M = 100\,mm, \Delta_Q = 0.1\,\mu m^{-1}$. *For large angles refractive index of the sample is not crucial in the filter shapes, therefore all the drawings were obtained for* $n_s = 1.3$. *The respective angle geometry is indicated in each label.*

Appendix B

Mini-TIMER supplementary material

In this appendix we will give further details on the experiment result shown in Ch. 6.

B.1 Experimental setup

The FEL focusing was provided by a Kirkpatrick-Baez active focusing system (located upstream the DiProI end-station [137]), that was detuned to relax the spot size at the sample in order to avoid sample damage. The FEL photo-diagnostic data were acquired on a shot-to-shot basis by the Photon Analysis, Delivery and Reduction System (PADReS)[138], that connects the FEL source to the end-station; an Al filter placed along the photon transport line was used to remove the seed laser radiation. The layout of the experimental set up used to generate and probe EUV transient gratings is shown in Fig. B.1. The system to split and recombine the FEL beams (see Fig. B.1a) is based on three 70 mm long carbon-coated mirrors (M1, M2 and M3) working at grazing incidence. It is mounted on a 580x280 mm^2 baseplate and in the present case the grazing angles were $\approx 3°$. M1 can be inserted into the path of the incoming FEL beam by a y-translation (see Fig. B.1a for the adopted reference frame) and is used as a wavefront division beamsplitter. The two split beams propagating downstream M1 are recombined on the sample by mirrors M2 and M3. The design position of the mirrors corresponds to a parallelogram geometry, where the splitting angle after M1 (2α) equals the crossing angle at the sample (2θ) and the M1-M2 distance (d1) equals the M3-sample one (d2). In this case the optical path difference (ΔL) between the FEL path 1 (FP1) and FEL path 2 (FP2) vanishes, ensuring the time coincidence of the crossed FEL beams. The design values of the system are $2\alpha=2\theta=6°$ and d1=d2=125 mm. The system has several motorized degrees of freedom to adjust the mirror positions and angles during the experiment, i.e.: i) the pitch and roll angles of all mirrors can be independently controlled in the $\pm 3.5°$ range with a resolution of ≈ 50 μrad by piezo-electric steering motors; ii) the y-position of M1 can be changed in the ± 20 mm range with ≈ 2 μm resolution; iii) the x and y positions of M2 and M3 can be independently varied in the ± 9.5 mm range by linear piezomotors with a resolution of ≈ 0.2 μm; iv) each mirror can be removed from the FEL paths; v) the whole system can be adjusted in x, y

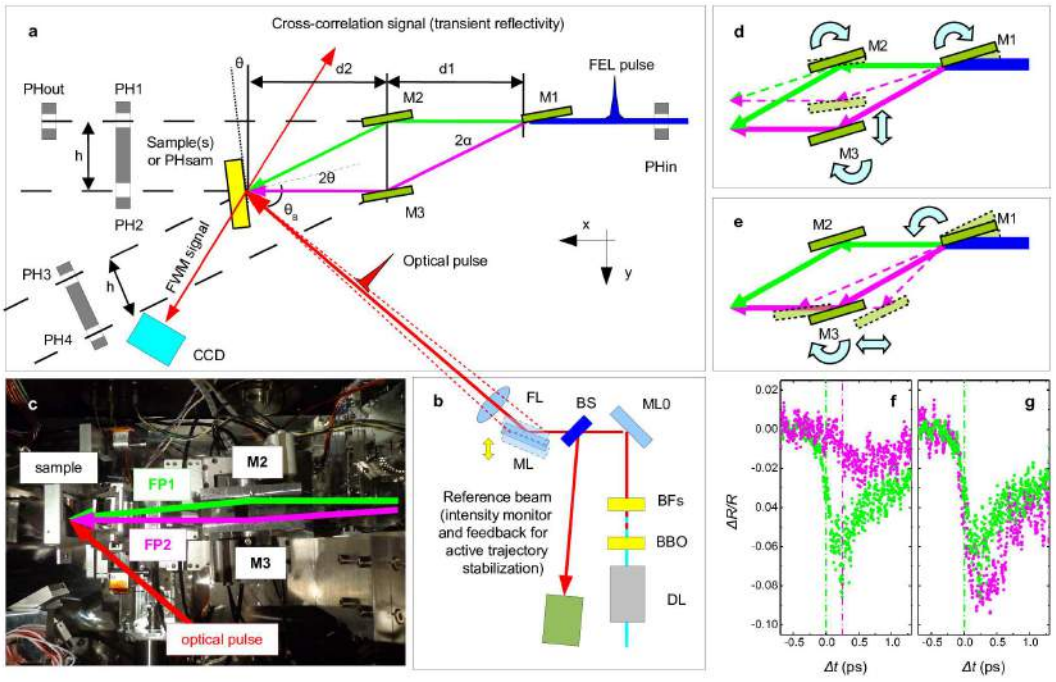

Figure B.1: Experimental setup for FEL-based FWM measurements. ***a****, Top-view layout of the experimental set-up used to split and recombine the FEL beams.* ***b****, Top-view layout of the experimental set-up used to control the optical beam.* ***c****, Top-view picture of the set-up: the two FEL paths (FP1 and FP2) downstream M1 and the trajectory of the optical pulse are indicated.* ***d****, sketch of the movements needed to change 2θ keeping fix* $\Delta t_{EUV-EUV}$*.* ***e****, sketch of the movements needed to change* $\Delta t_{EUV-EUV}$ *keeping fix 2θ.* ***f*** *and* ***g****, optical reflectivity changes in* Si_3N_4 *induced by the FEL beam propagating through FP1 (green dots) and FP2 (magenta dots). In (****f****) the mirrors were displaced with respect to the nominal position; a poor time coincidence and a different fluence level in the interaction region can be appreciated.* ***g****, same measurements as in (****f****) after optimization of the geometry; the superposition of the two traces indicates a large improvement in the time coincidence and a similar FEL fluence in the interaction region.*

and z. Furthermore, the sample is mounted on a (x,y,z,pitch,roll) adjustment stage, that also allows to replace the SiO_2 sample with a fluorescence screen, a pinhole (PHsam) or a Si_3N_4 reference sample (for cross-correlation measurements described further below). Such motors can be used to change the value of 2θ (in the 3°-9° range) keeping fix the arrival time difference of the two FEL pulses ($\Delta t_{EUV-EUV}$) or vice-versa; see sketches in Figs. B.1d and B.1e. The possibility to vary $\Delta t_{EUV-EUV}$ (in the ± 0.2 ps range for $2\theta \approx 6°$) at fixed 2θ de facto makes our setup a compact split and delay device, with the advantage of the angular discrimination of the two FEL pulses.

The system was pre-aligned using a Ti:sapphire laser to simulate the incoming FEL beam and optimizing the second harmonic signal generated by a non-linear

crystal placed at the sample position (this signal is sensitive to the time-space superposition of the beams coming from FP1 and FP2). The optimized geometry was then referenced by a set of 2 mm diameter pinholes (PHin, PHout, PH1, PH2, PH3, PH4, PHsam) before plugging the set-up into the end-station; PHsam can be inserted in place of the sample, while PHsam and PHout can be independently scanned in y in order to determine both the parallelism and the interaxis distance (h) between the trajectory of the incoming FEL beam (once removed M2 from the scattering plane) and FP2 downstream M3. This set of pinholes provides an accuracy of about 0.2° in the determination of 2θ. Indeed, from atomic force microscopy measurements on permanent gratings (carried out after the experiment) we were able to determine the actual value of 2θ (i.e. $6.16° \pm 0.02°$) used in the FWM measurements. Such deviations with respect to the design value can be compensated by changing the FEL wavelength (λ_{EUV}) and/or the incidence angle of the optical pulse at the sample (θ_B).

A sketch of the system (external to the end-station) used to control the optical pulse is shown in Fig. B.1b. This pulse is a fraction of the one that triggers the FEL emission, thus ensuring "jitter-free" conditions, i.e. the FEL-optical timing jitter (<10 fs) is much shorter than the pulse duration. An optical delay line (DL) is used to set the time delay (Δt) between the FEL pulses and the optical one in the -10 +300 ps range. The optical beam is frequency doubled at 392.8 nm wavelength by a BBO (Barium Boron Oxide) crystal and routed into the sample by a reflective mirror (ML; grazing angle $\approx 22.5°$) and a focusing lens (FL; focal length 600 mm), whose focal plane contains the crossing point of the two FEL beams. ML can be translated along the y-direction in order to change θ_B (in the $47° - 51°$ range) without varying the position of the laser spot at the sample. This degree of freedom is coupled to Δt, so that a change in θ_B has to be compensated by an adjustment of the DL to keep fix the actual value of Δt. Bandpass filters (BFs) are used to remove the residual fundamental radiation at 785.6 nm wavelength, while a beamsplitter (BS) provides a reference beam for intensity monitor and active stabilization [139], the latter is ensured by a tip-tilt stage action on the MLS mirror.

An accurate determination of the temporal and spatial coincidence of the three input beams is obtained by cross-correlation measurements [140]. These are based on FEL-induced transient optical reflectivity changes (ΔR/R) from a Si_3N_4 reference sample. In such measurements we first removed M3 from FP2 to collect the cross-correlation trace between the optical pulse and the FEL pulse coming from FP1. The half drop of the ΔR/R profile was assumed as Δt=0. Afterwards we removed M2 and inserted M3 in order to collect the cross-correlation trace associated to the FEL pulse coming from FP2. Iterative measurements, carried out by varying the pitch of M1 and roto-translating M3 keeping fix the FEL trajectory downstream M3 (see Fig. B.1e), allowed us to set the condition $\Delta t_{EUV-EUV} = 0$. Furthermore, since the amplitude of the ΔR/R drop is proportional to the FEL fluence at the sample, such measurements also allowed us to equalize the fluence level of the two FEL beams in the interaction region. Figs. B.1f and B.1g report typical ΔR/R traces collected out/in time coincidence and without/with similar fluence levels in the interaction region. Once set the time-space coincidence of the three beams we acted on θ_B to optimize the phase matching conditions necessary to observe the FWM signal. The

latter was recorded by a Princeton Instrument PI-MTE back illuminated Charged Coupled Device (CCD) camera with frame format 2048x2048 pixels and 13.5x13.5 μm^2 pixels size. The detector was positioned ≈250 mm downstream the sample and oriented at an angle of ≈ 49°. A 15x5 mm^2 slit was placed in front to the CCD in order to reduce spurious light, mainly coming from diffuse scattering of the optical pulse (transmitted through the sample) that impinged into the wall of the experimental chamber.

B.2 Atomic Force Microscopy (AFM) measurements on permanent gratings

Figs. B.2a, B.2b and B.2c show AFM topographies of a 8x8 μm^2 sample area not irradiated by the FEL pulses, irradiated by ≈300 shots at fluence larger than 50 mJ/cm^2 and continuously irradiated by FEL pulses at low fluence, respectively. AFM scans have been performed with a XE-100 (Park Instruments) instrument, in contact mode using commercial cantilevers (Mikromasch, CSC38, spring constant k=0.03-0.09 N/m) with samplings of 1024 pixels in both directions. Extended Data Figs. B.2d-B.2f report the corresponding depth profiles of the sample surface. The non-irradiated sample shows a roughness of about 0.6 nm root-mean-square and 5 nm peak-to-valley. A grating with a peak-to-valley amplitude of about 18 nm and a period of 256.7±0.9 nm (corresponding to 2θ=6.16°±0.02°) is clearly visible in the sample surface irradiated at high FEL fluence. The high grating visibility after multi-shot illumination indicates that the shot-by-shot fluctuations in the optical path difference (i.e. in the relative phase) between the crossed FEL pulses are lower than λ_{EUV}. Such a low phase jitter might in principle allow for lithographic applications. Indeed, the interference between coherent FEL pulses would permit to imprint permanent gratings with a pitch as short as a few nm's by exploiting larger crossing angles and shorter FEL wavelengths. Figs. B.2g-B.2i are the power spectral densities (PSD) of the data reported in Figs. B.2d-B.2f. No specific frequencies are found in the non-irradiated sample (the peak at ≈35 μm^{-1} is an artifact due to the electronic noise of the employed AFM device), while the first peak at ≈0.5 μm^{-1} in the PSD, shown in Fig. B.2h, reveals a modulation with a period of ≈2 μm, most likely due to diffraction effects from the mirrors. The sample surface irradiated at low fluence shows a roughness similar to that of the non-irradiated sample and frequencies ascribable to the formation of permanent gratings are absent.

B.3 Data Analysis

For each probed Δt-value we acquired 5 CCD images (exposure time: 1 minute) with the FEL ON and 2 ones with the FEL OFF. The FEL OFF images were used to remove the background due to diffuse scattering of the optical laser, mainly due to the fraction of the laser pulse transmitted through the sample, which then impinged into the wall of the experimental chamber. Such frequent and accurate determination of the background allowed us to account for small drifts in the CCD response during

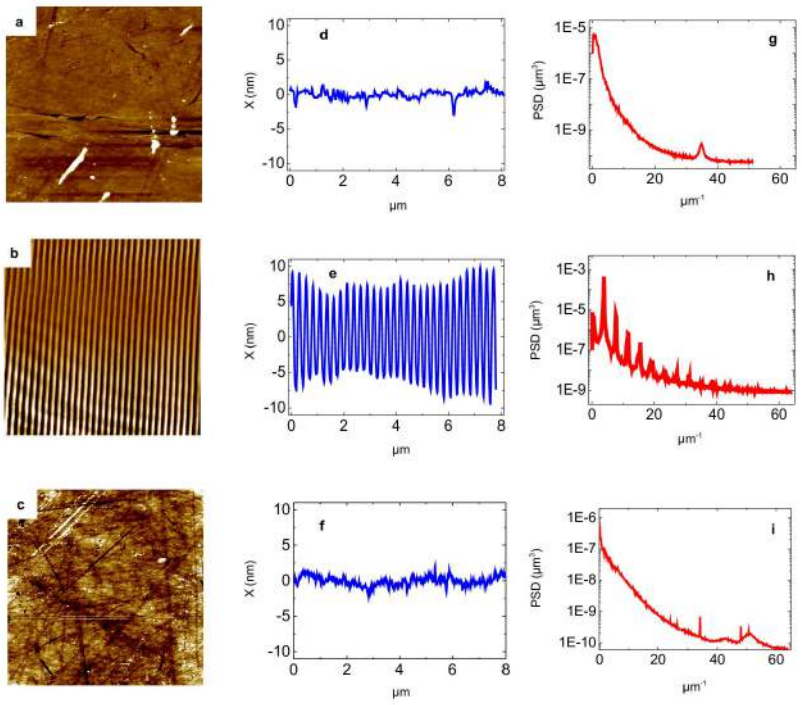

*Figure B.2: AFM topographies. AFM topographies of 8x8 μm^2 areas of the sample surface in a not irradiated region of the sample (**a**), in an area irradiated by ≈300 FEL shots at fluence larger than 50 mJ/cm^2 (**b**) and in an area continuously irradiated by FEL pulses at low fluence (**c**). **d**-**f** are representative depth profiles of the sample surface along the green lines shown in panels **a**-**c**. The power spectral densities (PSD) corresponding to data reported in **d**-**f** are shown in **g**-**i**.*

the Δt-scan, which lasted several hours. After background subtraction we applied a low-pass Fourier filter in order to reduce the noise and improve the contrast. In order to convert the ADC counts, recorded by the CCD, into incoming photons we assumed a sensibility of 8.5 photons per ADC count, which also takes into account the detector quantum efficiency. The total number of photons in the FWM beam was determined by fitting the peak in each image with a 2-dimensional Gaussian function plus a flat background and then calculating the volume under the Gaussian surface. The volume corresponding to each image was then averaged taking into account the normalization to the corresponding mean squared FEL intensity; error bars were estimated as one standard deviation of the set of CCD images corresponding to the same Δt value (in a few cases we have a single image and we hence set the error bar equal to zero). At negative time delays (Δt<0) and within the signal-to-noise of the employed CCD detector, the "FEL ON-FEL OFF" images can be fitted only by the background (see also Fig. B.3). Before starting the time delay scan, shown in Fig. B.3a, we optimized the FWM signal at Δt=0 by small tweaks of mirror positions and angles. The intensity stability of the FEL was typically better than 7% during the acquisition of the 5 FEL ON images and of about 20% throughout the whole Δt-scan. A few images were discarded due to occasional machine faults

occurring during the acquisitions. In a proof-of-principle spirit we assumed that the

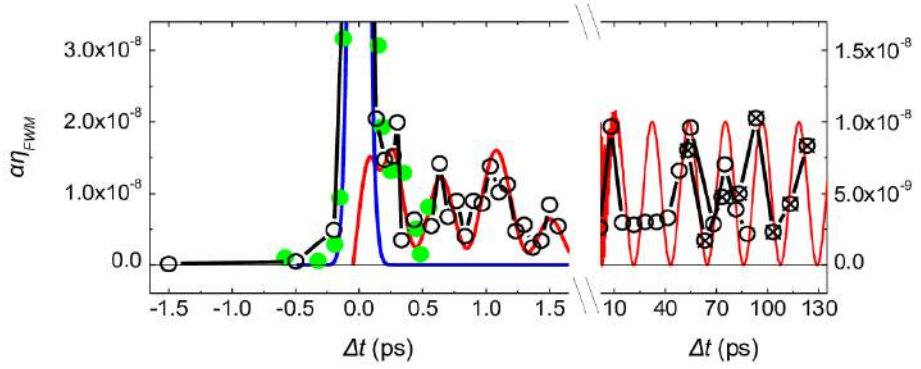

Figure B.3: Time sequence of acquired data. Black open and crossed circles connected by lines are data shown in Fig. 6.3; crossed circles correspond to a scan made several hours after the one corresponding to data shown as open circles, in both scans the time delay was continuously increased. Green dots are data collected before these two scans; here we had not yet optimized the FWM signal at Δt=0 (these data are scaled by a factor to fit the peak intensity of the data shown as black circles). Blue and red lines are the same shown in Fig. 6.3.

time dependence of the FWM signal is due to impulsively stimulated vibrational modes, which can be observed in the time-dependent coherent FWM signal [98]. We hence modeled the time dependent intensity of the normalized FWM signal ($\alpha I_{FWM}(\Delta t)/I_{opt}$; where I_{opt} and α are the intensity of the incoming optical beam and the normalizing factor quoted in the main text, respectively) with the following function:

$$\begin{aligned} \frac{\alpha I_{FWM}(\Delta t)}{I_{opt}} &= R(\Delta t) \otimes |A_0\delta(\Delta t) + \sum_i A_i e^{-\Delta t/\tau_i} \sin(2\pi\nu_i \Delta t)|^2 = \\ &= A_0^2 R(\Delta t) + R(\Delta t) \otimes |\sum_i e^{-\Delta t/\tau_i} \sin(2\pi\nu_i \Delta t)|^2 \end{aligned} \quad \text{(B.1)}$$

where A_0 and A_i are scaling factors, $\otimes$ is the convolution operator, $R(\Delta t)$ is the instrumental response function, while ν_i and τ_i are the frequencies and damping times of the impulsive stimulated modes, respectively. Since an independent determination of $R(\Delta t)$ is not available, it was assumed to be a Gaussian function of unit area with a full width at half maximum of 135 fs, which is equal to that of the Δt=0 peak in the FWM signal ($R_{cc}(\Delta t)$; see Fig. B.3a). Hence, the $A_0\delta(\Delta t)$ term accounts for processes occurring at timescales substantially shorter than ≈100 fs. The $e^{-\Delta t/\tau_i} \sin(2\pi\nu_i \Delta t)$ terms describe the time evolution of the impulsively excited vibrational modes. Considering that the excitable modes are those having vibrational periods (ν_i^{-1}) longer than the time duration of the stimulating FEL pulses (60-80 fs), the observed FWM signal could be related to: i) acoustic modes ($\nu_{LA} = c_s/L \approx 23.2$ GHz, where c_s=5970 m/s and L=256.8 nm are the sound velocity and the transient

grating pitch, respectively); ii) Raman modes within the broad band (3-14 THz) associated to tetrahedral bendings [141] and iii) F_1 modes (≈1 THz) involving coupled rotations of SiO_4 tetrahedra [142, 143]. Starting from such trial frequencies, we used Eq. B.3 to optimize the parameters that better describe the time structure of the FWM signal, once subtracted the $A_0^2 R(\Delta t)$ term.

The coarse sampling and the limited Δt-range prevented the direct determination of acoustic parameters, that were fixed to the expected values, i.e.: ν_{LA}=23.2 GHz and $\tau_{LA} > 1$ ns (we note that in the probed Δt-range $e^{-\Delta t/\tau_i} \approx 1$), while A_{LA} was fixed to $1{\cdot}10^{-4}$ in order to fit in the observed magnitude of the FWM signal at Δt>2 ps. The optimized values of the other parameters are: A_1/A_{LA}=1.4 ± 0.2, ν_1=1.15 ± 0.15 THz, τ_1=5 ± 2 ps, A_2/A_{LA}=1.4 ± 0.2, ν_2=4.1 ± 0.8 THz and τ_2=0.15 ± 0.06 ps. The value of ν_1 roughly matches the characteristic frequency of F_1 modes, while ν_2 locates in the low frequency side of the aforementioned broad Raman band, that corresponds to (highly damped) ν_{2b} bending modes. We finally notice that a slightly worse fit (but still satisfactory) is achieved without the A_2 term, while the addition of other high frequency terms (as the $\nu_{4b,4c}$ bendings) does not significantly improve the fitting results.

List of publications

- C. Masciovecchio, **A. Battistoni**, E. Giangrisostomi, F. Bencivenga, E. Principi, R. Borghes, R. Cucini, M. B. Danailov, A. Di Cicco, A. Filipponi, A. Gessini, R. Gunnella, K. Hatada, G. Kurdi, N. Mahne, R. Mincigrucci, L. Raimondi, C. Svetina and M. Zangrando "EIS: the scattering beamline at Fermi" (2015) (*Journal of Synchrotron Radiation*, accepted)

- F. Bencivenga, R. Cucini, F. Capotondi, **A. Battistoni**, R. Mincigrucci, E. Giangrisostomi, A.Gessini, M. Manfredda, I. P. Nikolov, E. Pedersoli, E. Principi, C. Svetina, P. Parisse, F.Casolari, M. B. Danailov, M. Kiskinova and C. Masciovecchio "Four wave mixing experiments with extreme ultraviolet transient gratings" (2015) (*Nature*, accepted)

- R. Cucini, **A. Battistoni**, F. Bencivenga, A. Gessini, R. Mincigrucci, E. Giangrisostomi, E. Principi, F. Capotondi, E. Pedersoli, M. Manfredda, M. Kiskinova, C. Masciovecchio "Toward the Extreme Ultra Violet Four Wave Mixing Experiments: From Table Top Lasers to Fourth Generation Light Sources." (2015) (*Photonics* 2, 57-70)

- R. Mincigrucci, E. Giangrisostomi, E. Principi, **A. Battistoni**, F. Bencivenga, R. Cucini, A. Gessini, M.G. Izzo, C. Masciovecchio. "Liquid Carbon Reflectivity at 19 nm" (2015) (*Photonics* 2, 50-56)

- **A. Battistoni**, F. Bencivenga, D. Fioretto and C. Masciovecchio "A practical way to avoid spurious geometrical contributions in Brillouin light scattering experiments at variable scattering angle" (2014) (*Optics Letters* 39, 5858-5861)

- R. Cucini, **A. Battistoni**, A. Gessini, F. Bencivenga, E. Principi, M. Saito, F. D'Amico, R. Sergo, and C. Masciovecchio "Determination of dynamical parameters in liquids by homodyne transient grating spectroscopy at large angles" (2014) (*Optics Letters* 39 (17), 5110-5113)

- F. Bencivenga, E. Principi, E. Giangrisostomi, R. Cucini, **A. Battistoni**, F. D'Amico, A. Di Cicco, S. Di Fonzo, A. Filipponi, A. Gessini, R. Gunnella, M. Marsi, L. Properzi, M. Saito, and C. Masciovecchio "Reflectivity enhancement in titanium by ultrafast EUV irradiation" (2014) (*Scientific Reports* 4, 4952)

- M. Saito, **A. Battistoni**, S. Kitao, Y. Kobayashi, M. Kurokuzu, Y. Yoda, M. Seto "Slow dynamics of supercooled liquid revealed by Rayleigh scattering of

Mössbauer radiation method in time domain" (2014) (*Hyperfine Interaction* 226, 629-636)

- F. D'Amico, M. Saito, F. Bencivenga, M. Marsi, A. Gessini, G. Camisasca, E. Principi, R. Cucini, S. Di Fonzo, **A. Battistoni**, E. Giangrisostomi, C. Masciovecchio "UV resonant Raman scattering facility at Elettra" (2013) (*Nuclear Instruments and Methods in Physics Research, Section A: Accelerators, Spectrometers, Detectors and Associated Equipment* 703, 33-37)

- E. Allaria, **A. Battistoni**, F. Bencivenga, R. Borghes, C. Callegari, F. Capotondi, D. Castronovo, P. Cinquegrana, D. Cocco, M. Coreno, P. Craievich, R. Cucini, F. D'Amico, M.B. Danailov, A. Demidovich, G. De Ninno, A. Di Cicco, S. Di Fonzo, M. Di Fraia, S. Di Mitri, B. Diviacco, W.M. Fawley, E. Ferrari, A. Filipponi, L. Froehlich, A. Gessini, E. Giangrisostomi, L. Giannessi, D. Giuressi, C. Grazioli, R. Gunnella, R. Ivanov, B. Mahieu, N. Mahne, C. Masciovecchio, I.P. Nikolov, G. Passos, E. Pedersoli, G. Penco, E. Principi, L. Raimondi, R. Sergo, P. Sigalotti, C. Spezzani, C. Svetina, M Trovò, M. Zangrando "Tunability experiments at the FERMI@Elettra free-electron laser" (2012) (*New Journal of Physics* 14, 113009)

- F. Bencivenga, **A. Battistoni**, D. Fioretto, A. Gessini, J.R. Sandercock, C. Masciovecchio "A high resolution ultraviolet Brillouin scattering set-up" (2012) (*Review of Scientific Instruments* 83 (10), 103102)

- A. Di Cicco, F. Bencivenga, **A. Battistoni**, D. Cocco, R. Cucini, F. D'Amico, S. Di Fonzo, A. Filipponi, A. Gessini, E. Giangrisostomi, R. Gunnella,C. Masciovecchio, E. Principi, C. Svetina "Probing matter under extreme conditions atFERMI@Elettra: the TIMEX beamline", (2011) (*Proceedings of SPIE - The International Society for Optical Engineering* 8077, 807704)

Bibliography

[1] C Thomsen, J Strait, Z Vardeny, Humphrey J Maris, J Tauc, and JJ Hauser. Coherent phonon generation and detection by picosecond light pulses. *Physical Review Letters*, 53(10):989, 1984.

[2] Emanuele Pontecorvo, Michele Ortolani, Dario Polli, Marco Ferretti, Giancarlo Ruocco, Giulio Cerullo, and Tullio Scopigno. Visualizing coherent phonon propagation in the 100 ghz range: A broadband picosecond acoustics approach. *Applied Physics Letters*, 98(1):011901, 2011.

[3] Arnaud Devos. Colored ultrafast acoustics: From fundamentals to applications. *Ultrasonics*, 56:90–97, 2015.

[4] T Pezeril, C Klieber, S Andrieu, and KA Nelson. Optical generation of gigahertz-frequency shear acoustic waves in liquid glycerol. *Physical review letters*, 102(10):107402, 2009.

[5] C Klieber, Emmanuel Péronne, K Katayama, J Choi, M Yamaguchi, T Pezeril, and Keith A Nelson. Narrow-band acoustic attenuation measurements in vitreous silica at frequencies between 20 and 400 ghz. *Applied Physics Letters*, 98(21):211908, 2011.

[6] A Devos, Marie Foret, Simon Ayrinhac, P Emery, and Benoît Rufflé. Hypersound damping in vitreous silica measured by picosecond acoustics. *Physical Review B*, 77(10):100201, 2008.

[7] C Ferrante, E Pontecorvo, G Cerullo, A Chiasera, G Ruocco, W Schirmacher, and T Scopigno. Acoustic dynamics of network-forming glasses at mesoscopic wavelengths. *Nature communications*, 4:1793, 2013.

[8] J.D. Jackson. *Classical Electrodynamics*. Wiley, NY, 1965.

[9] B.J. Berne and R. Pecora. *Dynamic Light Scattering*. Wiley, NY, 1976.

[10] A. Einstein. *Ann. Phys.*, 33:1275, 1910.

[11] D. Fioretto and F. Scarponi. Dynamics of a glassy polymer studied by brillouin light scattering. *Materials Science and Engineering: A*, 521–522(0):243 – 246, 2009. 15th International Conference on Internal Friction and Mechanical Spectroscopy.

[12] G. Hernandez. *Fabry-Perot interferometers*. Cambridge University Press, 1986.

[13] J.M. Vaughan. *The Fabry-Perot interferometer. History, theory, practise and applications*. Adam Hilger, Bristol, 1989.

[14] F. Nizzoli and J.R. Sandercock. *Dynamical Properties of Solids*. G. Horton and A.A. Maradudin, North-Holland, Amsterdam, 1990.

[15] J. G. Dil, N. C. J. A. van Hijningen, F. van Dorst, and R. M. Aarts. Tandem multipass fabry-perot interferometer for brillouin scattering. *Appl. Opt.*,

20(8):1374–1381, 1981.

[16] R. Vialla, B. Rufflé, G. Guimbretière, and R. Vacher. Eliminating the broadening by finite aperture in brillouin spectroscopy. *Review of Scientific Instruments*, 82(11):113110, 2011.

[17] H. G. Danielmeyer. Aperture corrections for sound absorption measurements with light scattering. *The Journal of the Acoustical Society of America*, 47(1B):151–154, 1970.

[18] W. F. Oliver, C. A. Herbst, S. M. Lindsay, and G. H. Wolf. A general method for determination of brillouin linewidths by correction for instrumental effects and aperture broadening: Application to high-pressure diamond anvil cell experiments. *Review of Scientific Instruments*, 63(3):1884–1895, 1992.

[19] C. Gigault and J.R. Dutcher. Analysis of a simple method for the reduction of phonon peak broadening in surface brillouin light scattering. *Appl. Opt.*, 37(15):3318–3323, 1998.

[20] A. Giugni and A. Cunsolo. Structural relaxation in the dynamics of glycerol: a joint visible, uv and x-ray inelastic scattering study. *Journal of Physics: Condensed Matter*, 18(3):889, 2006.

[21] P. Sassi, G. Paliani, and R. S. Cataliotti. Brillouin spectra and vibrational–translational energy exchange in liquid acetonitrile. *The Journal of Chemical Physics*, 108(24):10197–10204, 1998.

[22] C. Ferrante, E. Pontecorvo, G. Cerullo, A. Chiasera, G. Ruocco, W. Schirmacher, and T. Scopigno. Acoustic dynamics of network-forming glasses at mesoscopic wavelengths. *Nature Communications*, 4:1793, 2013.

[23] S. Santucci, D. Fioretto, L. Comez, A. Gessini, and C. Masciovecchio. Is there any fast sound in water? *Phys. Rev. Lett.*, 97:225701, 2006.

[24] F. Bencivenga, A. Cunsolo, M. Krisch, G. Monaco, G. Ruocco, and F. Sette. High-frequency dynamics of liquid and supercritical water. *Phys. Rev. E*, 75:051202, 2007.

[25] G. Monaco, A. Cunsolo, G. Ruocco, and F. Sette. Viscoelastic behavior of water in the terahertz-frequency range: An inelastic x-ray scattering study. *Phys. Rev. E*, 60:5505–5521, 1999.

[26] A. Battistoni, F. Bencivenga, D. Fioretto, and C. Masciovecchio. Practical way to avoid spurious geometrical contributions in brillouin light scattering experiments at variable scattering angles. *Opt. Lett.*, 39(20):5858–5861, Oct 2014.

[27] W. Wagner and A. Pruß. The iapws formulation 1995 for the thermodynamic properties of ordinary water substance for general and scientific use. *Journal of Physical and Chemical Reference Data*, 31(2):387–535, 2002.

[28] J. Rouch, C. C. Lai, and S. H. Chen. Brillouin scattering studies of normal and supercooled water. *The Journal of Chemical Physics*, 65(10):4016–4021, 1976.

[29] C. Della Volpe, G. Guarino, R. Sartorio, and V. Vitagliano. Diffusion, viscosity, and refractivity data on the system dimethylformamide-water at 20 and 40.degree.c. *Journal of Chemical & Engineering Data*, 31(1):37–40, 1986.

[30] A. Cunsolo and M. Nardone. Velocity dispersion and viscous relaxation in supercooled water. *The Journal of Chemical Physics*, 105(10):3911–3917, 1996.

[31] S. Hawley, J. Allegra, and G. Holton. Ultrasonic absorption and sound-speed data for nine liquids at high pressures. *The Journal of the Acoustical Society of America*, 47(1B):137–143, 1970.

[32] L. Comez, C. Masciovecchio, G. Monaco, and D. Fioretto. Chapter one - progress in liquid and glass physics by brillouin scattering spectroscopy. volume 63 of *Solid State Physics*, pages 1 – 77. Academic Press, 2012.

[33] E. D. Palik, H. Boukari, and R. W. Gammon. Line-shape studies for single- and triple-pass fabry–perot interferometer systems. *Appl. Opt.*, 34(1):58–68, 1995.

[34] L. Comez, G. Monaco, C. Masciovecchio, A. Paciaroni, A. Gessini, F. Scarponi, G. Ruocco, and D. Fioretto. Acoustic dissipation and density of states in liquid, supercooled, and glassy glycerol. *Phys. Rev. Lett.*, 106:155701, 2011.

[35] R. D. Hartschuh, A. Kisliuk, V. Novikov, A. P. Sokolov, P. R. Heyliger, C. M. Flannery, W. L. Johnson, C. L. Soles, and W.L. Wu. Acoustic modes and elastic properties of polymeric nanostructures. *Applied Physics Letters*, 87(17):173121, 2005.

[36] T. Still, M. Mattarelli, D. Kiefer, G. Fytas, and M. Montagna. Eigenvibrations of submicrometer colloidal spheres. *The Journal of Physical Chemistry Letters*, 1(16):2440–2444, 2010.

[37] L. Giovannini, F. Nizzoli, and A. Marvin. Theory of surface acoustic phonon normal modes and light scattering cross section in a periodically corrugated surface. *Phys. Rev. Lett.*, 69:1572–1575, 1992.

[38] F. Bencivenga, A. Battistoni, D. Fioretto, A. Gessini, J. R. Sandercock, and C. Masciovecchio. A high resolution ultraviolet brillouin scattering set-up. *Review of Scientific Instruments*, 83(10):103102, 2012.

[39] C. Masciovecchio, F. Bencivenga, and A. Gessini. Water dynamics at the nanoscale. *Condensed Matter Physics*, 11(1):47–56, 2008.

[40] P. Benassi, R. Eramo, A. Giugni, M. Nardone, and M. Sampoli. A spectrometer for high-resolution and high-contrast brillouin spectroscopy in the ultraviolet. *Review of Scientific Instruments*, 76(1):013904, 2005.

[41] F. Palombo, M. Madami, N. Stone, and D. Fioretto. Mechanical mapping with chemical specificity by confocal brillouin and raman microscopy. *Analyst*, 139(4):729–733, 2014.

[42] I. Jackson. Earth science: Lower mantle may be rich in silica. *Nature*, 485(7396):51–52, 2012.

[43] C. Masciovecchio, D. Cocco, and A. Gessini. Inelastic ultra-violet scattering as a tool to investigate collective excitations in condensed matter physics. *AIP Conference Proceedings*, 705(1):1190–1196, 2004.

[44] T. Tanaka and H. Kitamura. Figure-8 undulator as an insertion device with linear polarization and low on-axis power density. *Nuclear Instruments and Methods in Physics Research Section A: Accelerators, Spectrometers, Detectors and Associated Equipment*, 364(2):368 – 373, 1995.

[45] A. Messiah. *Quantum Mechanics*. Dover Publications, NY, 1999.

[46] E. Vauthey. *Introduction to nonlinear optical spectroscopic techniques for investigating ultrafast processes*. Univ. of Geneva, 2006.

[47] S. T. Cundiff and S. Mukamel. Optical multidimensional coherent spectroscopy. *Physics Today*, 66(7):44, 2013.

[48] L. Dhar, J. A. Rogers, and K. A. Nelson. Time-resolved vibrational spectroscopy in the impulsive limit. *Chemical Reviews*, 94(1):157–193, 1994.

[49] R. W. Boyd. *Nonlinear optics (Third Edition)*. Academic Press, 2010.

[50] F. Bencivenga, S. Baroni, C. Carbone, M. Chergui, M. B. Danailov, G. De Ninno, M. Kiskinova, L. Raimondi, C. Svetina, and C. Masciovecchio. Nanoscale dynamics by short-wavelength four wave mixing experiments. *New Journal of Physics*, 15(12):123023, 2013.

[51] H.J.Eichler, P. Günter, and D.W. Pohl. *Laser-Induced Dynamic Gratings*. Springer-Verlag, Berlin Heidelberg, 1986.

[52] A. A. Maznev, K. A. Nelson, and J.A. Rogers. Optical heterodyne detection of laser-induced gratings. *Opt. Lett.*, 23(16):1319–1321, 1998.

[53] R. Torre. *Time-Resolved Spectroscopy in Complex Liquids. An Experimental Perspective.* Springer, 2008.

[54] L. Onsager. Reciprocal relations in irreversible processes. i. *Phys. Rev.*, 37:405–426, 1931.

[55] L. Onsager. Reciprocal relations in irreversible processes. ii. *Phys. Rev.*, 38:2265–2279, 1931.

[56] C. J. Montrose, V. A. Solovyev, and T. A. Litovitz. Brillouin scattering and relaxation in liquids. *The Journal of the Acoustical Society of America*, 43(1):117–130, 1968.

[57] H. Callen and T. Welton. Irreversibility and generalized noise. *Phys. Rev.*, 83:34–40, Jul 1951.

[58] W. Bernard and H. Callen. Irreversible thermodynamics of nonlinear processes and noise in driven systems. *Rev. Mod. Phys.*, 31:1017–1044, Oct 1959.

[59] R. Kubo. Statistical-mechanical theory of irreversible processes. i. general theory and simple applications to magnetic and conduction problems. *Journal of the Physical Society of Japan*, 12(6):570–586, 1957.

[60] J.P. Hansen and I.R. McDonald. *Theory of Simple Liquids (Third Edition)*. Academic Press, 2006.

[61] H. Mori. Transport, collective motion, and brownian motion. *Progress of Theoretical Physics*, 33(3):423–455, 1965.

[62] H. Mori. A continued-fraction representation of the time-correlation functions. *Progress of Theoretical Physics*, 34(3):399–416, 1965.

[63] Zwanzig. Lectures in theoretical physics. volume 3. Wiley Interscience, New York, 1961.

[64] Lovesey S. W. Marshall W. *Theory of thermal neutron scattering*. Oxford, London, 1971.

[65] J. P. Boon and S. Yip. *Molecular hydrodynamics*. McGraw-Hill New York ; London, 1980.

[66] U. Balucani and M. Zoppi. *Dynamics of the Liquid State*. Oxford science publications. Clarendon Press, 1994.

[67] G. Ruocco, F. Sette, R. Di Leonardo, G. Monaco, M. Sampoli, T. Scopigno, and G. Viliani. Relaxation processes in harmonic glasses? *Phys. Rev. Lett.*, 84:5788–5791, Jun 2000.

[68] T. T. Bopp. Magnetic resonance studies of anisotropic molecular rotation in liquid acetonitrile-d3. *The Journal of Chemical Physics*, 47(9):3621–3626, 1967.

[69] T. E. Bull and J. Jonas. Effect of pressure on the anisotropic reorientation of acetonitrile-d3 in the liquid state. *The Journal of Chemical Physics*, 53(8):3315–3317, 1970.

[70] T. Tokuhiro, J. Freer, and K.W. Woo. Frequency dependence of intermolecular proton spin-lattice relaxation rate and pair-diffusion constant in neat acetonitrile-d2. *Chemical Physics Letters*, 65(3):613 – 615, 1979.

[71] W. G. Rothschild. Molecular motion in liquids: Rotational and vibrational relaxation in highly polar and strongly associated systems. *The Journal of Chemical Physics*, 57(2):991–1002, 1972.

[72] J. Schroeder, V. H. Schiemann, P. T. Sharko, and J. Jonas. Raman study of vibrational dephasing in liquid ch3cn and cd3cn. *The Journal of Chemical Physics*, 66(7):3215–3226, 1977.

[73] J. E. Griffiths. Molecular reorientational motion in liquid acetonitrile: Raman band shapes, diffusion constants and activation energy of reorientation. *The Journal of Chemical Physics*, 59(2):751–758, 1973.

[74] H. Bertagnolli, P. Chieux, and M.D. Zeidler. A neutron-diffraction study of liquid acetonitrile. *Molecular Physics*, 32(3):759–773, 1976.

[75] H. Bertagnolli, P. Chieux, and M.D. Zeidler. A neutron-diffraction study of liquid acetonitrile. *Molecular Physics*, 32(6):1731–1736, 1976.

[76] H. Bertagnolli and M.D. Zeidler. Molecular pair-correlation function of liquid acetonitrile from x-ray and neutron-diffraction studies. *Molecular Physics*, 35(1):177–192, 1978.

[77] R. Niepmann. Thermodynamic properties of acetonitrile 1. speeds of sound between 240 and 475 k and up to 60 {MPa}. *The Journal of Chemical Thermodynamics*, 16(8):779 – 785, 1984.

[78] W. E. Putnam, D. M. McEachern, and J. E. Kilpatrick. Entropy and related thermodynamic properties of acetonitrile (methyl cyanide). *The Journal of Chemical Physics*, 42(2):749–755, 1965.

[79] S. Miyanaga, K. Tamura, and S. Murakami. Excess molar volumes, isentropic and isothermal compressibilities, and isochoric heat capacities of (acetonitrile + benzene), (benzene + dimethylformamide), and (acetonitrile + dimethylformamide) at the temperature 298.15 k. *The Journal of Chemical Thermodynamics*, 24(10):1077 – 1086, 1992.

[80] A.M. Kolker, M.V. Kulikov, and Al.G. Krestov. Volumes and heat capacities of binary non-aqueous mixtures. part 2. the systems acetonitrile-n,n-dimethylformamide and acetonitrile-hexamethylphosphoric triamide. *Thermochimica Acta*, 211(0):73 – 84, 1992.

[81] Marcus Y. *The properties of solvents*. Wiley Series in Solution Chemistry. John Wiley & Sons, 1998.

[82] C. Caleman, P. J. van Maaren, M. Hong, J. S. Hub, L. T. Costa, and D. van der Spoel. Force field benchmark of organic liquids: Density, enthalpy of vaporization, heat capacities, surface tension, isothermal compressibility, volumetric expansion coefficient, and dielectric constant. *Journal of Chemical Theory and*

Computation, 8(1):61–74, 2012. PMID: 22241968.

[83] T. E. Daubert and R. P. Danner. *Data compilation tables of properties of pure compounds*. 1985.

[84] T. E. Daubert and R. P. Danner. Physical and thermodynamic properties of pure chemicals: data compilation. 1989.

[85] K. Marsh. *Recommended reference materials for the realization of physicochemical properties*. Blackwell Scientific Publications Oxford, UK, 1987.

[86] Lei Q.F., Lin R.S., Ni D.Y., and Hou Y.C. Thermal conductivities of some organic solvents and their binary mixtures. *Journal of Chemical & Engineering Data*, 42(5):971–974, 1997.

[87] T.A. Litovitz K.F. Herzfeld. *Absorption and Dispersion of Ultrasonic Waves*. Academic Press, London, 1965.

[88] A. M. Nikitin and A. P. Lyubartsev. New six-site acetonitrile model for simulations of liquid acetonitrile and its aqueous mixtures. *Journal of computational chemistry*, 28(12):2020–2026, 2007.

[89] JJ Salacuse, AR Denton, and PA Egelstaff. Finite-size effects in molecular dynamics simulations: Static structure factor and compressibility. i. theoretical method. *Physical Review E*, 53(3):2382, 1996.

[90] Jincheng Du, Chris J Benmore, Rene Corrales, Robert T Hart, and JK Richard Weber. A molecular dynamics simulation interpretation of neutron and x-ray diffraction measurements on single phase y2o3–al2o3 glasses. *Journal of Physics: Condensed Matter*, 21(20):205102, 2009.

[91] E Lorch. Neutron diffraction by germania, silica and radiation-damaged silica glasses. *Journal of Physics C Solid State Physics*, 2, 2 1969.

[92] Don T Cromer and Joseph B Mann. X-ray scattering factors computed from numerical hartree-fock wave functions. *Acta Crystallographica Section A: Crystal Physics, Diffraction, Theoretical and General Crystallography*, 24(2):321–324, 1968.

[93] CS Hsu, David Chandler, and L-J_ Lowden. Applications of the rism equation to diatomic fluids: the liquids nitrogen, oxygen and bromine. *Chemical Physics*, 14(2):213–228, 1976.

[94] Roger Gilmont. Liquid viscosity correlations for flowmeter calculations. *Chemical engineering progress*, 98(10):36–41, 2002.

[95] A Tokmakoff. Orientational correlation functions and polarization selectivity for nonlinear spectroscopy of isotropic media. i. third order. *The Journal of chemical physics*, 105(1):1–12, 1996.

[96] RW Hellwarth. Third-order optical susceptibilities of liquids and solids. *Progress in Quantum Electronics*, 5:1–68, 1977.

[97] DA Kleinman. Nonlinear dielectric polarization in optical media. *Physical Review*, 126(6):1977, 1962.

[98] S Ruhman, Leah R Williams, Alan G Joly, Bern Kohler, and Keith A Nelson. Nonrelaxational inertial motion in carbon disulfide liquid observed by femtosecond time-resolved impulsive stimulated scattering. *Journal of Physical Chemistry*, 91(9):2237–2240, 1987.

[99] Peter Voehringer and Norbert F Scherer. Transient grating optical heterodyne detected impulsive stimulated raman scattering in simple liquids. *The Journal*

of Physical Chemistry, 99(9):2684–2695, 1995.

[100] Jon Applequist, James R Carl, and Kwok-Kueng Fung. Atom dipole interaction model for molecular polarizability. application to polyatomic molecules and determination of atom polarizabilities. *Journal of the American Chemical Society*, 94(9):2952–2960, 1972.

[101] AK Burnham, GR Alms, and WH Flygare. The local electric field. i. the effect on isotropic and anisotropic rayleigh scattering. *The Journal of Chemical Physics*, 62(8):3289–3297, 1975.

[102] M Khalil, Oleg Golonzka, N Demirdöven, CJ Fecko, and A Tokmakoff. Polarization-selective femtosecond raman spectroscopy of isotropic and anisotropic vibrational dynamics in liquids. *Chemical Physics Letters*, 321(3):231–237, 2000.

[103] P Foggi, P Bartolini, M Bellini, MG Giorgini, A Morresi, P Sassi, and RS Cataliotti. Intermolecular and diffusive dynamics of pure acetonitrile isotopomers studied by depolarized rayleigh scattering and femtosecond optical kerr effect. *The European Physical Journal D-Atomic, Molecular, Optical and Plasma Physics*, 21(2):143–151, 2002.

[104] Werner Kunz, P Calmettes, and M-C Bellissent-Funel. Dynamics of liquid acetonitrile at high frequencies. *The Journal of chemical physics*, 99(3):2079–2082, 1993.

[105] M. H. Kuok, H. S. Lim, S. C. Ng, N. N. Liu, and Z. K. Wang. Brillouin study of the quantization of acoustic modes in nanospheres. *Phys. Rev. Lett.*, 90:255502, Jun 2003.

[106] M. Montagna. Brillouin and raman scattering from the acoustic vibrations of spherical particles with a size comparable to the wavelength of the light. *Phys. Rev. B*, 77:045418, Jan 2008.

[107] T. Still, W. Cheng, M. Retsch, U. Jonas, and G. Fytas. Colloidal systems: a promising material class for tailoring sound propagation at high frequencies. *Journal of Physics: Condensed Matter*, 20(40):404203, 2008.

[108] J. R. Sandercock. Simple stabilization scheme for maintenance of mirror alignment in a scanning fabry-perot interferometer. *Journal of Physics E: Scientific Instruments*, 9(7):566, 1976.

[109] R. D. Mountain. Spectral distribution of scattered light in a simple fluid. *Rev. Mod. Phys.*, 38:205–214, Jan 1966.

[110] Eberhard Burkel. Phonon spectroscopy by inelastic x-ray scattering. *Reports on Progress in Physics*, 63(2):171, 2000.

[111] S. W. Lovesey. *Theory of neutron scattering from condensed matter*. International Series of Monographs on Physics 72. Clarendon Press, 1986.

[112] Bernhard Adams. Nonlinear x-ray optics: The next phase for x-rays. *Nature Physics*, 7:675–676, 2011.

[113] Lukas Gallmann, Claudio Cirelli, , and Ursula Keller. Attosecond science: Recent highlights and future trends. *Annual Review of Physical Chemistry*, 63:447–469, 2012.

[114] P. Emma, R. Akre, J. Arthur, R. Bionta, C. Bostedt, J. Bozek, A. Brachmann, P. Bucksbaum, R. Coffee, F.J. Decker, Y. Ding, D. Dowell, S. Edstrom, A. Fisher, J. Frisch, S. Gilevich, J. Hastings, G. Hays, P. Hering, Z. Huang,

R. Iverson, H. Loos, M. Messerschmidt, A. Miahnahri, S. Moeller, H.-D. Nuhn, G. Pile, D. Ratner, J. Rzepiela, D. Schultz, T. Smith, P. Stefan, H. Tompkins, J. Turner, J. Welch, W. White, J. Wu, G. Yocky, and J. Galayda. First lasing and operation of an Ã¥ngstrom-wavelength free-electron laser. *Nature Photonics*, 4(9):641–647, 2010. cited By (since 1996)819.

[115] E. Allaria, R. Appio, L. Badano, W. A. Barletta, S. Bassanese, S. G. Biedron, A. Borga, E. Busetto, D. Castronovo, P. Cinquegrana, S. Cleva, D. Cocco, M. Cornacchia, P. Craievich, I. Cudin, G. D'Auria, M. Dal Forno, M. B. Danailov, R. De Monte, G. De Ninno, P. Delgiusto, A. Demidovich, S. Di Mitri, B. Diviacco, A. Fabris, R. Fabris, W. Fawley, M. Ferianis, E. Ferrari, S. Ferry, L. Froehlich, P. Furlan, G. Gaio, F. Gelmetti, L. Giannessi, M. Giannini, R. Gobessi, R. Ivanov, E. Karantzoulis, M. Lonza, A. Lutman, B. Mahieu, M. Milloch, S. V. Milton, M. Musardo, I. Nikolov, S. Noe, F. Parmigiani, G. Penco, M. Petronio, L. Pivetta, M. Predonzani, F. Rossi, L. Rumiz, A. Salom, C. Scafuri, C. Serpico, P. Sigalotti, S. Spampinati, C. Spezzani, M. Svandrlik, C. Svetina, S. Tazzari, M. Trovo, R. Umer, A. Vascotto, M. Veronese, R. Visintini, M. Zaccaria, D. Zangrando, and M. Zangrando. Highly coherent and stable pulses from the FERMI seeded free-electron laser in the extreme ultraviolet. *Nature Photonics*, 6(10):699–704, 2012.

[116] A. A. Lutman, R. Coffee, Y. Ding, Z. Huang, J. Krzywinski, T. Maxwell, M. Messerschmidt, and H.D. Nuhn. Experimental demonstration of femtosecond two-color x-ray free-electron lasers. *Phys. Rev. Lett.*, 110:134801, Mar 2013.

[117] E. Allaria, F. Bencivenga, R. Borghes, F. Capotondi, D. Castronovo, P. Charalambous, P. Cinquegrana, M.B. Danailov, G. De Ninno, A. Demidovich, S. Di Mitri, B. Diviacco, D. Fausti, W.M. Fawley, E. Ferrari, L. Froehlich, D. Gauthier, A. Gessini, L. Giannessi, R. Ivanov, M. Kiskinova, G. Kurdi, B. Mahieu, N. Mahne, I. Nikolov, C. Masciovecchio, E. Pedersoli, G. Penco, L. Raimondi, C. Serpico, P. Sigalotti, S. Spampinati, C. Spezzani, C. Svetina, M. Trovó, and M. Zangrando. Two-colour pump-probe experiments with a twin-pulse-seed extreme ultraviolet free-electron laser. *Nature Communications*, 4, 2013. cited By (since 1996)17.

[118] T. Hara, Y. Inubushi, T. Katayama, T. Sato, H. Tanaka, T. Tanaka, T. Togashi, K. Togawa, K. Tono, M. Yabashi, and T. Ishikawa. Two-colour hard x-ray free-electron laser with wide tunability. *Nature Communications*, 4, 2013. cited By (since 1996)3.

[119] G. Marcus, G. Penn, and A. A. Zholents. Free-electron laser design for four-wave mixing experiments with soft-x-ray pulses. *Phys. Rev. Lett.*, 113:024801, Jul 2014.

[120] Satoshi Tanaka and Shaul Mukamel. Coherent x-ray raman spectroscopy: A nonlinear local probe for electronic excitations. *Phys. Rev. Lett.*, 89:043001, Jul 2002.

[121] F. Bencivenga and C. Masciovecchio. Fel-based transient grating spectroscopy to investigate nanoscale dynamics. *Nuclear Instruments and Methods in Physics Research Section A: Accelerators, Spectrometers, Detectors and Associated Equipment*, 606(3):785 – 789, 2009.

[122] R. Cucini, F. Bencivenga, M. Zangrando, and C. Masciovecchio. Technical advances of the TIMER project. *Nuclear Instruments and Methods in Physics Research A*, 635:69, April 2011.

[123] R. Cucini, F. Bencivenga, and C.Masciovecchio. All-reflective femtosecond optical pump–probe setup for transient grating spectroscopy. *Opt. Lett.*, 36(7):1032–1034, Apr 2011.

[124] F. Bencivenga, F. Capotondi, F. Casolari, F. Dallari, M. B. Danailov, G. De Ninno, D. Fausti, M. Kiskinova, M. Manfredda, C. Masciovecchio, and E. Pedersoli. Multi-colour pulses from seeded free-electron-lasers: towards the development of non-linear core-level coherent spectroscopies. *Faraday Discuss.*, 2014.

[125] S. Mukamel. *Principles of Nonlinear Optical Spectroscopy*. Oxford University Press, 1995.

[126] Riccardo Cucini, Andrea Battistoni, Alessandro Gessini, Filippo Bencivenga, Emiliano Principi, Makina Saito, Francesco D'Amico, Rudi Sergo, and Claudio Masciovecchio. Determination of dynamical parameters in liquids by homodyne transient grating spectroscopy at large angles. *Opt. Lett.*, 39(17):5110–5113, Sep 2014.

[127] B. Patterson. Resource letter on stimulated inelastic x-ray scattering at an xfel. Report SLAC-TN-10-026, SLAC, Stanford, CA, USA, 2010.

[128] T.E. Glover, D.M. Fritz, M. Cammarata, T.K. Allison, S. Coh, J.M. Feldkamp, H. Lemke, D. Zhu, Y. Feng, R.N. Coffee, M. Fuchs, S. Ghimire, J. Chen, S. Shwartz, D.A. Reis, S.E. Harris, and J.B. Hastings. X-ray and optical wave mixing. *Nature*, 488(7413):603–608, 2012. cited By (since 1996)24.

[129] K. Tamasaku, K. Sawada, E. Nishibori, and T. Ishikawa. Visualizing the local optical response to extreme-ultraviolet radiation with a resolution of i Î»/380. *Nature Physics*, 7(9):705–708, 2011. cited By (since 1996)8.

[130] S. Shwartz, M. Fuchs, J.B. Hastings, Y. Inubushi, T. Ishikawa, T. Katayama, D.A. Reis, T. Sato, K. Tono, M. Yabashi, S. Yudovich, and S.E. Harris. X-ray second harmonic generation. *Physical Review Letters*, 112(16), 2014. cited By (since 1996)2.

[131] Miltcho B. Danailov, Filippo Bencivenga, Flavio Capotondi, Francesco Casolari, Paolo Cinquegrana, Alexander Demidovich, Erika Giangrisostomi, Maya P. Kiskinova, Gabor Kurdi, Michele Manfredda, Claudio Masciovecchio, Riccardo Mincigrucci, Ivaylo P. Nikolov, Emanuele Pedersoli, Emiliano Principi, and Paolo Sigalotti. Towards jitter-free pump-probe measurements at seeded free electron laser facilities. *Opt. Express*, 22(11):12869–12879, Jun 2014.

[132] JA Armstrong, N Bloembergen, J Ducuing, and PS Pershan. Interactions between light waves in a nonlinear dielectric. *Physical Review*, 127(6):1918, 1962.

[133] RI Tobey, ME Siemens, MM Murnane, HC Kapteyn, DH Torchinsky, and KA Nelson. Transient grating measurement of surface acoustic waves in thin metal films with extreme ultraviolet radiation. *Applied physics letters*, 89(9):091108, 2006.

[134] Emily F Sistrunk, Jakob Grilj, Jaewoo Jeong, Mahesh G Samant, Alexander X

Gray, Hermann A Durr, Stuart S Parkin, and Markus Gühr. Extreme ultraviolet transient grating measurement of insulator-metal transition dynamics of vo 2. In *International Conference on Ultrafast Phenomena*, pages 09–Wed. Optical Society of America, 2014.

[135] Mark A Foster, Amy C Turner, Jay E Sharping, Bradley S Schmidt, Michal Lipson, and Alexander L Gaeta. Broad-band optical parametric gain on a silicon photonic chip. *Nature*, 441(7096):960–963, 2006.

[136] Vincent Boyer, Alberto M Marino, Raphael C Pooser, and Paul D Lett. Entangled images from four-wave mixing. *Science*, 321(5888):544–547, 2008.

[137] F Capotondi, E Pedersoli, N Mahne, RH Menk, G Passos, L Raimondi, C Svetina, G Sandrin, M Zangrando, M Kiskinova, et al. Invited article: Coherent imaging using seeded free-electron laser pulses with variable polarization: First results and research opportunities. *Review of Scientific Instruments*, 84(5):051301, 2013.

[138] M Zangrando, A Abrami, D Bacescu, I Cudin, C Fava, F Frassetto, A Galimberti, R Godnig, D Giuressi, L Poletto, et al. The photon analysis, delivery, and reduction system at the fermi@ elettra free electron laser user facility. *Review of Scientific Instruments*, 80(11):113110, 2009.

[139] P Cinquegrana, S Cleva, A Demidovich, G Gaio, R Ivanov, G Kurdi, I Nikolov, P Sigalotti, and MB Danailov. Optical beam transport to a remote location for low jitter pump-probe experiments with a free electron laser. *Physical Review Special Topics-Accelerators and Beams*, 17(4):040702, 2014.

[140] Cornelius Gahl, Armin Azima, Martin Beye, Martin Deppe, Kristian Döbrich, Urs Hasslinger, Franz Hennies, Alexej Melnikov, Mitsuru Nagasono, Annette Pietzsch, et al. A femtosecond x-ray/optical cross-correlator. *Nature Photonics*, 2(3):165–169, 2008.

[141] AG Kalampounias, SN Yannopoulos, and GN Papatheodorou. Temperature-induced structural changes in glassy, supercooled, and molten silica from 77 to 2150 k. *The Journal of chemical physics*, 124(1):014504, 2006.

[142] B Hehlen, E Courtens, R Vacher, A Yamanaka, M Kataoka, and K Inoue. Hyper-raman scattering observation of the boson peak in vitreous silica. *Physical review letters*, 84(23):5355, 2000.

[143] U Buchenau, N Nücker, and AJ Dianoux. Neutron scattering study of the low-frequency vibrations in vitreous silica. *Physical Review Letters*, 53(24):2316, 1984.